TECHNISCHE UNIVERSITÄT MÜNCHEN
MAX-PLANCK-INSTUTUT FÜR ASTROPHYSIK

Simulations of the formation of a Milky Way like galaxy

Markus Andreas Wadepuhl

Vollständiger Abdruck der von der Fakultät für Physik der Technischen Universität München zur Erlangung des akademischen Grades eines

Doktors der Naturwissenschaften

genehmigten Dissertation.

Vorsitzender: Univ.-Prof. Shawn Bishop, Ph.D

Prüfer der Dissertation:

1. Hon.-Prof. Dr. Wolfgang Hillebrandt

2. Univ.-Prof. Dr. Wolfram Weise

Die Dissertation wurde am 16.01.2012 bei der Technischen Universität München eingereicht und durch die Fakultät für Physik am 23.02.2012 angenommen.

Contents

Page

1 Introduction 5
1.1 Motivation . . . 5
1.2 The cosmological standard model . . . 7
1.3 The formation of disk galaxies . . . 10
1.4 The puzzling abundance of satellite galaxies . . . 11

2 Numerical Methodology 14
2.1 Gravitational dynamics . . . 15
2.2 Hydrodynamics . . . 16
2.2.1 Smoothed particle hydrodynamics in GADGET . . . 17
2.2.2 The moving-mesh code AREPO . . . 18
2.3 Baryonic Physics . . . 20
2.3.1 Star formation and thermal feedback . . . 21
2.3.2 Wind model . . . 22
2.3.3 AGN feedback . . . 22
2.3.4 Cosmic Rays . . . 23
2.4 Initial Conditions . . . 24

3 Satellite galaxies in hydrodynamical simulations of Milky Way like galaxies 25
3.1 Introduction . . . 26
3.2 Methodology . . . 29
3.2.1 Star formation model . . . 29
3.2.2 Simulation set and analysis . . . 30
3.3 Observational knowledge . . . 32
3.4 Abundance of luminous satellites . . . 32
3.4.1 Kinematic results . . . 36
3.5 History of satellite galaxies . . . 37
3.6 Scaling relations . . . 44
3.7 Conclusions . . . 48

4 The Aquila cosmological code comparison project 54
4.1 Introduction . . . 55
4.2 Code descriptions . . . 56
4.2.1 GADGET3 models . . . 56
4.2.2 The CS model . . . 56
4.2.3 The TO model . . . 58
4.2.4 The GIMIC model . . . 58
4.2.5 The MM model . . . 59
4.2.6 The CK model . . . 59
4.2.7 The Gasoline model . . . 59

4.2.8 The Arepo model 60
4.2.9 The Ramses models 60
4.3 Initial conditions 60
4.4 Measurement definitions 63
4.5 Results 64
4.5.1 Morphology 64
4.5.2 Galaxy formation efficiency 66
4.5.3 Galaxy size 68
4.5.4 Circular velocities 70
4.5.5 Stellar mass assembly 72
4.5.6 Disk and stellar mass assembly 73
4.5.7 Gas fractions 76
4.5.8 Tully-Fisher relation 76
4.6 Conclusions 77

5 Effects of feedback physics and hydrodyn. technique in sim. of disk galaxy formation 82
5.1 Introduction 83
5.2 Simulation methodology 85
5.2.1 Initial conditions 85
5.2.2 Simulation codes 86
5.2.3 Models for star formation and cooling 89
5.3 Gaseous disks in AREPO and GADGET 93
5.3.1 Star formation histories of model galaxies 97
5.3.2 Growth history of halos 97
5.3.3 Kinematics of gaseous disks 101
5.3.4 The structure of the cold gas 101
5.4 Stellar mass mass distribution of the simulated galaxies 107
5.4.1 Kinematic disk and bulge components 111
5.4.2 Comparison with observational constraints 113
5.5 Convergence and global differences 113
5.5.1 Resolution study 113
5.5.2 Clumpy halos 114
5.6 Conclusions 115

6 Final conclusions and outlook 118

References 122
List of figures 122
List of tables 124
Bibliography 125

1 Introduction

Contents

1.1 Motivation 5
1.2 The cosmological standard model 7
1.3 The formation of disk galaxies 10
1.4 The puzzling abundance of satellite galaxies 11

1.1 Motivation

Modern cosmology can be considered a comparatively young research field, certainly in light of its close connection to one of the oldest, if not the oldest, science of all – astronomy. The foundations of modern cosmology where only laid in the beginning of the 20th century when Albert Einstein published his works on special (Einstein, 1905) and general (Einstein, 1915) relativity, and when Edwin Hubble (Hubble, 1925) realized the connection between the distance of galaxies and the redshift of their spectra. Together with simple solutions of Einstein's field equations (by Lemaitre, Friedman, Robertson, Walker, de Sitter, Minkowski, and others), this led to a dynamic description of the Universe, cumulating less than a 100 years later in the cosmological standard model as we know it today.

In addition to these advances on the very large scales, great discoveries were also made on much smaller scales. In December 1924, Hubble was able to resolve the outer regions of the Andromeda galaxy (M 31 or NGC 224) into individual stars, discovering several Cepheid variable stars from which he was able to proof in 1925 that Andromeda is a galaxy on its own, and not just a "nebula" inside the Milky Way (Hubble, 1925). In fact, Hubble coined the term "galaxy" to clarify the distinction between galactic nebula and extragalactic nebula (galaxies). Back at that time, all objects with a fuzzy appearance were called nebulae, even the so-called spiral nebulae. The "Map of Nebulae" of Charlier (1922), (Peebles, 1993) shows the distribution of all objects classified as nebulae at that time. In fact, most of these objects were discovered to be indeed spiral galaxies like our own Milky Way, clearly underlining the importance of this class of galaxies. On the other hand, other galaxy morphologies were identified as well, including large elliptical galaxies with different degrees of roundness. Explaining the origin of these different shapes of galaxies, and hence the morphological classification of galaxies expressed in Hubble's famous tuning-fork diagram shown in Figure 1.1 has become a major goal of physical cosmology.

Despite much progress in recent decades towards developing a successful theory of galaxy formation like the 'bottom up' theory of galaxy formation (e.g. Rees & Ostriker, 1977; White & Rees, 1978; Longair, 1999), a full understanding of all the relevant processes in forming a spiral galaxy has remained an elusive goal towards this day. However,

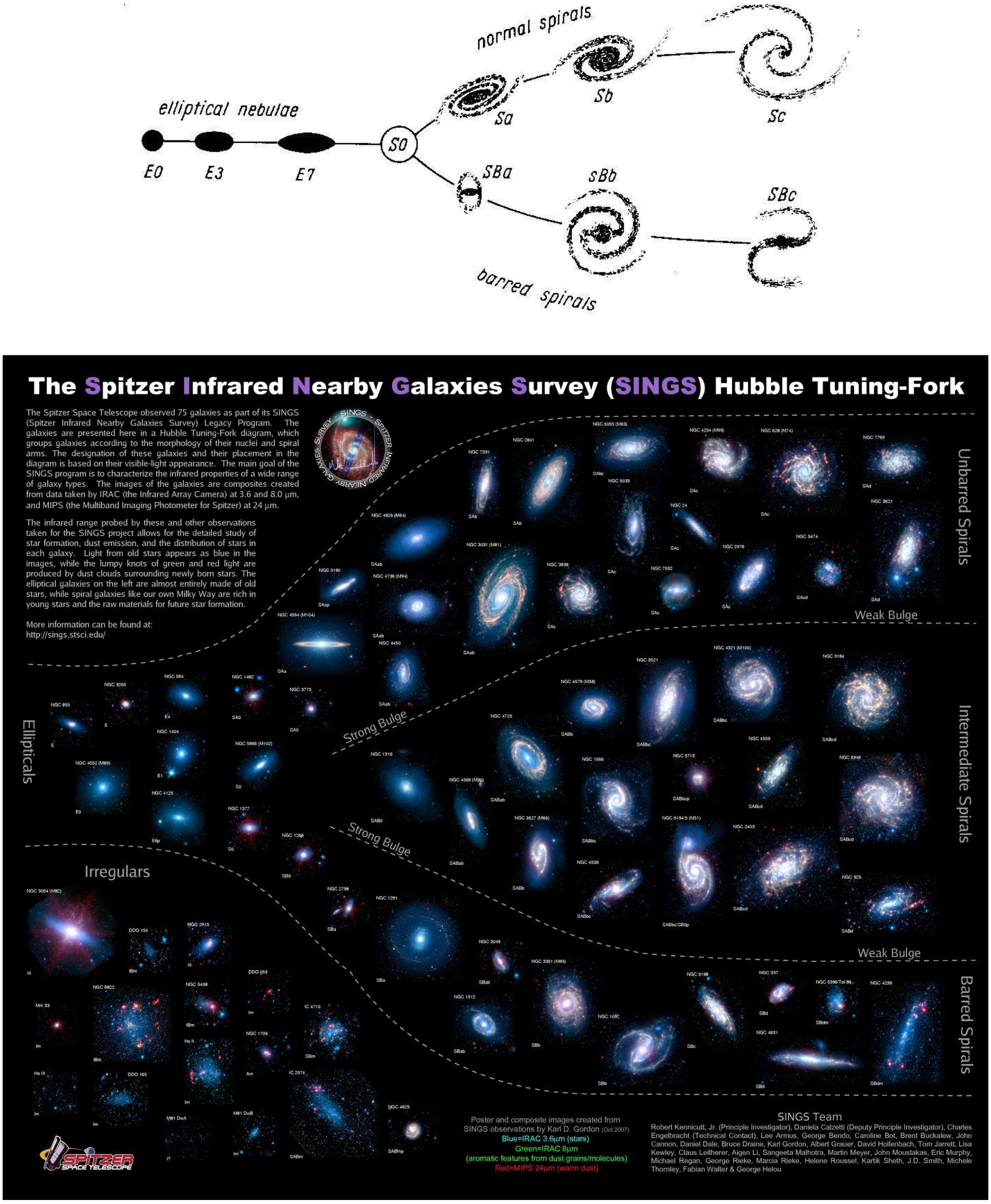

The Spitzer Infrared Nearby Galaxies Survey (SINGS) Hubble Tuning-Fork

The Spitzer Space Telescope observed 75 galaxies as part of its SINGS (Spitzer Infrared Nearby Galaxies Survey) Legacy Program. The galaxies are presented here in a Hubble Tuning-Fork diagram, which groups galaxies according to the morphology of their nuclei and spiral arms. The designation of these galaxies and their placement in the diagram is based on their visible-light appearance. The main goal of the SINGS program is to characterize the infrared properties of a wide range of galaxy types. The images of the galaxies are composites created from data taken by IRAC (the Infrared Array Camera) at 3.6 and 8.0 µm, and MIPS (the Multiband Imaging Photometer for Spitzer) at 24 µm.

The infrared range probed by these and other observations taken for the SINGS project allows for the detailed study of star formation, dust emission, and the distribution of stars in each galaxy. Light from old stars appears as blue in the images, while the lumpy knots of green and red light are produced by dust clouds surrounding newly born stars. The elliptical galaxies on the left are almost entirely made of old stars, while spiral galaxies like our own Milky Way are rich in young stars and the raw materials for future star formation.

More information can be found at:
http://sings.stsci.edu/

Poster and composite images created from SINGS observations by Karl D. Gordon (Oct 2007)
Blue=IRAC 3.6µm (stars)
Green=IRAC 8µm
(aromatic features from dust grains/molecules)
Red=MIPS 24µm (warm dust)

SINGS Team

Robert Kennicutt, Jr. (Principle Investigator), Daniela Calzetti (Deputy Principle Investigator), Charles Engelbracht (Technical Contact), Lee Armus, George Bendo, Caroline Bot, Brent Buckalew, John Cannon, Daniel Dale, Bruce Draine, Karl Gordon, Albert Grauer, David Hollenbach, Tom Jarrett, Lisa Kewley, Claus Leitherer, Aigen Li, Sangeeta Malhotra, Martin Meyer, John Moustakas, Eric Murphy, Michael Regan, George Rieke, Marcia Rieke, Helene Roussel, Kartik Sheth, J.D. Smith, Michele Thornley, Fabian Walter & George Helou

Figure 1.1: The 'tuning-fork' classification of galaxy morphologies. The top figure is the original version of this diagram introduced by Hubble (1936). The panel in the bottom shows a modern version of this diagram based on the SINGS survey (from the SINGS-team, http://www.stsci.edu).

the emergence of a well-defined background cosmological model with unambiguous initial conditions has made the problem accessible to predictive numerical calculations that follow the physics from briefly after the Big Bang over much of cosmic time towards the present day. Such simulations can follow highly non-linear processes and have become one of the most important methods in theoretical studies of galaxy formation. However, the simulations are very challenging from a numerical point of view, both because of the large dynamic range that needs to be addressed and the large array of diverse physical processes that are involved. Thus far, the results obtained with direct hydrodynamical simulations of galaxy formation have been fraught with a persistent failure to produce realistic disk-dominated galaxies with a structure similar to observed late-type galaxies (e.g. Navarro & Steinmetz, 2000). But gradual progress in the numerical techniques and in the modeling of the relevant physics (e.g. Sommer-Larsen et al., 2003; Okamoto et al., 2005; Scannapieco et al., 2008; Sales et al., 2010; Piontek & Steinmetz, 2011) justifies the hope that new work may be able to make significant progress on this long-standing problem.

It is the primary goal of this thesis to carry out important steps in this direction, by carrying out new simulations of disk galaxy formation that are more advanced than previous work. To this end we will incorporate a more complete description of physical processes in our hydrodynamical models, such as cosmic rays or black hole accretion and feedback. We will also investigate in some detail the influence of numerical technique on the results, in particular what role the hydrodynamical solver (particle-based or mesh-based) plays. Finally, we will also push to much higher numerical resolution than used thus far, and we will compare our results in a large international collaborative project that involves all the leading groups in the field to a set of completely independent simulation codes and physics parametrizations that are applied to the same initial conditions that we use. With this body of numerical experiments, we aim in this thesis to shed new light on the long-standing and important problem of understanding the formation of Milky-Way sized disk galaxies.

In the remaining sections of this introductory chapter, we will first briefly review the current cosmological standard model. We then describe the general paradigm of how disk galaxies are believed to be formed in this model, followed by a description of the so-called satellite problem of Milky Way sized galaxies, which will also be addressed in the thesis. In chapter 2, we will then give a brief summary of the most salient features of the hydrodynamical codes that we use in our simulations. We then turn to a description of our results, which is organized in three main parts. Chapter 3 focuses on the satellite population and describes our results for satellite properties when new physical processes such as cosmic ray feedback are included. In chapter 4, we show how our galaxies compare to other simulations carried out with different techniques in the so-called *Aquila* project. Finally, we present in chapter 5 more detailed results for disk galaxy formation simulations carried out with the GADGET and AREPO codes, where we in particular focus on the changes that are induced by different hydrodynamic solvers, or simple changes in the cooling or feedback prescription. Finally, we shall summarize the main findings of the thesis in chapter 6.

1.2 The cosmological standard model

The findings of modern cosmology have revealed an astonishing picture of the basic properties of the Universe (see for example Cervantes-Cota & Smoot, 2011, for a recent review). Its age, expansion rate, material content and the distribution of matter and energy can today be explained with impressive precision, quite in contrast to the state of affairs not long ago when these quantities were still notoriously uncertain. Today's cosmological standard model (ΛCDM) predicts that most of the matter in the Universe consists of some kind of non-baryonic "cold" dark matter (CDM), which is thought to be a non-relativistic, weakly interacting elementary particle that does not interact with any electromagnetic radiation. An even larger fraction of today's cosmic energy budget is contributed by the so-called dark energy. It provides about 75% of the total energy density of the Universe today and is assumed to cause its observed accelerated expansion. The ordinary baryonic matter we know from the laboratory and which makes up all directly observable objects such as stars, planets, etc., as well as all intra- and extra-galactic gas, only accounts for as little as 4% to the total energy budget. Due to this very uneven partitioning of matter and energy, large scales – where pressure forces are unimportant – are clearly dominated primarily by the two "dark" components. Thus, the formation of large-scale structures in the Universe (e.g. filaments, clusters and large voids) is dominated by dark matter and dark energy, whereas only on the smaller scales of individual galaxies the influence of baryonic physics becomes important. In general, the influence of baryonic matter increases with decreasing mass scale.

The basic concept of dark energy as a repulsive "cosmological constant" was originally introduced by Einstein in his own field equations of general relativity. This concept was picked up by modern cosmology (again), and is a crucial ingredient of the ΛCDM model. Einstein's original motivation for introducing the cosmological constant was however somewhat different to its modern function. Einstein invoked the cosmological constant Λ to find a static solution of his field equations. But later, when it was realized that the Universe does not have to be static and in fact is dynamically expanding as Hubble showed, Einstein dismissed the Λ term again from his equations, famously calling it his "greatest folly". Today, there is consensus that some kind of cosmological constant, or more generally a dark energy term, seems to be necessary to explain the observational data on the large-scale evolution of structure formation, coming for example from distant type Ia supernovae or from surveys of the cosmic microwave background (CMB) radiation. But the physical nature of this component is an even bigger mystery than the dark matter.

As its name already suggests, dark matter is not directly visible, neither in the infrared, optical, ultraviolet, X-ray or in any other part of the electromagnetic spectrum (unless dark matter self-annihilates and produces some gamma-rays, see below). This is because dark matter does not interact with electromagnetic radiation and has in most models only tiny residual weak interactions. In the latter case, a weak annihilation radiation could be caused by dark matter particles, assuming that they are the conjectured lightest supersymmetric particles. Neutralinos for example satisfy this and could self-annihilate as they are their own antiparticles, but the annihilation cross section is expected to be extremely low. However, if present, the faint annihilation radiation might be detected by satellites like FERMI (e.g. Kuhlen et al., 2008) or other gamma-ray observatories. Nevertheless even a detection of an annihilation signal would still be an indirect detection.

The existence of dark matter can be readily inferred from the gravitational force of its mass. These effects are observed on a large range of scales, from dwarf galaxies to large galactic superclusters. In short, all of these observations tell us that the available baryonic matter is not massive enough to explain, for example, why large galaxy clusters are bound or why spiral galaxies are rotating so fast. This hence calls for the existence of an additional dark matter component to provide the needed gravitational forces.

According to the current observational constraints, a fraction of about 85% of all matter is dark matter (about 21% in terms of today's energy density). The impossibility of observing this strange type of matter directly has led to many suggestions about its physical nature. Some of the most prominent candidates are weakly interacting massive particles (WIMPS), like neutralinos or axions, or possibly MACHOs (Massive Astrophysical Compact Halo Objects). The former could be detected by modern particle accelerators (e.g. LHC at CERN) while the latter should show up by their gravitational lensing effects. Nevertheless, it is still not clear what dark matter is really composed of. There are also alternative theories of gravity, such as 'MOdified Newtonian Dynamics' (MOND), which doubt its very existence. However, for the purposes of this work, we will take the existence of dark matter for granted and work within the cosmological standard ΛCDM model, where the dark matter is a massive, weakly interacting elementary particle.

Besides making a statement about the detailed composition of the Universe, the ΛCDM model also specifies the initial conditions for cosmic structure formation. Assuming a hot big bang that involved a primordial episode of exponential expansion (the epoch of cosmic inflation), ΛCDM makes a prediction of the very early state of the Universe, which constitutes the initial conditions for subsequent structure formation, on all scales ranging from giant voids and filaments down to galaxy clusters, individual galaxies and even dwarf galaxies. The epoch of cosmic inflation is believed to transform early quantum mechanical effects into tiny "ripples" in the otherwise homogeneous matter density which were later on amplified by gravity. The typical scales and the power spectrum of these "initial" perturbations from a homogeneous universe can be observed from the cosmic microwave background (CMB) (Alpher et al., 1948; Penzias & Wilson, 1965). Combining these small amplitude perturbations with the dynamically cold dark matter model, one obtains a simple model for the formation of cosmic structures. The driving mechanism for structure growth in this model is the gravitational instability of the small initial density perturbations (see Peebles, 1993, page 511). A slightly over-dense region is going to attract additional material from its close surroundings, hence increasing its own over-density. This process happens slowly in the beginning, and its early evolution can be described rather well using linear perturbation theory. Eventually, the growth of a perturbation accelerates and non-linear terms gain importance, leading finally to gravitational collapse and the virialization of bound objects, so-called *halos*. First, small low-mass structures are formed, which then tend to get ever more massive due to mergers with other structures and the accretion of further material. As a result, bigger halos are formed in a hierarchical, bottom-up fashion.

The linear part of the cosmic structure formation process can be well described using analytical methods. However, the non-linear processes which gain in importance at later times are largely inaccessible with analytical techniques. However, this evolution can be followed in computer simulations far into the non-linear regime. Large supercomputer calculations have hence become a powerful tool to study the profoundly non-linear processes which govern the formation and evolution of cosmic structures. The Millennium simulations (Springel et al., 2005b; Boylan-Kolchin et al., 2009) as well as the Aquarius project (Springel et al., 2008) are examples of state-of-the-art high-resolution simulations of cosmic structure formation, covering a very wide range of scales. In combination with so-called semi-analytic models for galaxy formation, they have been able to make detailed predictions for the galaxy content expected for dark matter halos, which is important for testing and validating the ΛCDM model. Overall, these models have produced quite successful descriptions of the observed galaxy population, reproducing many global measurements as well as the detailed clustering statistics. The coarse description of the baryonic physics in the semi-analytic models is however a major systematic uncertainty, and ideally one would like to directly simulate all the relevant hydrodynamical processes in sufficient detail as well, not just the dark matter and dark energy. A recent review of the cosmological standard model including the Big Bang, the CMB, Big Bang Nucleosynthesis and dark matter can be found in Olive (2010).

1.3 The formation of disk galaxies

The Milky Way's band on the night sky has been observed by mankind since ancient times. Back in 1750, Wright (1750) was probably the first to conjecture that we are residing within a flat layer of stars gravitationally bound to a common center of mass. However, in analogy to the rings of saturn, he considered the Milky Way to feature a large rotating annulus of stars or a huge thin sphere rotating around some sort of center. Some years later, Kant (1755), who was aware of the elliptical shaped nebulae observed by contemporary astronomers as well as of an incomplete summary of Wright's book, effectively introduced the modern concept of the disk-like galatic distribution of stars (Graham, 2011). But it was probably William Herschel in 1785 who made the first empiric attempt (A. Unsoeld, 2005, page 389) to reveal the structure of the Milky Way. Assuming a constant number density of stars, his systematic star counts showed a flattened stellar system with the Earth offset from its center, see Figure 1.2 for Herschel's original figure in his pioneering publication (Herschel, 1785). Later observations confirmed this interpretation.

Assuming a spherical protogalaxy with homogeneous density distribution and solid body rotation together with the assumption that the angular momentum of each mass element is conserved, one can analytically calculate the collapse from a spherical protogalaxy to a rotationally supported disk, see A. Unsoeld (2005, page 477 f.). Comparing this distribution of angular momentum with observations of several Sb- and Sc-galaxies as well as the Milky Way, Crampin & Hoyle (1964) and Oort (1970) were able to show that this formation mechanism is compatible with observations of real galaxies. However, these calculations are based on very idealized initial conditions which are heavily simplified compared to the geometrically complex circumstances of galaxy formation in the cosmic environment, which is characterized by large and small scale perturbations, a hierarchy of galaxy mergers of different mass ratios, and of course by non-linear physical processes such as star formation, supernova explosions, or black hole accretion. It is therefore clear that monolithic galaxy formation models may not be adequate in ΛCDM.

Following the complicated, non-linear processes of gravitationally driven structure growth requires time consuming calculations. Even prior to the age of computers, Holmberg (1941) carried out pioneering 'analog simulations' by investigating the interaction of two disk galaxies using a clever setup of light-bulbs and photocells to experimentally measure out the gravitational forces in terms of the light intensity field. Only much later, Miller & Prendergast (1968); Miller et al. (1969) and Hohl (1970) did some pioneering computer simulations on the evolution of disk galaxies with calculation techniques that are in principal similar to the ones we use today.

Despite the enormous increase in computer power since then, and the way more refined numerical methods available for galaxy formation today, modern simulations are still far from being able to form realistic disk galaxies based on ordinary cosmological initial

Fig. 4.

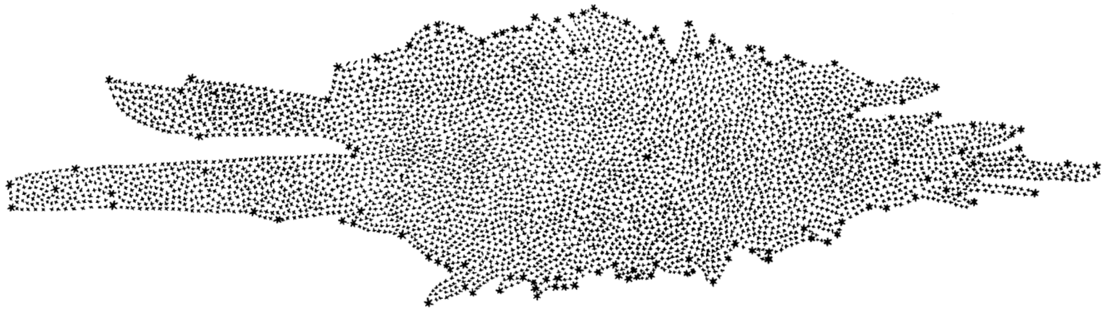

Figure 1.2: Assuming a constant number density of stars, William Herschel inferred the structure of the Milky Way by counting the number of stars in numerous small areas on the sky. His detailed survey showed a flattened stellar system where the position of the Sun was offset from the center. The image shows figure 4 of Herschel (1785).

conditions predicted by the ΛCDM theory. This is believed to be caused by a number of problems in adequately modeling the involved physics, as well as potentially by numerical inaccuracies inherent in the employed techniques. For example, most calculations have suffered from a huge loss of angular momentum of the gas at early times and an extremely high star formation rate within the small progenitor galaxies which later on merge to build the galaxy as it is observable now. In recent years, several authors have proposed different approaches for overcoming these problems, many of them related to parameterizations of various energetic feedback processes (see for example Okamoto et al., 2005, 2008b; Scannapieco et al., 2008, 2009; Agertz et al., 2011), but arguably no compelling solution has been found yet. Instead, it is still unclear which of these claims is the right physical solution, or whether perhaps only a combination of several of them leads to the formation of realistic disk galaxies. It is also possible that the crux of the problem is something completely different that has not been widely considered yet. In this thesis we will explore this important issue further by considering new, advanced simulation models with improved physics and a more accurate hydrodynamical technique, as well as by comparing the results of different simulation codes systematically with each other. For an insightful review of the current knowledge and known problems in galaxy formation (not only restricted to disk galaxies), see Benson (2010), where also the missing satellite problem, addressed in the next section and in chapter 3, is discussed in detail.

1.4 The puzzling abundance of satellite galaxies

High-resolution cosmological simulations of the dark matter component in ΛCDM universes have shown that the the density distribution of dark matter halos is by no means smooth. Rather, these halos exhibit a complex phase-space structure, consisting of thousands of small, gravitationally bound structures that orbit in the halos. These self-bound substructures are the remains of objects that have fallen in during halo assembly. Often they lost much of their outer mass due to the effects of gravitational tidal forces, but the inner parts have still survived. In large clusters of galaxies, it is attractive to associate these dark matter substructures with the galaxies in the cluster. On the scale of Milky-Way sized halos, a corresponding substructure population is predicted by ΛCDM as well

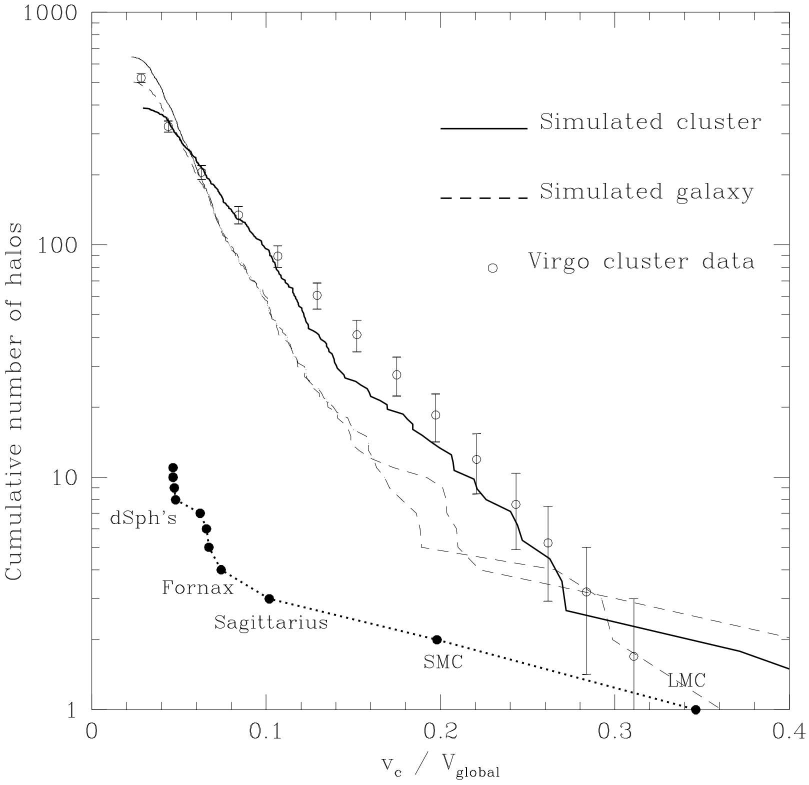

Figure 1.3: The *satellite problem* on galactic scales. This plot by Moore et al. (1999) highlights a significant discrepancy in the abundance of observed satellite galaxies around the Milky Way and the large number of dark matter substructures that are expected in such halos in the ΛCDM cosmology.

(e.g. Springel et al., 2008), but here it is less clear whether it corresponds to observed structures in these systems.

There are of course also luminous substructures in galaxies known from the observational point of view, see for example Mateo (1998). In case of our Galaxy, these substructures are the small dwarf galaxies surrounding the Milky Way. These satellite galaxies span a wide range of mass/luminosity. Again, one would naturally like to identify them with the dark matter substructures expected on simulations of galactic haloes in the ΛCDM. However, a direct comparison of the numbers of these systems as a function of their circular velocity (which is a comparatively robust measure of their size) reveals a huge discrepancy between the number of observed satellite systems and the number of dark matter substructures seen in simulations within halos of approximately the size of the Milky Way (see Figure 1.3). This has been pointed out prominently in two seminal papers by Klypin et al. (1999) and (Moore et al., 1999), and is since then known as the "satellite problem".

This discrepancy, which potentially reaches an order of magnitude or more at the scale of the faintest satellites, opens up a new important problem in the physics of galaxy formation. If the ΛCDM model is right, then there is apparently a large number of substructures that do not contain stars. It is however not clear how it can happen that some dark matter substructures remain *dark* with no observable stellar/gas content while others contain as many stars as the Magellanic Clouds. Evidently, there is no simple one-to-one relation between dark matter substructures and the luminous objects observed as satellite galaxies. The physical details responsible for the real relation between dark matter substructures and satellite galaxies are however not understood in detail.

There are many processes which might affect the evolution of satellite galaxies, for example tidal and ram pressure stripping, a photoheating UV background, supernova feedback, galactic winds, or cosmic rays, to name just the most important suspects. It is important to better understand the interplay of this physics, and hence satellite galaxy formation, because ultimately a resolution of the satellite problem is not only important for the theory of galaxy formation, but also for the viability of the ΛCDM theory. In one of the chapters of this thesis, we will therefore examine the first hydrodynamical simulations of forming Milky Way sized galaxies with enough resolution to study the formation of the satellite population in the proper cosmological context. This will allow us to also study the influence of different physical processes on the final luminosity function of the simulated satellite galaxies and to compare the simulation results with observational constraints.

2 Numerical Methodology

Contents

2.1 Gravitational dynamics 15
2.2 Hydrodynamics 16
2.2.1 Smoothed particle hydrodynamics in GADGET 17
2.2.2 The moving-mesh code AREPO 18
2.3 Baryonic Physics 20
2.3.1 Star formation and thermal feedback 21
2.3.2 Wind model 22
2.3.3 AGN feedback 22
2.3.4 Cosmic Rays 23
2.4 Initial Conditions 24

Summary

This chapter presents a short summary of the most important numerical and computational aspects of this thesis. In particular, the codes for running the simulations are presented here, including their fundamental functionalities and numerical concepts. This technical aspects are especially important for understanding and interpreting the parts of this thesis which deal with the advantages and disadvantages of the various applied numerical methods.

Most simulations discussed in this thesis were produced using the two cosmological codes GADGET (Springel, 2005) and AREPO (Springel, 2010a). Only in chapter 4, results from a number of further codes will be considered, in the context of a code comparison project. This other codes will then be concisely described in the corresponding context, while the following discussion focuses on GADGET and AREPO.

We shall first briefly review how the codes calculate gravitational forces in a cosmological simulation. As structure growth is driven primarily by gravity, this part of the simulations can hardly be overstated in importance. We will then turn to a discussion of the treatment of hydrodynamics, which a central aspect of this work. Only recently, it became feasible to include hydrodynamics in cosmological simulations while resolving spatial scales small enough to model galaxy formation. As this work utilizes two very different numerical schemes to tackle hydrodynamics, we will try to highlight the fundamental differences between these numerical approaches. Finally, in the last section of this chapter we shall describe various ways considered in our simulations of including kinetic and thermal feedback associated with star formation of black hole growth.

2.1 Gravitational dynamics

One of the most commonly used methods in purely gravitational problems is the N-body approach. This technique divides the smooth, continuous mass distribution into a finite number of macro particles of a given mass. Given the set of masses, positions and velocities of all these tracer particles, it is possible to calculate the approximated gravitational potential at any point in space and thus to calculate the gravitational forces acting on each particle. Strictly speaking, the phase-space density of the given matter distribution is sampled with a finite number of representative particles in this approach (see Springel, 2005, for a more detailed description). The dynamics of these particles in the collisionless case (as is appropriate for dark matter and the stars in large galaxies) is then described by the Hamiltonian

$$H = \sum_i \frac{\mathbf{p}_i^2}{2m_i a(t)^2} + \frac{1}{2} \sum_{ij} \frac{m_i m_j \ \varphi(\mathbf{x}_i - \mathbf{x}_j)}{a(t)}, \tag{2.1}$$

which takes into account the assumed expanding background space, described through a Friedman-Lemaître model. Here, $a(t)$ is the cosmological scale factor, $\mathbf{x}_i$ is the comoving coordinate of particle i, and $\mathbf{p}_i = a^2 \mathbf{x}_i$ is its conjugate momentum. Assuming periodic boundary conditions within a cube of size L^3, the interaction potential $\varphi(\mathbf{x})$ is the solution of

$$\nabla^2 \varphi(\mathbf{x}) = 4\pi G \left[-\frac{1}{L^3} + \sum_n \tilde{\delta}(\mathbf{x} - \mathbf{n}L) \right]. \tag{2.2}$$

Here, the mean density is subtracted, resulting in the solution being a so-called 'peculiar potential', which for the full mass distribution is defined by

$$\nabla^2 \Phi(\mathbf{x}) = 4\pi G \left[\rho(x) - \bar{\rho} \right]. \tag{2.3}$$

Hence, the peculiar potential for our finite point set can be written as

$$\Phi(\mathbf{x}) = \sum_i m_i \ \varphi(\mathbf{x} - \mathbf{x}_i). \tag{2.4}$$

The density distribution function $\tilde{\delta}$ for a single particle would be a Dirac δ-function if point masses are assumed. However, to avoid the problematic effects of close two-body encounters (large momentum transfer, two body scattering, Steinmetz & White (1997)), the point mass potentials need to be softened. Often this is done using a spline kernel of the form

$$W(r,h) = \frac{8}{\pi h^3} \begin{cases} 1 - 6\left(\frac{r}{h}\right)^2 + 6\left(\frac{r}{h}\right)^3, & 0 \le \frac{r}{h} \le \frac{1}{2}, \\ 2\left(1 - \frac{r}{h}\right)^3, & \frac{1}{2} < \frac{r}{h} \le 1, \\ 0, & \frac{r}{h} > 1. \end{cases} \tag{2.5}$$

In the case of the GADGET code, $\tilde{\delta}$ is then given by $W(|\mathbf{x}|, 2.8\epsilon)$, with ϵ being the Plummer-equivalent gravitational softening length.

As it can easily be seen from the Hamiltonian of equation (2.1), the only problem left is how to calculate the potential, or rather the gravitational force between individual particles. The easiest (and most accurate) way to do this would use basic direct summation. However, this would require the calculation of $N-1$ partial forces for each of the N particles, leading to $\mathcal{O}(N^2)$ force calculations in total. Clearly, this is not feasible when doing high resolution simulations. However, there are some early works on galactic dynamics which made use of this direct summation technique.

In modern simulation techniques, approximate calculations of the gravitational field are done instead, which can be much faster. One of these methods is the so called 'Particle-Mesh' (PM) approach. Here, all particles are binned to a global grid spanning the whole simulation box using some interpolation method like clouds-in-cell. The generated density grid can than be Fourier transformed, multiplied by the Greens function and Fourier transformed back to obtain the gravitational potential at each grid point. Using numerical differentiation and again a cloud-in-cell interpolation, one is able to calculate gravitational forces with a spatial resolution of the order of the cell size. This is a great way to calculate long-range forces but small scales are extremely hard to resolve as one has to use an extremely fine grid, quickly leading to huge memory and CPU-time consumption.

Another way of calculating gravitational forces is to gather the tracer particles in a spatial tree structure (an oct-tree in the case of GADGET). This is done by successively dividing the simulation volume into eight subvolumes of equal size and continuing this process until the lowermost tree nodes, the 'leafs', are small enough to contain only one particle each. To save memory resources, subvolumes which contain no particles are not divided into smaller volumes. After the tree is built, it can be recursively followed from the smallest tree nodes upwards, calculating the multipole moments (to lowest order only total mass and the center of gravity) of each tree node. It is then possible to estimate the gravitational force of a whole bunch of particles by calculating the gravitational attraction of the smallest tree node containing all of these particles. In practice, one defines an accuracy parameter α (sometimes called opening angle) and an opening criterion, for example

$$\frac{GM}{r^2}\left(\frac{l}{r}\right)^2 \leq \alpha\,|\mathbf{a}|, \tag{2.6}$$

which defines whether a tree node's multipole expansion is accurate enough or not. In this criterion, the node has mass M and characteristic size l, and it is at a distance r from the active particle which had a total acceleration of $|\mathbf{a}|$ in the last time step. One can then collect the total force on a particle by walking the tree, starting at the top; if the above condition is true, the multipole approximation of the node is accepted and the walk along this branch of the tree can be stopped, otherwise the tree node is opened, i.e. all its daughter nodes are considered in turn.

In practice, GADGET as well as AREPO are using a combination of both the particle-mesh and the tree technique. With an appropriate scale to switch between the tree force for short-range interactions and the mesh force for long-range interactions, it can be shown that force calculations can be made very accurate and independent on the clustering state, while at the same time the computational cost scales as $\mathcal{O}(\log N)$ gravitational interactions per particle.

2.2 Hydrodynamics

A central new aspect of the simulations described in this thesis compared to most previous high-resolution simulations of Milky Way sized halos is that baryonic physics is directly included, complementing the evolution of dark matter via gravity. To this end, it is necessary to simulate the gaseous component as well, and the final result depends on how accurately fluid mechanical processes as well as further physical processes related to star formation can be followed. Other than for the collisionless dynamics of dark matter, there is a greater variety of possible discretization schemes for hydrodynamics, each with its own advantages and disadvantages.

There are basically two different approaches widely in use in galaxy formation: Firstly, there is the Lagrangian smoothed particle hydrodynamics (SPH) method (Lucy, 1977; Gingold & Monaghan, 1977; Monaghan, 1992; Springel, 2010b) which divides the fluid into individual particles which are moving with the flow. Secondly, there are Eulerian mesh-based methods like adaptive mesh refinement (AMR) (Berger & Colella, 1989). GADGET is a typical representative of the SPH method while AREPO can be seen as a kind of hybrid of both methods. In the following, we briefly describe their principal features.

2.2.1 Smoothed particle hydrodynamics in GADGET

In this section, we describe the basic concept of SPH, referring especially to the implementation used in GADGET. For more detailed information on technical aspects of the actual SPH implementation, see Springel (2005), while Springel (2010b) gives a general review of SPH and its different applications.

As mentioned earlier, SPH makes use of a finite set of tracer particles to describe the state of a fluid. However, as the real underlying fluid resembles a smooth distribution of matter, it is necessary to obtain smoothed fluid quantities like density, temperature, etc., at any point in space. For this purpose, SPH uses kernel-interpolated quantities. For example, the density field is estimated as

$$\rho_i = \sum_{j=1}^{N} m_j W(|\mathbf{r}_{ij}|, h_i). \tag{2.7}$$

Here, $\mathbf{r}_{ij} \equiv \mathbf{r}_i - \mathbf{r}_j$ and $W(r,h)$ is the smoothing kernel, which is the same as used for the gravitational softening in formula (2.2). The smoothing length h_i is calculated adaptively so that the kernel volume of each particle contains a constant mass. This is done by solving the implicit equation

$$\frac{4\pi}{3} h_i^3 \rho_i = N_{\rm sph} \overline{m}, \tag{2.8}$$

where $N_{\rm sph}$ is a constant number of desired SPH neighbors and $\overline{m}$ is the averaged SPH particle mass. This automatically adapts the smoothing length of a particle to its surrounding sampling density, i.e. the smoothing length is smaller in dens regions and larger in less dens regions, leading to a correspondingly adaptive spatial resolution.

One can now use a discretized version of the fluid Lagrangian of an ideal gas to derive the equation of motion of an SPH particle as

$$\frac{\mathrm{d}\mathbf{v}_i}{\mathrm{d}t} = -\sum_{j=1}^{N} m_j \left[f_i \frac{P_i}{\rho_i^2} \nabla_i W_{ij}(h_i) + f_j \frac{P_j}{\rho_j^2} \nabla_i W_{ij}(h_j) \right]. \tag{2.9}$$

The coefficients f_i are defined as

$$f_i = \left(1 + \frac{h_i}{3\rho_i}\frac{\partial \rho_i}{\partial h_i}\right)^{-1} \tag{2.10}$$

and $W_{ij}(h)$ is the abbreviation of $W(|\mathbf{r}_i - \mathbf{r}_j|, h)$. Due to reasons given in Springel & Hernquist (2002), it is convenient to store the thermodynamic state of each fluid particle in terms of the entropy per unit mass, s_i, instead of the thermal energy per unit mass, u_i. With this definition, the pressure P_i is defined as $P_i = A_i\rho_i^\gamma$, where $A(s)$ is only a function of entropy for an ideal gas with adiabatic index γ, and is therefore often simply called 'entropy' as well.

Another important point of SPH is that a so-called artificial viscosity term needs to be added to the above equations. This viscosity acts as a friction force which can irreversibly transform kinetic energy into heat energy, thereby also raising the entropy of a particle. The artificial viscosity is necessary for capturing fluid discontinuities, in particular shocks, where entropy is generated in a real fluid by unresolved microphysics. There is a wide range of different approaches for parameterizing the artificial viscosity. GADGET applies the so called Monaghan-Balsara (Monaghan & Gingold, 1983; Balsara, 1995) form, which is one of the most frequently applied choices. GADGET applies a time stepping criterion of the form

$$\Delta t_i^{(\mathrm{hyd})} = \frac{C_{\mathrm{courant}}\, h_i}{\max_j (c_i + c_j - 3w_{ij})}, \tag{2.11}$$

for each SPH particle, and the actually used timesteps are arranged on a binary hierarchy. Equation (2.11) is a Courant-like timestepping criterion where C_{courant} is the so-called Courant factor which needs to be small enough for stability such that hydrodynamical wave information cannot travel more than half the effective particle size. The maximum in the denominator of equation (2.11) is calculated with respect of all neighboring particles j of particle i, and gives an estimate of the maximum signal velocity.

2.2.2 The moving-mesh code AREPO

AREPO (Springel, 2010a) follows a completely different approach to treat hydrodynamics compared with SPH. The key difference lies in the discretization scheme, which is done by subdividing the fluid volume into cells, whereas in SPH the total mass of the fluid is discretized. AREPO also uses a set of points, but not as tracer particles for the fluid. Instead, the code treats them as mesh-generating points which are used to construct a space-filling Voronoi tessellation. The left hand panel of Figure 2.1 shows the mesh-generating points in red and the corresponding Voronoi tessellation in black. The middle panel shows the corresponding Delaunay tessellation, which is used internally by the code to generate the Voronoi tessellation. This is done because Delaunay tessellations can be calculated much faster than Voronoi tessellations, and because of the fortunate fact that Voronoi tessellations and Delaunay tessellations are topological duals of each other. For this reason it is rather easy to derive the Voronoi tessellation form the Delaunay tessellation.

On the unstructured mesh defined by the Voronoi tessellation, AREPO implements a so-called finite volume scheme for hydrodynamics, similar to standard techniques for

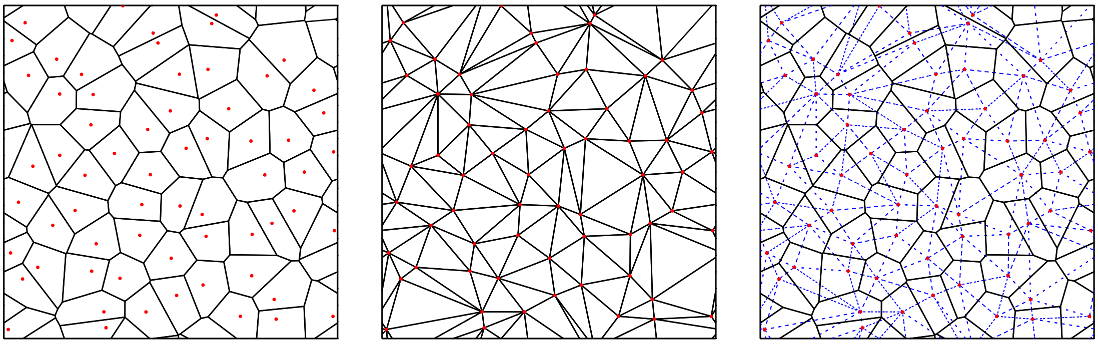

Figure 2.1: Two dimensional example of a Voronoi tessellation. The left panel shows the mesh generating points in red and the resulting Voronoi tessellation in black. The middle panel shows the corresponding Delaunay tessellation while the right panel visualizes their topological duality by showing both tessellations together. This plot has been taken form Springel (2010a).

Cartesian meshes. This can be phrased in terms of a state vector describing the fluid:

$$\mathbf{U} = \begin{pmatrix} \rho \\ \rho\mathbf{v} \\ \rho e \end{pmatrix} = \begin{pmatrix} \rho \\ \rho\mathbf{v} \\ \rho u + \frac{1}{2}\rho\mathbf{v}^2 \end{pmatrix} \tag{2.12}$$

If one defines a flux vector of the form

$$\mathbf{F}(\mathbf{U}) = \begin{pmatrix} \rho\mathbf{v} \\ \rho\mathbf{v}\mathbf{v}^T + P \\ (\rho e + P)\mathbf{v} \end{pmatrix}, \tag{2.13}$$

and introduces the equation of state of an ideal gas as $P = (\gamma - 1)\rho u$, then the Euler equations can be written compactly as

$$\frac{\partial \mathbf{U}}{\partial t} + \nabla \cdot \mathbf{F} = 0. \tag{2.14}$$

The equations are readily recognized in this form as a set of hyperbolic conservation laws for mass, momentum and energy. By integrating these equations over the finite volume of a cell, one can apply the divergence theorem to cast the second term in a surface term of hydrodynamical fluxes emanating from the cell. In essence, all that AREPO does is to estimate these fluxes, which correspond to exchanges of mass, momentum and energy between adjacent cells.

Figure 2.2 depicts a 2D example of the situation for two neighboring cells whose hydrodynamical interactions need to be calculated. After some coordinate transformation, one ends up with the situation of two fluid states i and j that are adjacent to each other, and which are interpreted by AREPO as the initial states of a Riemann problem. The flux between the two cells through their common surface is then calculated using a Riemann solver.

Up to this point, there is no major conceptual difference between AREPO and a finite-volume solver on an ordinary structured Cartesian grid. However, a novel feature of AREPO is that the mesh-generating points are actually allowed to move freely, and such

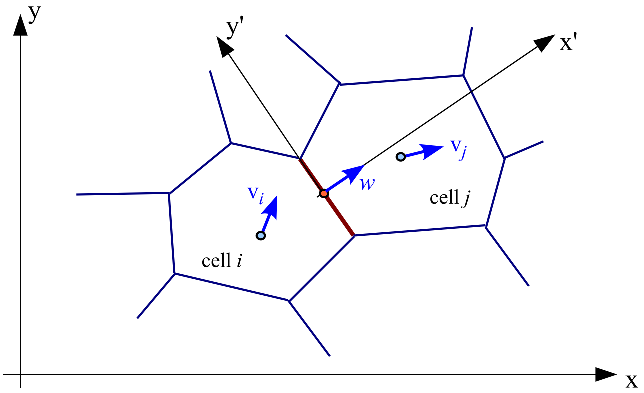

Figure 2.2: 2D example of the geometry involved in the flux computation. This plot has been taken form Springel (2010a).

motion introduces a dynamic transformation of the mesh. The most natural choice for the velocities of the mesh-generating points is to make them equal to the fluid velocity in each cell. Then the mesh automatically moves along with the flow, creating a pseudo-Lagrangian behaviour in which the mass flux over the surface of of each individual cell is minimized. In this mode, errors from advecting the fluid relative to the grid are greatly reduced and the flux calculation becomes Galilean-invariant. Also, the code adjusts its resolution automatically to the local density.

To a certain degree, AREPO can be seen as a hybrid between particle-based codes like GADGET and traditional grid-based codes like for example RAMSES (Teyssier, 2002). While still having the advantages of particle-based codes like Galilean-invariance and the inherent ability to concentrate the tracer particles at places where high resolution is needed, AREPO also benefits from the advantages of mesh-based codes, like their higher accuracy for shocks, the absence of spurious surface tension effects, and more accurate gradient estimates in the presence of density jumps. A full description of all details of AREPO and a comparison of its performance in a large number of test problems can be found in Springel (2010a).

2.3 Baryonic Physics

In the following sections we give a brief overview of the different baryonic processes that we include in our simulations and that go beyond the hydrodynamics of an ideal gas. These processes play a crucial role in galaxy formation and are in part still poorly understood. Arguably the most basic (and best understood) mechanism is the radiative cooling of diffuse gas due to line emission and bremsstrahlung. This process lets the gas lose its pressure support in virialized halos, such that it collapses to the center and becomes very dense.

Some of the dense gas can then become available for forming stars, at which point great uncertainties come into play, since star formation is not understood yet in detail. The same can be said for the energetic feedback processes that are associated with star formation, and that are a very important aspect in galaxy formation (Springel & Hernquist, 2003; Scannapieco et al., 2008). Below, we will hence first describe our models for star formation and feedback in section 2.3.1. Additionally to a purely thermal feedback, we also use a model for kinetic feedback in the form of supernova driven winds, see section 2.3.2. Another channel of energy feedback is radiation from a active galactic nuclei (AGN), as briefly described in section 2.3.3. Another potentially important factor in galaxy formation are cosmic rays generated by supernova explosions or particle acceleration at structure formation shock. This non-thermal component of energetic particles acts like an additional pressure contribution that adds to the thermal pressure of the gas. Section 2.3.4 describes the cosmic ray model used in this work. In the code comparison project described in chapter 4, a number of different parameterizations of these physical processes will also be considered, as implemented in the models of other authors. These will then be described separately in chapter 4.

2.3.1 Star formation and thermal feedback

The Springel & Hernquist (2003) subresolution model for star formation includes a uniform UV background which is switched on at redshift $z = 6$ (Haardt & Madau, 1996), and a primordial cooling following Katz et al. (1996). Stars are formed stochastically from sufficiently dense particles regulated by the underlying subgrid model assuming a Salpeter IMF. Here, each gas particle is modeled as a composition of three components ρ_h, ρ_c and $\rho_\star$ which are hot gas, cold gas and stars, respectively. Cold gas is converted to stars on a characteristic timescale $t_\star$, and a mass fraction β of these stars is assumed to be very massive and so short-lived that they nearly 'instantly' die as supernovae and their mass is instantaneously fed back – enriched with metals – to the cold gas clouds. The star formation rate is then given by

$$\frac{\mathrm{d}\rho_\star}{\mathrm{d}t} = \frac{\rho_c}{t_\star} - \beta\frac{\rho_c}{t_\star} = (1-\beta)\frac{\rho_c}{t_\star}. \tag{2.15}$$

The energy feedback of supernovae explosions of E_{SN} per supernova is used to heat the ambient hot gas as well as to evaporate cold clouds. Radiative cooling of the hot phase is assumed to increase the fraction of mass in the cold gas phase. The basic equation describing this process is

$$\left.\frac{\mathrm{d}\rho_c}{\mathrm{d}t}\right|_T I = -\left.\frac{\mathrm{d}\rho_h}{\mathrm{d}t}\right|_T I = \frac{1}{u_h - u_c}\Lambda_{\mathrm{net}}(\rho_h, u_h) \tag{2.16}$$

where the cooling function Λ_{net} is computed as in Katz et al. (1996) from radiative processes appropriate for a primordial plasma of hydrogen and helium.

As the procedure described above would continuously increase the mass fraction of the stellar phase of each multiphase particle, the tight coupling between the formed stars and the left over gas within each particle has to be eliminated somehow. This is done by spawning new collisionless particles called star particles. Assuming the star formation rate of a multiphase SPH particle of mass m is $\dot{M}_\star = (1-\beta)x\,m/t_\star$, a new star particle of mass $m_\star = m_0/N_g$ is spawned with a probability of

$$p_\star = \frac{m}{m_\star}\left\{1 - \exp\left(-\frac{(1-\beta)x\Delta t}{t_\star}\right)\right\}. \tag{2.17}$$

Here m_0 is the initial gas mass of each SPH particle and N_g is an integer value describing the maximum number of stars a gas particle can form. If a gas particle has already formed N_g-1 star particles it will simply be converted into a star particle in the next star forming event. After a star particles has been created, it is treated as a collisionless particle just like the dark matter, except that it carries with it some additional internal information, such as metallicity and formation time. With this scheme, stars are decoupled from the flow of the surrounding gas and are thus no longer affected by purely hydrodynamical effects like thermal pressure, turbulence or ram-pressure forces.

2.3.2 Wind model

Even though the above ISM model reproduces the star formation rates observed in disk galaxies, it overproduces the total amount of stars formed when applied in cosmological simulations. This is likely related to its inability to reproduce the observed galaxy-scale outflows seen around many star-bursting galaxies. We have therefore also investigated the phenomenological model for galactic winds introduced by Springel & Hernquist (2003). We adopted a constant wind velocity of $v_{\rm wind} = 484\,{\rm km\,s^{-1}}$ and mass loading factor of $\eta = 2$, i.e. the mass flux of the wind is twice the star formation rate. Individual gas particles were stochastically added to the galactic wind by changing their velocity to the prescribed wind velocity. We adopted an anisotropic distribution for the wind direction, launching it preferentially perpendicular to the disk.

The wind model causes an outflow of gas from the dense gaseous disc, transporting energy, matter and heavy elements out of the disk in proportion to the star formation rate. Not only the central galaxy is affected by the winds, all the star forming satellite galaxies produce winds, which will more quickly deplete their gas content. The effect of galactic winds is actually expected to be more effective in these low mass systems as their potential well is much shallower than the one of the main galaxy (Dekel & Silk, 1986), which should increase the mass loss due to outflows. Including winds in the simulation thus appears in principle promising as a mechanism to reduce the number of luminous satellites, but the effect may sensitively depend on how the wind properties are scaled with galaxy size (e.g. Oppenheimer & Davé, 2006).

2.3.3 AGN feedback

Supermassive black holes are thought to reside at the centers of most if not all spheroidal galaxies. The tight relation between their masses and the velocity dispersion of their hosting galaxies suggests a close evolutionary link, which is probably established by a self-limited growth mechanism in which the energy output of a growing black hole eventually terminates its further growth and the surrounding star formation, for example by expelling gas from the central region of the galaxy. Hydrodynamical simulation models have been successfully used to model this process in detail (Di Matteo et al., 2005; Springel et al., 2005a), and led to quite successful unified models of the formation of spheroidal galaxies (Hopkins et al., 2006).

While it is unclear whether the influence of the Milky Way's black hole has affected the formation of other components of the Galaxy besides the central bulge, it appears possible that the heating effects from different quasar episodes during the growth history of the MW's supermassive black hole have had an impact on the satellite population as well, for example by heating the environment of progenitor halos through strong quasar driven outflows. Indeed, in theoretical models outflow feedback has been found to be violent enough to be able to strongly affect even neighboring galaxies (Scannapieco et al., 2001; Thacker et al., 2002).

To study such effects, we have adopted the techniques introduced by Springel et al. (2005a) for tracking black hole growth and its associated energy feedback in cosmological simulations. In brief, we periodically call a FoF group finding algorithm that identifies newly formed halos that do not contain a black hole yet. If such a halo is sufficiently massive, its densest gas particle is converted to a black hole seed of mass $M_{\rm BH} = 10^5\,h^{-1}{\rm M}_\odot$. The black hole particles are treated as sinks particles that accrete gas from their surroundings at a rate estimate with a simple Bondi-Hoyle prescription, limited to the Eddington rate. The black hole accretion is assumed to have a fixed radiative efficiency of $0.1\,\dot{M}c^2$, and 5% of the produced radiation are assumed to couple thermally to the gas surrounding the black hole. The thermal feedback energy is then given by

$$\dot{E}_{\rm feed} = \epsilon_f \epsilon_r \dot{M}_{\rm BH} \tag{2.18}$$

with ϵ_r the radiative efficiency and ϵ_f the feedback efficiency. This energy feedback can eventually drive a quasar-driven outflow and regulates the mass growth of the black holes. We also allow for two black holes to merge with each other once they get sufficiently close to each other.

2.3.4 Cosmic Rays

In the interstellar medium of our own Galaxy, it is believed that thermal pressure, cosmic rays and magnetic fields are roughly in equipartition. Even though it is hence known that non-thermal particle populations play an important role in regulating the gas dynamics of the ISM, this component has usually been ignored in studies of galaxy formation. The cosmic ray particles may originate in acceleration processes in high Mach number shocks in supernova remnants or could be produced in structure formation shock waves. We here focus on cosmic ray injection associated with supernovae, and consider only Coulomb and hadronic interactions as loss processes for the cosmic ray particles (Enßlin et al., 2007).

A numerical treatment of the cosmic ray component is rather complicated as in principle their full, in general anisotropic distribution function has to be modeled. Also, the motion of the cosmic ray fluid is tightly coupled to the magnetic field, which in turn is non-trivial to calculate accurately. We therefore employ the subresolution model described by Jubelgas et al. (2008), which has already been successfully employed in previous work (Pfrommer et al., 2007, 2008; Pfrommer, 2008).

The cosmic ray component in the Jubelgas et al. (2008) formalism is modeled through a power law distribution function for the proton momentum,

$$\frac{{\rm d}^2 N}{{\rm d}p\,{\rm d}V} = C p^{-\alpha} \theta(p-q). \tag{2.19}$$

The pressure of this cosmic ray population is given by

$$P_{\rm CR} = \frac{C\,m_p\,c^2}{6} \mathcal{B}_{\frac{1}{1+q^2}} \left(\frac{\alpha-2}{2}, \frac{3-\alpha}{2} \right). \tag{2.20}$$

Here $\mathcal{B}_n(a,b) \equiv \int_0^n x^{a-1}(1-x)^{b-1}\mathrm{d}x$ denotes incomplete Beta functions and α is the power law slope. The energy injected by supernova explosions is given as

$$\Delta\tilde{\varepsilon}_{\mathrm{SN}} = \zeta_{\mathrm{SN}}\,\epsilon_{\mathrm{SN}}\,\dot{m}_\star \Delta t \tag{2.21}$$

where ζ_{SN} is the fraction of the supernova energy that appears as a cosmic ray population.

We model the decay of the cosmic ray population by accounting for Coulomb cooling and catastrophic hadronic losses as described in Jubelgas et al. (2008). Note that the 'cosmic ray cooling' mediated by these effects can occur on a different timescale as the ordinary thermal cooling. In particular, gas can end up being cosmic ray pressure supported after having lost much of its thermal support through radiative cooling. Finally, we adopt a simple source function for the injection of new cosmic ray particles, which we link directly to the star formation rate. This is motivated by observations of supernova remnants (Aharonian et al., 2006), where a large fraction of the supernovae energy is seen to initially appear as cosmic rays.

2.4 Initial Conditions

Our simulations are based on initial conditions originally constructed for the *Aquarius* Project (Springel et al., 2008) of the Virgo Consortium. This project carried out highly resolved dark matter only simulations of 6 different Milky Way-sized halos, at a variety of different numerical resolutions. In the nomenclature of Springel et al. (2008), the halo at the highest resolution level investigated in this thesis is called 'Aq-C-4' and has about 5.4 million dark matter particles in the final virial radius. The same object has also been studied in the hydrodynamic simulations of Scannapieco et al. (2009), albeit at the considerably lower resolution (by a factor of 8 in particle number) corresponding to 'Aq-C-5' which is also the resolution level used in the *Aquila* Project (Scannapieco et al., 2011a), see chapter 4 for a more detailed description. Scannapieco et al. (2009) also found that this 'C'-halo produced the lowest bulge-to-disk ratio among the 6 halos considered in the Aquarius Project, suggesting it as a particularly good candidate for the formation of a large disk galaxy. This is also why we selected this system for our studies.

Gas particles are introduced into the initial conditions by splitting each original dark matter particle into a dark matter and gas particle pair, displaced slightly with respect to each other (at fixed center-of-mass) to arrive at a regular distribution of the mean interparticle separations, and with a mass ratio corresponding to a baryon fraction of 16 percent. The adopted cosmological parameters are $\Omega_m = 0.25$, $\Omega_\Lambda = 0.75$, $\sigma_8 = 0.9$ and $h = 0.73$, the same ones used as in the original Aquarius simulations (Springel et al., 2008), as well as the Millenium-I (Springel et al., 2005b) and Millenium-II (Boylan-Kolchin et al., 2009) simulations, which are consistent with the WMAP3 (Spergel et al., 2007) cosmological constraints. Newer data from WMAP7 (Komatsu et al., 2011) are favouring $\sigma_8 = 0.8$, putting our adopted value on the high side. However, we don't expect to strongly influence our findings. periodic box of size $100\,h^{-1}$Mpc on a side is simulated in all our simulations, with varying spatial resolution that 'zooms in' on the formation of a single galaxy. In the corresponding high-resolution region, we reach in our standard runs a mass resolution of $\approx 2\times10^5\,h^{-1}\mathrm{M}_\odot$ and $\approx 2\times10^4\,h^{-1}\mathrm{M}_\odot$ for dark matter and gas particles, respectively. A constant comoving gravitational softening length of $\epsilon = 0.25\,h^{-1}$kpc is used for all high-resolution particles in these runs.

3 Satellite galaxies in hydrodynamical simulations of Milky Way like galaxies

Contents

3.1 Introduction **26**
3.2 Methodology **29**
  3.2.1 Star formation model 29
  3.2.2 Simulation set and analysis 30
3.3 Observational knowledge **32**
3.4 Abundance of luminous satellites **32**
  3.4.1 Kinematic results 36
3.5 History of satellite galaxies **37**
3.6 Scaling relations **44**
3.7 Conclusions **48**

Summary

In this chapter, we are investigating the discrepancy between the predictions of collisionless simulations of the CDM cosmology, which vaticinate a plethora of dark matter substructures in the halos of Milky Way sized galaxies, and the number of known luminous satellites galaxies, which is very much smaller, known as the 'missing satellite problem'. Collisionless simulations of the CDM cosmology predict a plethora of dark matter substructures in the halos of Milky Way sized galaxies, yet the number of known luminous satellites galaxies is very much smaller, a discrepancy that has become known as the 'missing satellite problem'. The most massive substructures have been shown to be plausibly the hosts of the brightest satellites, but it remains unclear which processes prevent star formation in the many other, purely dark substructures. We use high-resolution hydrodynamic simulations of the formation of Milky Way sized galaxies in order to test how well such self-consistent models of structure formation match the observed properties of the Galaxy's satellite population. For the first time, we include in such calculations feedback from cosmic rays injected into the star forming gas by supernovae as well as the energy input from supermassive black holes growing at the Milky Way's center and its progenitor systems. We find that non-thermal particle populations quite strongly suppress the star formation efficiency of the smallest galaxies. In fact, our cosmic ray model is able to reproduce the observed faint-end of the satellite luminosity function, while models that include only the effects of cosmic reionization, or galactic winds, do significantly worse. Our simulated satellite population approximately matches available kinematic data on the satellites and their observed spatial distribution. We conclude that a proper resolution of the missing satellite problem likely requires the inclusion of non-standard physics for regulating star formation in the smallest halos, and that cosmic reionization alone may not be sufficient.*

---

[*] This chapter has been submitted for publication in *Monthly Notices of the Royal Astronomical Society* and appeared as Wadepuhl & Springel (2011b).

3.1 Introduction

The leading ΛCDM cosmology predicts that galaxies form hierarchically in a 'bottom up' fashion (e.g. White & Rees, 1978; Longair, 1999), where small perturbations in the dark matter density distribution collapse earlier than larger perturbations, and low-mass halos grow by smooth accretion or mergers with other halos, successively building up ever bigger structures. But structures falling into bigger systems during this process are not always disrupted completely. As N-body simulations show, the inner cores of infalling objects often survive the various disruptive effects acting on them, like tidal truncation, tidal shocking or ram-pressure stripping. It is believed that the observed dwarf galaxies orbiting around the Milky Way are examples of such surviving remnants.

Based on the first generation of very high resolution collisionless CDM simulations, Klypin et al. (1999) and Moore et al. (1999) pointed out a very striking apparent discrepancy between theoretical predictions for such satellite systems and actual observations. Given the very large number of predicted dark matter substructures, there appears to be a dearth of luminous satellites in the Milky Way. In fact, the cumulative number of observed satellite galaxies and of predicted substructures above a given circular velocity value differed by a factor of ~ 10. This has become known as the 'missing satellite problem'.

The initial analysis of Moore et al. (1999) and Klypin et al. (1999) may have overstated the magnitude of the discrepancy, both because of uncertainties in assigning correct circular velocity values to the observed satellites (Stoehr et al., 2002) and because a number of additional faint satellites have been discovered meanwhile in the MW (see for example Irwin et al., 2007; Liu et al., 2008; Martin et al., 2008; Simon & Geha, 2007; Grebel, 2000; van den Bergh, 2000; Belokurov et al., 2008, 2009; Watkins et al., 2009; Belokurov et al., 2010). However, there is a consensus that the many low-mass satellites predicted by the N-body simulations need to be strongly suppressed in luminosity, otherwise a significant discrepancy with the observed satellite luminosity functions results, that, if confirmed, may in principle even be used to rule out cold dark matter.

With increasing numerical resolution, the missing satellite problem has become more acute. Modern cosmological dark matter simulations of Milky Way sized halos (Diemand et al., 2008; Springel et al., 2008; Stadel et al., 2009) resolve up to $\sim 300,000$ dark matter substructures, while the number of observed satellite galaxies still comprises just a few dozens. We note that the modern dark matter only simulations are even able to resolve substructures inside substructures, and interestingly, there is also some observational evidence for a satellite possibly orbiting around another satellite (Belokurov et al., 2008).

Klypin et al. (1999) did not only raise the missing satellite problem, they were also among the first to suggest a potential solution to this issue. In particular, they proposed that star formation inside low mass halos could be suppressed because of photo evaporation of gas due to a strong intergalactic ionizing UV background. This would keep most of the orbiting satellites dark and render them visually unobservable. Indeed, the simple filtering mass model of Gnedin (2000) for the impact of a UV background on the cooling efficiency of small halos predicts a quite sizable effect, with a nearly complete suppression of cooling in all halos with circular velocity below $50\,\mathrm{km\,s^{-1}}$. However, recent full hydrodynamical simulations have not confirmed this (Hoeft et al., 2006; Okamoto et al., 2008a). They find a considerably weaker effect, where only halos with circular velocities less than $\sim 25\,\mathrm{km\,s^{-1}}$ are affected. This also casts some doubt about the faint-end results of numerous semi-analytic models for the satellite population (e.g. Benson et al., 2002), which typically employed the filtering mass formalism and hence assumed an overly strong effect of the UV background. We will reexamine this question in this work based on our cosmological hydrodynamic simulations of Milky Way formation, which include a treatment of cosmic reionization.

Another possible solution for the satellite problem was proposed by Kravtsov et al. (2004) and Strigari et al. (2007) who suggested that not the satellite mass at the present epoch determines whether a satellite would be luminous or not, but rather the maximum mass it had before accretion onto the Milky Way's halo. This is based on the idea that tidal stripping and ram pressure unbinds the gas from an infalling satellite and thus stalls any further star formation. With this assumption, the stellar mass at the time of accretion is essentially retained until the present epoch, and it becomes a question of allowing high-redshift star formation only in satellites above a sufficiently high mass threshold.

A more radical conjecture is that the properties of the dark matter particles may have to be changed. Instead of having negligible velocity dispersion at the time of decoupling, we may instead be dealing with (slightly) warm dark matter (WDM). This can suppress the abundance of low mass structure considerably (e.g. Colín et al., 2000), but provided the particle mass is not lower than $\sim 1\,\mathrm{keV}$ a sufficiently large number of substructures still survives to explain the observed satellite abundance (Macciò & Fontanot, 2010).

In the most recent works on the subject, a number of interesting and encouraging results have been obtained. Observationally, it has been discovered that the satellites all have approximately the same central mass density (within 300 to 600 pc), independent of their luminosity (Gilmore et al., 2007; Strigari et al., 2008). Explaining this central density threshold has become an important additional challenge for theoretical models. Also, a significant number of new faint satellites have been discovered with the help of the SDSS (Irwin et al., 2007; Liu et al., 2008; Martin et al., 2008; Simon & Geha, 2007; Grebel, 2000; van den Bergh, 2000; Belokurov et al., 2008, 2009; Watkins et al., 2009; Belokurov et al., 2010), improving our knowledge about the full satellite population significantly, but at the same time also raising the question whether we may perhaps still be missing large numbers of satellites at ultra low surface brightnesses.

On the theoretical side, refined treatments of the effects of reionization, often coupled to the results of high-resolution collisionless simulations have been used to model the satellite population. Macciò et al. (2010) employed a number of different semi-analytic models and low-resolution hydrodynamic simulations to study the satellite luminosity function. Despite just invoking photoheating as primary feedback process, they achieved reasonable agreement for some of their models, leading them to argue that the satellite problem may be solved. Similarly, Li et al. (2010) invoked a strong impact of reionization in a semi-analytic model similar to those applied to the Millennium Simulation (Croton et al., 2006) to reproduce the luminosity function of galaxies around the Milky Way. Busha et al. (2010) used simple prescriptions for the impact of inhomogeneous reionization on the satellite population, pointing out that subtle changes in the assumptions about how reionization affects star formation in small galaxies can lead to large changes in the predicted number of satellites.

Recently, Strigari et al. (2010) examined the kinematics of five well-measured Milky

Way satellite galaxies and compared them to dark matter satellites of the high-resolution simulations of the Aquarius Project (Springel et al., 2008). They showed that these systems are fully consistent with ΛCDM expectations and may be hosted in cored dark matter structures with maximum circular velocities in the range 10 to $30\,\mathrm{km\,s^{-1}}$. Interestingly, Bullock et al. (2010) pointed out that the number of real satellite systems may in fact be much larger than commonly believed, with the majority of them being so far undetected because of their low surface brightness. In this scenario, the 'common mass scale' inferred for the observed satellites may in fact just arise from a selection bias.

The first high-resolution hydrodynamic simulation able to directly resolve the satellite population has recently been presented by Okamoto & Frenk (2009). They argue that the common mass scale identified in the observations arises from early reionization at redshift around $z \sim 12$, and that satellites that have not yet grown to a maximum circular velocity of $\sim 12\,\mathrm{km\,s^{-1}}$ *by the time of reionization*, will not be able to make any stars later on. Even if they grow above this threshold, Okamoto & Frenk (2009) predict them to remain dark.

Despite all of this progress, it is evident that there remain many open questions concerning the population of faint and ultra-faint satellite galaxies orbiting around Milky Way like galaxies. Especially the influence of different baryonic feedback processes on the luminosity function of the simulated satellites has not been investigated in sufficient detail. It is therefore far from clear whether photoheating from a UV background and ordinary supernovae feedback are indeed the correct physical solutions to the missing satellite problem. In fact, the problems of modern semi-analytical models as well as our simulational results shown below are indicating that the population of satellite galaxies around Milky Way like galaxies is shaped by the complex interplay between different baryonic processes.

We have therefore embarked on a research program where we use high-resolution hydrodynamic simulations of the formation of Milky Way-sized halos to shed more light on these questions, in particular by investigating a variety of feedback processes known to be important in galaxy formation. Besides the impact of reionization, these include galactic winds and outflows, energy input by growing supermassive black holes, or the non-thermal support of gas by cosmic rays or magnetic fields. Ultimately we aim to reach similar numerical resolution as has been obtained for recent collisionless simulations, even though this goal may still be several years away.

In this work, we present some of our first results. We use several well resolved hydrodynamical simulations of the formation of a Milky Way sized galaxy to investigate the properties of the predicted population of satellite galaxies, for different choices of the included physics. Besides a default reference model that includes only a treatment of radiative cooling, star formation, and cosmic reionization, we consider also models that add galactic winds, supermassive black hole growth, or cosmic ray injection by supernovae shock waves. By comparing the simulation results with a comprehensive catalogue of the known Milky Way satellites, we seek to determine which of these processes is most important in shaping the satellite population.

This paper is organized as follows. In Section 3.2, we describe the methodological details of our simulations, while the observational knowledge about the satellites is briefly summarized in Section 3.3. Sections 3.4, 3.5 and 3.6 present the results for our simulated populations of satellite galaxies, both with respect to individual satellite histories as well as with respect to their population as a whole. Our conclusions are summarized in Section 3.7.

3.2 Methodology

We employed the parallel TreeSPH code GADGET-3 for our runs, which is an improved and extended version of GADGET-2 (Springel, 2005). GADGET calculates the long-range gravitational field in Fourier space, and the short range forces in real space with a hierarchical multipole expansion, based on a tree. This approach guarantees a homogeneously high spatial resolution in the gravitational force calculation and can be efficiently combined with an individual timestep integration scheme. For the hydrodynamics, GADGET uses the 'entropy formulation' of SPH (Springel & Hernquist, 2002), which is derived from a variational principle and simultaneously conserves energy and entropy where appropriate.

In the hydrodynamic part of GADGET, different physical processes besides ordinary gas dynamics are calculated. Most importantly, these are radiative cooling, star formation and its regulation by supernovae feedback processes (Springel & Hernquist, 2003). The code can optionally also model black hole growth and (Springel et al., 2005a) and cosmic ray physics (Jubelgas et al., 2008). We shall now briefly describe the physics modules we used.

3.2.1 Star formation model

Radiative cooling is followed for a primordial mixture of helium and hydrogen under the assumption of collisional ionization equilibrium, using a formulation as in Katz et al. (1996). A spatially uniform, ionizing UV background is introduced with an amplitude and time evolution described by an updated version of Haardt & Madau (1996), leading to reionization of the universe by redshift $z \simeq 6$.

To model star formation, we use the hybrid multiphase model for star formation and supernova feedback introduced by Springel & Hernquist (2003), in which every sufficiently dense gas particle is treated as a representative region for the multiphase structure of the interstellar medium (ISM). These hybrid particles are pictured to be comprised of cold dense clouds in pressure equilibrium with a hot ambient gas phase, where only the clouds contribute material available for star formation. Mass and energy exchange processes between these two phases are computed by simple differential equations, as described in Springel & Hernquist (2003), giving rise to an effective equation of state that regulates the dense gas of the ISM. Collisionless star particles are spawned stochastically from this star-forming phase according to a local estimate of the star formation rate. The gas consumption timescale of the model is calibrated such that it reproduces the Kennicutt law (Kennicutt, 1989) between star formation rate and gas surface density observed in low-redshift disk galaxies.

Label	Mass resolution (gas)	Grav. softening	Physics
Ref	5.14×10^4 M$_\odot$	0.34 kpc	SF, SN feedback$^{(a)}$
BH	5.14×10^4 M$_\odot$	0.34 kpc	SF, SN feedback$^{(a)}$, AGN feedback$^{(b)}$
Wind	5.14×10^4 M$_\odot$	0.34 kpc	SF, SN feedback$^{(a)}$, galactic winds$^{(a)}$
CR	5.14×10^4 M$_\odot$	0.34 kpc	SF, SN feedback$^{(a)}$, AGN feedback$^{(b)}$, cosmic rays$^{(c)}$
LowRes	4.11×10^5 M$_\odot$	0.68 kpc	SF, SN feedback$^{(a)}$, AGN feedback$^{(b)}$

Table 3.1: Overview of the simulations used in this work. The label of each simulation will be used throughout the rest of this paper. The different physics models we use are described in detail in (a) Springel & Hernquist (2003), (b) Springel et al. (2005a), and (c) Jubelgas et al. (2008).

3.2.2 Simulation set and analysis

In Table 3.1, we summarize the primary properties of the simulations we analyze in this work. We consider four different high-resolution simulations of the same initial conditions, corresponding to the Aq-C-4 halo, but carried out with different physics in the baryonic sector. Our reference calculation (labeled 'Ref') includes star formation and supernova feedback as described by our multi-phase model, as well as ordinary radiative cooling and heating by a UV background that reionizes the universe by redshift $z = 6$. We have repeated this calculation by adding in turn each of the three additional feedback models described above. This yields the three simulations 'BH' (with black hole growth and feedback), 'Wind' (with the phenomenological wind model), and 'CR' (with cosmic ray physics). Our primary simulation set is composed of these four simulations. They are of equal numerical resolution and hence allow a relatively clean assessment of the impact of the different physics components on the satellite population. We note that our primary aim in this work is not to construct a best-fitting model for the Milky Way, as this may require a combination of the different physics models and a fine-tuning of their free parameters. Rather we want to highlight the importance of different physics for the satellite population.

We also briefly consider a further simulation, labeled 'LowRes'. This is a rerun of our reference model at lower resolution, corresponding to 'Aq-C-5'. We use this simulation for an assessment of the numerical resolution and convergence limits of our simulations.

To analyze the time evolution of the simulated galaxies, several snapshots were stored at different times. As a basic analysis step, the snapshots were first processed by a group finding algorithm in order to identify individual halos. The group finding was done with a simple friend-of-friends (FOF) algorithm applied only to the dark matter particles with a linking length equal to 20% of their mean particle spacing. The gas and star particles were linked to their nearest dark matter particle. Next, each halo found in the first step was subjected to a substructure detection procedure, for which we used the SUBFIND algorithm (Springel et al., 2001) in a version extended to allow a treatment of gas as well (Dolag et al., 2009). SUBFIND calculates the local density everywhere and searches for substructure candidates that are locally overdense. It then computes the gravitational potential at the positions of all particles in the candidate structures, and determines the subset of particles that are gravitationally bound. In this way, only real physical structures are found. To avoid noise from substructures composed of only a few particles, only substructures containing at least 20 particles were kept for further analysis.

Label	α_{2000}	δ_{2000}	D (kpc)	$\mathrm{M}_{\mathrm{V,tot}}$ (mag)	$\mu_{0,V}$ (mag/arcsec^2)	Mass ($10^6\mathrm{M}_\odot$)
BooI$^{(e)}$	$14^{\mathrm{h}}00^{\mathrm{m}}$	$+14°30'$	66 ± 3	-6.3 ± 0.2	27.5 ± 0.3	–
BooII$^{(e)}$	13 58	+12 51	42 ± 8	-2.7 ± 0.9	28.1 ± 1.6	–
Carina$^{(b)}$	60 42	−50 58	101 ± 5	-9.3	$25.5 \pm 0.4^{(h)}$	13
Com$^{(e)}$	12 27	+23 54	44 ± 4	-4.1 ± 0.5	$27.3^{+0.7}_{-0.6}$	$1.2 \pm 0.4^{(f)}$
CVnI$^{(e)}$	13 28	+33 33	218 ± 10	$-8.6^{+0.2}_{-0.1}$	27.1 ± 0.2	$27 \pm 4^{(f)}$
CVnII$^{(e)}$	12 57	+34 19	160^{+4}_{-5}	-4.9 ± 0.5	$26.1^{+0.7}_{-0.6}$	$2.4 \pm 1.1^{(f)}$
Draco$^{(e)}$	17 20	+57 55	76 ± 5	-8.8 ± 0.2	25.5 ± 0.2	22
Fornax$^{(b)}$	02 40	−34 27	138 ± 8	-13.2	$23 \pm 0.3^{(h)}$	68
Her$^{(e)}$	16 31	+12 48	132 ± 12	-6.6 ± 0.3	$27.2^{+0.6}_{-0.5}$	$7.1 \pm 2.6^{(f)}$
LeoA$^{(b)}$	09 59	+30 45	690 ± 100	-11.4	–	11
LeoI$^{(b)}$	10 08	+12 19	250 ± 30	-11.9	$22.4 \pm 0.3^{(h)}$	22
LeoII$^{(b)}$	11 13	+22 09	205 ± 12	-9.6	$24.0 \pm 0.3^{(h)}$	9.7
LeoIV$^{(e)}$	11 33	−00 32	160^{+15}_{-14}	$-5.0^{+0.6}_{-0.5}$	$27.5^{+1.3}_{-1.2}$	$1.4 \pm 1.5^{(f)}$
LeoV$^{(j)}$	11 31	+02 13	180	-4.3	27.5 ± 0.5	–
LeoT$^{(e)}$	09 35	+17 03	407 ± 38	$-7.1^{(c)}$	$26.9^{(c)}$	$8.2 \pm 3.6^{(f)}$
LiuI$^{(d)}$	10 00	+57 30	$83.2^{+9.3}_{-8.4}$	-4.15	28.8	–
LiuII$^{(d)}$	13 29	+28 41	$75.9^{+8.5}_{-7.6}$	-3.91	29.2	–
LMC$^{(a)}$	05 24	−69 50	49	$-18.5^{(i)}$	$20.7 \pm 0.1^{(h)}$	$10.000^{(g)}$
NGC6822$^{(b)}$	19 45	−14 48	490 ± 40	-15.2	$21.4 \pm 0.2^{(h)}$	1640
Pegasus$^{(b)}$	23 29	+14 45	955 ± 50	-12.9	–	58
Phoenix$^{(b)}$	01 51	−44 27	445 ± 30	-10.1	–	33
PscI$^{(l)}$	23 19	0 0	80	–	–	0.1
PscII$^{(m)}$	22 58	5 57	180	-5.0	–	–
Sag$^{(b)}$	18 55	−30 29	24 ± 2	-13.4	$25.4 \pm 0.2^{(h)}$	$150^{(i)}$
Sculpor$^{(b)}$	01 00	−72 50	79 ± 4	-11.1	$23.7 \pm 0.4^{(h)}$	6.4
Seg1$^{(e)}$	10 07	+16 04	23 ± 2	$-1.5^{+0.6}_{-0.8}$	$27.6^{+1.0}_{-0.7}$	–
Seg2$^{(k)}$	02 19	+20 10	35	-2.5 ± 0.2	–	$0.55^{+1.1}_{-0.3}$
Seg3$^{(m)}$	21 21	+19 07	16	-1.2	–	–
Sextans$^{(b)}$	10 13	−01 37	86 ± 4	-9.5	$26.2 \pm 0.5^{(h)}$	19
SMC$^{(a)}$	00 51	−73 10	58	$-17.1^{(i)}$	$22.1 \pm 0.1^{(h)}$	$400^{(g)}$
Tucana$^{(b)}$	22 42	−64 25	880 ± 40	-9.6	$25.1 \pm 0.1^{(h)}$	–
UMaI$^{(e)}$	10 35	+51 55	96.8 ± 4	-5.5 ± 0.3	$27.7^{+0.5}_{-0.4}$	$15 \pm 4^{(f)}$
UMaII$^{(e)}$	08 07	+63 07	30 ± 5	-4.2 ± 0.5	27.9 ± 0.6	$4.9 \pm 2.2^{(f)}$
UMi$^{(b)}$	15 09	+67 13	66 ± 3	-8.9	$25.5 \pm 0.5^{(h)}$	23
Wil1$^{(e)}$	10 49	+51 03	38 ± 7	-2.7 ± 0.7	26.1 ± 0.9	–

Table 3.2: Compilation of all presently known Milky Way satellite galaxies. The values are taken from the following studies: (a) van den Bergh (1994), (b) Mateo (1998),(c) Irwin et al. (2007),(d) Liu et al. (2008),(e) Martin et al. (2008), (f) Simon & Geha (2007), (g) Bekki (2008), (h) Grebel (2000), (i) van den Bergh (2000), (j) Belokurov et al. (2008), (k) Belokurov et al. (2009), (l) Watkins et al. (2009), (m) Belokurov et al. (2010). All errors are from the corresponding papers. The different columns list the position in galactic coordinates, the proper distance, the total V-band magnitude, the surface brightness and the total estimated mass of the individual satellites.

The gravitationally bound structures found by SUBFIND in this way form our catalogue of simulated galaxies, including both central galaxies as well as genuine satellites. For the simulated galaxies, we applied a stellar population synthesis model (Bruzual & Charlot, 2003) to estimate their luminosities and colors, based on the formation times and masses of the star particles created in the simulations. We made no attempt to account for the metallicity dependence of the stellar population synthesis model or dust corrections.

3.3 Observational knowledge

Before we present our simulation results, we summarize in this section the most recent observational data with respect to the Milky Way's satellite population. We will later use this comprehensive catalogue of the known satellites together with predictions for their total number over the whole sky when comparing with our simulations.

Table 3.2 gives a compilation of the properties of all Milky Way satellites known today. The basic data of the 'classical' satellites, which were already known in 1998, are given by Mateo (1998) and were only slightly extended using van den Bergh (2000) who updated the data on the Small and the Large Magellanic Cloud (SMC and LMC, respectively). Up to this time, the number of known satellites was just 16, but during the different data releases[†] (York et al., 2000; Willman et al., 2002) of the Sloan Digital Sky Survey (SDSS), the number of known satellites increased significantly thanks to new discoveries made with the survey. Table 3.2 includes the new satellite galaxies found with SDSS (Willman et al., 2005a,b; Zucker et al., 2006b; Belokurov et al., 2006; Zucker et al., 2006a; Belokurov et al., 2007; Irwin et al., 2007; Walsh et al., 2007; Liu et al., 2008; Walsh et al., 2008; Belokurov et al., 2008, 2009; Watkins et al., 2009; Belokurov et al., 2010), using the recently published structural parameters given in Martin et al. (2008). To estimate the half light radius of the Large Magellanic Cloud, the formula $r_h = 1.68\, r_e$ (Martin et al., 2008) was adopted.

Up to now, there are 35 known Milky Way satellites. However, this sample is not complete, as the recently found satellites are all limited to the area of the sky covered by SDSS, which corresponds to a fraction of 0.194 of the full sky. Effectively, only this region of the whole sky has been scanned for faint satellites (see Tollerud et al., 2008). Taking into account the detection limits and the sky coverage of the SDSS survey, Simon & Geha (2007) estimate the number of satellite galaxies with a surface brightness above ≈ 28 mag/arcsec^2 (Martin et al., 2008) expected over the whole sky to be 57. However, more recent works favor a limit of 30 mag/arcsec^2 (Bullock et al., 2010), which we adopt throughout the rest of this paper. Using this threshold, we denote simulated satellite galaxies as 'observable' if their surface brightness exceeds 30 mag/arcsec^2.

3.4 Abundance of luminous satellites

Arguably the most fundamental property of the subhalo population is the abundance of satellites as a function of luminosity. In Figure 3.1, we show the differential luminosity function of the simulated satellite galaxies for our four primary simulations, and compare

---

[†] `http://www.sdss.org/dr6/index.html`

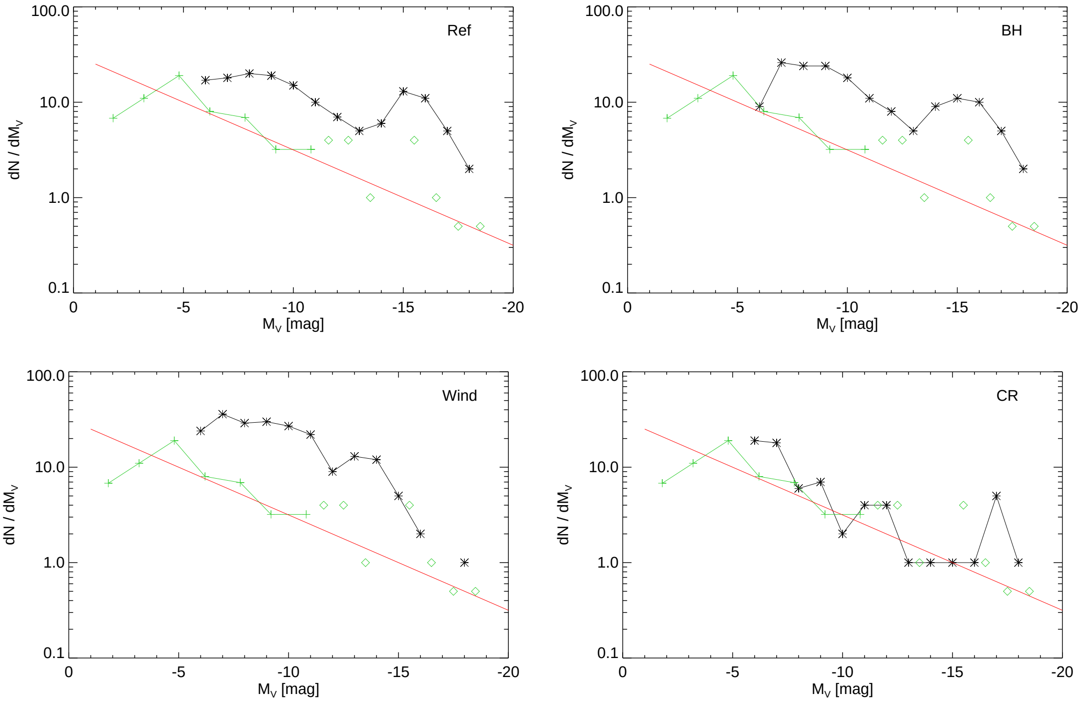

Figure 3.1: The differential luminosity function of the simulated satellites (black curve) compared to the observational data. The latter are represented by the red line, which is the fitting function given by Koposov et al. (2008). The green line shows the scaled luminosity function they obtained for the SDSS satellites while the open diamonds give an extended version using also the luminous satellites of the Milky Way and Andromeda. The different panels show our results for the Ref, BH, Wind and CR simulations, respectively.

to the observations for the Milky Way. The latter are expressed in terms of the fitting formula given by Koposov et al. (2008):

$$\frac{\mathrm{d}N}{\mathrm{d}M_V} = 10 \times 10^{0.1(M_V+5)}. \tag{3.1}$$

As explained in Section 3.6, we only show satellites within a distance of 280 kpc from the assumed position of the Sun which is placed at a distance of 8.5 kpc from the galactic center and within the galactic disk. If not mentioned otherwise, this radial cut has been applied throughout the rest of this paper.

The upper left panel of Figure 3.1 shows our result for the reference simulation. There is a sizable offset between the simulated and the observed luminosity functions, shown in black and green, respectively. Satellites with large stellar masses are even more strongly overproduced than low luminosity ones. This shows that photoheating and supernova feedback as included in the reference model are insufficient to match the observed satellite abundance.

The other panels of the Figure show the results we obtained for our alternative physics simulations. As one might expect, including supermassive black holes has no substantial influence on the population of satellites, yielding essentially the same result as for our

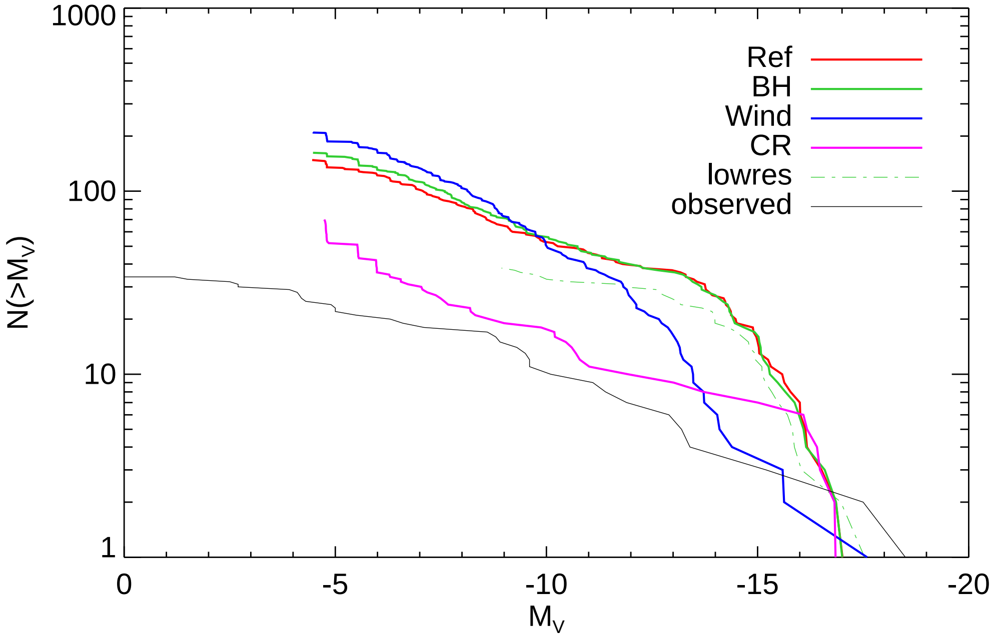

Figure 3.2: Cumulative satellite luminosity function for our different simulation models, compared to the observed luminosity function. Note that the observed luminosity function in this plot includes only known satellites without any incompleteness correction and should thus be seen as a lower limit, especially below $\approx -7\ M_V$ where satellites can only be detected within the 19.4% sky coverage of SDSS.

reference simulation. This shows that environmental heating effects from quasar feedback, in particular the possible quenching of star formation in nearby small halos, play no important role in the history of the Aq-C halo. Interestingly, galactic outflows with our standard wind prescription are also unable to significantly improve the agreement with the observations. While the most luminous satellites are moderately suppressed in stellar mass, the satellites tend to pile up on the faint side of the luminosity function, yielding to a slight steepening effect of the luminosity function, quite different from what is needed to match the data. Finally, the simulation including cosmic rays yields a substantial modification of the results. Here we actually obtain very good agreement with the luminosity function inferred from the observations, because compared with the reference model the luminosity of the satellites is efficiently suppressed by the CR feedback.

Another view on the satellite abundance is given in Figure 3.2, where we show the cumulative abundance of the satellite population as a function of luminosity, comparing all four simulation results to the observations. Here, the observational data is based only on direct observations, meaning that the black line should be taken as a lower limit for magnitudes lower than $\approx -7\ M_V$, because of the incomplete sky coverage of the SDSS. The Figure confirms the conclusions we reached from the different results of Fig. 3.1. The 'Wind' simulation is efficient in reducing the luminosity of large satellites of the size of the LMC/SMC, but does not manage to suppress the abundance of low luminosity satellites. In contrast, while the CR simulation does not reduce the luminosity of the brightest satellites much, it is very efficient in suppressing star formation in low-mass subhalos, ultimately producing a much reduced amplitude of the luminosity at the faint

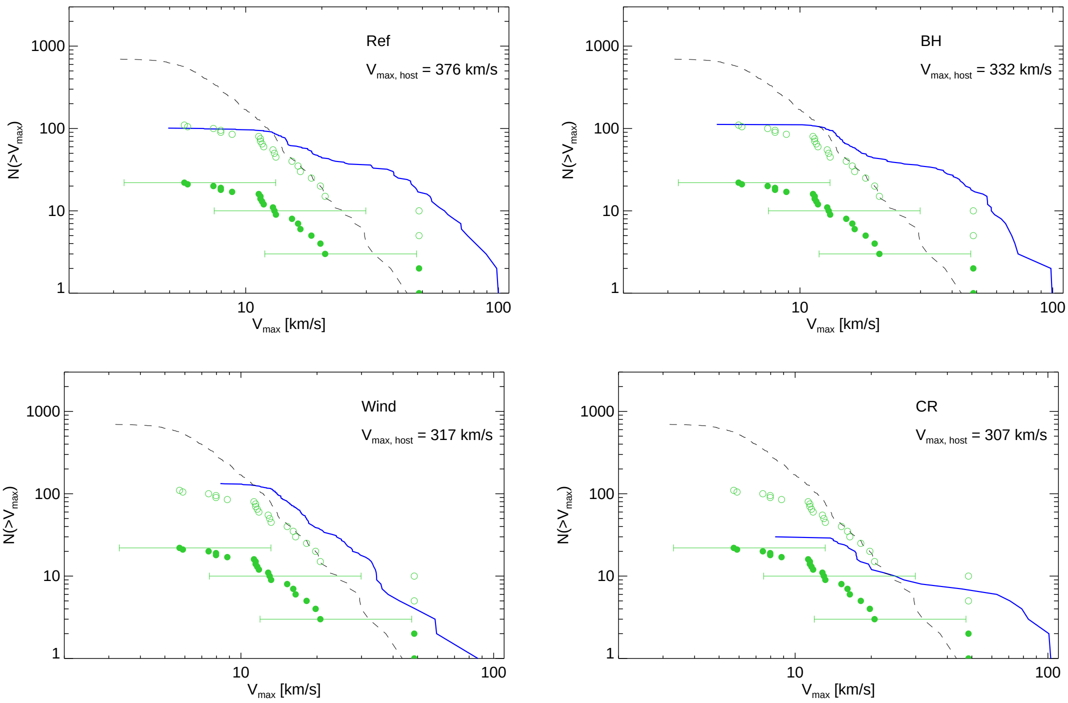

Figure 3.3: The cumulative number of luminous satellites (with stellar mass larger than $10^5\,h^{-1}\mathrm{M}_\odot$) as function of their maximum circular velocity. We compare results for our different physics simulations with data for the Milky Way satellites, taken from Madau et al. (2008); Simon & Geha (2007); Mateo (1998); Martin et al. (2007) and plotted as green filled circles together with the assumption that the circular velocity equals $\sqrt{3}$ times the central velocity dispersion σ (Primack, 2009). The error bars indicate a plausible range of circular velocities between σ and $4 \times \sigma$. Open circles show the same data as the solid circles, but scaled by a factor of 5 to roughly account for SDSS sky coverage and incompleteness. The real cumulative velocity function might be expected to lie between these two groups of symbols. In fact, we would expect it to be close to the solid (open) symbols at the high (low) velocity end with a smooth transition in between. The blue line shows the cumulative mass function of the observable satellites in each hydrodynamical simulation, while for comparison the black dashed line gives the mass function of all substructures in the corresponding dark matter only simulation. The variations in the maximum circular velocity obtained for the host halos in the different simulations are due to the different sizes of the stellar bulges grown in the different runs.

end. As a result, the CR simulation stays quite close to the observational data up to the completeness limit of the SDSS.

Figure 3.2 also includes the result of the ‘LowRes’ simulation, shown as a green dot-dashed line. We can see that the population of satellite galaxies is independent of resolution to good accuracy up to a magnitude of $\approx -12\ M_V$. Taking into account that the resolution limit of our high resolution runs is shifted by ≈ 4 magnitudes, we expect that our simulated satellite abundance should be numerically converged for satellites brighter than $\approx -8\ M_V$.

Figure 3.3 shows yet another way to compare the counts of simulated satellites with the observations. Here we use the maximum circular velocity of satellites, $v_{\max}$, on the abscissa, because circular velocities are a good proxy for the (original) mass of the subhalos, but can be much more reliably measured than the mass itself. We note that such velocity functions have already been used in the first discussions of the missing satellite problem, and are still frequently used to compare the number of observed satellites with the substructure abundance in collisionless N-body simulations (e.g. Madau et al., 2008). The filled green circles in Fig. 3.3 show the raw observational data, while the open circles are a scaled version that accounts for the SDSS sky coverage and incompleteness. The real cumulative velocity function might thus be expected to lie close to the filled symbols at high circular velocities and to approach the open circles at low circular velocities. The dashed black line shows the cumulative velocity function of all satellite galaxies produced in a dark matter only simulation, using the same initial conditions as for the high resolution hydrodynamical simulations. Finally, the blue line in each panel shows the cumulative mass function of all satellites containing at least $1 \times 10^4\, h^{-1}\mathrm{M}_\odot$ of stellar mass (one star particle) in the corresponding hydrodynamic simulation.

The differences between the observations and the simulation results for the different physics models appear large at first sight. This however confirms and is consistent with our earlier findings. In particular, the reference simulation and the simulation with black hole feedback overpredict the satellite counts for all velocities, while the wind simulation at least manages to give a reasonable abundance of the brightest satellite systems. Again, we find the cosmic ray simulation to produce the best match to the data. Whereas there may still be a moderate overproduction of bright systems, the extrapolated faint end abundance is matched quite well, and, in particular, the shape of the predicted luminosity function is in quite good agreement with the observations.

There is another interesting aspect of Figure 3.3 that concerns the comparison with the dark matter only results. It is a generally assumed that satellite galaxies are dark matter dominated. However, comparing the black dashed line, which shows the mass function of satellites in the corresponding dark matter only simulation starting from the same initial conditions, with the result of the individual hydrodynamic simulations, we note some sizable differences. The high mass satellites show clear evidence that gas cooling has led to a higher concentration of their mass profiles, thereby increasing their circular velocities. Despite the relatively low stellar mass content in these bright satellites, they hence show some structural changes due to baryonic effects. We note however that invoking yet stronger supernovae feedback may reduce these effects if the cooling rate is more effectively reduced.

3.4.1 Kinematic results

We close this section with an analysis of some of the structural properties of the simulated satellite population. As noted earlier, the total mass of a satellite galaxy is difficult to measure, so other tracers are usually used as a proxy for mass. An observationally readily accessible measure of this type is the central velocity dispersion, which is very commonly used (e.g. Simon & Geha, 2007). In Figure 3.4, we compare the relation between central velocity dispersion and luminosity for our simulation satellites with data from Simon & Geha (2007), updated with the latest values for the known satellites from Walker et al. (2009).

There seems to be quite good agreement between the observations and the dark matter velocity dispersions of the Ref simulation. As the sample of measured satellites is quite small and has rather large error bars, the weak trend of rising velocity dispersion with rising luminosity is not very well determined, but the simulation apparently follows the same trend. We note that the alignment of the simulated satellites on the left hand side of the plot is due to resolution issues from discreteness effects. In fact, the different 'stripes' are separated by just one star particle. The stellar mass in each stripe is therefore equal, even though some scatter in luminosity is still present because the luminosity was calculated with the Bruzual & Charlot (2003) model, taking into account the age and metallicity of the star particles, effectively giving each stellar particle its own mass-to-light ratio.

3.5 History of satellite galaxies

In this section we track the evolution of individual satellites, with the aim to study their formation paths for a range of individual accretion, mass loss and star formation histories. To this end we select nine representative satellite galaxies, split into groups of three that are taken from three different mass ranges. In Figure 3.5, we show our 'high mass sample', consisting of three satellite galaxies with a final stellar mass higher than 5×10^8 $\mathrm{M}_\odot$. Satellites with intermediate final stellar mass between 5×10^8 $\mathrm{M}_\odot$ and 5×10^6 $\mathrm{M}_\odot$ are shown in Figure 3.6, while Figure 3.7 gives three low-mass examples of satellites with a final stellar mass less than 5×10^6 $\mathrm{M}_\odot$.

The different panels in the three Figures 3.5 to 3.7 are organized in the same way, and show in each case the history of one individual satellite (with a final stellar mass as labeled in the Figure). For each satellite, the top panel gives the redshift evolution of the dark matter, gas and stellar components as blue, green and red solid lines, respectively. The total mass of the satellite is shown as the black line. The middle panel shows both the star formation rate (solid line) and the maximum circular velocity (dashed line), as a function of time. Finally, the bottom panel gives the evolution of the radial distance of the satellite to the host galaxy (solid line) and compares this to the virial radius of the host (R_{200}, dashed line). Finally, the dotted vertical line running through all panels highlights the epoch $z = 6$, which is the time when the UV background reionizes the universe in our simulations.

The different satellite histories we have selected in Figs. 3.5 to 3.7 show a variety of interesting evolutionary effects that we now discuss in turn. For definiteness, we have here selected the BH run, but our other simulations show qualitatively very similar results. The left panel of Fig. 3.5 gives a nice illustration of the tidal and ram pressure stripping effects that play an important role in shaping the properties of the satellites. It is clearly seen that the dark matter mass starts decreasing in distinctive steps as soon as the satellite has fallen into the host halo and orbits with rather high eccentricity. These mass stripping events correspond to individual pericentric passages, as is clearly seen in the panel that gives the distance to the host halo. Note however that the stellar component is not noticeably affected by this tidal stripping process, as expected from the fact that the stars of the satellite are much more concentrated than the dark matter. In contrast, the gas component behaves rather differently. Here we see clear evidence for ram pressure stripping as the dominant source of mass loss even in high mass satellites. Interestingly, this effect starts to set in even before the satellite crosses the virial radius of the host, probably because the gaseous halo of the host is more extended than R_{200}.

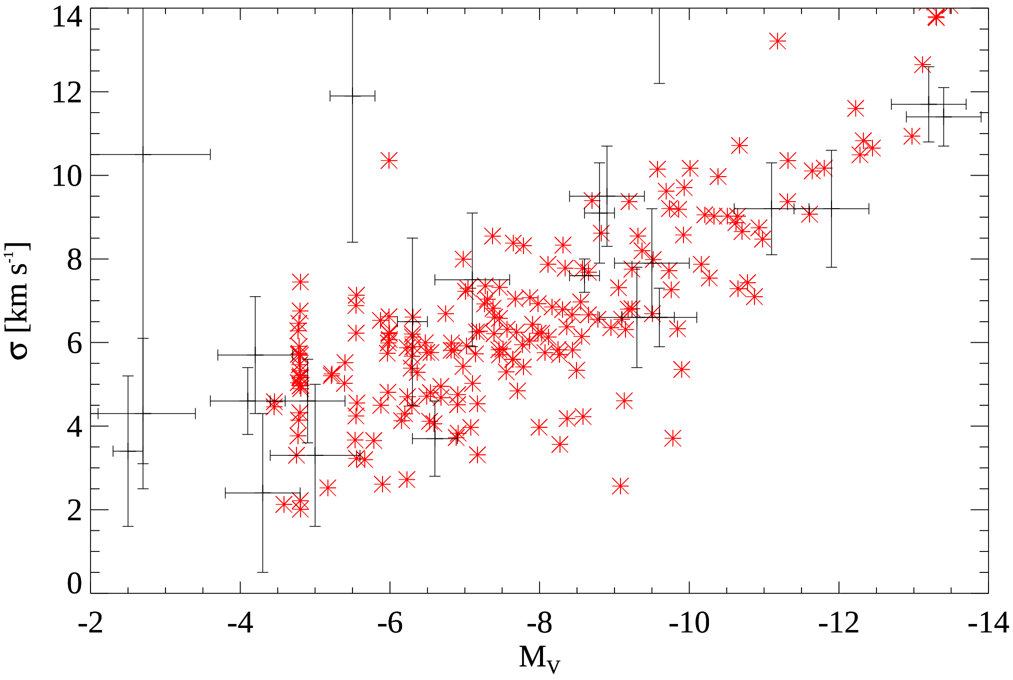

Figure 3.4: Total V-band luminosity against velocity dispersion. We show the observational data points of Simon & Geha (2007) combined with velocity dispersions taken from Walker et al. (2009) as black crosses, and compare to the simulated satellites plotted as red symbols. The two samples are in good agreement, except perhaps for slightly different slopes.

This has also been pointed out in a recent study by Book & Benson (2010).

Because ram pressure stripping depends on the density of the surrounding gas, one should expect to see variations of the mass loss rate with the radial position of the infalling satellite. This is indeed seen if one compares the results for the three different satellites shown in Fig. 3.5 with each other. The satellite on the left follows a very eccentric orbit and spends most of the time in the outer parts of the halo, resulting in a comparatively slow gaseous mass loss. The satellite shown in the middle panel has an orbit with a lower eccentricity that keeps it at apocenter well inside the virial radius, yielding a consistently higher mass loss rate. Finally, the satellite shown on the right panel has a nearly circular orbit at small radius, and loses its gas component even faster.

Perhaps one of the most interesting effects seen in Figures 3.5 to 3.7 is the effect of reionization on the star formation of the satellite galaxies. Quite often the simplifying assumption is made that reionization would be able to stop star formation in satellite galaxies entirely, yet this is clearly in contradiction with the findings of our simulations. In fact, all satellites shown in these Figures (and the same is true for the majority of other satellites too) are producing most of their stars at times later than $z = 6$. Star formation continues in all examples until the gas component is removed by ram pressure stripping, but this time can be considerably later than the epoch of reionization. We hence find that the detailed orbit of a satellite galaxies tends to be more important for determining its final luminosity than the circular velocity it had at the epoch of reionization. An illustration of this can be seen in the histories of the satellites shown in the middle and

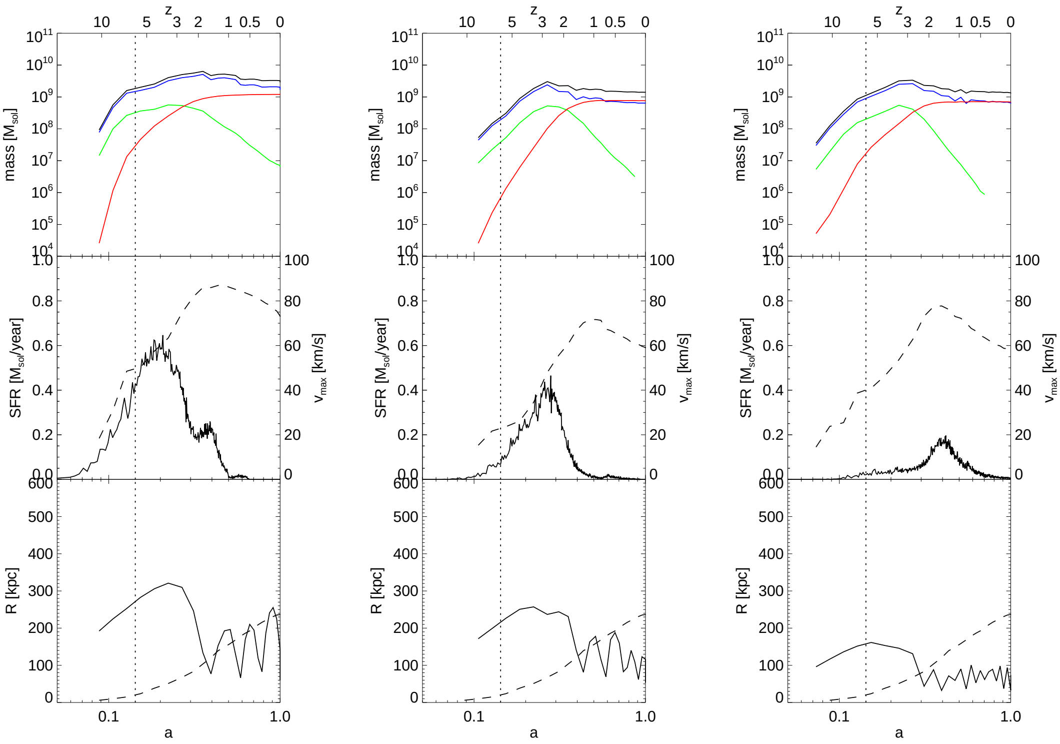

Figure 3.5: Detailed time evolution of three representative examples of high-mass satellites, from the time of their first appearance as individual galaxies until $z = 0$. In each case, the top panel shows the evolution of the dark matter, gas and stellar mass components as blue, green and red lines, respectively while the total mass is shown as the black line. The middle panel shows the star formation rate as solid line, and the maximum circular velocity as a dashed line (with the corresponding scale on the right y-axis). The bottom panel gives the radial distance of the satellite to the host galaxy at each timestep (solid line), and compares this to the virial radius (R_{200}) shown with a dashed line. The dotted vertical lines in all panels mark the $z = 6$ epoch of reionization in our simulations.

right panels of Figure 3.6. These two satellites have quite similar dark matter, gas and stellar masses shortly before they enter the hot gaseous halo of the host galaxy, but they are moving on very different orbits. The satellite in the middle panel is on a relatively circular orbit, resulting in a small effect of tidal stripping on the dark matter component and no noticeable effect on the stellar component. In contrast, the satellite shown in the right panel is on a highly eccentric orbit with $\epsilon \geq 10$. This satellite dives deeply into the host halo, resulting in a tidal radius that is even smaller than the characteristic radius of the stellar component. Because of this, the stellar component looses nearly 90 % of its mass due to tidal effects.

Many early simulation studies (e.g. Benson et al., 2001; Somerville, 2002) simply prevented additional gas accretion after the time of reionization. Comparing this approach with our simulated satellites shows also a big discrepancy. Most of the simulated satellites are at least doubling their gas content after $z = 6$.

As can be seen from Figures 3.5 to 3.7, most of the simulated satellites are loosing their whole gas content. Only a few of the most massive satellites are able to keep some gas, ending up with gaseous masses of $\approx 10^6$ M$_\odot$ $-$ 10^9 M$_\odot$ which seems to be in reasonable

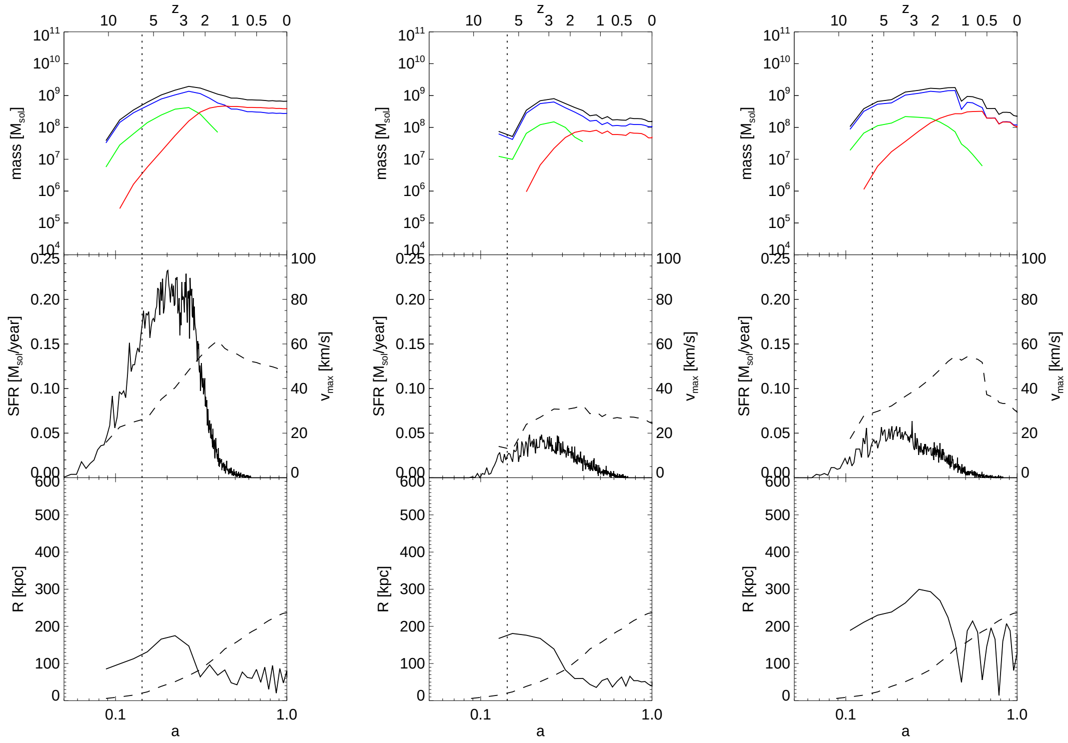

Figure 3.6: The same as Fig. 3.5, but for three intermediate mass satellites.

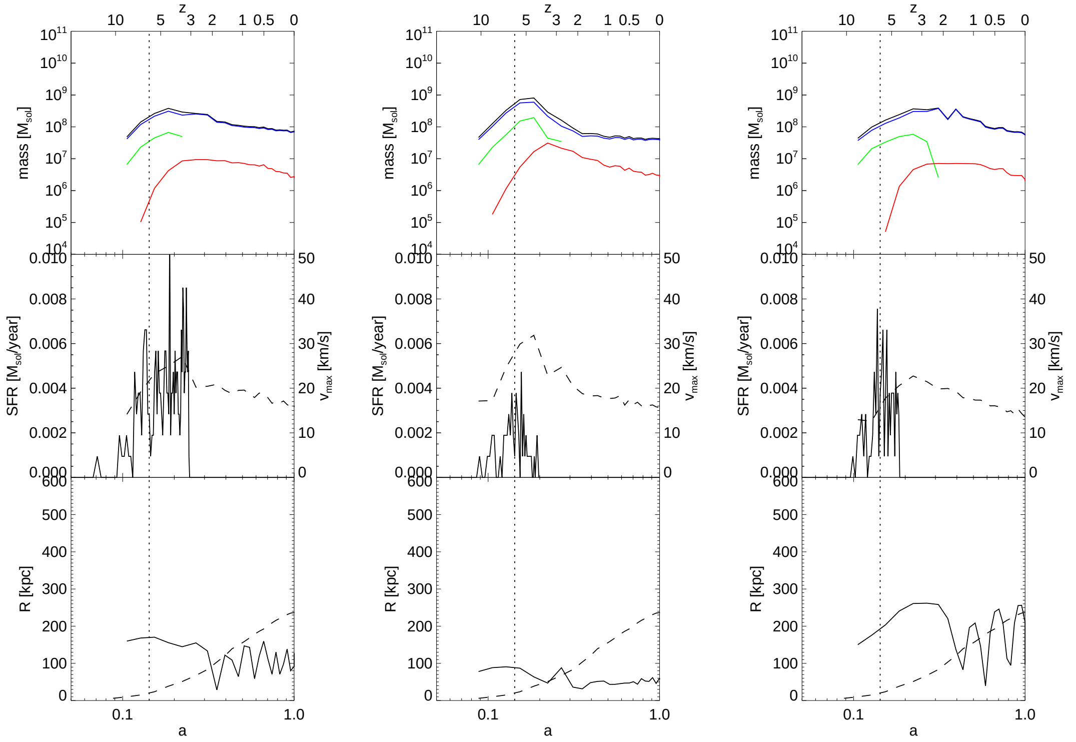

Figure 3.7: The same as Fig. 3.5 but for three low mass satellites.

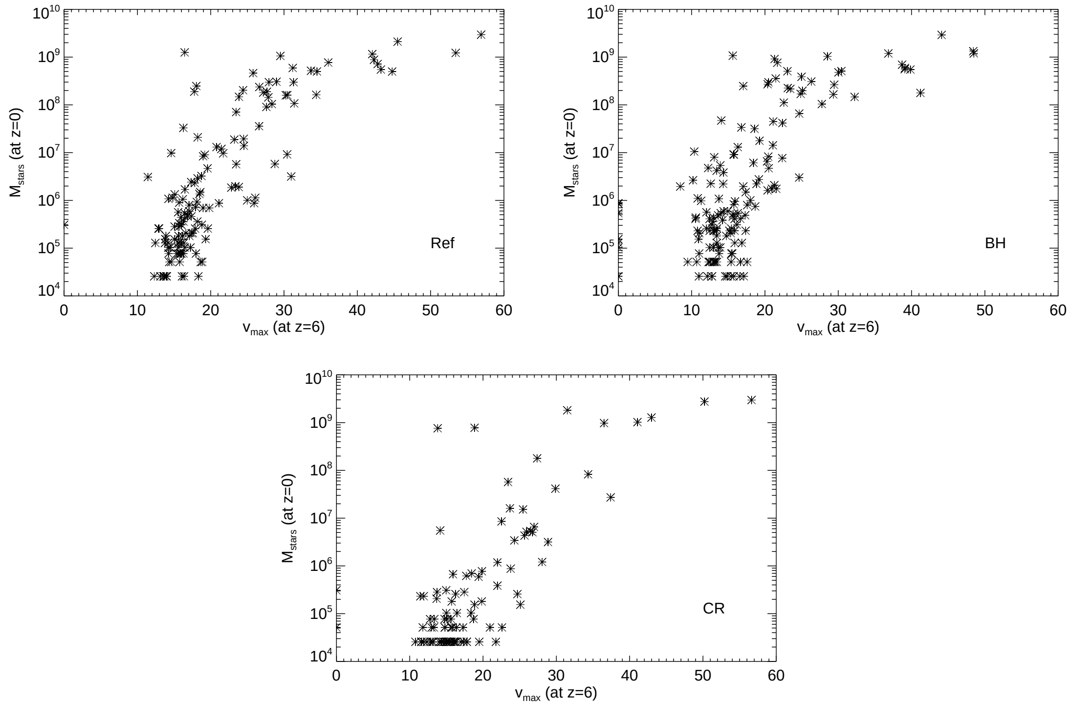

Figure 3.8: Current stellar mass of satellites versus their maximum circular velocity at $z = 6$. We do not find a clear threshold in $v_{\max}$ at $z = 6$ that could be used to decide whether or not a satellite galaxy is able to form stars later on. Instead, we find that the final stellar mass shows large scatter over a considerable range of circular velocities at the epoch of reionization.

agreement with observations, see for example van den Bergh (2000).

In Figure 3.8, we compare the final stellar mass of the satellites against the maximum circular velocity $v_{\max}$ they had at redshift $z = 6$. This provides another way to test the popular hypothesis that the mass at the time of reionization determines the final luminosity of a satellite galaxy. We show results for the simulations Ref, BH and CR[‡]. While most satellites with circular velocities below $\sim 20\,\mathrm{km\,s^{-1}}$ are strongly suppressed in stellar mass, there are a few objects with such low circular velocities that have stellar masses as high as 10^8 $M_\odot$, or even 10^9 $M_\odot$, at the present epoch. In the range of $\sim 20\,\mathrm{km\,s^{-1}}$ to $\sim 30\,\mathrm{km\,s^{-1}}$, no sharp cut-off is readily apparent that could be identified with reionization. Instead there is considerable scatter in the relation between final stellar mass and maximum circular velocity at $z = 6$. We note that the simulation with cosmic rays shows a strong suppression in the stellar mass for low circular velocities when compared with the other simulations, as expected from our luminosity function results.

A complementary of view of the above relation is shown in Figure 3.9, where we plot the current maximum circular velocity of satellites against their current stellar mass. Different symbols encode the circular velocity they had at redshift $z = 6$, where satellites with $v_{\max} \geq 16\ \mathrm{km\,s^{-1}}$ at $z = 6$ are shown as red diamonds while satellites below this threshold are shown as green stars. Note that there is considerable overlap between the regions occupied by the different symbols, showing again that the correlation between

---

[‡] Unfortunately, all snapshots before $z = 2.7$ of the simulation Wind where accidentally deleted, making this comparison impossible for this model.

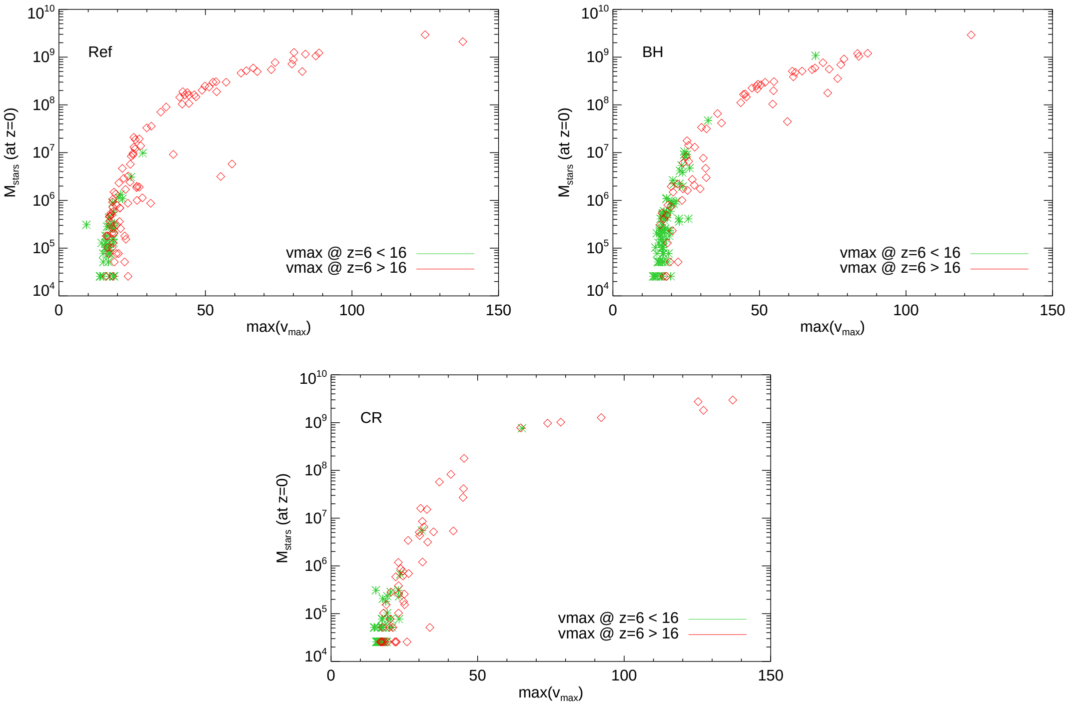

Figure 3.9: Current stellar mass versus current maximum circular velocity. Satellite galaxies with $v_{\rm max} \geq 16$ km/s at $z = 6$ are shown as red diamonds, and satellites below this limit as green stars. There is again no evidence that this threshold or one nearby is able to distinguish between satellites with or without a significant amount of stars.

the circular velocity at the epoch of reionization and the current stellar mass is not overly strong. In particular, there are some examples (especially in the BH simulation) of satellite galaxies with very low circular velocity at $z = 6$ which were nevertheless able to form many stars later on and to turn into reasonably luminous satellites.

Finally, in Figure 3.10, we directly compare the results of the different physics simulations with each other, in terms of the relationship between $v_{\rm max}$ and the stellar mass at the time of reionization. Interestingly, we see that AGN feedback is in fact able to reduce the stellar mass formed at high redshift in many of the progenitor systems of today's satellites, even though the effect is considerably weaker than for cosmic rays. As we have already seen, the influence of BH feedback tends to become low at later times, so that the present day properties of satellites are only mildly effected. This is presumably because most satellites do simply not grow a massive black hole, but they are nevertheless affected at high redshift by the seed black hole that is injected into their halo.

In Figure 3.11, we plot the baryon fraction of satellites against $v_{\rm max}$, at the present epoch. The baryon fraction is here simply defined as the total bound baryonic mass relative to the total bound mass of a halo. It is interesting to compare this value with the universal cosmic baryon fraction $\Omega_b/(\Omega_b + \Omega_{\rm dm}) = 0.16$ (shown as dashed horizontal line). As one expects, the baryon fraction is usually lower than the cosmic baryon fraction, especially for very low mass satellites that have lost most of their gas and did not form many stars either. However, in the simulation with comparatively weak feedback, some satellites have also baryon fractions above the cosmic mean value. These are satellites which lost a lot of dark matter through tidal stripping whereas they could hold on to most of their stars. Both the Wind and CR models are leading to considerably reduced baryon fractions in low mass satellites. In the former case, this is readily expected as a signature of the winds. In the latter, it is because more baryons stay in a diffuse gaseous phase, allowing them to be more easily ram-pressure stripped.

An analysis of the evolution of the baryon fraction between $z = 6$ and $z = 0$ is given in Figure 3.12. We here only show results for the Ref simulation, as the qualitative behavior of the other simulations is similar. We use two symbols for each satellite, one showing the data point at $z = 6$ (red stars), while the corresponding values at $z = 0$ are given by green stars. Every pair of points belonging to the same satellite is connected by a dotted line. Most satellites with circular velocities below $\sim 20\,\mathrm{km\,s^{-1}}$ at $z = 6$ lower their baryon fraction substantially until the present epoch, and they also do not tend to grow much. In contrast, most larger satellites tend to keep their baryon fraction or increase it slightly, often accompanied by a significant increase in v_{max}. In the most massive satellites, part of this increase stems from modifications of the inner rotation curve due to the formation of a quite concentrated stellar component, i.e. these satellites are not really bona-fide dark matter dominated systems as often assumed. We note however that the threshold at $\sim 20\,\mathrm{km\,s^{-1}}$ is not sharp; there are still many examples of satellites with an initially high v_{max} that end up as low mass satellites with a stripped baryonic component.

The last quantity we analyze in this section are the cumulative star formation histories of our satellites, as shown in Figure 3.13. The solid black line shows the total cumulative star formation history of all satellites in the final virial radius, normalized by their total final stellar mass. The gray shaded area gives the 1σ scatter around this mean for the ensemble of all satellite star formation histories. The vertical dotted, dashed and dot dashed lines mark the times when 10 %, 50 % and 90 % of the stars present at $z = 0$ were formed. Finally, the dashed blue line repeats the result of the Ref simulation in all the panels corresponding to the other simulations, in order to ease a comparison between them. As we have already seen in the other results, AGN feedback shows little effect on the cumulative star formation history of the satellites. The Wind model on the other hand leads on an earlier production of the bulk of the stars, which is what one would expect if galactic outflows are efficiently removing gas from star-forming dwarf galaxies and are thus shutting down star formation earlier. In contrast, the CR model shows exactly the opposite effect. Due to the additional pressure component, the galactic gas has a lower overall cooling rate. This hampers star formation in low mass systems but does not by itself remove significant amounts of fuel for star formation; the latter can however be achieved by ram pressure stripping. Thus, star formation shifts to considerably later times in the CR run than in any of the other models.

Interestingly, the scatter around the mean history of the satellites is also modified by the different physics. The Wind simulation shows a rather small scatter, presumably because most satellites form their stars in the first significant phase of star formation at high redshift, which is terminated quickly and for the most part coevally. In the case of the CR simulation, much of the gas is not removed by the primary feedback process itself, but instead is affected by stripping processes at intermediate and low redshifts, after the satellites have fallen into the parent halo. This means that the individual infall history of each satellite is of larger importance in this model, leading to a higher overall variability in the star formation history of the satellites.

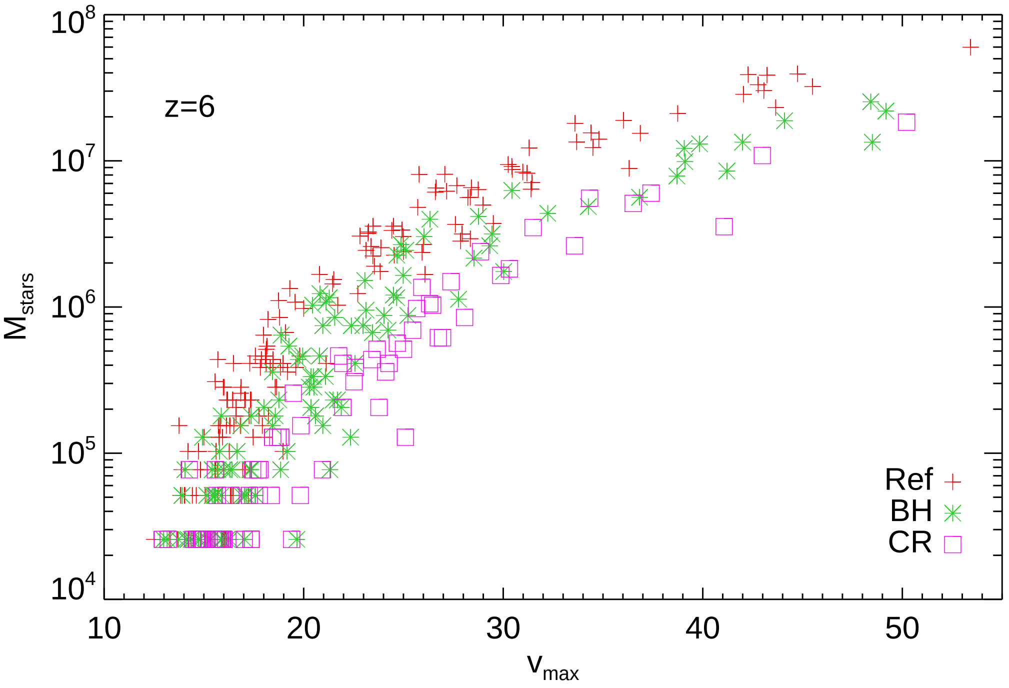

Figure 3.10: Stellar mass versus maximum circular velocity at $z = 6$, compared for different simulation models. Interestingly, a weak influence of AGN feedback on the satellite population is found at high redshift, but this difference largely vanishes later on, as most of the satellites are simply not able to grow a large supermassive black hole. In contrast, the additional pressure component of cosmic rays affects all satellites more strongly, and here the effect remains large in small galaxies even down to $z = 0$.

Finally, it is very interesting to compare the results of our simulations with observational data. The points with error bars in all panels of Figure 3.13 show the data given in Orban et al. (2008). The best agreement is again found for our CR simulation, providing further support for this model.

3.6 Scaling relations

In this section, we investigate in more detail how the properties of our simulated satellites scale with their size. Where possible, we compare with observational results and other theoretical predictions. We want to caution however that especially our smallest luminous satellites are pretty close to our resolution limit. While the satellites above the detection limits of SDSS should be sufficiently well resolved in our high resolution simulation to give reliable results, a considerable numerical uncertainty persists, a fact that should be taken into account in interpreting the results.

We begin with the scaling relations derived by Woo et al. (2008) for local group dwarf galaxies. We focus on the relations between stellar mass and circular velocity, and stellar mass and star formation rate, as they have the highest statistical significance and are thus best suited to benchmark the simulation results. Figure 3.14 shows these two relations in separate panels, comparing in each case the fits derived by Woo et al. (2008) with our simulation data. The correlation between stellar mass and maximum circular velocity is comparatively tight, in fact, Woo et al. (2008) cite a correlation coefficient of 0.94 for the observations, which are represented by the solid red line. The simulated satellites show a similarly strong correlation (formally yielding a correlation coefficient of 0.94), but the results for the Ref simulation are slightly offset towards higher stellar masses. The CR results (shown with magenta symbols) agree considerably better. Our lowest mass satellites start to deviate from the fit given by Woo et al. (2008) but the differences are of comparable size as in some observed systems such as Ursua Minor, and the growing scatter in the numerical results also indicates that resolution effects start to play a role.

The right panel in Fig. 3.14 compares the correlations between stellar mass and current star formation rate. Here we find a much worse agreement with the observational results of Woo et al. (2008), which are again characterized by a remarkably good correlation (with coefficient 0.96). While our results bracket the observationally inferred relation, the scatter is large and the formal correlation is only 0.72. In addition, most of our satellite galaxies show only a vanishingly small star formation rate at the present epoch, and those systems were omitted from the plot. But again, the CR results seem to agree better with observations. Simulations with better mass resolution will be needed to shine more light on this potential discrepancy.

Simon & Geha (2007) calculated the mass-to-light ratio for the sample of Milky Way satellites found in the SDSS, obtaining values ranging from about 100 to 1200, with a mean of ~ 380. Doing the same calculation for the whole sample of known satellites resulted in values between 1.5 and 1200 with a mean of ~ 170. This suggests that the faint satellites discovered with the SDSS are even more dark matter dominated than the more luminous 'classical' satellites. For the complete sample of simulated luminous satellites, we obtain mass-to-light ratios between 12 $(11, 16, 10)$ and 13000 $(18000, 23000, 18000)$ with a mean of ~ 1500 $(1350, 1550, 3500)$ for the Ref (BH, Wind, CR) simulation. As mentioned earlier, very small satellites are strongly affected by numerical effects and thus the very large mass-to-light ratios we find for these satellites may be unreliable. Also, the mean value may be biased high by the large number of small satellites. If we restrict the mass-to-light ratio calculation to satellites with $M_V \leq -8.0$, we obtain a mean of 232 $(217, 315, 345)$, which is much closer to the observed values. If we select only satellites with a surface brightness $\mu \leq 30$, then the mean mass-to-light ratio is 33 $(33, 73, 33)$, which is about 5 times smaller than the observed mean value for this selection.

This difference in the mean mass-to-light ratio can also be seen from the "Mateo Plot" shown in Figure 3.15, which compares the luminosities of the satellite galaxies with their mass-to-light ratio in units of the solar mass-to-light ratio. In the original paper where this plot was introduced, Mateo (1998) overplotted the function

$$\frac{(M/L)}{(M/L)_\odot} = 2.5 + 10^7/(L/L_\odot), \tag{3.2}$$

which we also included as the dark red dot-dashed line in Fig. 3.15. To guide the eye, we also simply scaled this function by a factor of ≈ 5.2 and plotted it again as the purple dot-dashed line. It can be seen that this scaled function fits the simulated galaxies of the Ref simulation very well, while the observed systems (shown with red and green triangles) are well described by the original function. This result is consistently reproduced by all simulations. Only the constant horizontal offset between observations and simulations

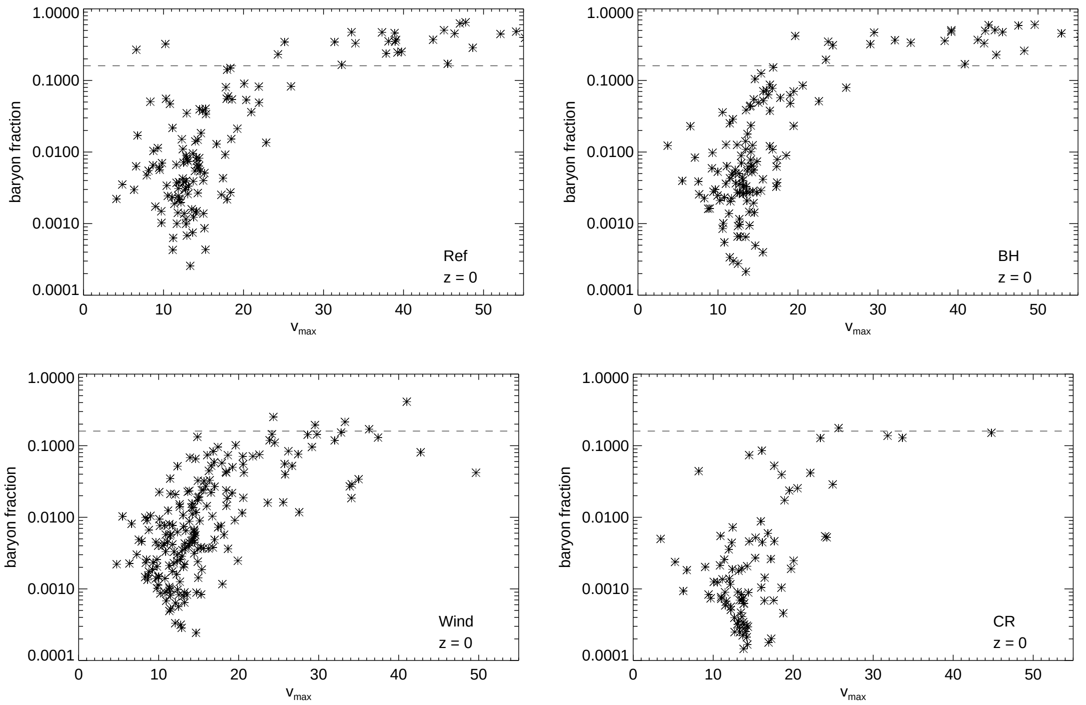

Figure 3.11: Baryon fraction of $z = 0$ satellite galaxies as a function of their circular velocity. We show results for our four primary simulation models, and define the baryon fraction in terms of the bound particles identified by SUBFIND for each satellite. The horizontal dashed line gives the universal cosmic baryon fraction.

changes by ≈ 10% while the general trend remains the same.

We note that the nearly constant offset between the simulated and observed satellite galaxies could in part be caused by the rather uncertain procedure applied to estimate the total mass of observed satellites. This effectively involves an extrapolation to the outer edge of the satellite, which is uncertain. An alternative would be that the simulated galaxies simply contain fewer stars than expected for an observed satellite of the same mass. However, the REF simulation already has comparatively weak feedback, and allowing for brighter satellites by a constant factor would cause the most luminous satellites, which are in good agreement with the Magellanic Clouds, to become too bright. Furthermore, making the star formation more efficient in all satellites would shift the points in Fig. 3.15 both down and to the right, hence spoiling the good agreement with the location of the break in the observed relation.

Wolf et al. (2010) recently developed a new method to estimate the mass of dispersion-supported galaxies. The corresponding new mass-to-light ratios are shown in Fig. 3.15 as black open triangles. It is interesting to note that these newer data points, based on a more sophisticated method, in fact yield systematically higher mass-to-light ratios. This strengthens our argument given above, that the total mass of the Milky Way satellite galaxies might be underestimated by the methods currently applied in analyzing the observational data. In any case, it is encouraging that more sophisticated and likely more accurate mass estimates tend to diminish the gap between observations and simulations.

In Figure 3.16, we show the relation between photometric surface brightness of all

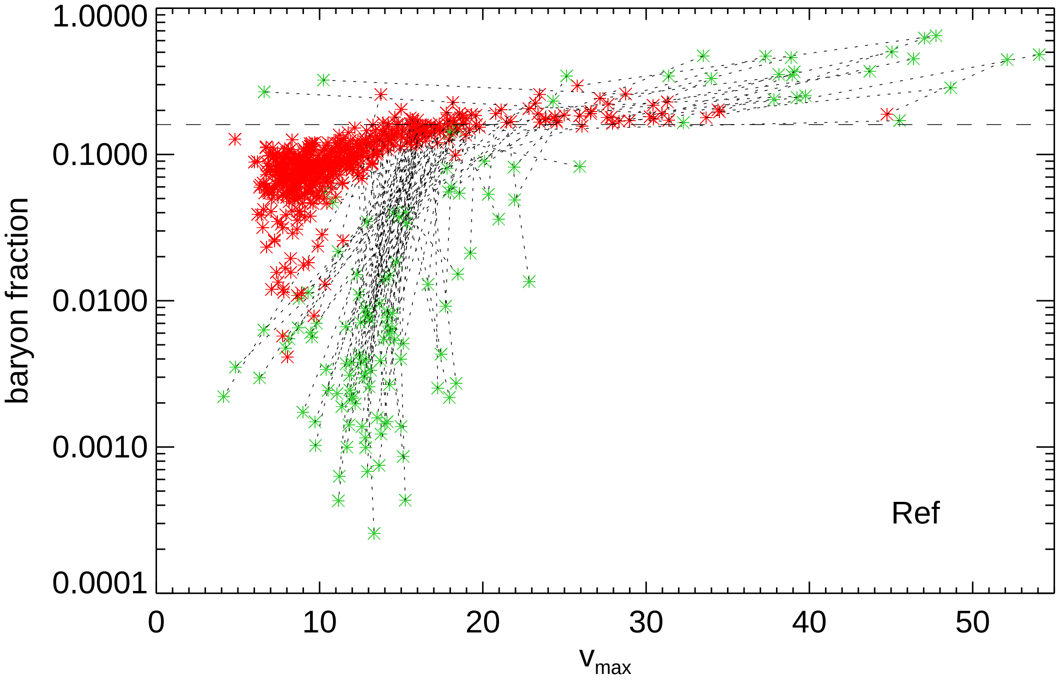

Figure 3.12: Evolution of the baryon fraction and circular velocity between $z = 6$ and $z = 0$. For each satellite, we mark the high redshift $z = 6$ data with a red star and the $z = 0$ value with a green star, and we connect each pair of two points with a dotted line. There is clearly a pivotal maximum circular velocity of about $\sim 25\,\mathrm{km\,s^{-1}}$ below which most satellites lose a large fraction of their baryons, while they retain their baryon fraction above this threshold.

simulated dwarf galaxies inside a sphere of radius 350 kpc centered on a fiducial position of the Sun. The Sun was assumed to lie 8.5 kpc away from the center of the galaxy, in the central plane of the stellar disk. As can be seen from the relatively large scatter of the plot, the simulation produces also satellites that are well above the SDSS surface brightness detection limit. Counting the galaxies with a photometric magnitude brighter then 30 mag/arcsec^2 (dashed red line) and a distance smaller than 280 kpc (dot dashed blue line) results in observable 46 (77, 18, 70) satellites for the REF (BH, CR, WIND) simulation. This is actually in reasonable agreement with the prediction of 57 satellites for the Milky Way. The cutoff radius of 280 kpc was chosen as a compromise between the measured distances to all known satellites, which reach up to ≈ 1 Mpc, and the virial radius of $r_{200} = 238$ kpc of the simulated host galaxy. This is also the same cut off radius that has been used in previous work (Koposov et al., 2008; Macciò et al., 2010), although we note that some studies have adopted a different choice (e.g. Diemand et al., 2007). The rather small number of satellites classified as ‘observable’ for the CR simulation can easily be explained by the lower luminosity function shown in Figure 3.1.

Finally, we consider the relation between the dark matter masses of our simulated satellites with their stellar mass and luminosity, as shown in Figure 3.17. For each satellite, we plot the dark matter mass with different symbols, both at the epoch of accretion and at the present epoch. To simplify a comparison with Figure 5 of Macciò et al. (2010), we used exactly the same axis range in our plot as they did. Unlike

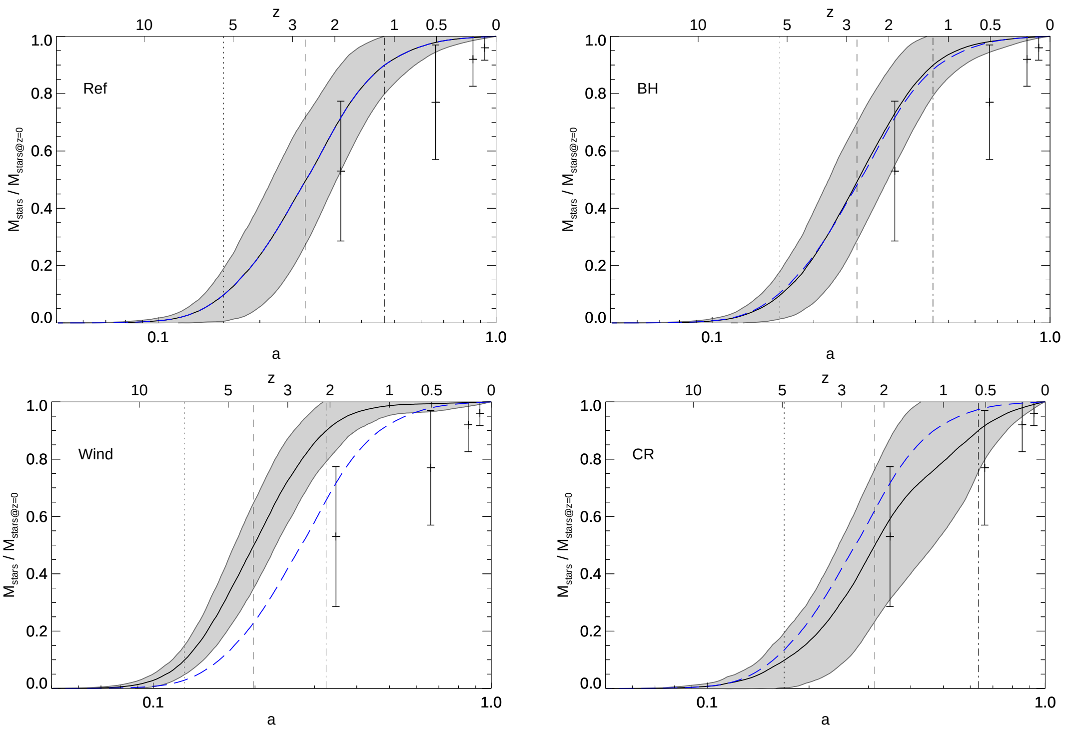

Figure 3.13: Average cumulative star formation histories of all satellite galaxies, for all four primary simulation models. In each panel, the solid line shows the average star formation history, with the grey bands mark the 1 σ scatter of the distribution. The vertical dashed and dotted lines give the times when 10%, 50%, and 90% of all the stars have formed. To ease the comparison between the different simulations, the result of the Ref simulation is repeated in all the panels as a dashed blue line. Datapoints with error bars are showing the results from Orban et al. (2008).

in the results of Macciò et al. (2010), we find a clear bend in the relation, meaning that our satellites tend to have higher stellar masses, especially at the low mass end, than the satellites of Macciò et al. (2010). The latter results are based on a semi-analytic model where the orbits of an infalling satellite are estimated based on a random choice of plausible infall parameters. It is possible that this explains the discrepancy, or that it originates in approximate treatments of tidal or ram pressure stripping in the semi-analytic model. In future work, it will be interesting to inter-compare direct hydrodynamical simulations and the semi-analytic models on a satellite by satellite basis, in order to better understands the origin of these differences in the predictions.

3.7 Conclusions

In this work, we studied a set of high-resolution hydrodynamical simulations of the formation of a Milky Way sized galaxy, starting from cosmological initial conditions. Such simulations are now able to reach sufficiently high resolution to directly resolve the formation of the small dwarf galaxies that orbit in the halo, thereby allowing studies of the missing satellite problem and of the properties predicted by simulations for the population of satellite galaxies. These galaxies are especially interesting both because the dark

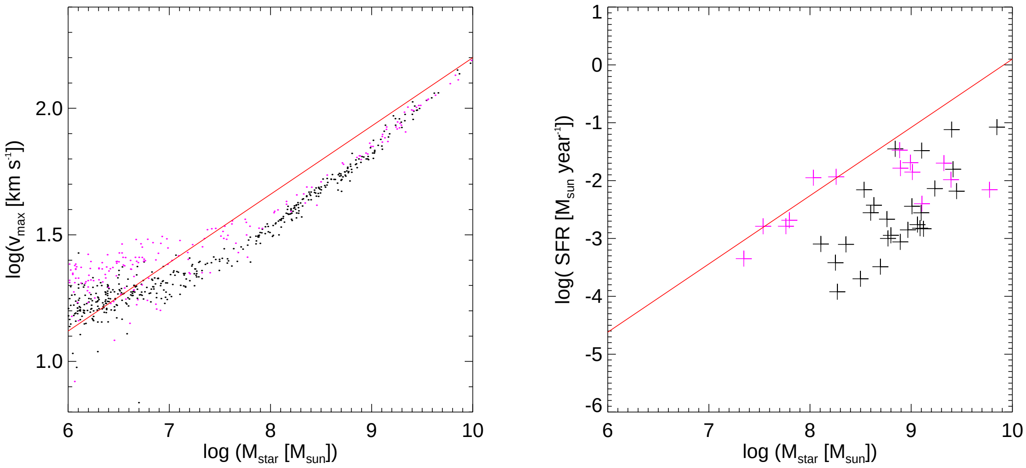

Figure 3.14: The left panel shows the relation between stellar mass and maximum circular velocity at the present time, while the right panel gives the relation between stellar mass and star formation rate. The red lines give the best fits Woo et al. (2008) derived for the observational data. We here included all simulated dwarf galaxies within the full high resolution region of the Ref simulation (in black) and of the CR simulation (in magenta), since Woo et al. (2008) did also include dwarfs outside of the virial radius of the Milky Way.

matter substructure abundance is a fundamental challenge for the ΛCDM cosmology, and because the low star formation efficiencies of the satellites provide crucial information about the physics of feedback.

We have therefore repeated our simulations using different models for feedback physics, with the goal to test the sensitive of the results for the satellites with respect to these physics assumptions. In the Ref model, we considered only star formation and SN feedback, together with instantaneous reionization at $z = 6$. The three other models included additional processes like AGN feedback (BH), wind driven galactic outflows (Wind) and the generation and decay of cosmic rays (CR). Not unexpectedly, the BH model showed no significant differences compared to the reference Ref model, as most of the satellites are simply too small to grow a large supermassive black hole and are rarely affected by strong quasar feedback in neighboring galaxies. In contrast, the Wind model showed a significant reduction of the number of high mass satellites, but did not give a significantly different abundance of low mass systems. We can not exclude that this behavior is in part induced by a too simplistic kinetic feedback model applied in this work. A better understanding of the wind physics is needed to study this issue further, and to see whether an improved modeling of wind feedback can produce a more successful satellite population. The CR model had exactly the opposite effect as it did not change the high mass satellites but suppressed star formation in low mass satellites. This made the cosmic ray model most successful in matching the faint-end of the observed satellite luminosity function. Our results further suggest that a combination of the Wind and CR feedback models should be able to yield a nearly perfect match of the luminosity function.

The total number of satellites observable with an SDSS-like survey covering the whole sky has been estimated to be 57 (Simon & Geha, 2007). Interestingly, imposing the same surface brightness detection threshold on all of our simulated systems yields a prediction

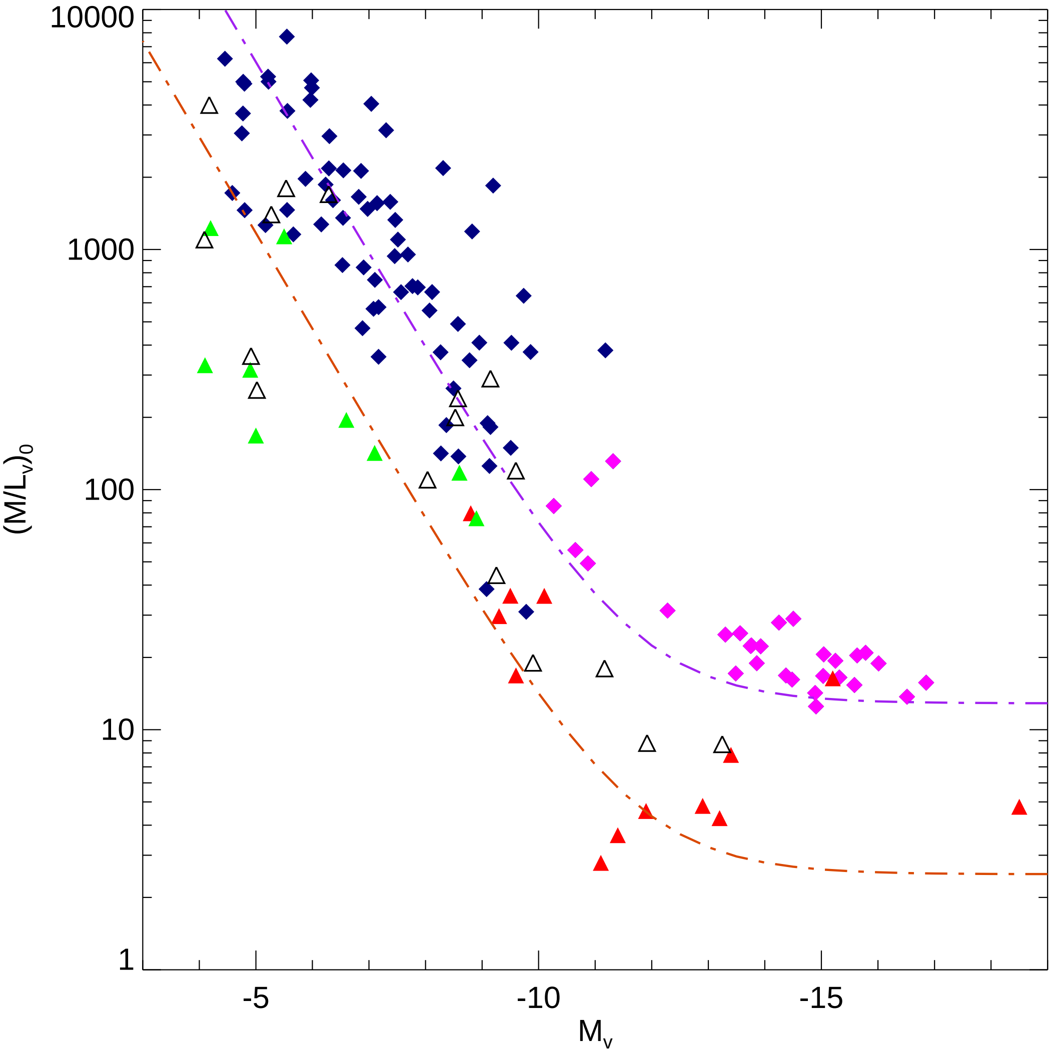

Figure 3.15: The relation between mass-to-light ratio and luminosity of satellite galaxies (see Mateo, 1998). The observed satellites are plotted as triangles, with red symbols marking satellites known before SDSS and green symbols marking the newly discovered satellites discovered in the SDSS data. Diamonds give our simulated satellites (REF model), color-coded as magenta if their surface brightness is high ($\mu \leq 30$) or as dark blue if it is low. The dot-dashed lines represent the fitting function suggested by Mateo (1998), for the observed sample (red) and shifted upwards by a factor of 5.2 (dark purple) to match the simulated sample. Additionally, the black open triangles show the mass-to-light ratios calculated recently by Wolf et al. (2010) using a novel and potentially more accurate mass estimate for dispersion-supported galaxies.

of 77 observable satellites for our BH model, which is only moderately higher than the observations despite the fact that this simulation overpredicts the satellite luminosity function considerably. For our CR model instead, the number drops considerably, to 18, perhaps caused in part by an overprediction of the effective stellar radii of the satellites, which could easily arise from the limited spatial resolution of our simulations. In any case, this stresses that a large number of additional satellites may actually still be hidden

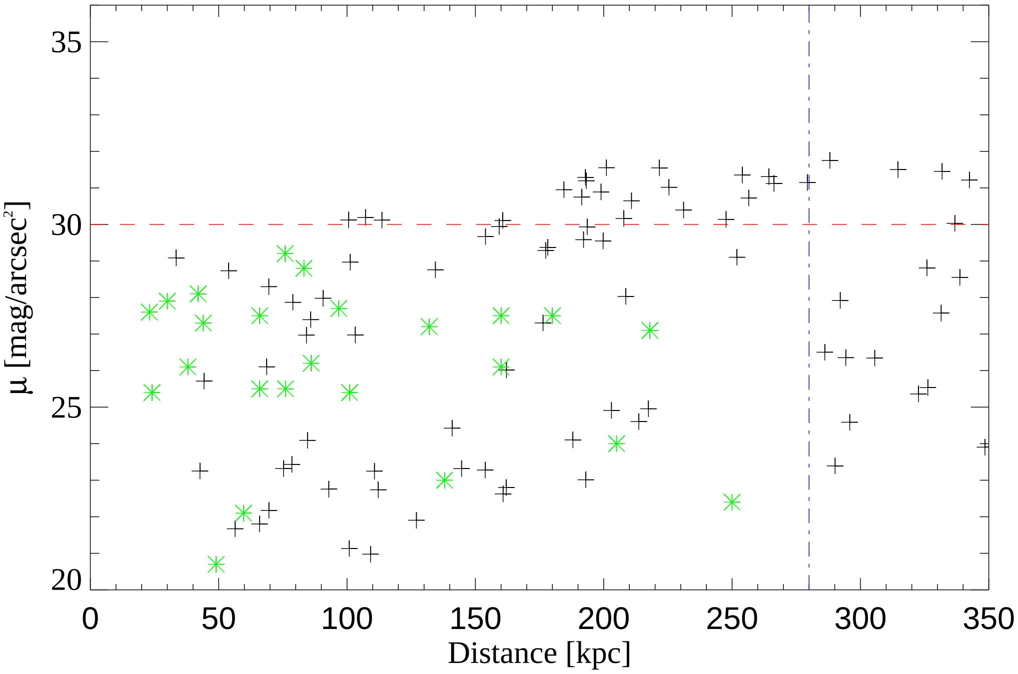

Figure 3.16: Photometric V-band surface brightness of the simulated satellites (black crosses), inside a sphere of radius 350 kpc around a fiducial position of the Sun in the simulations. The red line shows the surface brightness detection limit of the SDSS survey, while the blue vertical line gives the radial cut at 280 kpc that we frequently used in this work. There are 46 Satellites below this limit within a radius of 280 kpc which is relatively close to the 57 satellites predicted for an all-sky extrapolation of the observational data. The green stars give the observed satellites with well determined surface brightnesses.

just below the surface brightness limit of the SDSS (see also Bullock et al., 2010).

Our simulations have also highlighted the relative importance of some of the evolutionary aspects of satellite galaxies. In particular, we do not find a very distinctive mark of the epoch of reionization on the satellites, and most satellites continue their star formation activity in our simulations to much lower redshift than $z = 6$. This suggests that simplified treatments of satellite histories, where relatively high cooling thresholds due to a ionizing UV background are invoked, are not particularly realistic. Our simulation results agree much better with the scenario outlined in Strigari et al. (2007), which in fact resembles many of our simulation findings quite closely.

We find that the observed relationship between V-band luminosity and velocity dispersion is quite well reproduced by our simulations, albeit with large scatter. The small amount of reliable observational data for the velocity dispersions leaves it unclear at present whether the larger scatter we find indicates a problem of the simulations or whether is is also present in reality. What is comparatively clear though is that the observed relation between stellar mass and maximum circular velocity is really tight, a finding that is also reproduced by our simulation results. On the other hand, the correlation between present-day stellar mass and star formation rate seen in our simulations seems to be not nearly as well-defined as in the observational data. This is related to

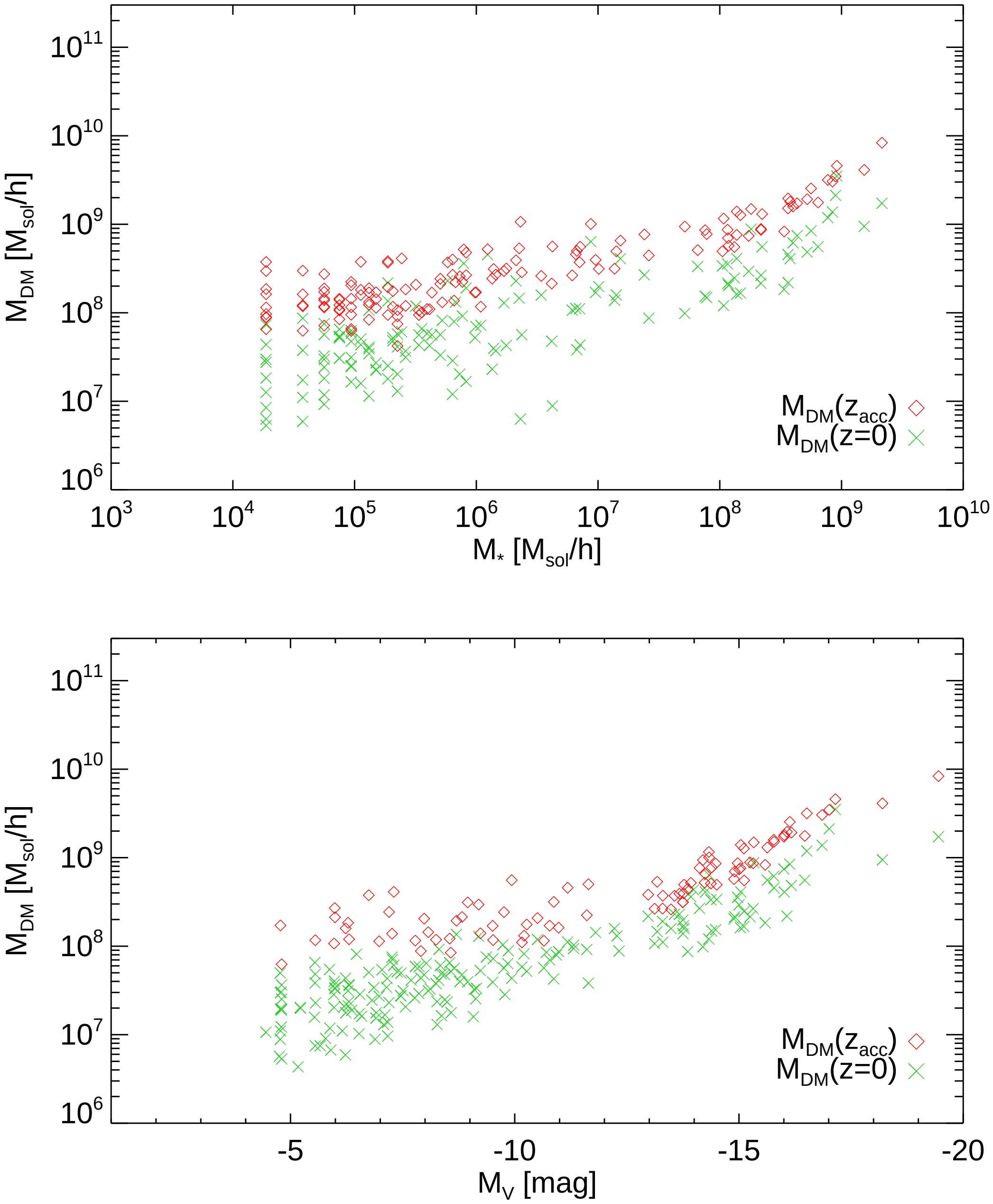

Figure 3.17: Relation between dark matter satellite mass and stellar mass, or stellar luminosity, respectively. For each satellite we show both the dark matter mass today and at redshift $z = 6$. This plot may be compared directly to Figure 5 of Macciò et al. (2010), which is representative for semi-analytic models constructed to describe the satellite population. Unlike in their results, there is clearly some curvature found with the hydrodynamical simulation in this relation.

the fact that we do not find a good correlation between the present stellar and gaseous masses; many simulated satellites have comparable stellar masses but differ in their gas fractions by huge factors. Gas-rich and completely gas-depleted satellites coexist in the same total and stellar mass regime, rendering a tight correlation with the star formation rate unlikely.

But perhaps the most significant discrepancy between the simulation results and observations lies in the inferred mass-to-light ratios. The mass-to-light ratios of the simulated galaxies are off by about a factor of 5 when compared at face value to the observational estimates. This means that they are either too massive, or too faint for their mass. The discrepancy could also be caused by a systematic underestimate of the total satellite masses in the observations. Due to the difficulty of reliably determining the 'outer edge' of the dark matter halo of an orbiting satellite, this possibility cannot be easily excluded.

In summary, we find that the current generation of cosmological hydrodynamic simulations is able to explain many properties of the observed satellite population surprisingly well. We have shown that different feedback physics affects the satellite population strongly, with respect to quantities such as luminosity function, scaling relations, or star formation histories. This emphasizes the significant potential of "near-field cosmology" within our Local Group to inform the general theory of galaxy formation. Our work has also shown that it is not necessarily the physics of cosmic reionization and supernova feedback alone that is responsible for resolving the missing satellite problem. In fact, the role of reionization has probably been grossly overstated in many previous works, while other important feedback, such as cosmic rays, has been ignored. It will therefore be very interesting to refine the hydrodynamical simulations further in future work, and to make them more faithful in capturing all the relevant physics.

4 The Aquila cosmological code comparison project

Contents

4.1 Introduction 55
4.2 Code descriptions 56
4.2.1 GADGET3 models 56
4.2.2 The CS model 56
4.2.3 The TO model 58
4.2.4 The GIMIC model 58
4.2.5 The MM model 59
4.2.6 The CK model 59
4.2.7 The Gasoline model 59
4.2.8 The Arepo model 60
4.2.9 The Ramses models 60
4.3 Initial conditions 60
4.4 Measurement definitions 63
4.5 Results 64
4.5.1 Morphology 64
4.5.2 Galaxy formation efficiency 66
4.5.3 Galaxy size 68
4.5.4 Circular velocities 70
4.5.5 Stellar mass assembly 72
4.5.6 Disk and stellar mass assembly 73
4.5.7 Gas fractions 76
4.5.8 Tully-Fisher relation 76
4.6 Conclusions 77

Summary

In this chapter, we compare thirteen cosmological hydrodynamical codes from leading groups who work on simulations of the formation of Milky-Way like galaxies in the ΛCDM structure formation paradigm. All of the adopted codes differ in terms of their numerical treatment of hydrodynamics (SPH, AMR, or moving-mesh) as well as in their detailed treatment of cooling, star formation and feedback, but they start from exactly the same initial conditions. We are thus ensuring a common mass assembly history of the forming galaxy. Nevertheless, we are finding large variations in the final properties of the formed galaxy, in terms of stellar mass, size, morphology as well as gas content. Most of the codes produce galaxies which are too massive, too compact and too gas-rich compared with observations. This manifests itself in a very massive bulge component and a declining instead of a flat rotation curve. The prominence of the stellar disk component varies strongly from code to code, but there is a well-defined trend which shows that stronger feedback implementations tend to produce more realistic disk galaxies. We are also noticing systematic differences between particle- and mesh-based hydrodynamical codes, indicating that the latter ones are able to cool more gas at late times, an effect that in principle favors the formation of a massive, young stellar disk component. Interpreting the variety of outcomes we obtained as a measure for the systematic uncertainty of the modeling techniques, we conclude that current state-of-the-art simulations are not able to reliably predict the properties of the baryonic component of a galaxy, even if the dark matter assembly history stays fixed between the individual runs. In addition, our results show that none of the current implementations of feedback physics is yet able to form a fully satisfactory disk galaxy model, suggesting that more work is needed to improve the treatment of these processes.*

4.1 Introduction

Over the last decade, explaining the formation of Milky Way type galaxies within the ΛCDM standard cosmological model has become an ever more acute challenge for computer simulations. A sizable number of groups around the world have developed different codes and numerical recipes to tackle this problem, but for many years the achieved results have been disappointing for the most part. The so-called overcooling problem caused overluminous galaxies, and the so-called angular momentum problem was held responsible for too small sizes of the produced galaxies. These problems have been found to be very difficult to overcome, but in recent years, gradual progress has been achieved (Saitoh et al., 2008; Scannapieco et al., 2009; Brooks, 2010; Sales et al., 2010; Agertz et al., 2011; Piontek & Steinmetz, 2011), and even some first claims of a successful formation of a disk galaxy have appeared (Guedes et al., 2011). But because of the different initial conditions and cosmological models assumed by each group, an unbiased assessment of the real performance of the corresponding models has been unavailable thus far.

The *Aquila Project*, initiated and organized by the international Virgo Consortium, was created to address this problem. In this project, we tried to assemble a wide variety of different cosmological codes from all the leading groups worldwide for participation in a large code comparison project. In the end, we were able to compare 13 different simulation techniques applied to the assembly of the very same galaxy within a fully consistent cosmological environment, starting from identical initial conditions in all cases. This enables us to track important characteristics of the individual models without complications and uncertainties from disentangling the influence of varying initial conditions. As a result, we are able to arrive at a clean assessment of the capabilities and limitations of the current generation of hydrodynamic galaxy formation codes.

The following section 4.2 provides short descriptions of all the simulation models/codes included in the Aquila project. Section 4.3 describes the initial conditions used by all the groups while section 4.4 specifies basic definitions of various quantities used in the analysis of all the results. Section 4.5 describes the results of the Aquila project, and section 4.6 presents our conclusions.

---

[*] Results similar to the ones discussed in this chapter have been submitted in different form to the *Monthly Notices of the Royal Astronomical Society*, Scannapieco, Wadepuhl, Parry, Navarro, Jenkins, Springel, et al., 2011.

4.2 Code descriptions

The following subsections are dedicated to a description of the different codes compared in the Aquila project. As a fully detailed description of all of these codes is clearly beyond the scope of this work, the code descriptions are kept as concise as possible and focus on highlighting the most important characteristics of the corresponding models. Additional details can be found in our joint Aquila paper (Scannapieco et al., 2011a), and in references given therein.

Table 4.1 gives a compact summary of all codes and references to the corresponding code-papers used in this comparison, as well as an overview of the applied physics. In table 4.2, we have summarized all relevant physical input parameters adopted by the different groups. We note that several of the codes used in the Aquila code comparison are originally based on GADGET (Springel, 2005), which can be viewed as a reference implementation of classic SPH. To highlight this connection of the models, all of them are labeled "G3" with an extension that clarifies the way they are deviating from the standard model included in GADGET.

A first impression of the different models is provided in Figure 4.1, which compares the star formation rate densities predicted by each code with the Kennicutt-Schmidt law. We also include the temporal evolution of our simulations in the $\Sigma_{\rm sfr} - \Sigma_{\rm gas}$ plane. It can be clearly seen that all GADGET based codes are matching the observed Kennicutt-Schmidt law at all times. The SPH-code GASOLINE tends to have a higher star formation rate density at early times while the simulation R-AGN is evolving away from the Kennicutt-Schmidt law with time. The simulation R-LSFE constantly lies below the observed Kennicutt-Schmidt law, as is also expected based on the construction of this model, see the more detailed description below.

4.2.1 GADGET3 models

The GADGET code has already been explained in some detail in chapter 2, so it is not necessary to repeat everything here. However, it should be mentioned that besides of the "standard" star formation model "G3" (section 2.3.1), also the AGN feedback model (section 2.3.3) "G3-BH" and the cosmic ray model (section 2.3.4) "G3-CR" are included in the comparison project.

4.2.2 The CS model

The "G3-CS" model includes stochastic star formation, chemical enrichment, thermal supernova feedback from Type II and Type Ia SN explosions, a multi-phase model of the gas component as well as metal-dependent cooling. Details of the implementation of this model can be found in Scannapieco et al. (2005) and Scannapieco et al. (2006).

The UV background included in this simulation is turned on at $z = 6$, following the formulation of Haardt & Madau (1996). It uses the metal-dependent cooling functions of Sutherland & Dopita (1993). Star formation happens stochastically in gas particles above some threshold density ($\rho > \rho_{\rm th}$) if the local gas flow is convergent, following the

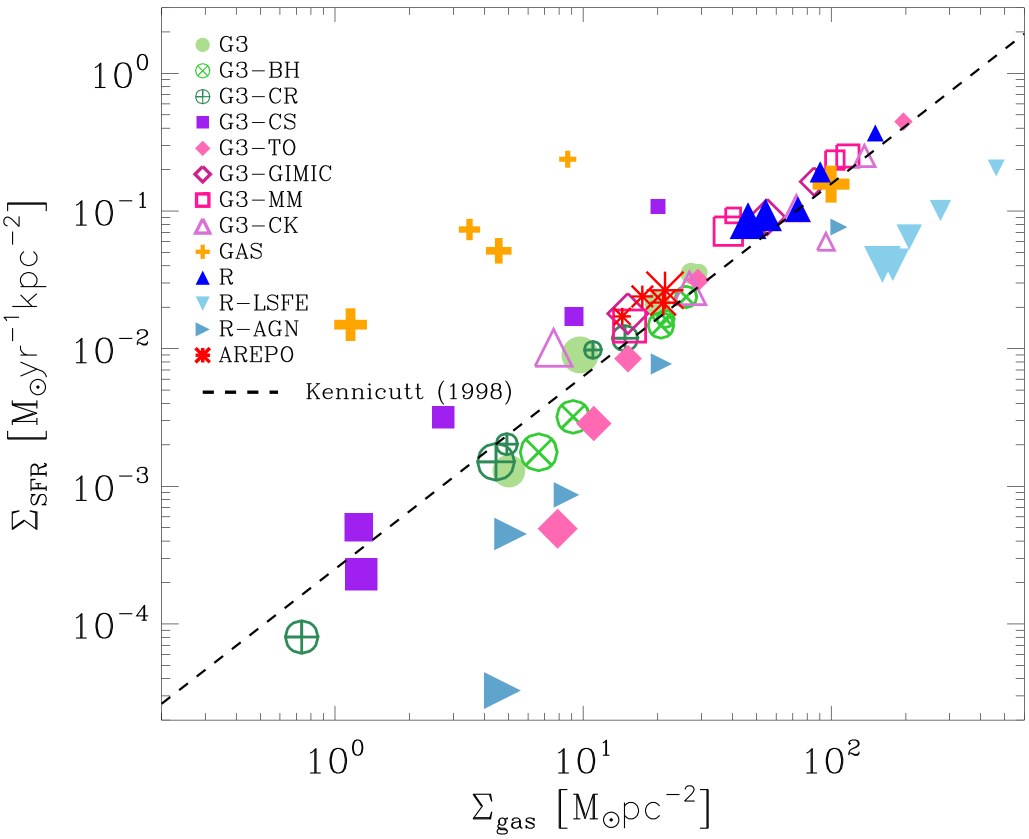

Figure 4.1: Cold gas surface density vs. star formation rate per unit area. Both quantities are measured face-on within a cylinder with radius equal to the projected stellar half mass radius. The time evolution of both quantities is shown for redshifts $z = 2$, 1.5, 1, 0.5 and 0, with the size of the symbols increasing with decreasing redshift. The Kennicutt-Schmidt law for nearby "normal" and "star-bursting" disks (Kennicutt, 1998) is shown as the dashed line. This plot has been created by O. Parry as part of our joint work on the *Aquila* project.

Schmidt-Kennicutt law

$$\frac{d\rho_*}{dt} = c_* \frac{\rho_{\rm gas}}{t_{\rm dyn}}. \tag{4.1}$$

The stellar metal yield of Type II and Type Ia supernovae is assumed to be different, as well as their explosion times, while their energy yield is assumed to be identical. To prevent an artificial loss of SN energy in high-density regions, the energy deposition into cold particles is delayed depending on some local conditions while the deposition into hot gas particles happens instantaneously.

The multi-phase gas model treats gas particles independently according to their temperature, splitting the gas particles into "hot" and "cold" particles. This allows the coexistence of dense and diffuse phases in the same spatial region and makes the deposition of SN energy more efficient.

4.2.3 The TO model

The "G3-TO" model includes metal-dependent cooling, star formation, thermal and kinetic supernova feedback as well as metal enrichment from AGB stars and SNe. A detailed description can be found in Okamoto et al. (2010).

Photo-heating and radiative cooling are implemented as described in Wiersma et al. (2009a). The implementation includes contributions from eleven elements as well as a uniform, time-dependent UV background calculated as given in Haardt & Madau (2001). Star formation is enabled above some density threshold and is normalized to reproduce the Kennicutt-Schmidt law. The energetic feedback as well as the mass and metal returned to the ISM by AGB stars, Type Ia and II SNe are implemented following Wiersma et al. (2009b). The appropriate timescales, the yields and stellar lifetimes are taken from Portinari et al. (1998) and Marigo (2001).

The multi-phase model describing the unresolved interstellar medium is based on a subgrid prescription. Each gas particle above some density threshold $\rho > \rho_{\rm th}$ is internally treated as a set of cold clouds embedded in a hot ambient gas. Both phases exchange mass through thermal instabilities and cloud evaporation. Every cloud has its own star formation rate which is inversely proportional to its dynamical time. Type Ia SN are increasing the thermal energy of the surrounding gas while Type II SNe are used to trigger large-scale winds. The wind speed is calculated using the local dark matter velocity dispersion as a proxy for the halo circular velocity. Gas particles which are currently part of the wind are hydrodynamically decoupled to allow them to escape from the star forming region.

4.2.4 The GIMIC model

The "G3-GIMIC" includes metal dependent cooling, stochastic star formation, supernovae driven winds together with mass and metal recycling by AGB stars, Type Ia and Type II SN. A more detailed description can be found in Crain et al. (2009).

The spatially uniform, time evolving UV background is modeled following Haardt & Madau (2001). In this model, hydrogen reionizes at $z = 9$ and Helium II at $z = 3.5$ (Schaye et al., 2000; Theuns et al., 2002). The metal dependent cooling and heating processes are calculated element-by-element using interpolation tables from CLOUDY (Ferland et al., 1998), following Wiersma et al. (2009a). Star formation is modeled as described in Schaye & Dalla Vecchia (2008) and enforces a local Kennicutt-Schmidt law. Star formation occurs stochastically from gas particles with a probability depending on the associated star formation rate. As described in Wiersma et al. (2009b), the chemodynamical evolution of each star particle and the recycling of heavy elements is calculated element-by-element taking into account AGB stars, Type Ia and Type II SNe.

The energetic feedback from stars is modeled using a phenomenological treatment assuming that the energy is used to pressurize the dense gas such that $P = \kappa\rho^{4/3}$, see Schaye & Dalla Vecchia (2008). SN energy is also partially used to drive large scale winds. To do so, gas particles near star-forming regions get a randomly orientated velocity kick of $600\,\mathrm{km\,s^{-1}}$. The probability of this velocity kick is tuned to ensure that the mass put into the wind is four times the star formation rate. It should be mentioned that wind particles in this scheme are not temporarily decoupled from hydrodynamics.

4.2.5 The MM model

The "G3-MM" includes a multi-phase model for the star forming gas, a stochastic star formation model and energetic feedback from Type II SN. For a detailed description of this model, see Murante et al. (2010).

Star particles are produced stochastically with a probability proportional to the local star formation rate. The UV background of the form of Haardt & Madau (1996) is turned on at redshift $z = 6$. The multi-phase model of the gas particles includes a cold and hot gas phase as well as a stellar phase for each gas particle. The star formation rate is based on the fraction of cold molecular gas which is calculated using the relation described in Blitz & Rosolowsky (2006), assuming that the disk pressure equals the SPH pressure. The star formation efficiency is modeled to scale with the dynamical time of the cold phase. This means that there is no imposed Kennicutt-Schmidt relation, instead it is produced by the code on its own. Thermal supernova feedback includes only Type II SNe and the amount of energy is deposited both into the hot and the cold phase of the gas particles. The thermodynamical energy changes based on the SPH computations are also included in the system of differential equations solved in this model, see Murante et al. (2010) for more details.

4.2.6 The CK model

The "CK" model includes star formation, chemical enrichment as well as thermal feedback from core-collapse, Type Ia supernovae and AGB stars. For a more detailed description, see Kobayashi (2004), Kobayashi et al. (2007), and Kobayashi & Nakasato (2011).

The UV background is added at $z = 6$ following Haardt & Madau (1996). Radiative cooling is calculated using the metal dependent cooling functions of Sutherland & Dopita (1993). Star formation is enabled if a gas particle is in a converging flow, has rapid cooling and is Jeans unstable. The appropriate star formation rate is determined from the Kennicutt-Schmidt law. The evolution of the stellar population is calculated for each star particle every timestep assuming each star particle is representing a whole population of stars following a Salpeter initial mass function. The metal and energy feedback is calculated taking care of the detailed evolution of the stellar population including stellar winds, supernovae and AGB stars, and is distributed to the surrounding 64 gas particles.

4.2.7 The Gasoline model

The "GAS" model is the only SPH code taking part in this comparison which is not related to GADGET in one way or another. The GASOLINE code is described in detail in Wadsley et al. (2004). It includes metal dependent cooling based on CLOUDY, assuming an external UV radiation after $z = 8.9$, see Shen et al. (2010) for more details. Star formation and supernova feedback are implemented following the blast wave formalism which is described in Stinson et al. (2006).

Star formation is allowed below a temperature threshold of $15,000\,\mathrm{K}$ and above a density threshold of 1 $\mathrm{amu\,cm^{-3}}$. Each stellar particle is considered to represent a single stellar population using the initial mass function of Kroupa et al. (1993). Metal and energy feedback from both Type Ia and Type II supernovae are considered in this context and are distributed between the gas particles surrounding the star particle. As this feedback energy would be radiated away very quickly because of the high densities, cooling is temporarily disabled for these particles following Thacker & Couchman (2001).

4.2.8 The Arepo model

The AREPO code, which corresponds to the "Arepo" model in this comparison, has already been described in detail in section 2.2.2. The only thing that needs to be emphasized here is the fact that the models "G3" and "Arepo" differ *only* in their implementation of hydrodynamics. The star formation model, feedback, etc., as well as the computation of gravity, are exactly the same. So all differences seen between these two models are only caused by their different treatment of hydrodynamics.

4.2.9 The Ramses models

RAMSES is the second mesh-based code taking part in this comparison study. It uses a Eulerian Adaptive Mesh Refinement scheme together with shock-capturing, an unsplit second-order MUSCL scheme, and a HLLC Rieman solver combined with a MinMod slope limiter. The N-body part (i.e. stars and dark matter particles) is treated with a particle mesh approach. See Teyssier (2002) for more details.

Star formation is modeled stochastically adopting a Schmidt law and a fixed density threshold of $\rho_{\rm th} = 0.1\ {\rm amu\,cm^{-3}}$. The star formation efficiency varies between 1 % ("R-LSFE") and 5 % ("R", "R-AGN"). Cooling is modeled using a metal dependent cooling function where the metallicity is calculated as an additional scalar variable which is injected by supernovae, assuming a yield of $y = 10\,\%$ (Rasera & Teyssier, 2006; Dubois & Teyssier, 2008). The simulation "R-AGN" also includes AGN feedback which is implemented following Booth & Schaye (2010).

4.3 Initial conditions

The initial conditions for the suite of simulations presented in this work are based on the initial conditions of the *Aquarius* simulations (Springel et al., 2008). Particularly, the halo studied here corresponds to halo Aq-C at the resolution levels 6 and 5, following the naming convention of the Aquarius project.

The initial conditions consist of a periodic cube of side $100\,h^{-1}{\rm Mpc} \simeq 137\,{\rm Mpc}$ on a side, and adopt a cosmology using the parameters $\Omega_m = 0.25$, $\Omega_\Lambda = 0.75$, $\sigma_8 = 0.9$, $n_s = 1$, and Hubble constant $H_0 = 100\,h\,{\rm km\,s^{-1}\,Mpc^{-1}} = 73\,{\rm km\,s^{-1}\,Mpc^{-1}}$. These parameters are consistent with the WMAP 1- and 5-year results, and are identical to the parameters used in the Millennium and Millennium-II simulations (Springel et al., 2005b; Boylan-Kolchin et al., 2009). To achieve the high spatial resolution necessary to follow the formation of an individual galaxy, the initial conditions are designed as zoomed initial conditions, i.e. the Lagrangian region from which our target halo forms is identified in an initial coarse simulation of the full box and all particles within this region are then replaced by a larger number of high-resolution particles which also receive additional small-scale power. Regions far away from the target halo are downgraded in

Table 4.1. Summary of code characteristics and implemented physics.

Code	Reference	Type	UV background z_{UV}	UV background spectrum	Cooling	Feedback
G3	[1]	SPH	6	[10]	primordial [12]	SN (thermal)
G3-BH	[1]	SPH	6	[10]	primordial [12]	SN (thermal), BH
G3-CR	[1]	SPH	6	[10]	primordial [12]	SN (thermal), BH, CR
G3-CS	[2]	SPH	6	[10]	metal-dependent [13]	SN (thermal)
G3-TO	[3]	SPH	9	[11]	metal-dependent [14]	SN (thermal+kinetic)
G3-GIMIC	[4]	SPH	9	[11]	metal-dependent [14]	SN (kinetic)
G3-MM	[5]	SPH	6	[10]	primordial []	SN (thermal)
G3-CK	[6]	SPH	6	[10]	metal-dependent [13]	SN (thermal)
GAS	[7]	SPH	10	[]	metal-dependent [15]	SN (thermal)
R	[8]	AMR	12	[10]	metal-dependent []	SN (thermal)
R-LSFE	[8]	AMR	12	[10]	metal-dependent []	SN (thermal)
R-AGN	[8]	AMR	12	[10]	metal-dependent []	SN (thermal), BH
Arepo	[9]	Moving Mesh	6	[10]	primordial [12]	SN (thermal)

Note. — [1] Springel et al. (2008); [2] Scannapieco et al. (2005); Scannapieco et al. (2006); [3] Okamoto et al. (2010); [4] Crain et al. (2009); [5] Murante et al. (2010); [6] Kobayashi et al. (2007); [7] Stinson et al. (2006); [8] Teyssier (2002); Rasera & Teyssier (2006); Dubois & Teyssier (2008); [9] Springel (2010b); [10] Haardt & Madau (1996); [11] Haardt & Madau (2001); [12] Katz et al. (1996); [13] Sutherland & Dopita (1993); [14] Wiersma et al. (2009a); [15] Shen et al. (2010);

resolution. This procedure results in a highly resolved target galaxy while maintaining the full cosmological context at a reduced computational costs, as can be seen in Fig. 4.2. A more detailed description of the generation of the initial conditions can be found in Springel et al. (2008). The selected halo, Aq-C, has a present day mass of $\sim 1.6 \times 10^{12}$ $\mathrm{M}_{\odot}$ which is similar to the estimated mass of the Milky Way. Together with its relatively quiet merger history and its mildly isolated position within its cosmological environment, it can thus be expected to be a well-suited host for forming a Milky Way like galaxy.

The original initial conditions of the *Aquarius* project contained only dark matter particles, in a 'glass-like' configuration. Each of these dark matter particles (depending on the simulation code only particles in the high resolution region or all particles within the whole box) are then split into two and replaced by one dark matter and one gas particle each. This is done by distributing the initial particle mass among the two new particles such that $\Omega_{\mathrm{baryon}} = 0.045$ is achieved. The particles are displaced in such a way that their center of mass stays fixed at the position of the original particle while at the same time the new particles are separated by $0.5\times$ the mean interparticle spacing of the dark matter only initial conditions.

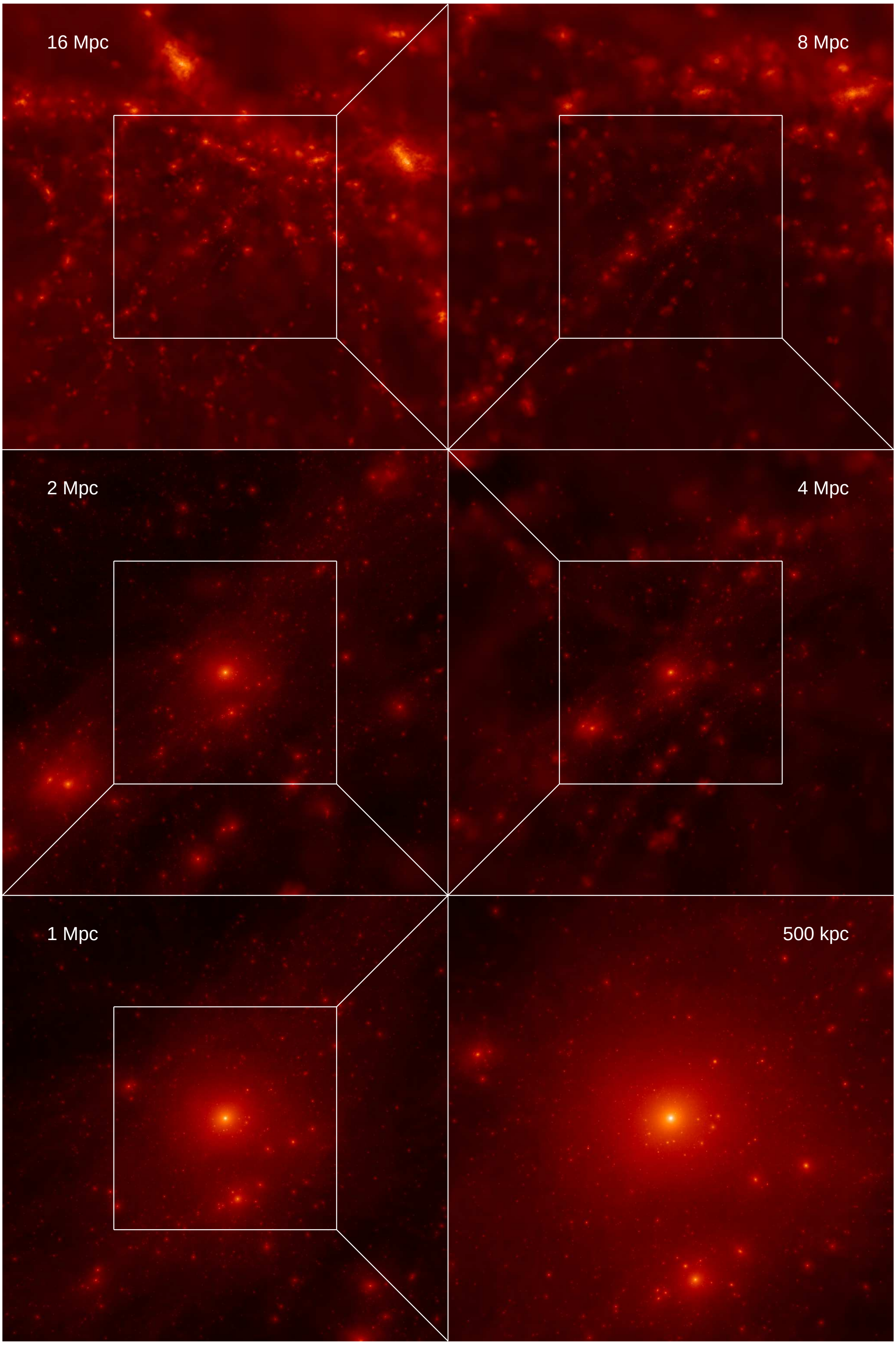

Figure 4.2: Projected density maps of the dark matter distribution around the Aquila halo at $z = 0$. The sidelength of the projected cube is indicated in each panel. Density values are visualized using a logarithmic color scale.

Table 4.2. Code parameters for simulations of level 5 resolution (level 6 parameters are given in parentheses where appropriate)

Code	f_{b} $(\Omega_{\mathrm{b}}/\Omega_{\mathrm{m}})$	m_{DM} $[10^6\mathrm{M}_\odot]$	m_{gas} $[10^6\mathrm{M}_\odot]$	ϵ_{g} $\epsilon_{\mathrm{g}}^{z=0}$ [kpc]	z_{fix}
G3					
G3-BH	0.16	2.2	0.4	0.7	0
G3-CR		(17)	(3.3)	(1.4)	(0)
G3-CS					
Arepo					
G3-TO	0.18	2.1	0.5	1.5	(3)
G3-GIMIC		(17)	(3.7)	(3)	(3)
GAS	0.177	2.16	0.43	0.457	8
	(0.176)	(17)	(2.9)	(0.913)	(8)
R	0.16	1.37	0.22	0.261	9
R-LSFE		(10.96)	(1.75)	(0.522)	(9)
R-AGN					

Note. — f_{b}: baryon fraction; m_{DM}: mass of dark matter particles; m_{gas}: initial mass of gas particles; $\epsilon_{\mathrm{g}}^{z=0}$: gravitational softening at $z = 0$; z_{fix}: redshift at which the gravitational softening is fixed in physical coordinates.

4.4 Measurement definitions

In this section, we summarize some of the basic definitions of relevant quantities that are used in the analysis of the simulation results of this comparison project. By developing very detailed definitions and algorithms for calculating specific measurements and distributing these to other groups involved in the project, we tried to ensure a homogeneous analysis of the individual simulations.

The center of the simulated galaxy is defined as the potential minimum of the most massive gravitationally bound structure at $z = 0$. The virial radius, R_{vir}, is defined as the radius of the sphere, centered on the galactic center which contains a mean density of 200 times the critical density $\rho_{\mathrm{crit}} = 3H^2/8\pi G$. The galactic radius R_{gal} is defined as $0.1 \times R_{\mathrm{vir}}$.

The *halo* refers to everything within the virial radius R_{vir}, while all baryonic matter inside R_{gal} is referred to as the *galaxy*. The gas component is split up into a *hot* and a *cold* phase. The distinction between these two phases is made based on the temperature of the gas particle using a threshold value of 10^5 K. If the conditions for star formation are met in the case of subgrid models, the corresponding gas is also counted as part of the cold gas phase.

As it was necessary to orientate the simulated galaxies to calculate some specific quantities like the surface density profiles, etc., we defined a galactic coordinate system following this algorithm: The z-axis of the galactic coordinate system is defined as the direction of the angular momentum vector of all stars within three times the stellar half mass radius. The galactic x-axis was defined as the cross product of the initial y-axis and the new galactic z-axis. The galactic y-axis is then the cross product of galactic z- and the galactic x-axis.

To further improve the comparability of results, we also circulated detailed definitions of, e.g., the number and spacing of the bins used for density profiles, etc., to all participants. By defining such tight rules on how every quantity has to be calculated, we are very confident that the results presented in this comparison project are as comparable as one can get in a collaborative project such as this one.

4.5 Results

4.5.1 Morphology

To get a first visual impression of the morphology of the simulated galaxies, we show face-on and edge-on projections of the stellar surface density in Figure 4.3. The corresponding maps for our additional simulations ("G3-BH", "G3-CR", "R-LSFE", "R-AGN") are shown in figure 4.5. The final stellar masses are indicated in the lower left corner for each simulations.

It is immediately obvious that all galaxies are composed of several components. Basically, all simulated galaxies suffer from an enormous bulge component, and most of them show a more or less pronounced bar. The stellar disk shows a very broad range of appearance in the different galaxies. Some simulation models like "G3" and "G3-MM" display hardly any indication of a stellar disk, while in other a disk component is clearly apparent. But even among the simulations showing a clear disk component, their vertical thickness and radial extent varies greatly between the different simulations.

To get a quantitatively more objective view of the galactic morphology, we show the normalized distributions of stellar circularities in Figures 4.4 and 4.5. Circularities are defined as the ratio between the z-component of the angular momentum of a star particle and the angular momentum of a circular orbit at the same radius:

$$\epsilon = \frac{J_z}{J_c(r)} = \frac{J_z}{r\,V_c(r)}, \tag{4.2}$$

where $V_c(r)$ is the circular velocity at radius r. This means that stars on circular orbits (which are typically disk stars) have a ϵ value of ≈ 1 while stars on randomly oriented orbits should have a distribution of ϵ values with a mean of ≈ 0. Thus, the bulge and disk components in the histogram of stellar epsilons show up as a broad, symmetric peak around $\epsilon = 0$ and a narrow peak around $\epsilon = 1$, respectively.

The visual impressions from Figures 4.3 and 4.5 are confirmed and corroborated by the distributions of ϵ. The simulations "G3-CS", "G3-TO", "G3-GIMIC", "GAS", "R" and "R-LSFE" exhibit a well defined disk component while the simulations "G3", "G3-MM", "G3-CK", "AREPO", "G3-CR", "G3-BH" and "R-AGN" only show small bumps instead of peaks at $\epsilon = 1$, or at least an excess of co-rotating stars. As will be discussed later on, the simulations comprising clear disk components are also exhibiting very inefficient star formation at early times, an observation that will also be analyzed in more detail in chapter 5.

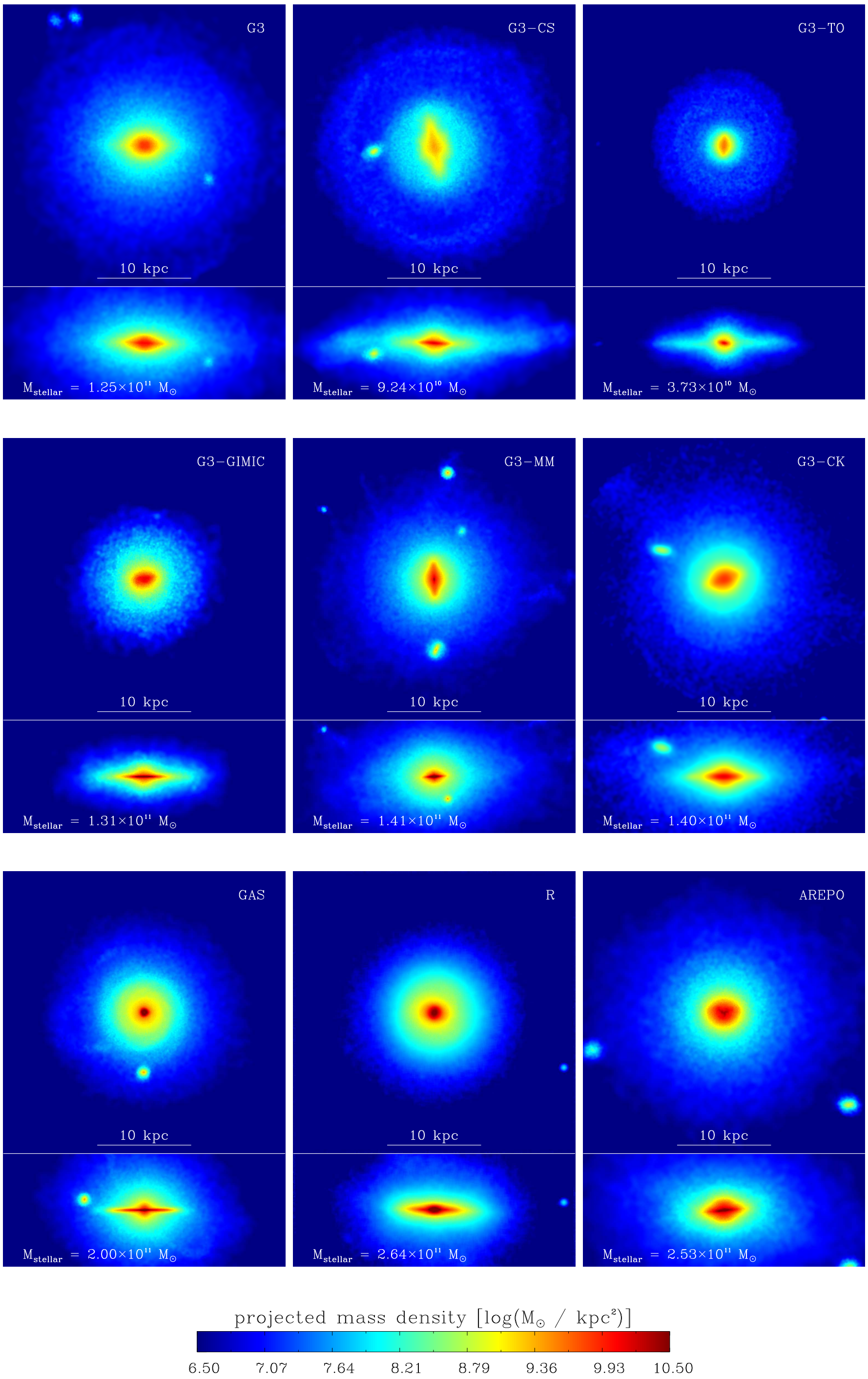

Figure 4.3: Face-on and edge-on projected maps of the stellar mass density. The galaxies are aligned by defining the direction of their angular momentum vector as the z-axis of these plots. The projected regions are 30×30 kpc^2 and 30×12 kpc^2, respectively. Pixel colors are mapped to density according to the colorbar shown below. For each simulation, the total stellar mass within the galactic radius (defined as $r_{\rm gal} = 0.1\, r_{\rm vir}$) is given in the lower left corner. For results of the simulations G3-BH, G3-CR, R-LSFE and R-AGN, see Fig. 4.5.

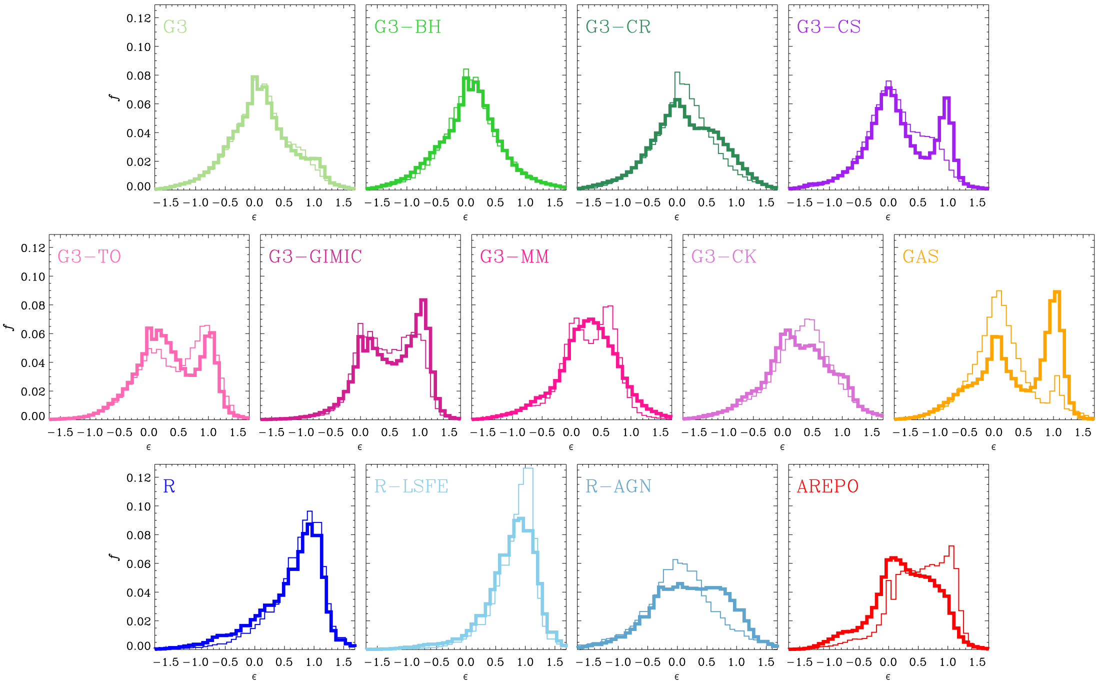

Figure 4.4: Stellar circularities, defined as $\epsilon = J_z/J_c$ for the main Aquila simulations. A value for ϵ of about 1 indicates that the corresponding star particle is on a co-rotating circular orbit. $\epsilon = 0$ and $\epsilon = -1$ indicate radial and counter rotation orbits, respectively. A disk component should thus appear as a rather narrow peak at $\epsilon = 1$ while the bulge produces a broad, symmetric peak at $\epsilon = 0$. Thick lines show the results for level 5 simulations and thin lines the corresponding results for resolution level 6. This plot has been created by C. Scannapieco as part of our joint work on the *Aquila* project.

4.5.2 Galaxy formation efficiency

In Figure 4.6 we show the joint evolution of the stellar mass and the virial mass of the simulated galaxies. The lines are tracing their evolution from redshift $z = 2$ to $z = 0$ where symbols are indicating the position of $z = 0$. As additional references, we also show the stellar mass expected based on the abundance matching analysis of Guo et al. (2010), and the expected stellar mass if all available baryonic matter would have turned into stars. Finally, we also include the results of the semi-analytic codes GALFORM (Cooper et al., 2010) and L-GALAXIES (Guo et al., 2011) applied to the same object as embedded in the Millennium-II simulation.

Given the rather good agreement in virial mass, a surprisingly large scatter in the final stellar masses is found, ranging between $\sim 4 \times 10^{10}$ $M_\odot$ and $\sim 3 \times 10^{11}$ $M_\odot$. Nearly all simulations lie well above the relation found by Guo et al. (2010). Interestingly, this is also the case to a smaller extent for the semi-analytic results of GALFORM and L-GALAXIES, even though the latter model matches in the mean the mass to light ratio of the abundance matching argument. This suggests that the Aq-C halo should probably be expected to host a galaxy that is more luminous than average for halos of the same mass.

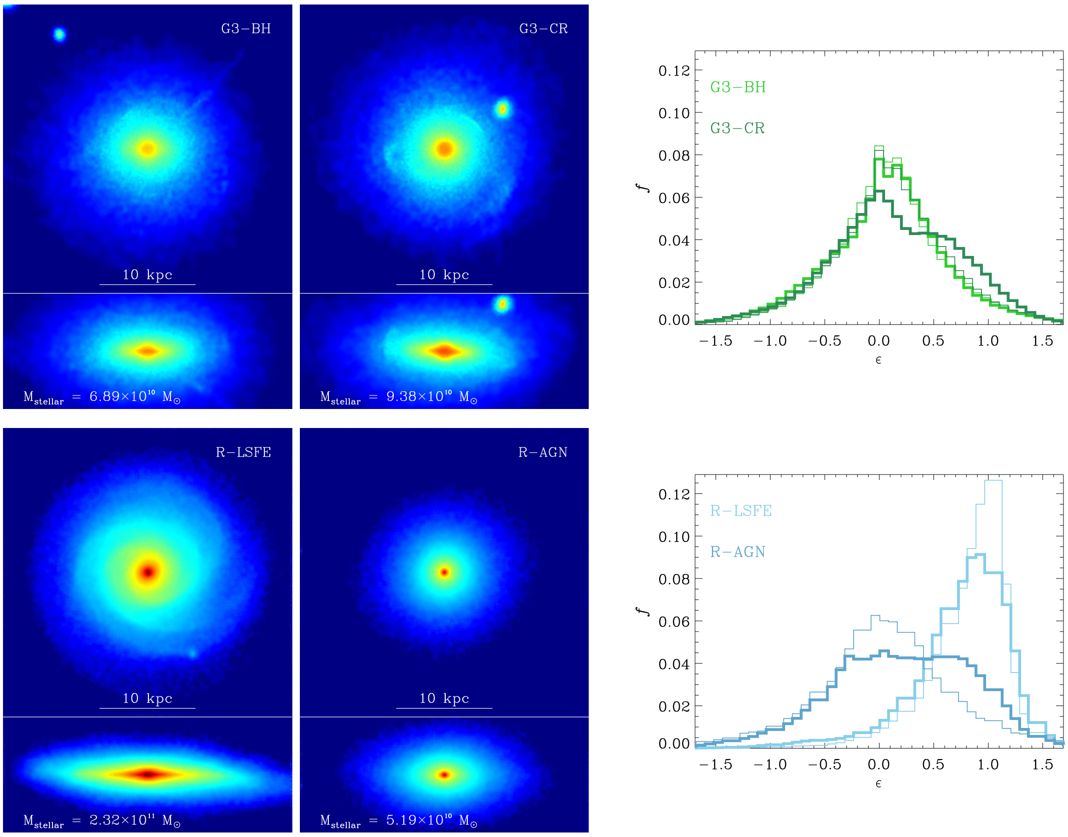

Figure 4.5: *Left panels*: Same as Fig. 4.3 but for the additional Aquila simulations. *Right panels*: Same as Fig. 4.4 but for the additional Aquila simulations. The right panels of this plot have been created by C. Scannapieco as part of our joint work on the *Aquila* project.

In any case, as the relation between stellar mass and virial mass is a measure for the efficiency of feedback and of the relative importance of cooling and heating processes, this means that in most of our cases, the average feedback was not strong enough to inhibit star formation efficiently. It is quite obvious from Figure 4.6 that codes including strong feedback and/or galactic winds like “G3-TO” and “R-AGN” are forming the least amount of stars. The effect of increasing feedback is clearly visible from the three simulations “G3”, “G3-BH” and “G3-CR”. Here, “G3” does only include supernova feedback following Springel & Hernquist (2003), “G3-BH” includes additional AGN feedback and “G3-CR” includes AGN + cosmic ray pressure. As a result, one clearly sees from Figure 4.6 that with an increasing amount of feedback, the stellar mass is reduced while the virial mass stays basically constant for this series of simulations.

Another striking feature visible in Figure 4.6 is the tendency of mesh codes to produce the highest stellar masses. The simulations “G3” and “AREPO” only differ in their implementation of hydrodynamics while the star formation criteria and feedback mechanisms are identical. However, their stellar mass differs by a factor of 2. At the same time, the mesh-based “R-AGN” simulation shows the second smallest stellar mass. This leads to the conclusion that the star formation efficiency cannot be solely related to the hydrodynamical technique or the implementation of feedback alone. Instead, both aspects are important. We note that the strong influence of the accuracy of the hydrodynami-

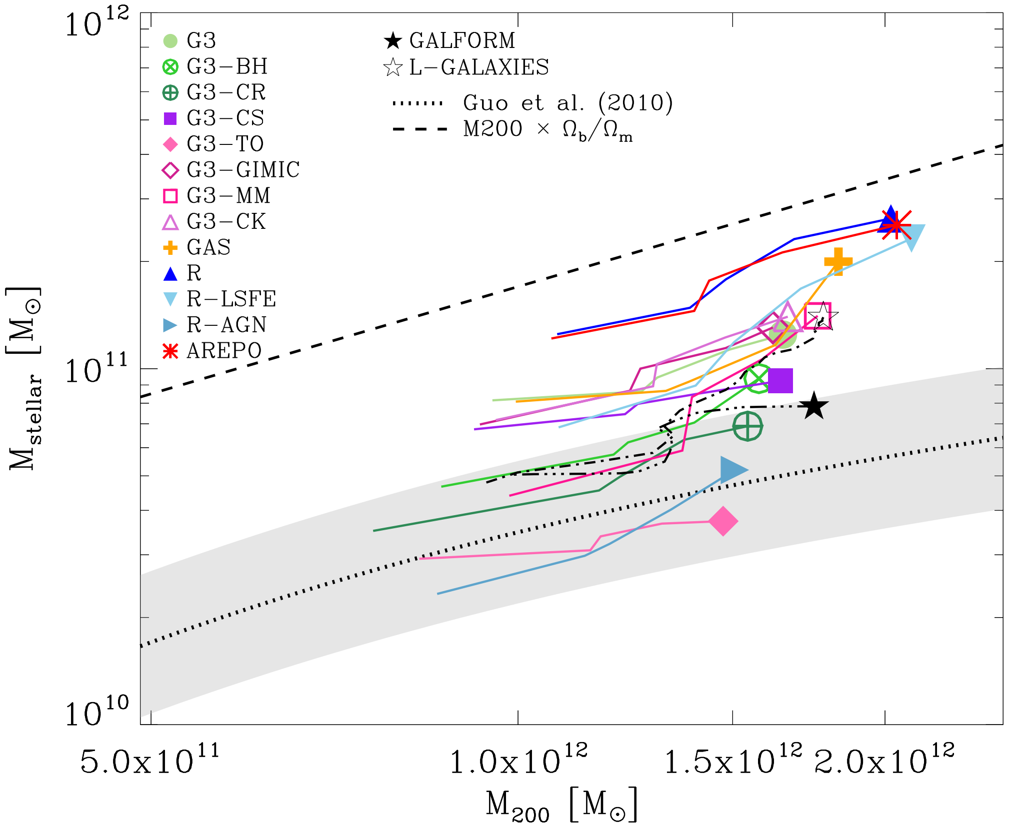

Figure 4.6: This plot shows the evolution of the stellar mass versus the virial mass of all Aquila simulations. The solid lines show the time evolution of both quantities beginning at $z = 2$ up to $z = 0$. The black dotted line shows the expected results for ΛCDM based on abundance-matching, as derived byGuo et al. (2010). The black dashed line shows $M_{\rm vir} \times \Omega_{\rm b}/\Omega_{\rm m}$ which is the expected stellar mass if all available baryonic matter would turn into stars. The filled star symbol shows the results of Cooper et al. (2010), which were obtained by applying the semi-analytic model GALFORM on the Aquarius C-halo. The results from the semi-analytic L-GALAXIES code (calculated by Guo et al., 2011) is shown as the open star symbol. This plot has been created by O. Parry as part of our joint work on the *Aquila* project.

cal treatment has only been appreciated recently, see Wadepuhl & Springel (2011a) and chapter 5.

4.5.3 Galaxy size

After investigating the morphology of the simulated galaxies and the mass of their stellar component, we now focus on the extent of the individual galaxies. Figure 4.7 shows the projected stellar half mass radius vs. the stellar mass in the left panel. We again show the results from the GALFORM and L-GALAXIES models for reference as well as the approximate location of the Milky Way in this diagram. Red and blue dots in the background give a sample of nearby ($z < 0.1$) SDSS galaxies, taken from the MPA-

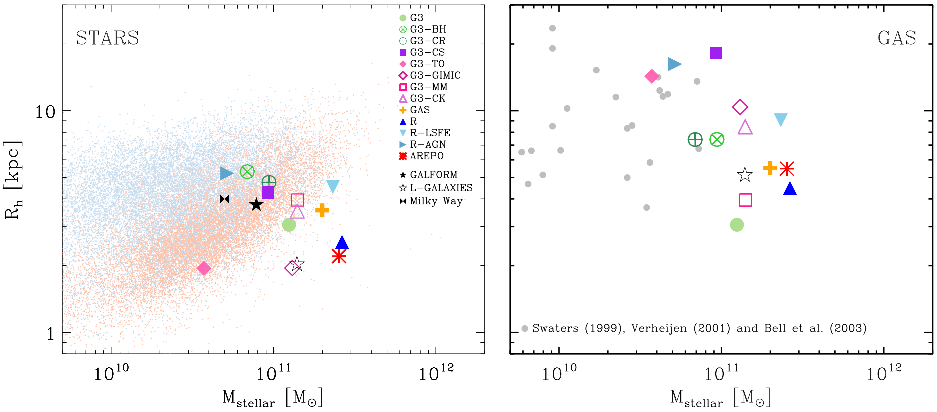

Figure 4.7: *Left panel:* Projected stellar half-mass radius vs. stellar mass enclosed within the galactic radius $r_{\rm gal}$ ($0.1 \times R_{\rm vir}$). Red and blue dots show the Petrosian half light radius of a sample of nearby ($z < 0.1$) SDSS galaxies utilizing the MPA-JHU DR7 data release. Blue points indicate galaxies belonging to the “blue cloud” while red points represent “red sequence”-galaxies, respectively. SDSS galaxies were split into these two groups according to the color condition $(g - r) = 0.59 + 0.052 \log_{10}(M_\star/M_\odot) - 10.0$. The bow-tie symbol shows the approximate position of the Milky Way. *Right panel:* Projected half mass radius of cold gas (all gas which is able to form stars) vs. stellar mass within the galactic radius. Grey circles show the radii of HI disks from Swaters et al. (1999) and Verheijen (2001) while the corresponding stellar masses are taken from Bell et al. (2003). The solid star symbol shows the position of the semi-analytic GALFORM model and the open star symbol the corresponding L-GALAXIES value. The right panel of this plot has been created by O. Parry as part of our joint work on the *Aquila* project.

JHU DR7 release[†]. It should be noted that the observations correspond to the r-band Petrosian half-light radii while the simulation results show simply the stellar half-mass radius. The comparison between these quantities should thus be taken with a grain of salt.

The stellar half-mass radii span a range of 1.5 − 6 kpc which, if compared to the SDSS data, indicates a too concentrated stellar distribution. Besides the outlier “G3-TO”, there is a clear trend of increasing half-mass radius with decreasing stellar mass. This means that especially the simulations at the lower stellar mass end are in good agreement with the observational results. The other simulations are clearly too concentrated if compared to the SDSS data. A possible explanation for this behavior might be found if one compares the stellar maps in Figure 4.3 and 4.5 carefully. Nearly all simulations appear to contain a very concentrated stellar bulge which automatically lowers the stellar half-mass radius. It might thus be that the stellar disk of some simulated galaxies would nicely fit the observations if one would somehow be able to circumvent the formation of the massive bulge.

Interestingly, the two models including kinetic feedback, “G3-TO” and “G3-GIMIC”, show the smallest stellar half mass radii. However, the reason for this might not be the same in the two cases. The “G3-TO” model can be characterized by a very efficient late time feedback. This is caused by the specific wind implementation where the wind speed

---

[†] `http://www.mpa-garching.mpg.de/SDSS/DR7`

increases with the mass of the main progenitor and the wind particles are hydrodynamically decoupled. As a consequence, wind particles at late times can still be efficiently expelled. In contrast to this, "G3-GIMIC" assumes a constant wind speed and no decoupling. This results in a very ineffective wind feedback at late times when the potential wells get deeper and the ISM pressure increases. A more detailed analysis of coupled and decoupled kinetic feedback can be found in Dalla Vecchia & Schaye (2008).

The right hand panel of Figure 4.7 shows the projected half-mass radius of the cold gas as a function of stellar mass. Observational results from Swaters et al. (1999), Verheijen (2001) and Bell et al. (2003) as well as the predictions from the GALFORM and L-GALAXIES models are included for reference. Although the stellar masses of the simulated galaxies are generally larger than expected, the extent of the cold gas disks is comparable with the observations. There is again a trend of small half-mass radii with increasing stellar mass, but in this case it is much stronger and more clearly visible as in the case of the stellar half-mass radii. Another promising finding is the general trend of gas half-mass radii being larger than the corresponding stellar half-mass radii. With the exception of "G3" and "G3-MM", where they are basically identical, all simulations host larger gaseous disk than stellar disks. This is in good agreement with the findings for our Milky Way, see Kalberla & Dedes (2008).

These results suggest that the size of the gaseous and stellar disk depends strongly on the included physics and on the strength of the adopted feedback. This can again be nicely demonstrated by comparing simulations "G3" and "G3-BH" or "G3-CR". If the amount of feedback is increased, the stellar half-mass radius grows by $\sim 60\,\%$ while the gaseous half-mass radius even doubles.

4.5.4 Circular velocities

A key characteristic of observed spiral galaxies is their rotation curve. In Figure 4.8, we show the simulated circular velocity profiles where the circular velocity is defined as

$$V_{\mathrm{c}}(r) \equiv \sqrt{\frac{GM(<r)}{r}}, \tag{4.3}$$

and $M(<r)$ is the total mass within radius r and G is the gravitational constant. The circular velocity is thus not necessarily a measure for the real motions around the galactic center but rather a proxy for the mass distribution. As an additional reference, we also include the circular velocity curve of the corresponding dark matter only simulation Aq-C-4 of the Aquarius Project (Springel et al., 2008) and the observational results for the Milky Way, see Sofue et al. (2009). Solid circles in the figure indicate the stellar half-mass radius of each simulation.

In agreement with our findings in the previous sections, simulations with high stellar mass and low stellar half-mass radius show the largest peak velocities of about $450 - 600\,\mathrm{km\,s^{-1}}$ whereas the simulations with lower stellar mass and higher stellar half-mass radius are in better agreement with observations. Comparing the rotation curves of our simulations with the dark matter only simulation indicates clearly that the innermost regions of the simulated galaxies are strongly dominated by a very massive, very concentrated stellar bulge component.

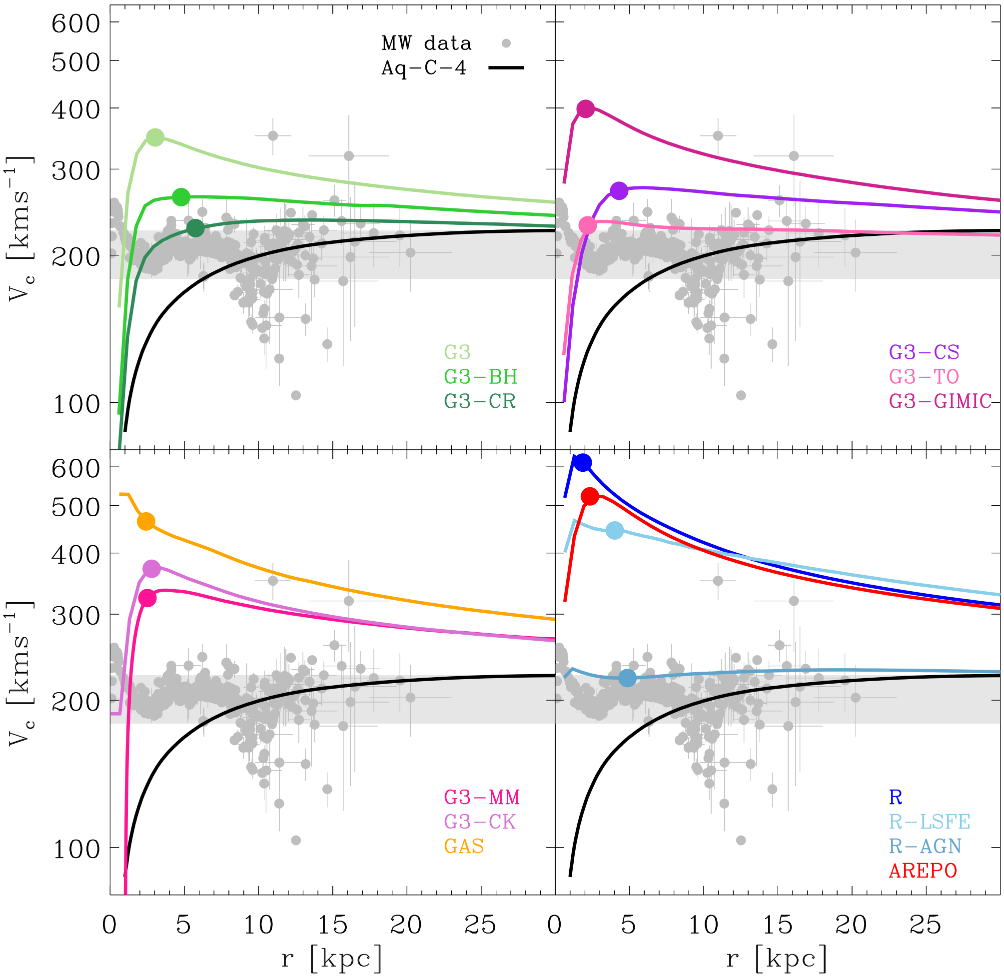

Figure 4.8: Circular velocity profiles ($V_c = [GM(< r)/r]^{1/2}$) of the simulated galaxies, grouped to show similar codes in each of the different panel: Various feedback models of GADGET3 are given in the top-left panel, independent star formation and feedback models as well as GASOLINE are in the top-right and bottom-left panels, and finally the mesh codes RAMSES and AREPO are in the bottom-right panel. The thick black line shows the rotation curve of the dark matter only simulation Aquarius C 4. The solid circles indicate the position of the stellar half-mass radius. The dark grey data points with error bars are observations of the Milky Way's rotation curve (Sofue et al., 2009). The light grey shaded area indicates the values between the peak and virial velocities of the Aquarius halo. This plot has been created by O. Parry as part of our joint work on the *Aquila* project.

4.5.5 Stellar mass assembly

Up to this point, we have basically investigated the morphology of the simulated galaxy using different techniques, ranging form the visual impression in Figures 4.3 and 4.5 to more quantitative measures like the analysis of the distribution of stellar epsilons or half-mass radii. As the morphologies of the simulated galaxies are now rather clearly established, we should now turn to addressing the question why the morphologies are the way they turned out.

In Figures 4.9 and 4.10 we show the cumulative and differential distribution of stellar ages for the different simulations. It should be noted that these are not star formation rate histories for a certain volume but rather histograms of the stellar ages of all the stars that end up within $r_{\rm gal}$ at $z = 0$. In Figure 4.9, solid circles (squares) indicate the time when 50 % (10 %) of the final stellar mass had formed. The star formation histories of our simulations clearly show some large differences between the individual codes. The expansion factor at which 50 per cent of the final stellar mass has formed varies between 0.17 and 0.46, which corresponds to a significant range of 3 Gyr in time. These large differences are based on the evolution of the feedback efficiency. Taking the case of "G3-GIMIC" as an example, we have already found that the kinetic feedback model becomes ineffective at late times due to its fixed wind speed. The very low star formation rate at early times together with the high star formation rate at late times (see Fig. 4.10) reflect this characteristic. In the case of "G3-TO", where the feedback model responds to a rising halo mass with an increasing wind velocity, the star formation rate is effectively reduced over the whole time range.

As can be seen also from Figures 4.3 and 4.5, the feedback efficiency of the "G3-CS" model is very low in the beginning but increases to a very strong level at later times. This is due to the absence of the instantaneous recycling formalism where the ISM is only affected by SN feedback some time after the corresponding star particles where formed.

But not only the feedback efficiency is dictating the star formation rate, also the star formation efficiency and the amount of cold gas are shaping the star formation rate history. This can be nicely seen in the "R-LSFE" simulation which has a high star formation rate despite its low star formation efficiency. As can be seen from Table 4.3, "R-LSFE' has lots of cold gas available at late times, allowing it to form lots of stars at late times.

In Figure 4.11, we show the present-day star formation rate as a function of stellar mass. We compare the simulated values with our sample of nearby SDSS galaxies already shown in Fig. 4.7. This plot clearly shows that none of the simulations compared in this work is able to form a galaxy which would be comparable to observed disk galaxies of the blue cloud. Instead, for galaxies with a reasonable stellar mass, the present-day star formation rate is too low while galaxies with a correct present-day star formation rate are way to massive. This can be interpreted as a problem with the star formation rate history. It appears that all of our galaxies are forming stars too early. This means that galaxies like "G3", "G3-BH", "G3-AGN", "G3-CS" and "G3-TO" have used up their gas too early and are now running out of fuel due to an insufficient replenishment of gas in the disk. On the other hand, the simulation models "GAS", "R", "R-LSFE" and "AREPO" are able to keep up the replenishment of cold gas until today, but their extremely high early star formation rate leads to an unphysically high final stellar mass. This shows again that the star formation rate efficiency depends strongly on the specific implementation

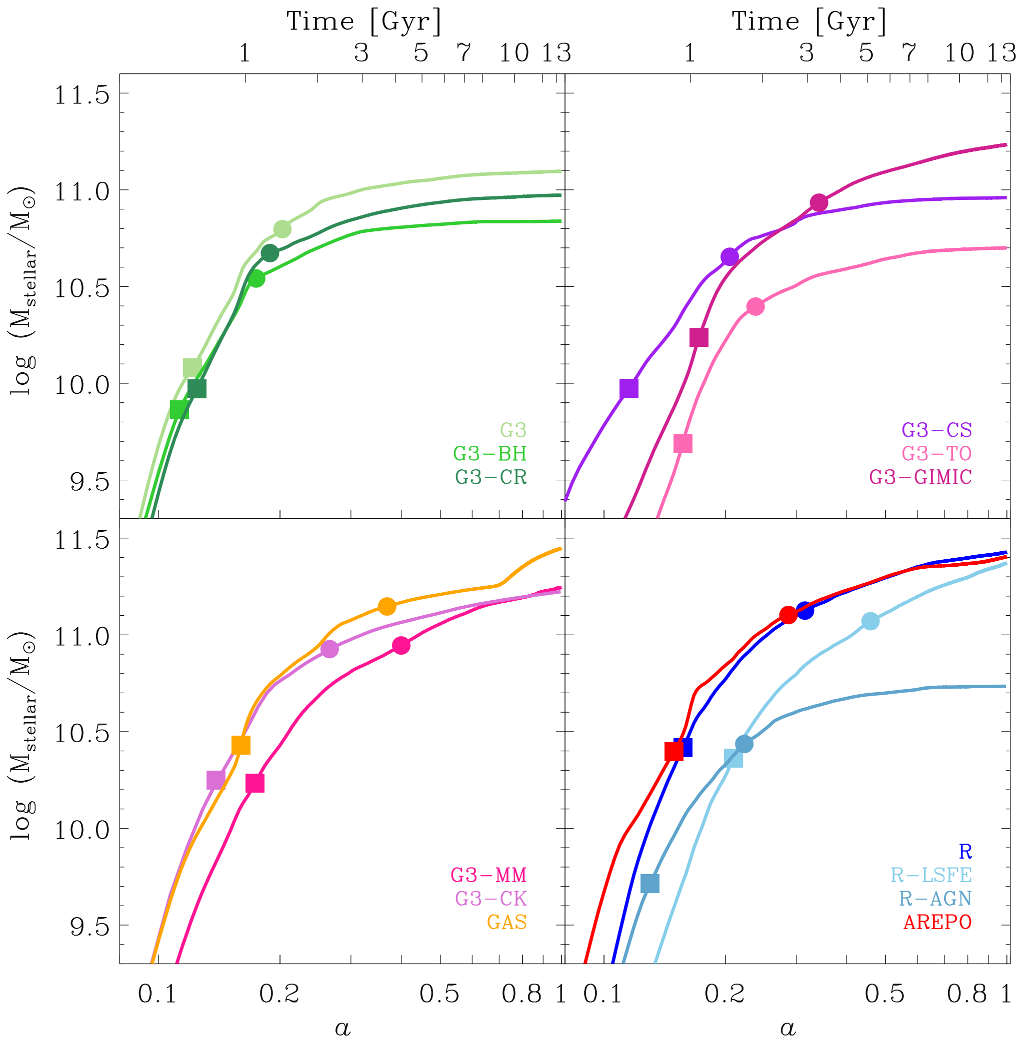

Figure 4.9: Cumulative histogram of stellar ages vs. expansion factor / time. Codes are grouped according to the same scheme as in Fig. 4.8. Solid squares indicate the time when 50% (10%) of the final stellar mass were formed. This plot has been created by C. Scannapieco as part of our joint work on the *Aquila* project.

of feedback processes, in addition to being sensitive also to the numerical treatment of hydrodynamics.

4.5.6 Disk and stellar mass assembly

To investigate the influence of the star formation rate history on the formation of a stellar disk, we plot the relationship between $a_{50\,\%}$, the expansion factor at which 50 % of the stellar mass was formed, and the fraction $f(\epsilon > 0.8)$ of stars with circularities $\epsilon > 0.8$ in the left hand panel of Figure 4.12. High values of $f(\epsilon > 0.8)$ are indicating better defined stellar disks.

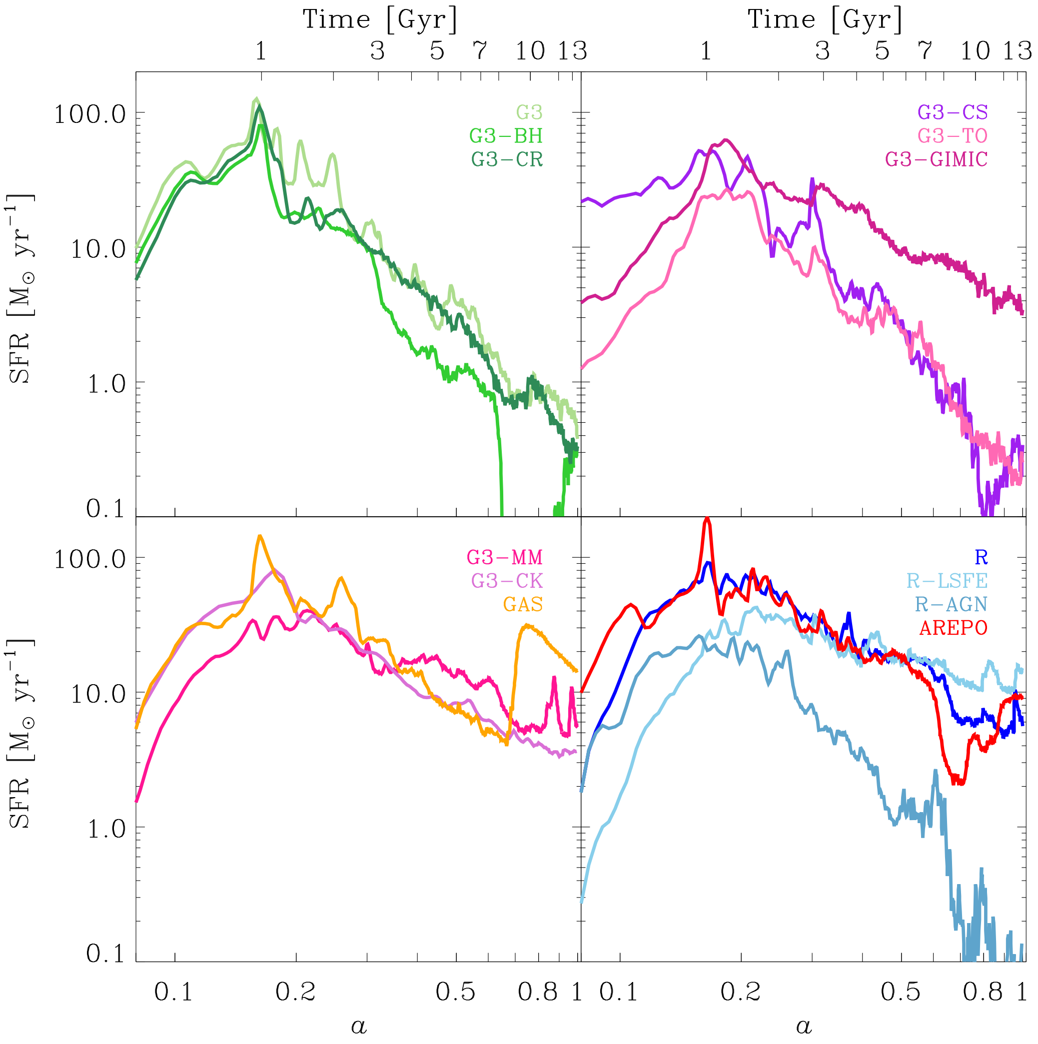

Figure 4.10: Histogram of stellar ages vs. expansion factor / time. Codes are grouped according to the same scheme as in Fig. 4.8. This plot has been created by C. Scannapieco as part of our joint work on the *Aquila* project.

There is a clear trend showing that simulations with high values for $f(\epsilon > 0.8)$ have also high $a_{50\,\%}$ values. This reflects the finding that stars formed at later times are more likely to form a stellar disk. However, as the right panel of Figure 4.12 shows, late time star formation is not sufficient to produce realistic stellar disks. Here we show again $a_{50\,\%}$ but as a function of the final stellar mass in this case. There is again a correlation between $a_{50\,\%}$ and the final stellar mass, demonstrating a strong trend of our disky galaxies being too massive, see Figure 4.11 as a reference for the observed stellar masses of disk galaxies. This means that galaxies which are able to form stars at late times and form the best disks seen in this comparison are still suffering from an overly massive, early formed bulge component. One outlier in this respect is the “G3-CS” simulation which manages to produce a rather extended stellar disk despite its high early star formation rate.

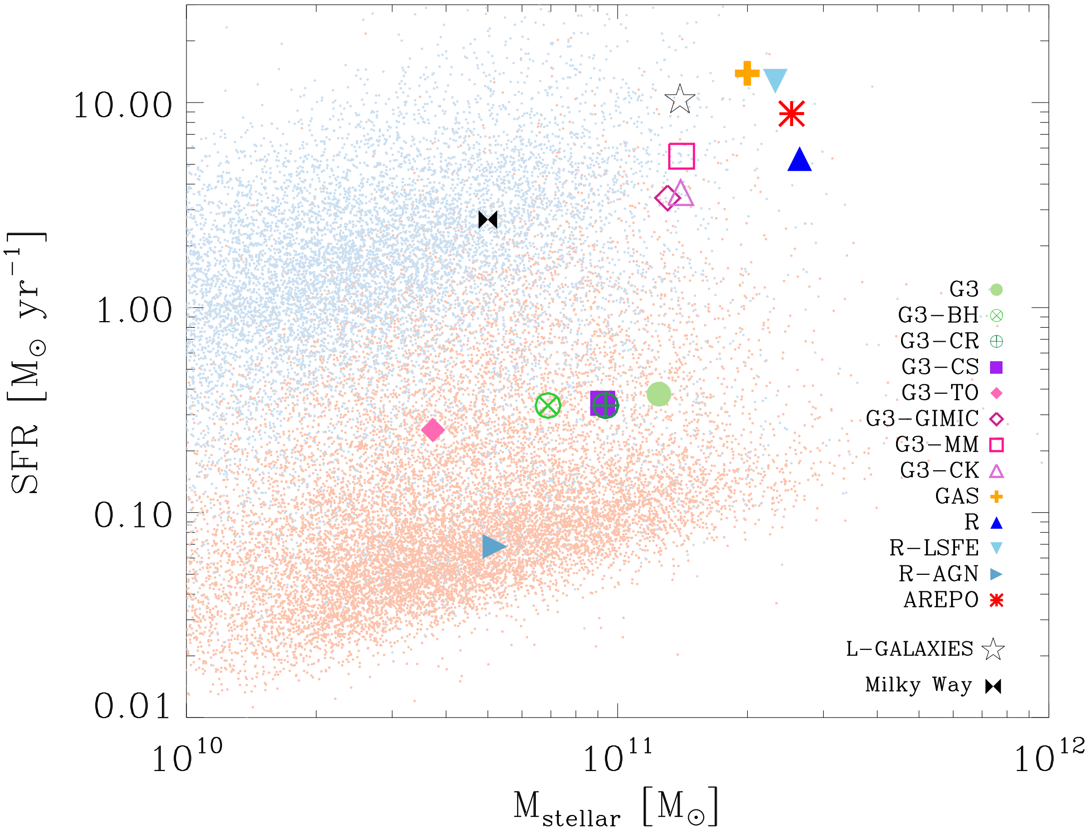

Figure 4.11: Star formation rate at $z = 0$ vs. stellar mass. Blue and red dots correspond to the nearby SDSS galaxy sample as described in Fig. 4.7. The bow-tie symbol indicates the approximate position of the Milky Way, see Oliver et al. (2010); Leitner & Kravtsov (2011) for more details. This plot has been created by C. Scannapieco as part of our joint work on the *Aquila* project.

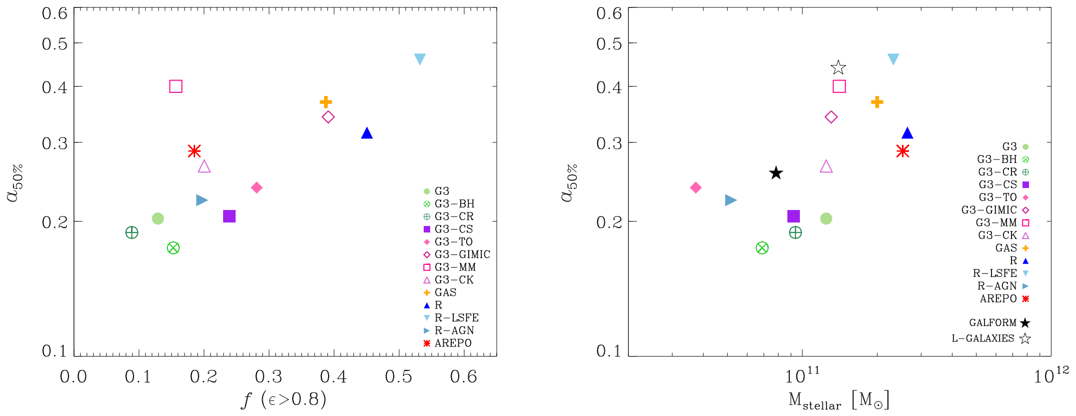

Figure 4.12: *Left panel:* Expansion factor at which 50% of the final stellar mass were formed vs. the disk fraction (stars with circularity $\epsilon > 0.8$). *Right panel:* Expansion factor at which 50% of the final stellar mass were formed vs. final stellar mass This plot has been created by C. Scannapieco as part of our joint work on the *Aquila* project.

4.5.7 Gas fractions

The gas content of the simulated galaxies has a controlling influence on the star formation rate. Thus it is important to have enough cold gas left at late times to be able to build up a stellar disk. In Figure 4.13, we show the present day gas fractions of our simulated galaxies versus their R-band absolute magnitude. We calculate these magnitudes using the dust-free Bruzual & Charlot (2003) population synthesis models for a Chabrier IMF, assuming solar metallicity. We would like to stress that even though some of our simulations track metallicity information, we decided to use solar metallicity throughout in post-processing in order to make the analysis more homogeneous and to allow an easier interpretation of the results. As a reference, we also include observational data from Schombert et al. (2001), Bell & de Jong (2000) and Haynes et al. (1999).

The overall finding of this comparison is that most of our simulated galaxies have a too low gas fraction. The models are also not able to reproduce the trend seen in the data according to which brighter galaxies have lower gas fractions. In our simulations, there is no apparent relation between the final magnitude and the gas fraction.

From this finding one can conclude that in order to match the observed stellar masses together with the star formation rates and gas fractions, a simulation has to be able to regulate star formation efficiently without removing huge amounts of gas from the galaxy. Apparently, none of the shown simulations is really successful in doing so.

4.5.8 Tully-Fisher relation

Finally, we compare the simulated galaxies against the well-known Tully-Fisher scaling relation. In Figure 4.14 we plot the stellar mass versus the circular velocity at the stellar half-mass radius. Additionally, we show observations from Pizagno et al. (2007), Verheijen (2001) and Courteau et al. (2007) to indicate the observed Tully-Fisher relation.

Especially at the highest stellar masses, our simulations fail to reproduce the Tully-Fisher relation. Their circular velocity is significantly too high, consistent with our earlier conclusion that basically all of our galaxies feature a too massive bulge component, especially the simulations with high stellar masses. In the case of the simulations with lower stellar masses, the circular velocity is still too high, but at least their location parallel to the Tully-Fisher relation suggests that decreasing their peak circular velocity or concentration in some fashion would automatically move them closer to the observed Tully-Fisher relation.

The symbols connected with lines in Figure 4.14 show the contribution of dark matter to the circular velocity at the stellar half mass radius. The solid line indicates the contribution of the dark matter component of each individual simulation at the stellar half mass radius while the dotted line shows the circular velocity of the dark matter only simulation Aq-C-4, renormalized by $(1 - \Omega_{\mathrm{b}}/\Omega_{\mathrm{m}})$. This means that the difference between the symbols connected by the solid line and the symbols connected with the dotted line represents the amount of contraction of the dark matter halo. We observe that the amount of contraction increases with stellar mass, again indicating that these galaxies are dominated by a compact, very massive stellar bulge component.

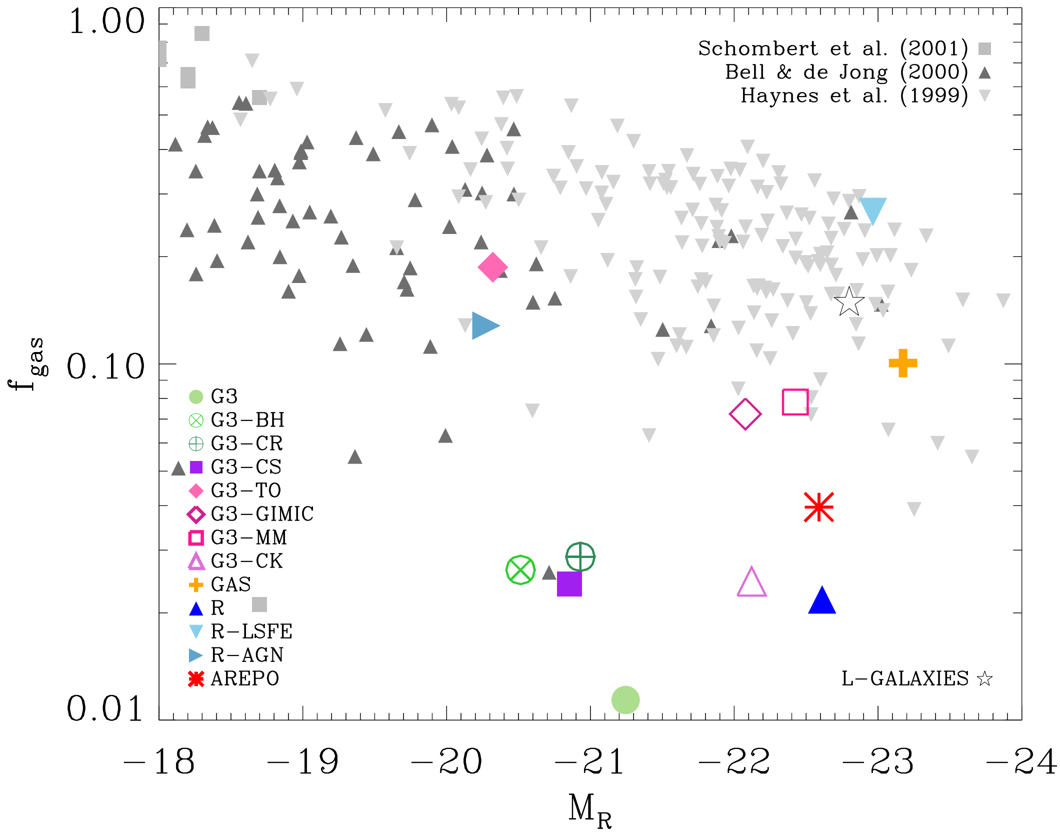

Figure 4.13: Absolute R-band magnitude vs. galactic gas fraction. R-band luminosities where calculated using the Bruzual & Charlot (2003) model for solar metallicity and a Chambrier IMF. Dust extinction/reddening was neglected. The different triangles and squares in grey shade show observational data points from the references listed in the legend.

4.6 Conclusions

In this work, we have performed thirteen simulations of the same Milky Way-sized galaxy using different cosmological codes, and different star formation and feedback implementations. By using a common set of initial conditions and analysis methods, we were able to eliminate any possible influence of these aspects on our comparison results, thereby creating a clean panoramic overview of the relative performance of current state-of-the art hydrodynamical modeling techniques.

We have found a great variety of different stellar morphologies in our sample of simulated galaxies. Some of our simulations, like “G3” and “G3-MM”, are hardly showing any visually detectable disk component, despite our expectation that the conditions for the formation of a Milky Way like disk galaxy in this particular dark matter halo are particularly favourable. Among the other simulations, the vertical thickness and the radial extent of the stellar disks are varying a lot between the different simulations. The only thing in common for basically all of our simulated galaxies is that they are suffering from a huge bulge component and are more often than not showing evidence for a more

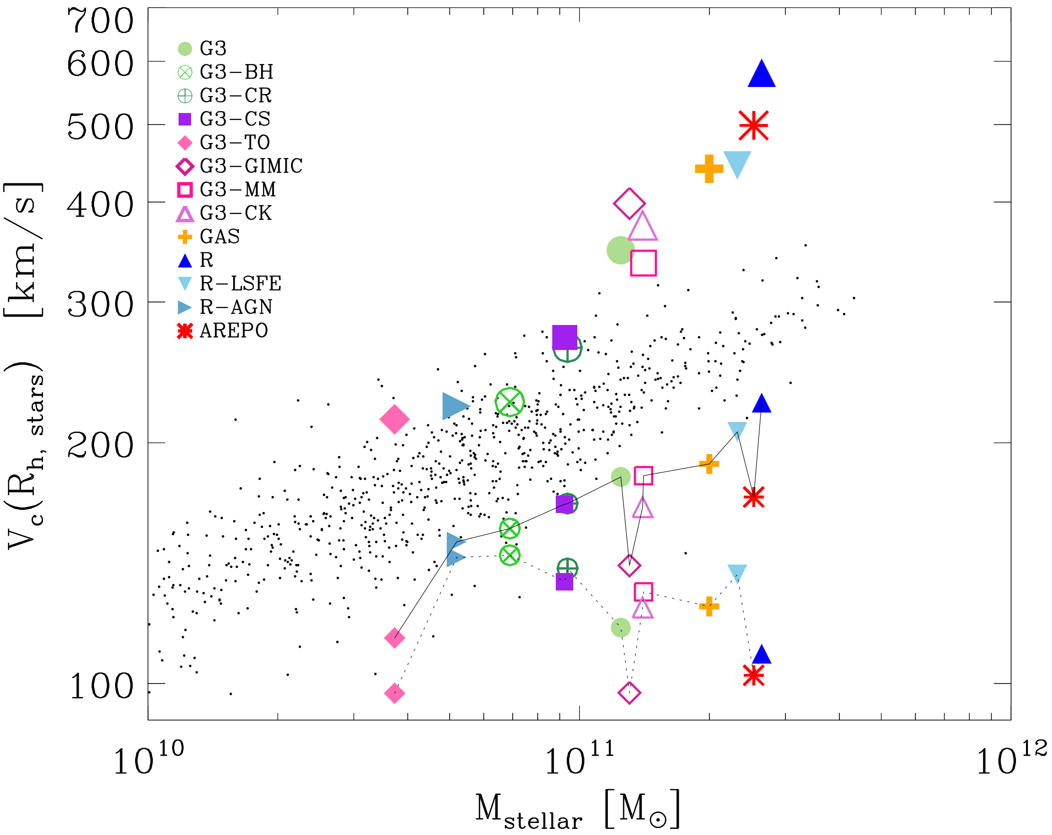

Figure 4.14: This plot shows the Tully-Fisher relation, i.e. circular velocity at the stellar half-mass radius vs. the final stellar mass. Black points show data points taken from Pizagno et al. (2007), Verheijen (2001) and Courteau et al. (2007). The symbols connected by a solid line show the contribution of the dark matter to the circular velocity at $R_{\mathrm{h,stars}}$. Those connected by the dotted line show the circular velocity of the dark matter-only Aquarius simulation (Aq-C-4) at the corresponding radii.

or less pronounced bar.

As one would expect when simulating the same object with different codes we find a pretty good agreement in the final virial mass. This confirms that all the codes reliably track the large-scale gravitational growth of structures with high accuracy. The scatter in the final stellar mass is however surprisingly large, extending over nearly a complete order of magnitude, with stellar masses ranging between $\sim 4 \times 10^{10}$ $M_\odot$ and $\sim 3 \times 10^{11}$ $M_\odot$. We find a clear trend showing that codes including strong feedback and/or explicit galactic wind schemes are forming the least amount of stars. A nice example of this trend is the sequence of simulations “G3”, “G3-BH” and “G3-CR”, where additional energy feedback processes are included that subsequently lead to a systematic reduction of the final stellar mass. Also, we find a tendency of mesh codes to produce higher stellar masses than SPH simulations. We conclude from this that the star formation efficiency does not only depend on the precise implementation of star formation and feedback but also on the accuracy with which basic hydrodynamics is treated. We would like to stress that this last finding has only gained fully attention lately, probably because up to now an objective comparison of the different hydrodynamical schemes carried out on the same initial conditions has been unavailable.

Given the massive stellar bulge of most of the simulated galaxies, it is not surprising that the stellar half-mass radii of our simulated galaxies are generally too low. This means that the distribution of the total stellar component is too concentrated. If one could find a physical way to suppress the formation of a massive bulge, we would expect that the stellar half-mass radii increase significantly, making the simulated galaxies more comparable to observed late-type galaxies through a reduction of their total stellar mass and a simultaneous increase of their stellar half-mass radius. The conclusion that the disks by themselves are actually closer to the sample of observed galaxies than the simulated galaxies as a whole is also supported by the fact that the extent of the cold gas disks is comparable with observations.

Given these results, it is perhaps not too surprising that we found that all of our galaxies host larger gaseous disks than stellar disks. In fact, the gas disk sizes are in good agreement with the findings for our own Milky Way, and we are confident that this would remain true in simulations with a suppressed formation of a central bulge. However, we note that our findings also suggest that the size of the gaseous and stellar disk depend quite strongly on the included physics and the strength of the adopted feedback processes, so this is ultimately not guaranteed. Again, the simulations "G3", "G3-BH" and "G3-CR" are a nice example for a sequence that illustrates this trend. With increasing amounts of energetic feedback, the stellar half-mass radius increases by 60 % while the gaseous half mass radius even doubles.

We have found that the circular velocity profiles of our simulations generally show a large peak close to the center, created by the high central concentration of stellar mass. Such a shape for the rotation curves is incompatible with observations but expected given our other findings. There is again a visible trend that simulations with lower stellar masses and higher stellar half-mass radii are in better agreement with observations as these show the smallest peak velocities. This means that these galaxies are not that strongly dominated by the stellar bulge component at the very center of the galaxy.

Comparing the relation of present-day star formation rate and stellar mass with observations shows again that none of the simulations is consistent with the structure of observed disk galaxies. Generally speaking, the present-day star formation rate at a given stellar mass is too low compared with observations of disk galaxies. This means that simulations with a suitable stellar mass have too low present-day star formation rates while galaxies with the right star formation rates contain way too many stars. The behaviour of the simulations presented here can be divided into two categories: Some of the simulations produce the right amount of stars but are running out of fuel at late times. On the other hand, some of the simulations are able to keep up the replenishment of cold gas until today. However, these galaxies are thus forming too many stars over their lifetime, leading to unphysically high stellar masses. From this finding, we can conclude that is is important to reduce early star formation while simultaneously ensuring a sufficiently strong replenishment of cold gas at late times.

This conclusion is also supported by our examination of the correlation between star formation history and galactic morphology. We find that late time star formation alone is not sufficient to produce realistic stellar disks. While the galaxies which are able to form significant amounts of stars at late times show the best disks in this comparison, they are still suffering from a huge bulge component. Again, this stresses our principal finding that early star formation is one of the key problems in basically all simulations of this comparison. This issue is also the reason behind the problems of our simulations in matching the observed data of the Tully-Fisher relation, because the dense bulge created by the excessive early star formation distorts the rotation curves.

Finally, considering all the results mentioned above, we arrive at the sobering conclusion that present hydrodynamical simulation models are still unable to form realistic spiral galaxies. More successful models need to be able to regulate star formation at high redshift efficiently, but leave enough gas to support copious low redshift star formation. Already in the present set of models, the simulations with the strongest feedback schemes tend to achieve the best results, but in the future significant further improvements in the feedback description will be necessary. Another interesting result of our study is that there appear to be significant systematic differences between SPH and the mesh codes in the amount of gas that cools out, which originates in different treatments of the hydrodynamics. It hence remains important to constantly verify and improve the accuracy of the underlying hydrodynamic solvers.

Table 4.3. Properties of simulated galaxies at $z = 0$, for the level 5 (upper row) and level 6 (lower row) resolution simulations.

Code	M_{200} [10^{10}M$_\odot$]	R_{200} [kpc]	V_{200} km s^{-1}	$M_{\rm stellar}$ [10^{10}M$_\odot$]	$M_{\rm cold\,gas}$ [10^{10}M$_\odot$]	$f(\epsilon > 0.8)$	$a_{50\%}$	$R_{\rm h,stars}$ [kpc]	$R_{\rm h,gas}$ [kpc]	$V_{1/2}$ km s^{-1}	SFR M$_\odot$ yr^{-1}	$M_{\rm R}$	$f_{\rm gas}$	$V_{\rm DM(R_h)}/V_{\rm C(R_h)}$
G3	164.94	239.12	172.24	12.47	0.063	0.13	0.20	3.06	3.06	348.19	0.500	-21.25	0.011	0.521
	172.39	242.23	174.95	11.54	0.003	0.11	0.20	3.43	1.00	325.44	0.039	-21.17	0.046	0.552
G3-BH	157.61	233.48	170.39	6.89	0.161	0.15	0.17	5.31	7.42	224.88	0.389	-20.51	0.026	0.695
	167.38	242.35	172.34	11.07	0.027	0.10	0.19	3.43	8.36	304.63	0.189	-20.99	0.070	0.557
G3-CR	154.32	234.29	168.31	9.38	0.247	0.09	0.19	4.75	7.41	262.93	0.438	-20.93	0.029	0.639
	172.85	239.25	176.27	9.22	0.001	0.09	0.19	4.28	2.45	272.73	0.000	-20.77	0.016	0.652
G3-CS	164.11	237.45	172.41	9.24	0.200	0.24	0.21	4.27	18.22	270.82	0.331	-20.85	0.024	0.619
	149.46	230.01	167.17	5.28	0.061	0.13	0.18	3.79	7.37	236.04	0.062	-20.19	0.018	0.706
G3-TO	147.32	228.40	166.56	3.73	0.850	0.28	0.24	1.94	14.30	213.98	0.354	-20.32	0.187	0.533
	147.85	228.70	166.74	3.94	0.084	0.35	0.24	3.39	3.39	216.65	0.380	-20.43	0.028	0.677
G3-GIMIC	161.84	235.76	171.82	13.06	0.982	0.39	0.34	1.95	10.39	398.37	6.969	-22.08	0.072	0.353
	167.57	238.41	173.86	14.10	1.082	0.31	0.34	2.44	5.97	388.78	7.792	-22.18	0.073	0.355
G3-MM	176.11	245.02	175.82	14.07	0.205	0.16	0.31	3.96	3.96	335.49	1.159	-22.43	0.078	0.542
	176.69	242.57	177.00	13.74	0.318	0.11	0.34	2.28	2.54	362.90	5.797	-22.33	0.087	0.374
G3-CK	166.45	237.61	173.57	14.00	0.324	0.20	0.27	3.52	8.46	373.97	2.392	-22.12	0.025	0.444
	177.52	243.66	177.01	12.30	0.263	0.18	0.26	3.18	3.96	346.24	4.501	-22.15	0.033	0.421
GAS	183.18	246.12	178.91	19.98	0.749	0.39	0.37	3.55	5.52	440.25	18.131	-23.17	0.101	0.427
	183.31	246.23	178.93	17.31	1.090	0.12	0.33	2.85	3.55	505.07	20.796	-22.90	0.147	0.385
R	202.25	256.20	184.26	26.43	1.084	0.45	0.32	2.56	4.48	580.44	6.066	-22.61	0.022	0.387
	178.74	244.00	177.49	26.67	2.063	0.51	0.35	3.66	10.37	504.81	6.056	-22.66	0.054	0.457
R-LSFE	210.27	258.70	186.97	23.21	3.101	0.53	0.46	4.53	9.06	444.55	14.095	-22.96	0.267	0.464
	180.34	245.10	177.89	23.28	3.450	0.62	0.44	5.51	12.25	428.59	8.075	-22.73	0.199	0.554
R-AGN	150.63	231.80	167.17	5.19	0.512	0.20	0.22	5.22	16.23	222.24	0.027	-20.28	0.128	0.677
	147.61	229.10	166.46	1.50	0.319	0.11	0.21	6.87	14.89	169.58	0.000	-18.86	0.014	0.834
AREPO	204.54	257.45	184.85	25.33	0.382	0.19	0.29	2.21	5.47	498.77	4.042	-22.59	0.040	0.343
	206.21	257.54	185.57	28.68	0.951	0.36	0.37	3.48	8.61	464.29	5.116	-22.88	0.051	0.416
GALFORM	203.27	261.01	183.01	7.84	0.004		0.26	3.77	10.43		0.004	-20.99	0.001	
L-GALAXIES	178.01	243.10	177.46	13.95	2.44		0.44	2.03	5.13		10.328	-22.80	0.149	

5 Effects of feedback physics and hydrodynamical technique in simulations of disk galaxy formation

Contents

5.1 Introduction 83

5.2 Simulation methodology 85

5.2.1 Initial conditions 85

5.2.2 Simulation codes 86

5.2.3 Models for star formation and cooling 89

5.3 Gaseous disks in AREPO and GADGET 93

5.3.1 Star formation histories of model galaxies 97

5.3.2 Growth history of halos 97

5.3.3 Kinematics of gaseous disks 101

5.3.4 The structure of the cold gas 101

5.4 Stellar mass mass distribution of the simulated galaxies . . . 107

5.4.1 Kinematic disk and bulge components 111

5.4.2 Comparison with observational constraints 113

5.5 Convergence and global differences 113

5.5.1 Resolution study 113

5.5.2 Clumpy halos 114

5.6 Conclusions 115

Summary

In this chapter, we investigate hydrodynamical simulations of a Milky-Way sized galaxy in the full cosmological context. Using the much higher numerical resolution allowed by a zoom simulation set-up, we confirm recent findings that the moving-mesh code AREPO cools more gas at late times than the SPH-code GADGET, and produces much better defined gaseous disks and higher star formation rates at low redshift. This also makes the young stellar disk in our moving-mesh galaxy simulations better defined, giving them a profile that is fit by an exponential with a reasonable scale length. However, in both simulation methods an overly massive central bulge forms in the particular halo studied here, which is taken to be the same one examined in the recent *Aquila* comparison project (Scannapieco et al., 2011a). In fact, the stellar and gaseous disks are largely destroyed in our simulations by the disturbing influence of a satellite interaction at redshift $z \sim 0.7$. Through a series of simple experiments that modify the star formation recipe and the cooling prescription we investigate whether a higher star-formation threshold or a longer gas consumption timescale alone can significantly improve the bulge-to-disk ratio of the final galaxy. We find however that the $z = 0$ galaxy properties are largely invariant to these changes. Even an ad-hoc suppression of any gas cooling at high redshift produces a disk-dominated galaxy only at $z = 1$, but this morphology does not survive to the present due to the destabilizing influence of the disk's own strong self-gravity (which has excessive mass) and the mergers occurring in the environment of the particular halo examined. We thus conclude that both, an accurate hydrodynamic solver, and a suppression of high redshift star formation through feedback processes that reduce the remaining baryon fraction in the halo, are key factors for obtaining disk galaxies that match the properties of observed late-type galaxies. Our results also caution against relying on single realizations of dark matter halos for evaluating the success or failure of galaxy formation simulations.*

5.1 Introduction

Simulations of structure formation in the ΛCDM concordance cosmology have been very successful in explaining cosmic large-scale structure (e.g. Davis et al., 1985; Springel et al., 2006). Combined with semi-analytic galaxy formation models, they have also yielded stunningly successful descriptions of a multitude of observational data about the galaxy population at different epochs (e.g. Guo et al., 2011). However, full hydrodynamical simulations of galaxy formation in the ΛCDM framework have traditionally been much less successful, especially with respect to reproducing the observed morphological mix of galaxies or their luminosity function.

Early simulation work (e.g. Navarro & Steinmetz, 2000) identified an angular momentum deficit of formed disk galaxies due to the early condensation of baryons in small progenitor systems, causing baryons to loose angular momentum by dynamical friction and sink to the center. Additionally, the so-called overcooling problem manifests itself in an excess of star formation in small and large dark matter halos alike, unless somehow curtailed through efficient feedback processes. It has proven difficult however to successfully account for such feedback processes in hydrodynamic cosmological simulations. Even the most recent simulation models based on optimistic assumptions about the feedback efficiency still create overly large stellar masses for their host dark matter halos, as revealed by abundance matching analysis with the observed stellar mass function of the Sloan Digital Sky Survey (Guo et al., 2010; Sawala et al., 2011). Much of this overproduction of stars occurs at high redshift, with the material then ending up in an excessively massive central bulge component. Indeed, it has been a long-standing challenge in computational cosmology to form disk galaxies with small bulges, and hence to successfully reproduce the structural properties of many late type galaxies.

Improvements in the modeling of feedback associated with star formation and in the accuracy of the numerical techniques have led to important incremental progress on this problem over the past decade (Governato et al., 2004, 2007; Robertson et al., 2004; Scannapieco et al., 2008, 2009, 2011b; Sales et al., 2009, 2010; Stinson et al., 2010; Piontek & Steinmetz, 2011). In particular, the most recent generation of cosmological hydrodynamical simulations of galaxy formation have reported some impressive successes (Governato et al., 2010; Agertz et al., 2011; Guedes et al., 2011; Brooks et al., 2011). However, the degree and universality of this success, as well as some of the modeling details required for achieving them, remain debated. Some studies have argued that very high numerical resolution is a central and potentially sufficient requirement (e.g. Kaufmann et al., 2007; Governato et al., 2007), whereas other studies emphasized that

---

[*] To be submitted to *Monthly Notices of the Royal Astronomical Society*, Wadepuhl & Springel, 2011.

the degree of success critically depends on the modeling of the physics of star formation and feedback (e.g. Okamoto et al., 2005; Scannapieco et al., 2008; Sales et al., 2010). Recently, Guedes et al. (2011) have pointed out that a high density threshold for star formation appears crucial to successfully form a late-spiral galaxy that is a close analogue to the Milky Way. On the other hand, Agertz et al. (2011) find that a low star-formation efficiency, particularly at high redshift, is a key factor in making large disk galaxies, whereas an opposite conclusion was reached by Sommer-Larsen et al. (2003) and Sales et al. (2010), who favored a high star formation efficiency instead. In light of these findings, it appears clear that a full understanding of disk galaxy formation through hydrodynamic simulations is still an elusive goal.

Interestingly, even if identical initial conditions are used, the outcome of disk galaxy formation simulations appears to depend particularly sensitively on the implementation of feedback physics. For example, in Okamoto et al. (2005) either a nice disk galaxy or an elliptical galaxy was formed in the *same* dark matter halo, depending on details of the feedback prescription. This sensitivity of the outcome of galaxy formation simulations on details of the numerical code and physics implementations has recently been further examined in the "Aquila" comparison project (Scannapieco et al., 2011a), where a large number of hydrodynamical codes by different groups was compared for identical initial conditions, corresponding to a halo selected from the Aquarius project (Springel et al., 2008) of high-resolution dark matter simulations. Many of the examined 13 codes have been based on the SPH formalism as implemented in the GADGET (Springel, 2005) or GASOLINE (Wadsley et al., 2004) codes, but they differed widely in their implementation of star formation and feedback processes. In addition, the Eulerian adaptive mesh refinement (AMR) code RAMSES (Teyssier, 2002) and the new moving-mesh code AREPO (Springel, 2010a) have been included in the comparison as well.

In a series of recent papers (Vogelsberger et al., 2011; Keres et al., 2011; Torrey et al., 2011) which compared cosmological simulations of galaxy formation between SPH and the moving-mesh code AREPO, the accuracy of the underlying hydrodynamics solver has been identified as another important factor in determining the morphology of the resulting disk galaxies. In these comparison studies, the same initial conditions were used as well, but this time in the form of homogeneously sampled cosmological boxes. Also, the same implementation for radiative cooling, star formation and feedback, together with an identical gravity solver, were used. This allowed a clean assessment of the impact of the different hydrodynamical techniques on the final morphology of the simulated galaxies. Interestingly, the moving-mesh code produced a consistently larger amount of gas-cooling out of halos at low redshift, and on average significantly larger gas disks. This has been attributed to numerical inaccuracies of the SPH technique in comparison to the mesh-based treatment (Sijacki et al., 2011; Bauer & Springel, 2011).

Here we present an extended comparison of a subset of the simulation models contained in the Aquila project, namely the runs with GADGET and AREPO that were based on the subresolution model for star formation and feedback introduced by Springel & Hernquist (2003). This physics model also corresponds closely to that explored in the cosmological simulations of Vogelsberger et al. (2011), except that we here use zoom-simulations of a single individual halo at much higher resolution. This hence allows to check whether the general findings obtained through the comparison of homogeneously sampled cosmological boxes continue to hold at much higher resolution for in individual galaxies. We note however an important caveat right away: a single system may always be relatively far away from the mean behavior of halos of the same mass, hence any difference we find here between the codes may not necessarily be representative for the population of all galaxies as a whole (see also Torrey et al., 2011). As we will see, the halo Aq-C of the Aquarius project studied here and in the Aquila project is actually somewhat problematic in this respect. The halo in fact experiences a quite strong low redshift ($z \sim 0.7$) perturbation from a massive satellite in that largely destroys the disk component that is present at this time in most of our runs. We note that this is also an important reason why both simulation methods produce a strongly bulge dominated galaxy at $z = 0$ in this particular halo, with AREPO forming only a moderately better (but subdominant) disk at $z = 0$.

We also carry out a number of additional test simulations that modify the cooling and star formation prescription in the AREPO physics implementation, but without alluding to strong feedback that could expel baryons from the halo. This is meant to investigate whether a higher star formation threshold alone, a longer star-formation timescale, or a suppression of star formation at high redshift can prevent the formation of a large bulge or spheroidal galaxy in this particular halo. We also study the effect of varying the numerical resolution in our simulations. Our default resolution corresponds to a mass resolution of $2.2 \times 10^6\,\mathrm{M}_\odot$ and a gravitational softening length of 0.68 kpc, matching what has been used in the Aquila project. Additionally we compare with results both with a lower and a higher resolution, reaching up to a mass resolution of $0.28 \times 10^6\,\mathrm{M}_\odot$ and a spatial resolution of 0.34 kpc. These are currently among the best resolved hydrodynamical simulations of the formation of a Milky Way-sized galaxy within a full cosmological context published thus far.

This paper is structured as follows. In Section 5.2, we briefly summarize the numerical methodology used in our SPH and moving-mesh simulations, and we detail the simulation set we examine. In Section 5.3, we first compare the gas disks formed in the different simulations as a function of time. We then relate this to the star formation histories of the different galaxies, and their global structural properties in the stellar component in Section 5.4. We consider runs at different resolution and the gas clumping in the halo in Section 5.5. Finally, we present our conclusions in Section 5.6.

5.2 Simulation methodology

5.2.1 Initial conditions

We use the initial conditions of the ‘Aq-C’ halo of the *Aquarius* suite of high-resolution dark matter simulations of Milky-Way sized halos (Springel et al., 2008). This object was also selected in the *Aquila* hydrodynamical code comparison project (Scannapieco et al., 2011a), and the particular choice of this halo among the 6 *Aquarius* halos was in part motivated by earlier hydrodynamical simulations of the whole set of *Aquarius* halos at comparatively low resolution (Scannapieco et al., 2009), which suggested that ‘Aq-C’ should be a particularly promising candidate for disk formation (see also Boylan-Kolchin et al., 2010).

Corresponding to the nomenclature used in the *Aquarius* project, the realizations simulated in this work correspond to resolution levels 4, 5 and 6 of the Aq-C halo. The majority of our simulations uses resolution level 5, corresponding to a baryonic mass resolution of $0.4 \times 10^6\,\mathrm{M}_\odot$ with a comoving gravitational softening of $0.5\,h^{-1}\mathrm{kpc} = 0.68\,\mathrm{kpc}$. In our resolution study, we also consider simulations adopting a baryonic mass resolution of $3.2 \times 10^6\,\mathrm{M}_\odot$ with a gravitational softening of $1.0\,h^{-1}\mathrm{kpc} = 1.36$ kpc, as well as $0.05 \times 10^6\,\mathrm{M}_\odot$ with a gravitational softening of $0.25\,h^{-1}\mathrm{kpc} = 0.34$ kpc, which correspond to resolution levels 6 and 4 in the *Aquarius* paper, respectively.

The simulated volume is a periodic cube with a side length of $100\,h^{-1}\mathrm{Mpc}$. The adopted ΛCDM cosmology uses the parameters $\Omega_m = 0.25$, $\Omega_\Lambda = 0.75$, $\sigma_8 = 0.9$, $n_s = 1$, and a Hubble constant of $H_0 = 100\,h\,\mathrm{km\,s^{-1}\,Mpc^{-1}} = 73\,\mathrm{km\,s^{-1}\,Mpc^{-1}}$. These parameters are the same as in the Millenium and Millenium-II simulations (Springel et al., 2005b; Boylan-Kolchin et al., 2009). While they are still in marginable agreement with the latest cosmological constraints, the adopted σ_8 value lies on the high side compared to the most recent determinations, which is however of no relevance for the present study. In order to achieve the high resolution needed to resolve the formation of a Milky Way like galaxy, our initial conditions are utilizing the "zoom-in technique", i.e. the Lagrangian region from which the main galaxy forms is sampled with a high number of low mass particles whereas the rest of the simulation volume is filled with progressively higher mass particles whose mass grows with distance from the target galaxy. This saves computational time while still ensuring the correct cosmological tidal field and mass infall rate for the forming target galaxy.

The selected halo has a present-day virial mass[†] of $M_{200} = 1.6 \times 10^{12}\,\mathrm{M}_\odot$, which is within the range of current estimates of the Milky Way's mass. The original *Aquarius* initial conditions contained only dark matter particles. For our simulations, we add gas by splitting each dark matter particle into a pair of one dark matter and one gaseous cell or particle, with their masses set according to the cosmological baryon mass fraction, and a separation equal to half the original mean interparticle spacing, keeping the the center-of-mass and center-of-mass velocity of each pair fixed. In this way, two interleaved grids (or actually 'glasses', in the case of our high resolution region) of dark matter particles and gaseous particles/cells are formed. We note that we split *all* the particles, regardless of whether they are part of the high-resolution region or the surrounding low resolution volume, such that the whole volume is filled with gas. There is hence no pressure discontinuity at the boundary of the high-resolution region.

5.2.2 Simulation codes

In the following, we briefly describe the simulation codes and their most important parameter settings used in this work. In the interest of brevity, we only describe the most important code characteristics and refer the interested reader to the technical implementation papers (Springel, 2005, 2010a) for further details.

The SPH-code GADGET-3

Smoothed particle hydrodynamics (SPH) uses a set of discrete tracer particles to describe the state of a fluid (Lucy, 1977; Gingold & Monaghan, 1977; Monaghan, 1992). To represent continuous fluid quantities and to calculate spatial derivatives, a kernel in-

---

[†] We define the virial mass as the mass contained within a sphere that encloses a mean matter density 200 times the critical density for closure, $\rho_{\mathrm{crit}} = 3H_0^2/(8\pi G)$.

Name	Code	Gas mass	DM mass	Physics	ϵ_{DM}
G6	GADGET	$3.2 \times 10^6 \mathrm{M}_\odot$	$17.6 \times 10^6 \mathrm{M}_\odot$	default subresolution model	$1.0\, h^{-1}$kpc
A6	AREPO	$3.2 \times 10^6 \mathrm{M}_\odot$	$17.6 \times 10^6 \mathrm{M}_\odot$	default subresolution model	$1.0\, h^{-1}$kpc
G5	GADGET	$0.4 \times 10^6 \mathrm{M}_\odot$	$2.2 \times 10^6 \mathrm{M}_\odot$	default subresolution model	$0.5\, h^{-1}$kpc
A5	AREPO	$0.4 \times 10^6 \mathrm{M}_\odot$	$2.2 \times 10^6 \mathrm{M}_\odot$	default subresolution model	$0.5\, h^{-1}$kpc
A5-cooloff	AREPO	$0.4 \times 10^6 \mathrm{M}_\odot$	$2.2 \times 10^6 \mathrm{M}_\odot$	SF / cooling switched off up to $z = 2.5$	$0.5\, h^{-1}$kpc
A5-highthresh	AREPO	$0.4 \times 10^6 \mathrm{M}_\odot$	$2.2 \times 10^6 \mathrm{M}_\odot$	threshold for SF increased by a factor of 100	$0.5\, h^{-1}$kpc
A5-slowsfr	AREPO	$0.4 \times 10^6 \mathrm{M}_\odot$	$2.2 \times 10^6 \mathrm{M}_\odot$	SF timescale increased by a factor of 3	$0.5\, h^{-1}$kpc
A5-preheat	AREPO	$0.4 \times 10^6 \mathrm{M}_\odot$	$2.2 \times 10^6 \mathrm{M}_\odot$	art. heating of all gas to 5×10^6 K at $z = 12$	$0.5\, h^{-1}$kpc
G4	GADGET	$0.05 \times 10^6 \mathrm{M}_\odot$	$0.28 \times 10^6 \mathrm{M}_\odot$	default subresolution model	$0.25\, h^{-1}$kpc
A4	AREPO	$0.05 \times 10^6 \mathrm{M}_\odot$	$0.28 \times 10^6 \mathrm{M}_\odot$	default subresolution model	$0.25\, h^{-1}$kpc

Table 5.1: Simulation set analyzed in this study. Each row specifies a specific run, for which we list its symbolic simulation name, the code used, the gas and dark matter mass resolutions in the high-resolution region, the specifics of its setup with respect to cooling and star formation, as well as the comoving gravitational softening length in the high-resolution region.

terpolation technique is used. Thanks to the Lagrangian discretization in terms of mass, the Euler equations are converted to a set of ordinary differential equations, which are far easier to integrate in time. In fact, in SPH this reduces to equations of motion for the fluid particles under their mutual pressure forces, and a time evolution equation for the thermal energy or entropy per unit mass. A proper description of flows that involve shocks additionally requires the introduction of an artificial viscosity.

The mesh-free SPH technique accurately obeys the fundamental conservation laws for mass, energy, momentum and angular momentum. Furthermore, it automatically adjusts is spatial resolution to the clustering of matter, which is close to ideal for galaxy formation applications. However, SPH is also known to suffer from accuracy problems in the treatment of fluid instabilities (e.g. Agertz et al., 2007; Sijacki et al., 2011) and subsonic turbulence (Bauer & Springel, 2011). It is also a relatively noisy technique that exhibits a few unwanted numerical artifacts like a surface tension across strong contact discontinuities, a suppression of mixing, and particle clumping. Until recently, it has been unclear, however, whether these effects manifest themselves in significant quantitative problems in the results of cosmological simulations.

In this study, we employ the SPH code GADGET-3, which is an updated and improved version of the publicly released version of the same code (Springel, 2005). The code follows dark matter and collisionless particles through a TreePM gravity solver, which combines a long-range gravity computation with mesh-based Fourier techniques with a hierarchical multipole expansion (calculated with a tree algorithm) for the short-range gravity forces in real space. This combination yields an efficient and accurate gravity solver with a uniformly high force resolution. Finally, we note that the SPH implementation employs the entropy conserving formulation of Springel & Hernquist (2002), which implicitly accounts for all correction terms due to the fully adaptive smoothing lengths at all orders.

The moving-mesh code AREPO

The moving-mesh code AREPO (Springel, 2010a) employs a dynamic Voronoi mesh for a finite-volume discretization of the Euler equations. The fluxes between the individual Voronoi cells are calculated using a second-order Godunov scheme together with an exact Riemann solver. This approach is akin to ordinary grid-based Eulerian schemes for hydrodynamics, except that an unstructured mesh is used that is generated as the Voronoi tessellation of a set of mesh-generating points. In addition, these mesh-generating points may be moved freely, inducing a dynamical and continuous transformation of the mesh without the occurrence of pathological mesh distortions. The most interesting way to exploit this freedom of a dynamic mesh is to move the mesh-generating points with the local flow velocity. In this default mode of operating AREPO, a pseudo-Lagrangian method results where the mass per cell is kept approximately constant and a Galilean-invariant numerical method is obtained.

The automatic adaptivity of AREPO thus obtained is similar to that of SPH, but the mass per cell is not forced to stay strictly constant. In fact, local variations in the gas mass per cell may occur, but in case the mass deviates by more than a factor of two from the target gas mass resolution, we either split the cell into two, or dissolve it (as in Vogelsberger et al., 2011), which is very similar to a Lagrangian refinement criterion in AMR codes. But thanks to the adaptive nature of the dynamic mesh, such refinement and derefinement operations are needed much less frequently. Perhaps the most important advantage of AREPO compared to traditional mesh codes with a static mesh is a significant reduction of advection errors, which becomes particularly relevant for highly supersonic motions. Compared to SPH, the most important advantages are the absence of an artificial viscosity, a reduced sampling noise, and a faster convergence rate in multi-dimensional flow.

As far as the gravity solver and collisionless dynamics is concerned, AREPO applies the same techniques as the TreePM code GADGET. This makes the two codes particularly well suited for a code comparison that focuses on an analysis of the differences induced due to the hydrodynamic treatment alone. This is further helped by the ability of both codes to start from identical initial condition files, and by the similarity of the output structure, which allows largely identical analysis and postprocessing routines to be applied.

5.2.3 Models for star formation and cooling

Star formation and the corresponding supernova feedback are modeled in all of our simulations with a simple subresolution model for the interstellar medium (ISM), which pictures the ISM as a two-phase medium that is predominantly composed of cold clouds embedded in a tenuous, supernova-heated phase (Springel & Hernquist, 2003). Radiative cooling gives rise to cloud formation. Stars form out of the clouds, and the energy associated with supernova explosions of massive stars heats the low-density phase and evaporates some of the cold clouds through conduction. This establishes a self-regulation cycle for star formation, which can be phrased in terms of an effective equation of state for the star-forming phase.

The model is calibrated to reproduce the observed Kennicutt relation between total gas surface density and star formation rate density in local disk galaxies. No attempt is however made to account for the molecular hydrogen content in the ISM, metallicity effects, radiation pressure, or the small-scale turbulent structure of the ISM. Also, even though supernova feedback prevents a run-away collapse of the gas and very short gas consumption time scales in this model, it does not produce galaxy-wide outflows. In this sense the model can be considered a minimum feedback model.

Collisionless star particles with mass equal to the gas-mass resolution are created out of the star-forming gas stochastically according to the local star-formation rate. These star particles are afterwards treated as collisionless particles, in exactly the same way as the dark matter particles. Radiative cooling and heating of hydrogen and helium are treated as in Katz et al. (1996), and we adopt a spatially uniform UV-background with the time time dependence of Haardt & Madau (1996), leading to reionization of the model universe at $z = 6$.

This physical model for cooling, star formation and feedback is adopted in our default set of simulations with GADGET and AREPO, which we denote as ‘G5’ and ‘A5’, respectively. Here the leading character stands for the simulation code, whereas the number 5 designates the resolution level in correspondence to the *Aquarius* project from which the initial conditions were taken. Similarly, the labels A4 and A6, for example, refer to AREPO simulations one resolution level higher or lower compared to our default runs, respectively.

In addition to our basic simulations G5 and A5, we have carried out a number of test simulations with AREPO where we varied some aspects of the cooling and star formation

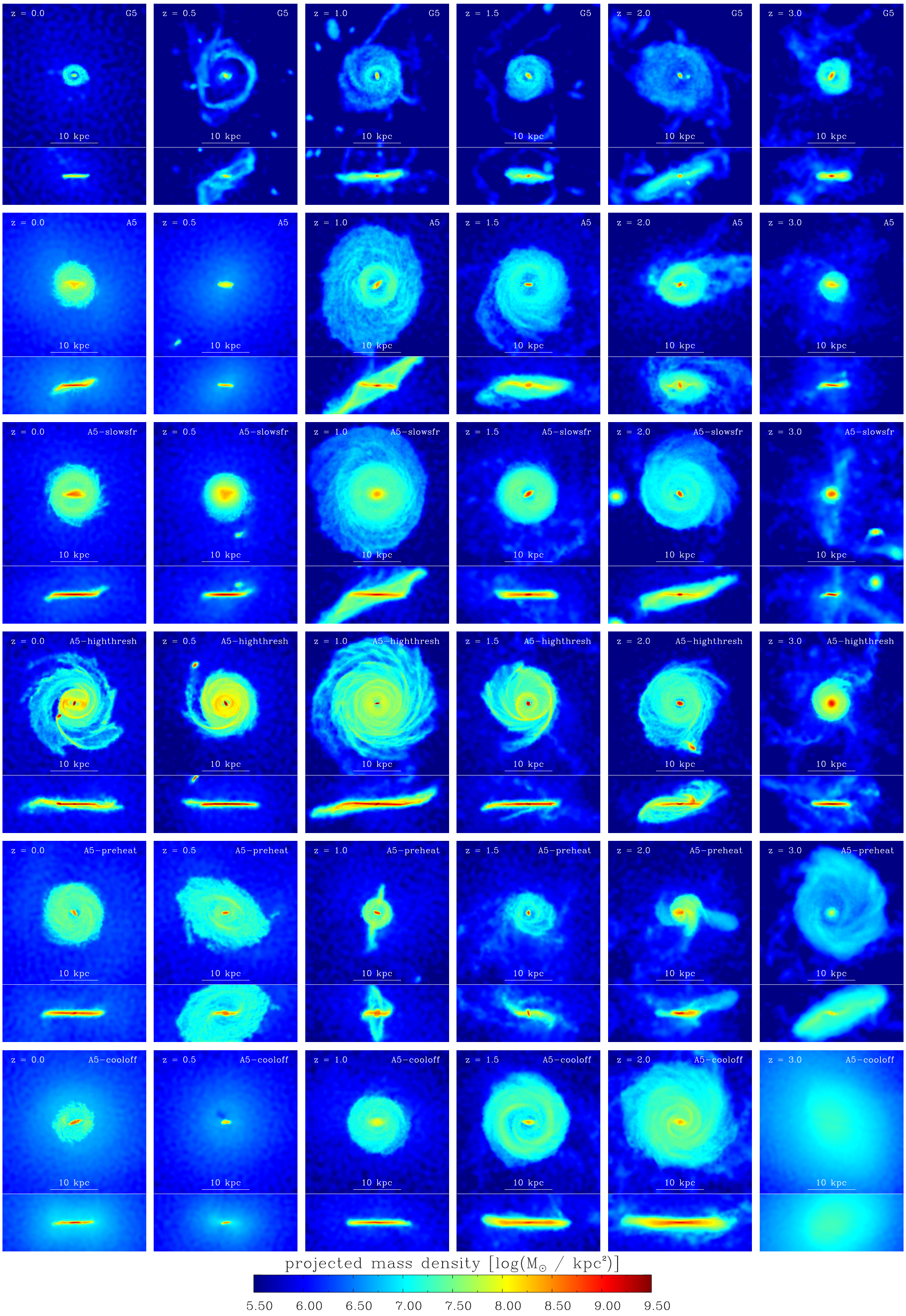

Figure 5.1: Projected gas density maps in our zoom simulations at level-5 resolution in face-on and edge-on projections, at different redshifts as labeled. The color-scale is logarithmic in the surface density, as shown in the color-bar. The size of the region shown is 30 kpc × 30 kpc for the face-on maps and 30 kpc × 12 kpc in case of the edge-on maps. The depth of the projected volume is 30 kpc in both cases.

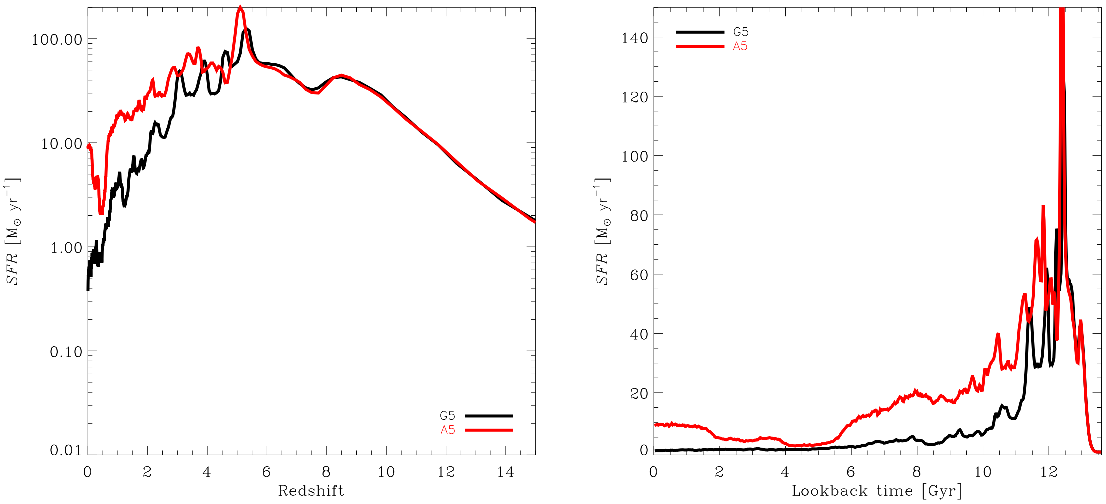

Figure 5.2: Comparison of the star formation rate history in our default GADGET and AREPO runs, both displayed as a function of redshift (left panel) or on a linear scale as a function of lookback time (right panel). Only the history of stellar material that ends up in the central galaxy of the primary halo is shown. Clearly visible is that AREPO cools considerably more gas at late times, fueling a higher star formation at low redshift.

prescriptions in order to examine the sensitivity of the results to various modeling aspects. In the first simulation of this type, 'A5-slowsfr', we adopted a longer star formation timescale by a factor of 3, meaning that we increased the gas consumption timescale due to star formation at the star formation density threshold to 6.3 Gyr. At the same time, we also formally increased the energy returned by supernovae and the evaporation factor by a factor of 3, so that the effective equation of state of the ISM remained unchanged (see Springel & Hernquist, 2003, for a derivation of the corresponding equation). This model is hence expected to yield identical gas dynamics if the amount of gas is equal, but the gas is depleted by star formation on a much longer timescale. The model is motivated as a simple test of the finding by Agertz et al. (2011) that a lower star formation efficiency appears necessary to form realistic disk galaxies.

Another test simulation, 'A5-highthresh', is motivated by Guedes et al. (2011) who claimed that a higher star formation threshold is necessary to form realistic disk galaxies. We therefore carried out a fiducial simulation where a higher density threshold for star formation of $n \approx 10\,\mathrm{cm}^{-3}$ was adopted, corresponding to a 100 times higher density threshold compared to our default simulations. Due to this change, much higher densities will characterize the star-forming phase of the ISM of the simulated galaxy, presumably implying a more inhomogeneous distribution of the gas within the galactic disk and a significant change in the feedback efficiency. Allowing the gas to reach higher densities also lowers the thickness of the gaseous disk and shifts the maximum of the star formation history to later times as the gas has to reach higher densities to allow star formation.

Previous studies, in particular those of the *Aquila* comparison project of Scannapieco et al. (2011a), have shown that simulated disk galaxies suffer particular strongly from high star formation rates at early times. In fact, there is a clear correlation in the sense that the more successful runs are those which manage to suppress high-redshift star formation.

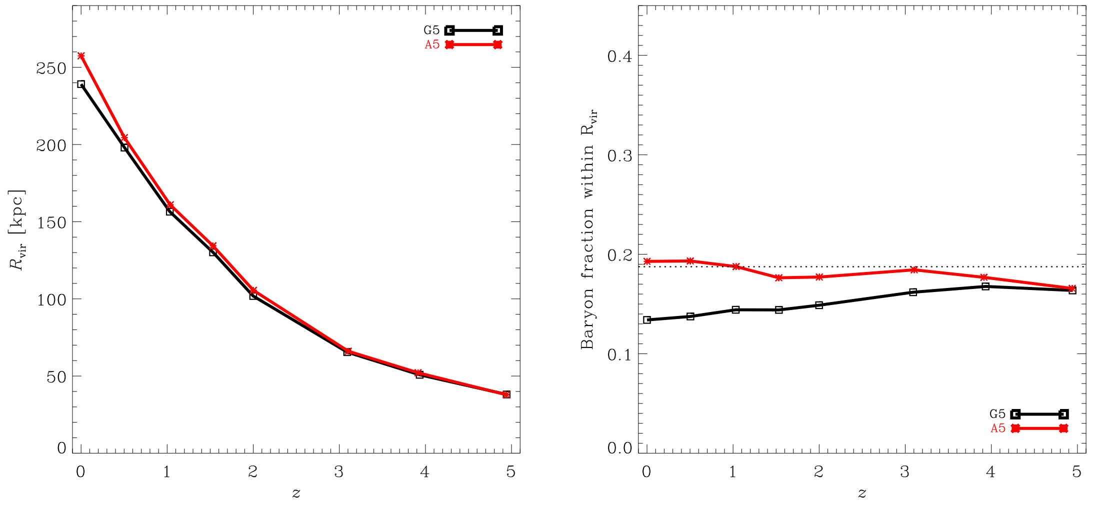

Figure 5.3: Comparison of the evolution of the virial radius and the baryon fraction in our default GADGET and AREPO runs. Interestingly, the SPH simulation falls slightly short of the universal baryon fraction within the virial radius at late times, whereas the moving-mesh calculation stays close to the universal value. This is presumably directly related to the spurious heating of the gas in the halo of the GADGET simulation, which in turn also slightly lowers the virial radius and virial mass.

To investigate the potential impact of reducing this early star formation, we have run two additional fiducial simulation. In one, 'A5-preheat', all the gas in the simulation box was simply reheated to a temperature of 5×10^6 K at redshift $z = 12$, thereby preventing in an (admittedly extreme) ad-hoc fashion the formation of many small galaxies at high redshift. Such reheating schemes have previously often been invoked in the context of attempts to explain the observed scaling laws of galaxy clusters (e.g. Muanwong et al., 2002; Borgani et al., 2005), but here it is only meant as a means to mock up some unknown efficient feedback mechanism at high redshift. The expectation for this model would be that it reduces the angular momentum problem and the formation of an excessive bulge component at high redshift.

Finally, we consider a yet more artificial scenario in which we disable radiative cooling entirely until $z = 2.5$. This means that the simulation was evolved in purely non-radiative (sometimes misleadingly called "adiabatic") mode until $z = 2.5$, from which point onwards radiative cooling and star formation was followed normally again, as in our default models. Of course, in this simulation, very old stars in bulges cannot be produced by construction, so that the conditions for an inside-out formation (Fall & Efstathiou, 1980) of a large disk galaxy can in principal be expected to be very good.

In Table 5.1, we give an overview of the simulation set considered in this work, including also a brief summary of the most important numerical parameters, such as the the spatial and mass resolutions of the individual simulations. In all the runs, the gravitational softening has been kept fixed in comoving units at all times.

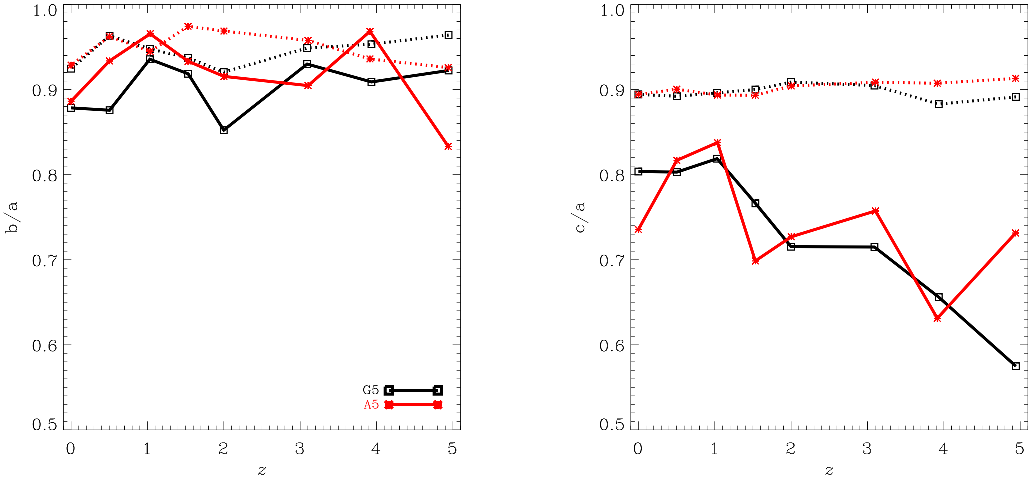

Figure 5.4: Comparison of the evolution of the shape of the dark matter halo in our default GADGET and AREPO runs. Here we give the ratios of eigenvalues of the dark matter moment-of-inertia tensor within the virial radius (solid lines) and within the galactic radius (dashed lines), both for the intermediate-to-major (left panel) and minor-to-major (right panel) eigenvalue ratios. The shapes of the dark matter halo in our GADGET and AREPO runs resemble each other closely at all times. The shape is slightly oblate and has a consistent tendency of getting rounder with time, especially in the outer parts. The inner part of the halo within the galactic radius is pretty round at all times and does show significant variations of its shape.

5.3 Gaseous disks in AREPO and GADGET

Figure 5.1 compares projected gas density maps of the central 30 kpc in our primary simulation set, with each row giving the time evolution of a different model. The six images for each model show face-on and edge-on projections of the gas disks at epochs $z = 0$, 0.5, 1, 1.5, 2 and 3. All projections are done in physical coordinates and use the same logarithmic mapping for assigning colors to a projected density value.

In the top row, our default GADGET-3 simulation is shown. It can be most directly compared with the corresponding default AREPO run in the second row, as the difference between these simulations lies only in the employed hydrodynamical technique. Quite noticeably, the gas disks seen at redshifts $z = 1$ and higher are larger in AREPO compared to the SPH simulation. This is consistent with the findings obtained in recent cosmological simulations of galaxy formation at lower resolution per object (Vogelsberger et al., 2011; Keres et al., 2011; Torrey et al., 2011). At redshift $z = 0.5$, however, the gas disks in both the G5 and A5 runs appear to be largely destroyed, with the G5 simulation showing residual signs of a strong perturbing event in the form of a gas ring that is tilted with respect to the small residual gas disk left or reformed at the very center. Towards redshift $z = 0$, a sizable gas disk reforms in A5, whereas G5 has regrown only a much smaller gas disk. We will return to a more detailed discussion of the perturbing event between $z = 0.5$ and $z = 1.0$ later on.

It is now interesting to consider the impact of different simple modifications of the

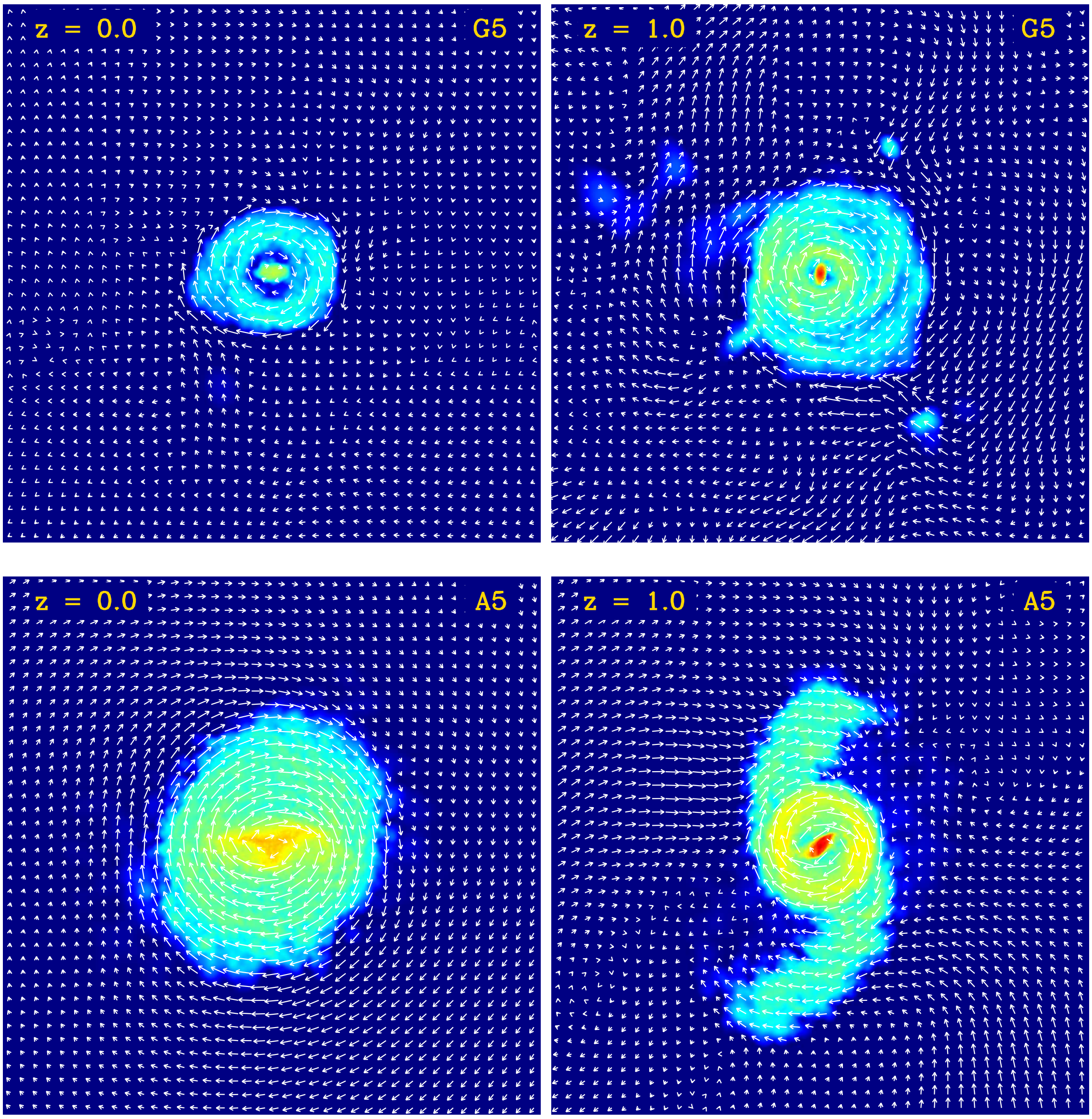

Figure 5.5: Velocity field in the plane of the disk at $z = 0$ and $z = 1$, for our default simulations with AREPO and GADGET, as labeled. We show the projected velocity field of the gas component within a thin slice (of thickness 4 kpc) centered on the galactic gas disk. The width of the projected maps is 20 kpc on a side. For reference, we include underneath a logarithmically color-coded map of the gas density in the same slice. It is evident that the ordered motion of the gas component in the case of the AREPO run reaches out to larger radii than in case of the GADGET simulation.

star formation and cooling prescription on the morphology of the gas disks. In the A5-slowsfr simulation, a considerably longer star formation timescale of 6.3 Gyr has been adopted (three times longer than our default), whereas the effective equation of state that pressurizes the dense star-forming gas has been kept invariant. This means that gas at a given density is more slowly depleted into stars, but that the density stratification created for a given amount of gas is not changed. We hence expect the cold gas to stay around longer before it is consumed, allowing larger gas disks to be

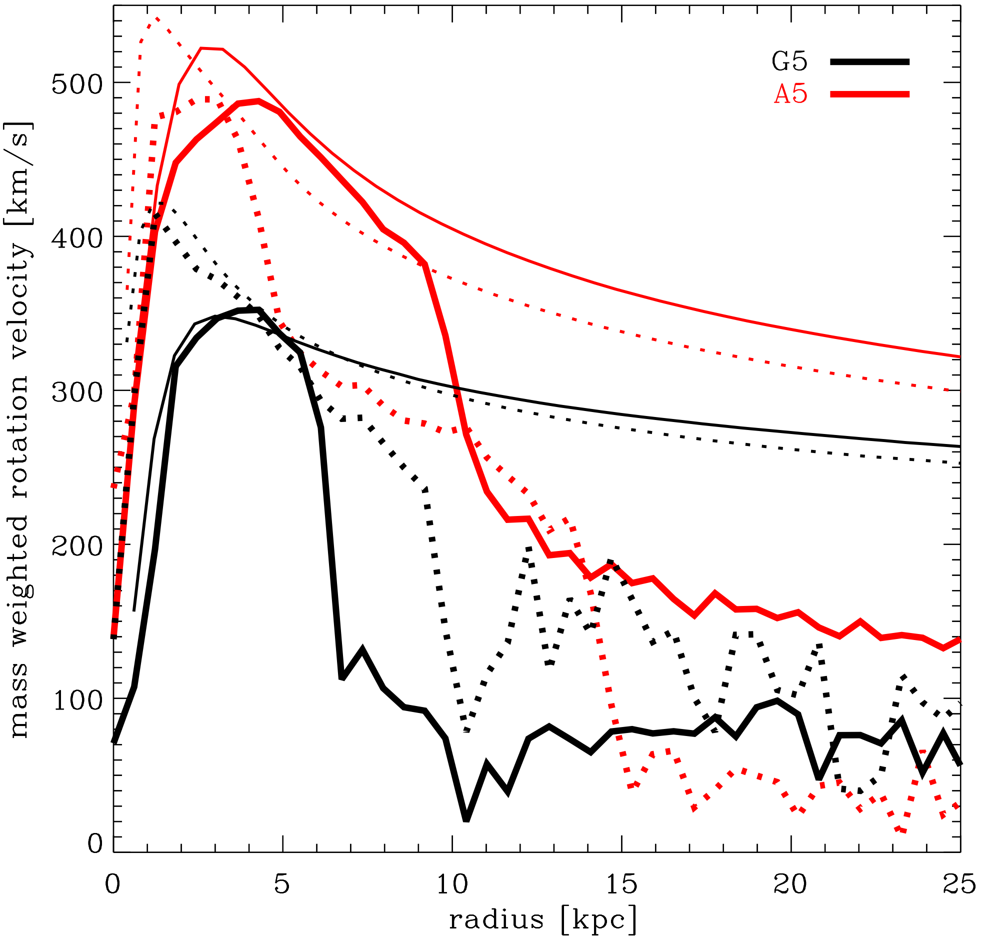

Figure 5.6: Velocity profile of the gas in the central plane of the simulated galaxy. Here we show the mass-weighted azimuthal rotation velocity within a thin cylindrical slice (4 kpc thick) centered on the galactic gas disk. Figure 5.5 shows the projected velocity field of exactly the same slice of gas. The $z = 0$ results are shown as thick solid lines, while thick dotted lines indicate $z = 1$ results, both for our default simulations with GADGET and AREPO. The thin lines show the circular velocity, $v_{\rm c}(r) \equiv \sqrt{G\,M(<r)/r}$, based on the enclosed total mass at the same radius, for comparison.

grown. This is in principle born out by a comparison of A5-slowsfr with A5. Both runs actually show a high degree of similarity despite the drastic change in the star formation timescale. As we will see, their star formation rates are in fact relatively similar, because the reduced star formation efficiency in A5-slowsfr is in part compensated by higher gas densities that are reached when the larger accumulated amount of gas contracts under self-gravity. The most significant difference between the models as far as the gas disks are concerned occurs in the aftermath of the perturbing event that strikes before $z = 0.5$. The A5-slowsfr model appears to be able to more quickly reform a sizable gas disk, perhaps simply because of the fact that more cold gas has remained available at this time.

When the threshold for star formation is increased, as in our A5-highthresh model, the gas needs to contract to considerably higher densities before it can be depleted by star formation. We thus expect the formation of thinner gaseous disks that are more susceptible to the formation of spiral patters and tidal disturbances. This is clearly evident in the fourth row of Fig. 5.1, which shows the time evolution of our A5-highthresh model. We note that a high density threshold for star-formation has recently been advocated as a primary requirement for successfully forming disk galaxies (e.g. Guedes et al., 2011). Here we confirm that this is clearly conducive for creating thin, dynamically cold gaseous disks. But as we shall see later on, this alone is not yet sufficient to induce a significant modification and improvement of the formed stellar disks.

Finally, we consider our two fiducial simulation models which aim to reduce high-redshift star formation in an ad-hoc fashion. These models are meant to investigate in a simple way to which extent this may help in improving the final disk morphologies, but we stress that these runs are not meant to be physically self-consistent models. We recall that it has long been recognized that star formation in efficiently cooling small galaxies at high redshift can be a significant problem for the hierarchical formation of large late-type galaxies. This is because the stars formed in such progenitor systems at high redshift tend to end up in galactic bulges at the present epoch, and furthermore their gaseous components may induce an angular momentum transport in galaxies, reducing their disk scale lengths. The recent *Aquila* comparison project (Scannapieco et al., 2011a) has again highlighted this connection; the models with the lowest high-redshift star formation tended to be also the ones which formed the most successful disk galaxies at low redshift.

The simulation models A5-preheat and A5-cooloff examine this behavior through two different modifications relative to A5. The run A5-preheat attempts to suppress star formation in small galaxies at high redshift by imposing a homogeneous “pre-heating” event of all the gas in the simulation to a temperature of 5×10^6 K at redshift $z = 12$. This temperature is higher than the virial temperature of many of the small galaxies forming at this redshift, hence we expect it to have a strong impact on these systems. However, we note that a sizable amount of this thermal energy is also quickly radiatively lost, and the rest is rapidly redshifting away towards lower redshifts, such that the impact of this reheating on the cooling of the assembled galaxy halo at low redshift is expected to be weak. Interestingly, the formation of a gas disk at high redshift in the progenitor halo appears indeed delayed, and only at the lowest redshift a sizable gas disk has formed. Also, the time sequence of the perturbing event that affects the galaxy in the other runs at $z = 0.5 - 1.0$ now appears to happen earlier. Connected to this one sees already at $z = 1$ signs of the formation of a ring-like gas structure roughly orthogonal to the primary disk, and also at $z = 5$ the perturbed state of the galaxy is noticeably different than in the other simulations. These differences can be understood as a consequence of the substantial modification of subhalo orbits due to their changed central gas content and concentration. Unfortunately, due to the perturbing events in the assembly of the Aq-C halo, the simple reheating scenario does not succeed in forming a nice unperturbed gas disk at low redshift. It appears however that after the last significant perturbation has eventually taken place, a large gas disk can again reform by $z = 0$.

Finally, the model A5-cooloff features a rather drastic modification of the radiative cooling history. Here the cooling has simply been disabled until $z = 2.5$, thus preventing by construction the condensation of cold gas and star formation in all galaxies at high redshift. Immediately after cooling is allowed, a large gas disk forms inside out in the halo, as is clearly seen in the panels corresponding to $z = 2$, $z = 1.5$ and $z = 1$. Also, the star formation history (to be discussed later on in more detail) catches up to the other simulations. However, we again observe that the gas disk is almost completely destroyed by $z = 0.5$, consistent with the A5 and G5 simulations. A small gas disk then reforms by $z = 0$, just as in our default simulation model A5.

5.3.1 Star formation histories of model galaxies

In Figure 5.2, we compare the star formation rate histories of our model galaxies A5 and G5. These measurements are constructed from the formation times of the star particles inside the virial radius of the target galaxies at redshift $z = 0$, i.e. only the star formation history of the corresponding halo and all its progenitor systems is shown. For easier interpretation, we give the result both as a log-plot as a function of redshift, and linearly as a function of lookback time such that area under the curve corresponds to the amount of stars formed.

Interestingly, the star formation history at high redshift is essentially identical for $z \geq 5$ in the SPH and moving-mesh calculations. This is consistent with the finding of Vogelsberger et al. (2011) that in cosmological simulations at high redshift the two codes reproduce the same result. This can be understood as a consequence of the fact that the gravitational growth of structure is followed extremely similarly by the codes, and because pressure forces are comparatively unimportant in the first generation of systems as they do not support quasi-stationary hydrostatic halos. However, at late times, when the progenitor halo has largely formed (its mass at $z = 5$ is $4 \times 10^{11}\,\mathrm{M}_\odot$), the AREPO-based simulation shows a considerably higher star formation rate on average, which must be fueled by a correspondingly higher cooling rate of the halo. We also see that beginning at look-back time $\sim 6\,\mathrm{Gyr}$, or $z \sim 0.66$, a sudden reduction in the SFR takes place from which only the moving-mesh calculation recovers to some extent. In the log-plot on the left, it is seen that the SPH run also suffers from a factor ~ 4 reduction in the SFR at this time, but in the moving mesh calculation this amounts temporarily even to a factor of ~ 10. But unlike the SPH calculation, the SFR recovers again from this reduction in the moving-mesh case, especially during the last 2 Gyr.

5.3.2 Growth history of halos

Interestingly, the different cooling history of the halos also reflects itself in the baryon fraction of the halos, and ultimately in the precise value of their virial masses. In Figure 5.3, the right panel compares the baryon fraction within the virial radius as a function of redshift for both the G5 and A5 simulations. The mesh-based calculation stays close to the universal baryon fraction at all times. If anything, the baryon fraction slightly increases at the lowest redshift, which can be understood as a result of the loss of pressure support in the halo due to cooling effects. In contrast, the G5 simulation actually shows a slight decline of the baryon fraction in the halo towards low redshift. This appears to be a consequence of the dissipative heating in SPH identified in Vogelsberger et al. (2011), which spuriously adds thermal energy to the halo gas, reducing the cooling rate and pushing the gas slightly outward, causing the total baryon fraction to decrease. This effect appears to be surprisingly strong in this halo.

Related to the variation of the baryon fraction is an induced small change in the total

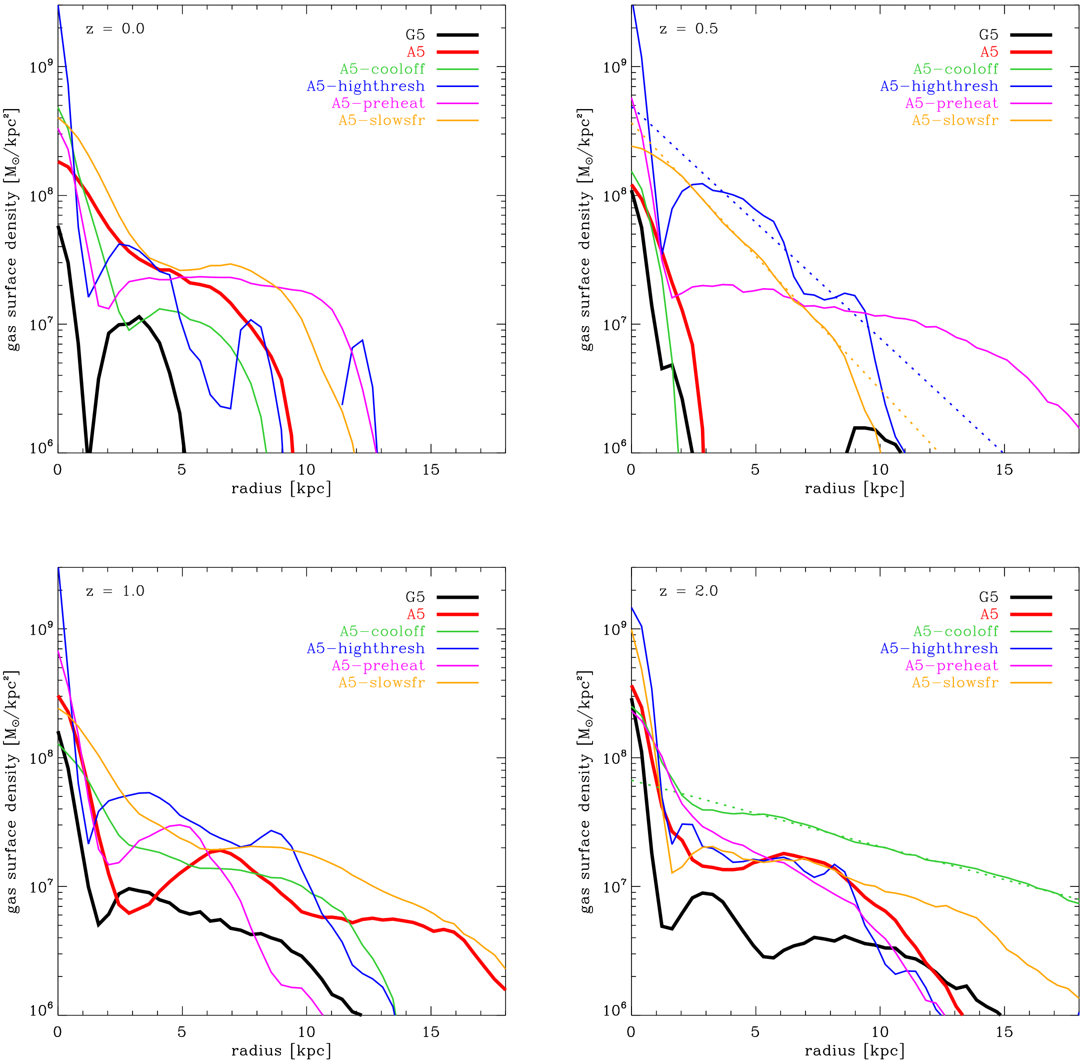

Figure 5.7: Comparison of the gaseous surface density profiles (computed in a face-on projection) of "cold gas" (gas fulfilling the star formation criterion) in our different simulations at times $z = 0$, $z = 0.5$, $z = 1$, and $z = 2$. Besides our default simulation models G5 and A5 with GADGET and AREPO, further variants of the moving-mesh calculation are included, as labelled. As can already be inferred from Fig. 5.1, the default AREPO simulation always shows a more extended gas disk than the default GADGET run. The disks are especially large in some of our variants of the moving-mesh run, notably in the case of the A5-preheating simulation. Some fits of exponential profiles mentioned in the corresponding sections of the text are included in the plots as dotted lines. All of our simulations show a concentrated gas component at the very center, particularly at late times. This is especially pronounced in the A5-hightresh model.

virial mass and virial radius of the halo. This is shown in the left panel of Fig. 5.3, which demonstrates that the final virial radius ends up slightly lower in the SPH run G5 compared with A5 due to the reduction of the baryon fraction. The strength of the effect is quantitatively consistent with what is seen in other codes when the baryon fraction deviates from the universal mean (see for example the *Aquila* study Scannapieco et al.,

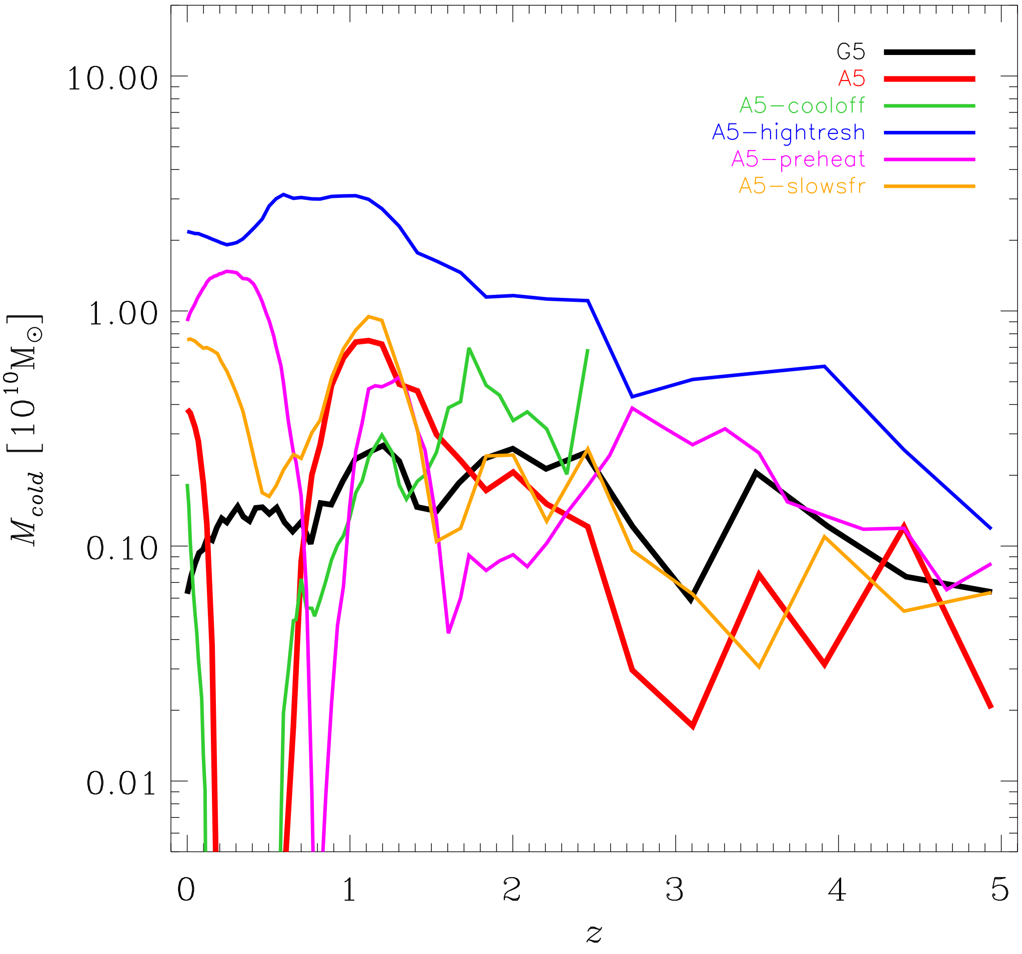

Figure 5.8: The cold gas mass within the galactic radius as a function of time. There is clear evidence for a substantial disturbance at around $z \sim 0.7$ in the majority of the runs, only the high threshold AREPO run appears comparatively resistant to this perturbation, at least when examined through this quantity.

2011a).

Apart from this gravitational influence of the baryons on the dark matter, the growth of the halos is apparently followed with very similar accuracy in both codes. One way to check this is to consider shape measurements of the halo at different redshift, and at different enclosing radii. In Figure 5.4, the left and right panels show the b/a and c/a axis ratios of the moment-of-inertia tensor of the halo mass as a function of time, where $a \geq b \geq c$ are the eigenvalues of the inertia tensor. We compare results for A5 and G5, both for the virial radius (solid) and for the 'galactic radius' (dotted), defined here as $0.1\, R_{\rm vir}$. The halo as a whole has an oblate shape, which is actually somewhat unusual as most dark matter halos have a prolate shape (Frenk et al., 1988). We note that the shape of the Milky Way halo is still somewhat unclear, with the majority of studies arguing for a nearly spherical or prolate shape (e.g Ibata et al., 2001; Law & Majewski, 2010), while some recent analysis favors a prolate shape (Banerjee & Jog, 2011). The shape of the

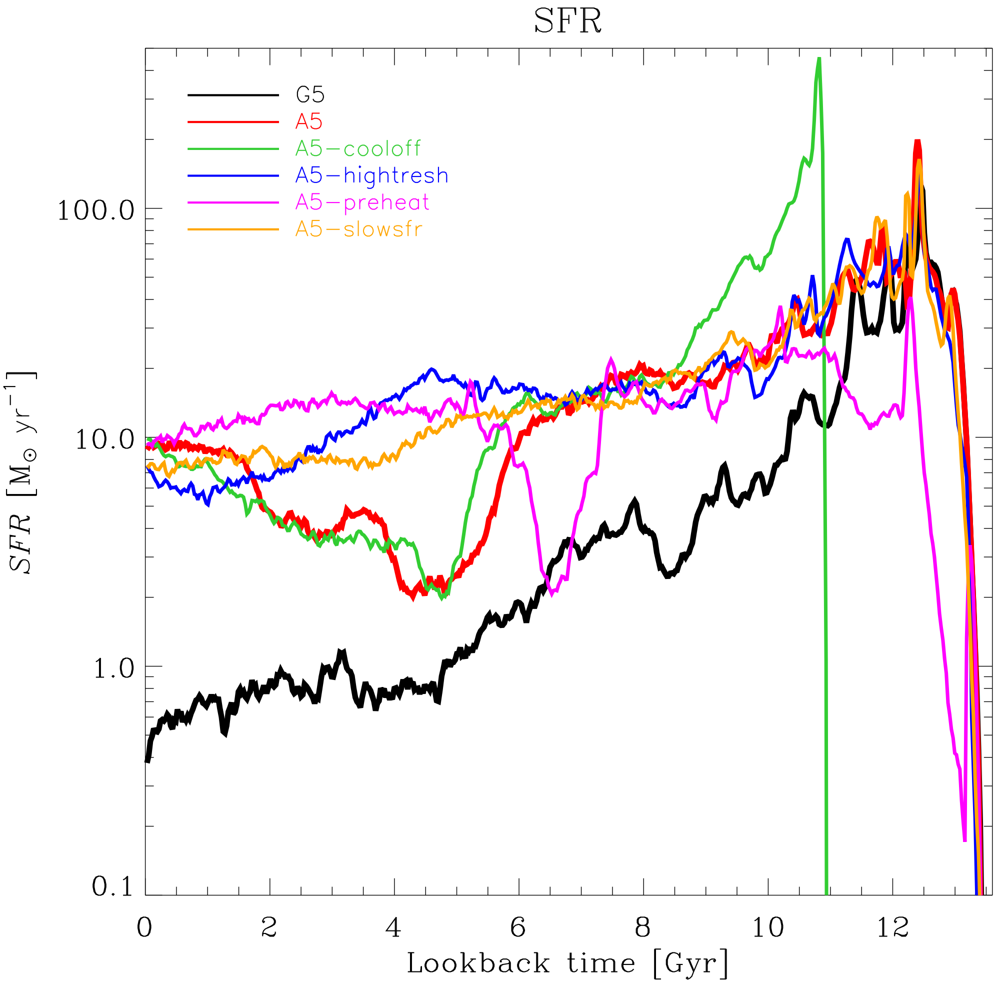

Figure 5.9: Comparison of the star formation rate history in all of our primary simulation models. We only account for the formation history of all the stars that end up in the central galaxy of the primary halo. Clearly visible is that AREPO cools considerably more gas at late times, inducing a higher star formation rate then. The star formation rate histories do also reflect the sudden drop in the cold gas mass visible in Fig. 5.8 for most of the models at low redshift. The relatively late epoch at which star formation in simulation A5-cooloff was eventually allowed appears as a strong star burst in the figure. It is also interesting to note that the A5-preheat model is very efficient in suppressing the early star burst at lookback times of ≈ 12 Gyr, where the early star formation rate is reduced by nearly a factor of 10.

halo of our simulated target galaxy becomes rounder with time, and is found to be very similar between the moving-mesh and SPH calculations at all times. The inner halo is found to be much rounder at all times, and its shape shows hardly any time variation, consistent with an early assembly of the inner mass distribution of the halo (Wang et al., 2011).

5.3.3 Kinematics of gaseous disks

In Figure 5.5, we take a closer look at the kinematics of the gas disks in AREPO and GADGET at times $z = 0$ and $z = 1$. We overplot the velocity field in a thin slice around the disk plane, with the gas density distribution color-coded underneath. It is clearly seen that at $z = 0$ the gas disk in the moving-mesh code is substantially larger, and that even gas outside of the dense disk shows significant rotational support. Evidently this gas must have also higher angular momentum content than the gas present at these distances in the corresponding SPH simulation.

At redshift $z = 1$, the situation is less clear cut, as both simulations show a less ordered velocity field with some degree of radial inflow or outflow. The moving-mesh calculation shows a prominent bisymmetric leading spiral pattern in the gas, as well as a relatively dense gaseous bar in the very center. This bar appears to have created a kind of density hole adjacent to the bar, and a gaseous ring outside of its maximum length. A similar type of behavior is seen in the SPH run, both at redshifts $z = 0$ and $z = 1$, as well as in some of the various snapshots displayed in Fig. 5.1.

The fact that the gas is indeed closely in rotational support is confirmed in Fig. 5.6, where we show the mean azimuthal streaming velocity of the gas as a function of radius in the plane of the disk. The thick lines show the measured gas velocities, and the thing lines the circular velocity based on the mass distribution in the halo. At $z = 0$, the gas in the A5 run is in centrifugal support out to nearly 10 kpc, while this is true only to about half this distance in the SPH run. The absolute circular velocities in both systems are also quite different, with the A5 run featuring extremely fast rotation in the center as a result of the more massive central stellar system that has formed there. At the higher redshift of $z = 1$, the differences are generally less strong, although also here the inner part of the A5 galaxy rotates already a lot faster than that in G5.

5.3.4 The structure of the cold gas

In Figure 5.7, we compare the projected surface mass density profiles of cold, star-forming gas in our different simulation models at four different epochs. In each case, the gas disks were oriented in a face-on orientation, and in order to slightly reduce temporal fluctuations, we averaged over two adjacent output times at the displayed redshifts. The profiles provide a quantitative measure of the different extent of the gas disks seen in the projected maps of Fig. 5.1.

An interpretation of the profiles is arguably easiest at redshift $z = 2$. Here the A5-cooloff simulation shows a clean exponential gas disk profile with a quite large scale length of 8.4 kpc. In comparison, the run with slow star formation threshold and the default A5 run show a similar exponential scale length, but a reduced surface density, and a somewhat faster decline at very large radii, $r > 10$ kpc. It is here particularly interesting that the A5, A5-slowsfr, and A5-highthres runs are quite close to each other out to $r = 10$ kpc. The preheating run A5-preheat is also similar over this range, although some of its gas appears to have been reshuffled to smaller radii. The SPH-based G5 simulation on the other hand has a considerably lower gas surface density at $z = 2$ over most of the disk, and this difference persists or becomes even larger at later times. The disk scale length of G5 at $z = 2$ is nearly as large as that of the mesh-based simulations, if one is willing to ignore the quite large fluctuations in G5's surface density at radii of a

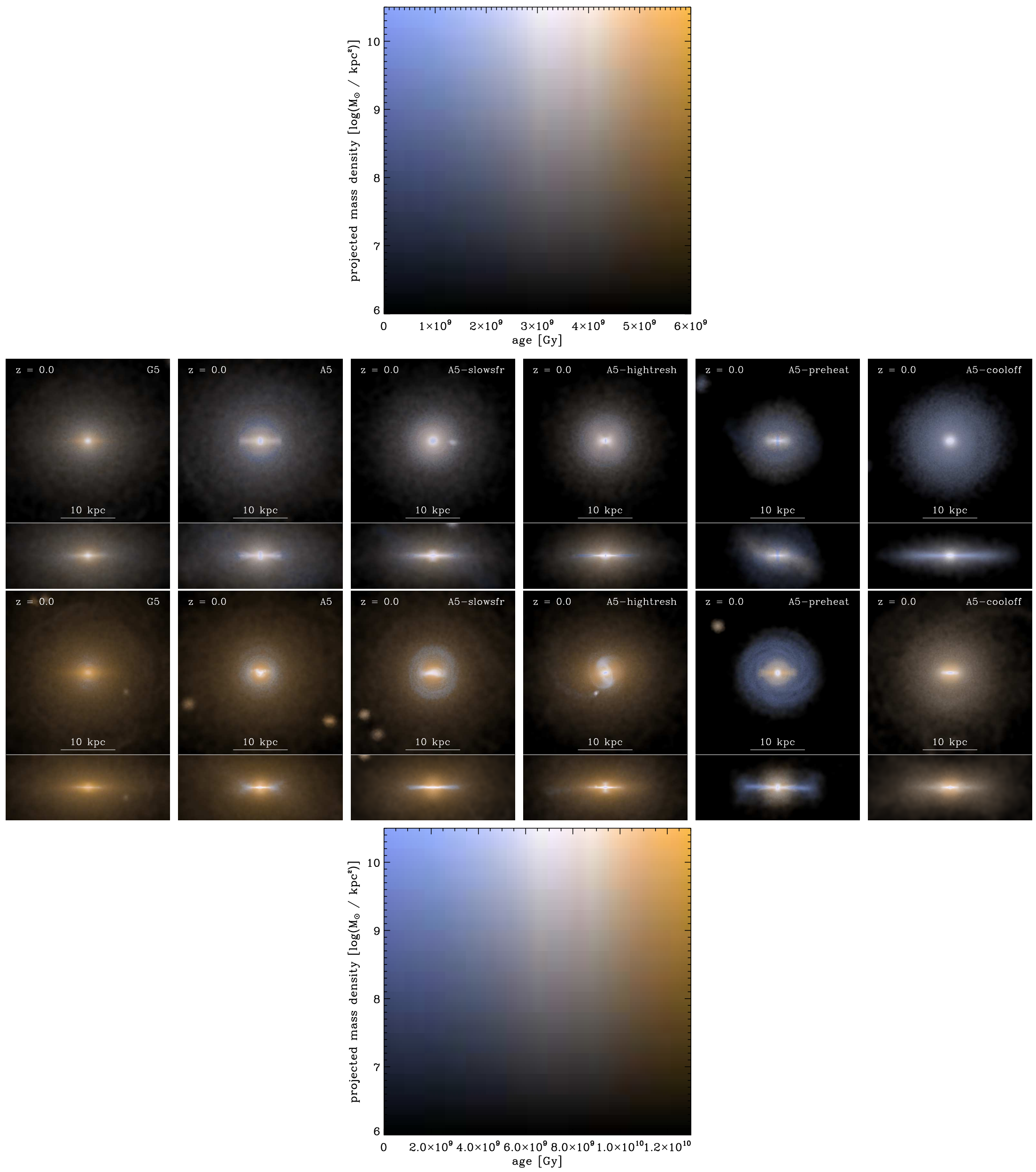

Figure 5.10: Projected stellar mass maps at redshifts $z = 1$ (top row) and $z = 0$ (bottom row), for GADGET and for AREPO runs carried out with different parameters for the subresolution model, or modifications of the cooling/heating history, as labeled. The hue and intensity values are determinded using the mass weighted stellar age and the projected mass density corresponding color-maps shown above or below the rows of plots, respectively. All panels give the stellar component both in a face-on and an edge-on projection. The color scale is logarithmic in the surface density, as shown in the color-maps. The size of the projected maps is 30 kpc × 30 kpc for the face-on maps and 30 kpc × 12 kpc for the edge-on maps. The depth of the projected volume is 30 kpc in both cases. Especially the bottom row shows that the disc component of our simulated galaxies is built up at late times from young stars, as expected.

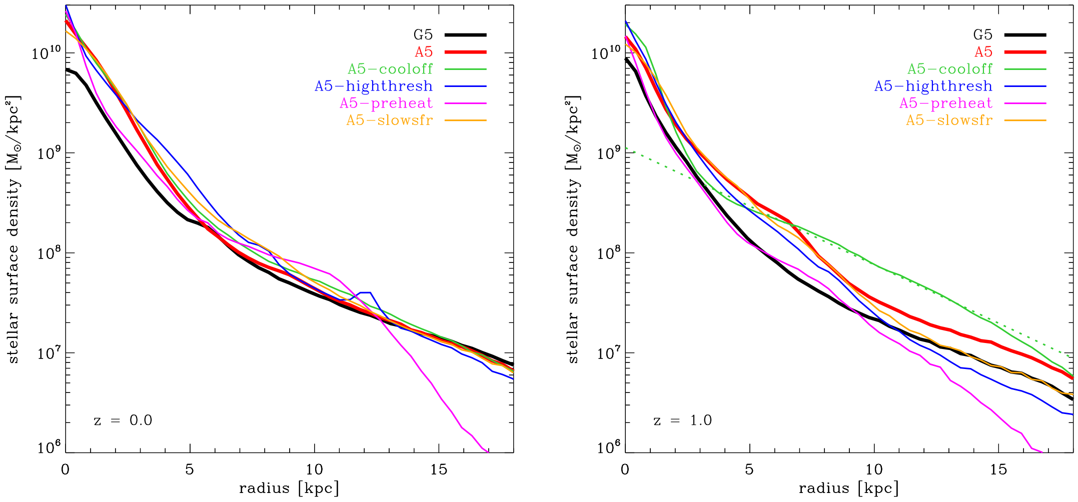

Figure 5.11: Surface density profiles of all stars at two different redshifts, $z = 1$ and $z = 0$, for our different simulation models. Comparing the lines at $z = 1$ and $z = 0$, we see that there are nearly no new stars formed in case of the G5 simulation. On the other hand, comparison of the lines corresponding to the AREPO simulations indicates that the stellar mass of these galaxies still increases with time, especially at radii between 2 kpc and 10 kpc, i.e. in the region of the stellar disk. The dotted line indicates the fit of an exponential profile mentioned in the corresponding section of the text.

few kpc. A ‘ring-like’ feature at $r \sim 3\,\mathrm{kpc}$ is quite strong in this simulation, but similar features also appear in the mesh-based simulations by redshift $z = 1$. It appears as if this is related to the formation of a central bar-like structure that accumulates gas in a central concentration of gas, which is seen in all the simulations at the four displayed epochs.

The trend of a more massive and more extended gas disk in the mesh-based runs relative to the SPH simulation becomes more apparent at redshift $z = 1$, whereas at $z = 0.5$ the disks are almost completely gone in most of the runs, which is triggered by a strong perturbation just before this output time. Only in the A5-preheat run this actually already happens earlier, slightly before $z = 1$, as evidenced by the signs of a strong perturbation already at this time. This also explains why the A5-preheat run managed to regrow an extended gas disk already by $z = 0.5$. Interestingly, it appears that the A5-slowsfr and A5-highthresh runs manage to more quickly recover at $z = 0.5$ from the perturbation, showing a regrown disk with a small scale-length of 2.1 kpc and 2.9 kpc, respectively. By $z = 0$, all the mesh-based simulations show a central gas density spike, surrounded by gas disks of approximately constant surface density that are truncated sharply at radii between 7 to 12 kpc. In the SPH run in comparison, there is not much of a disk to begin with, only a kind of circumnuclear ring of gas with radius $\sim 3\,\mathrm{kpc}$, surrounding again a central gas concentration, which contains considerably less gas than in the mesh-based simulations.

Another view on the disk evolution is provided by the total cold gas mass in the galactic radius (defined as $0.1\,R_{\mathrm{vir}}$) as a function of time, which is shown in Figure 5.8. The comparison clearly shows that the largest amount of cold gas at any given time

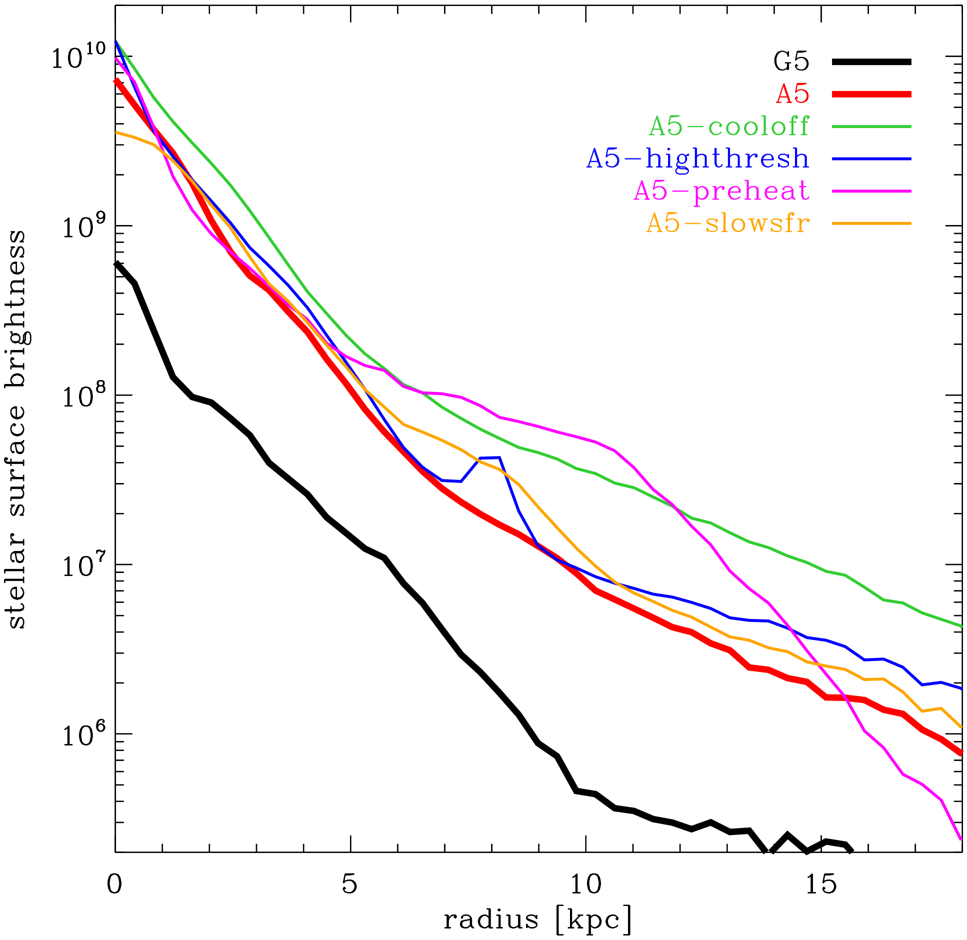

Figure 5.12: Surface brightness profile of young stars in our simulation models. Here we plot the U-band surface brightness of young stars (age $<$ 8 Gyr) calculated from a face-on projection, see the bottom row in Fig. 5.10 for the corresponding surface density maps. We find a bright central bulge in essentially all of our simulations. The run A5-slowSFR is a bit of an exception as we here see from Fig. 5.10 that the central component clearly resembles a bar more closely than a spherical bulge. It is worth noticing that simulation A5-preheat shows a nice distinction between the central bar and the disk component, with a really flat luminosity profile for the latter.

is present in the A5-highthresh simulation, demonstrating that a good fraction of the gas in this run must lies at densities below the star-formation threshold imposed in this simulation, thereby escaping consumption by star formation. It is interesting that the A5-slowsfr run does not result in an equally strong effect; while also here more gas accumulates at redshifts $z > 2$ due to the delayed star formation timescale, the difference to A5 eventually nearly vanishes once the age of the universe reaches of order the star formation timescale. But the difference reappear at some level after the strong disturbing event at $z \sim 0.7$, which can be clearly identified in the plot as a sudden and rapid decline of the cold gas. All the simulations show such strong decline in the cold gas beginning

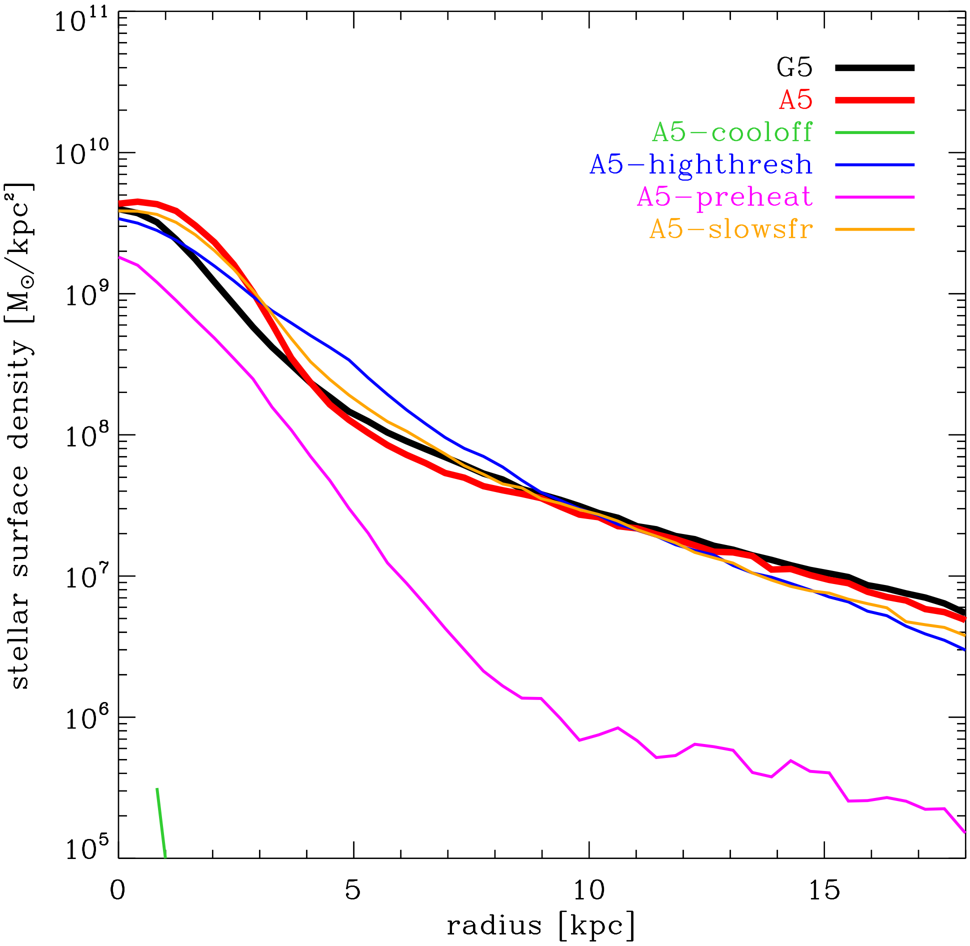

Figure 5.13: Surface mass density profiles of old stars. In these measurements, we only include old stars (> 8 Gyr) as a proxy for the stellar bulge and halo components. We notice that the central bulge of our AREPO simulations seems to be more extended than in the case of our GADGET simulation. This figure also clearly shows that changing the density threshold for star formation, or the star formation timescale, had nearly no effect on the bulge/halo components. However, quite a significant change in the bulge/halo component occurs in our A5-preheat simulation. Despite reaching a similar central density, the profile falls off much quicker with radius than in any other case. This is also seen in Fig. 5.10 where only simulation A5-preheat shows a nice, thin disk in the edge-on projection while in all other simulations the extended stellar halo dominates over the stellar disk.

at around $z \sim 1$. We note however that this event happens somewhat earlier in the A5-preheat run, consistent with our earlier observations, and in this simulation the cold gas mass also recovers earlier than in the other runs. Interestingly, the cold gas mass recovers in all the simulations *except* for the SPH run.

The influence of the substantial perturbation in the low-redshift galaxy evolution is also clearly evident in the SFR histories, which we now compare in Figure 5.9 for all our primary simulations. Here the A5-preheat simulation exhibits the drop already at

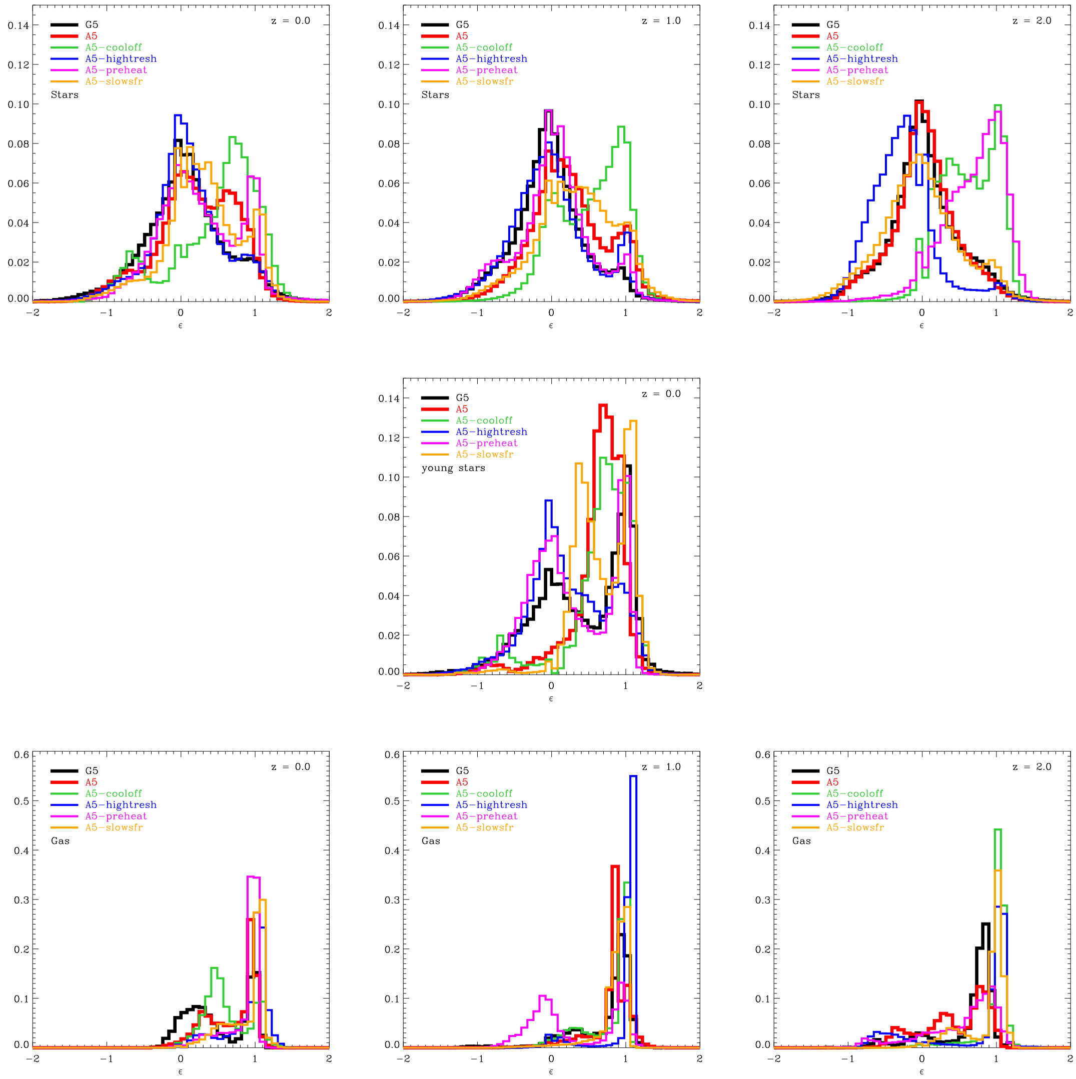

Figure 5.14: Circularity distribution of stars at redshifts $z = 2$, 1, and 0 (top panels) for all of our primary simulation models. The circularity ϵ of a star particle is here defined as $\epsilon = j/j_{\rm circ}$ where j is the actual specific angular momentum of the particle and $j_{\rm circ}$ is the specific angular momentum of a circular orbit at the same radial distance. The central panel shows the circularity distribution for young stars ($< 8\,$Gyr), whereas the panels in the bottom row show the distribution of ϵ for the gas component at the epochs $z = 2$, 1, and 0. Stars in a spheroidal bulge populate unordered orbits and are thus showing up as a broad, symmetric distribution around $\epsilon = 0$ in this plot, while disk stars on nearly circular orbits should form a rather narrow distribution around $\epsilon = 1$. The results hence quantify our visual finding of a nice, thin disk component in the case of the A5-preheat simulation and the presence of only comparatively anemic disk components in the other simulations. It is also clear based on the circularity distributions that the thin disk component builds up at relatively late times.

lookback time $t = 8\,$Gyr, while A5, A5-cooloff and G5 show it at $t = 6\,$Gyr. Runs A5-highthresh and A5-slowsfr also show a decline of the SFR at about this time, but the effect is much weaker. Another interesting observation to make about Fig. 5.9 is that

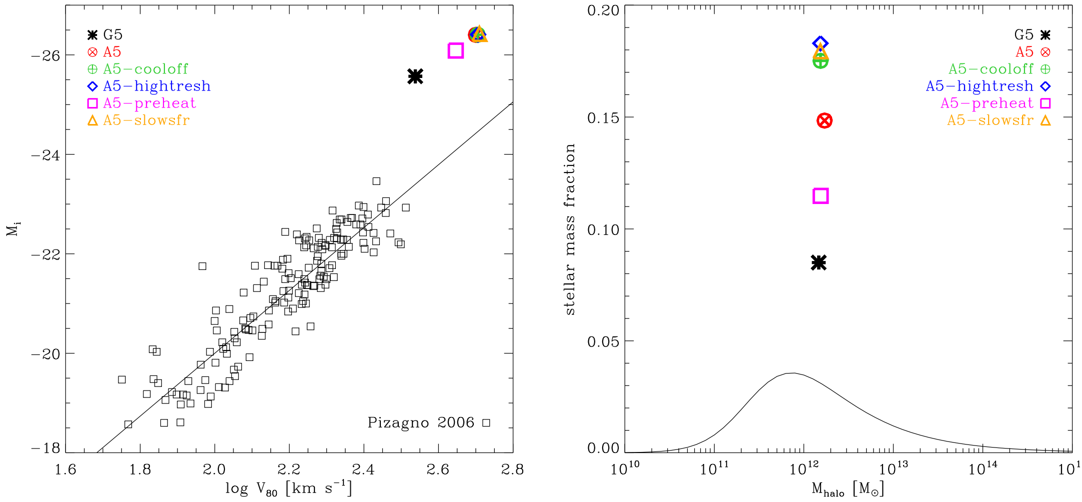

Figure 5.15: *Left panel:* Comparison of the I-Band Tully Fisher relation of observed galaxies (based on Pizagno, 2006) with the properties of our simulated galaxies. As largely expected because of their huge stellar mass, our simulated galaxies are all significantly too bright while having a too high circular velocity as well. We note that both defects are interrelated; the rotation velocities are excessively high due to an overly massive, centrally concentrated bulge. If the formation of these stars can be successfully suppressed by stronger feedback processes, model galaxies should have much less of a problem to end up on top of the observed Tully Fisher relation. *Right panel:* Comparison of the stellar mass in our simulated galaxies with expectations based on abundance matching of the ΛCDM halos mass function and the observed SDSS stellar mass function (Guo et al., 2010). Here we again find that the stellar content of our galaxies exceeds the amount required in halos of this mass for consistency of observations with the ΛCDM cosmology by a large factor.

the A5-cooloff simulation produces a strong surge of star formation immediately after cooling is enabled in this simulation, but then the star formation rate rather quickly joins on to the result obtained for A5, creating essentially no change in the total stellar mass formed by the present epoch.

5.4 Stellar mass mass distribution of the simulated galaxies

In Figure 5.10, we show maps of the projected stellar mass density for our primary simulation runs. Similar to Fig. 5.1, we show face-on and edge-on projections, but here we restrict ourselves to redshifts $z = 1$ (top row) and $z = 0$ (bottom row). The hue and intensity values of each pixel are determined with respect to the mass weighted stellar age and the projected mass density following the color maps shown above and below the rows of plots, respectively.

At $z = 1$, shown in the top row, it is evident that the stellar disk-component is more pronounced in all the mesh-based calculations compared with G5. However, *all* the simulations feature a relative strong bulge component as well. Particularly in the A5-highthresh and A5-preheating runs, a stellar bar component is visible too.

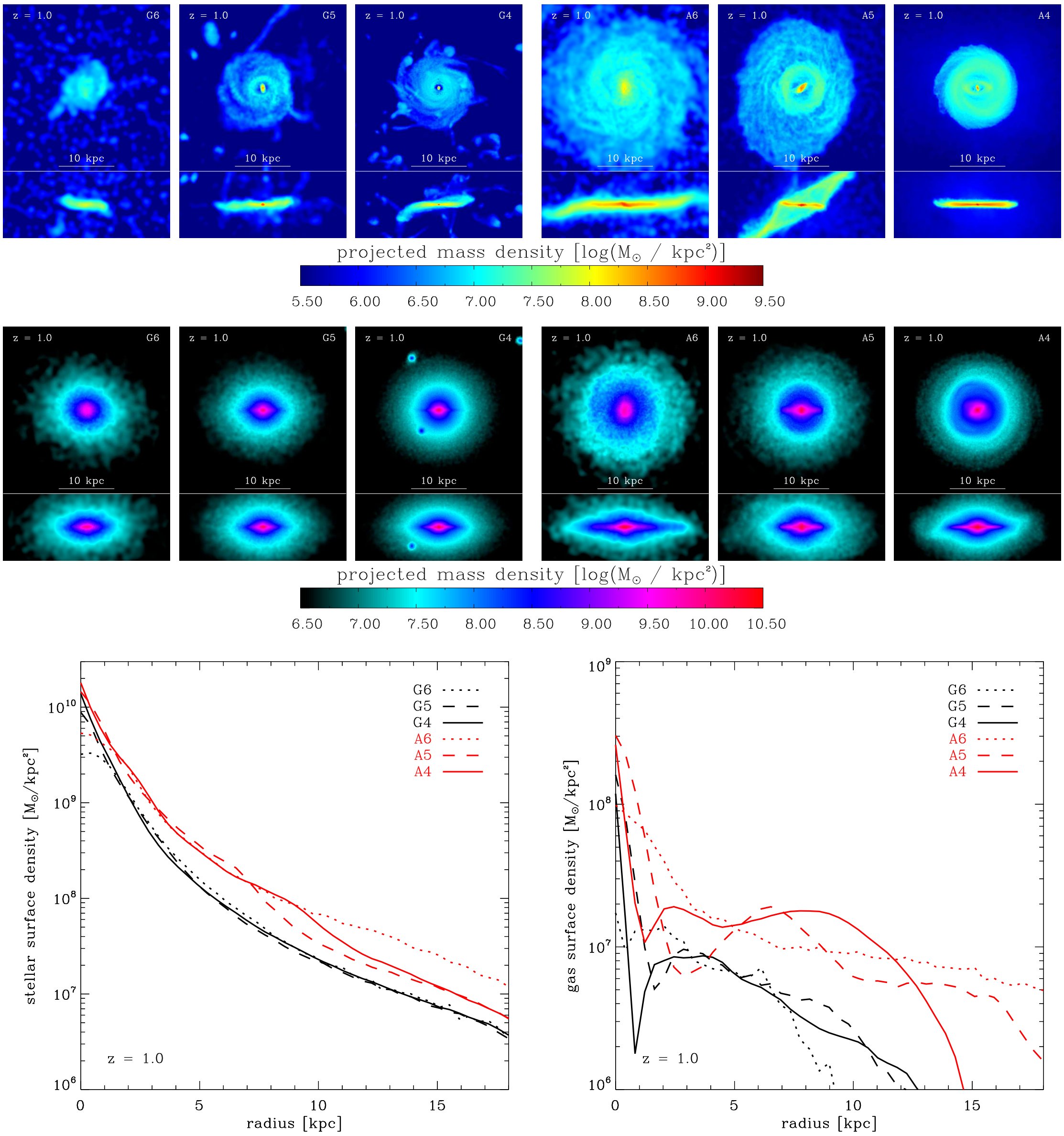

Figure 5.16: Resolution comparison of our default simulation model using the GADGET and AREPO codes. In the top row, we show projected gas maps st $z = 1$ of our GADGET and AREPO runs at different resolutions, spanning a factor of 64 in mass resolution and a factor 4 in spatial resolution. In the second row, we plot the corresponding stellar density maps. Unsurprisingly, simulations calculated with higher spatial resolution are able to resolve finer details and are producing somewhat thinner stellar and gaseous disks. However, changing the hydrodynamical solver has a more pronounced effect than changing the spatial resolution of either the SPH or moving-mesh runs. At the same time, the results for either code are quite robust when the resolution is changed, which is quantitatively demonstrated by the surface density profiles of stellar and gaseous mass shown in the bottom two panels. We thus argue that while improving the resolution is clearly helpful to form more realistic disk galaxies, this alone is unlikely to resolve the disk formation puzzle. Rather, a combination of an adequate model for star formation and feedback physics, an accurate treatment of hydrodynamics, and sufficient numerical resolution is required to accomplish this task.

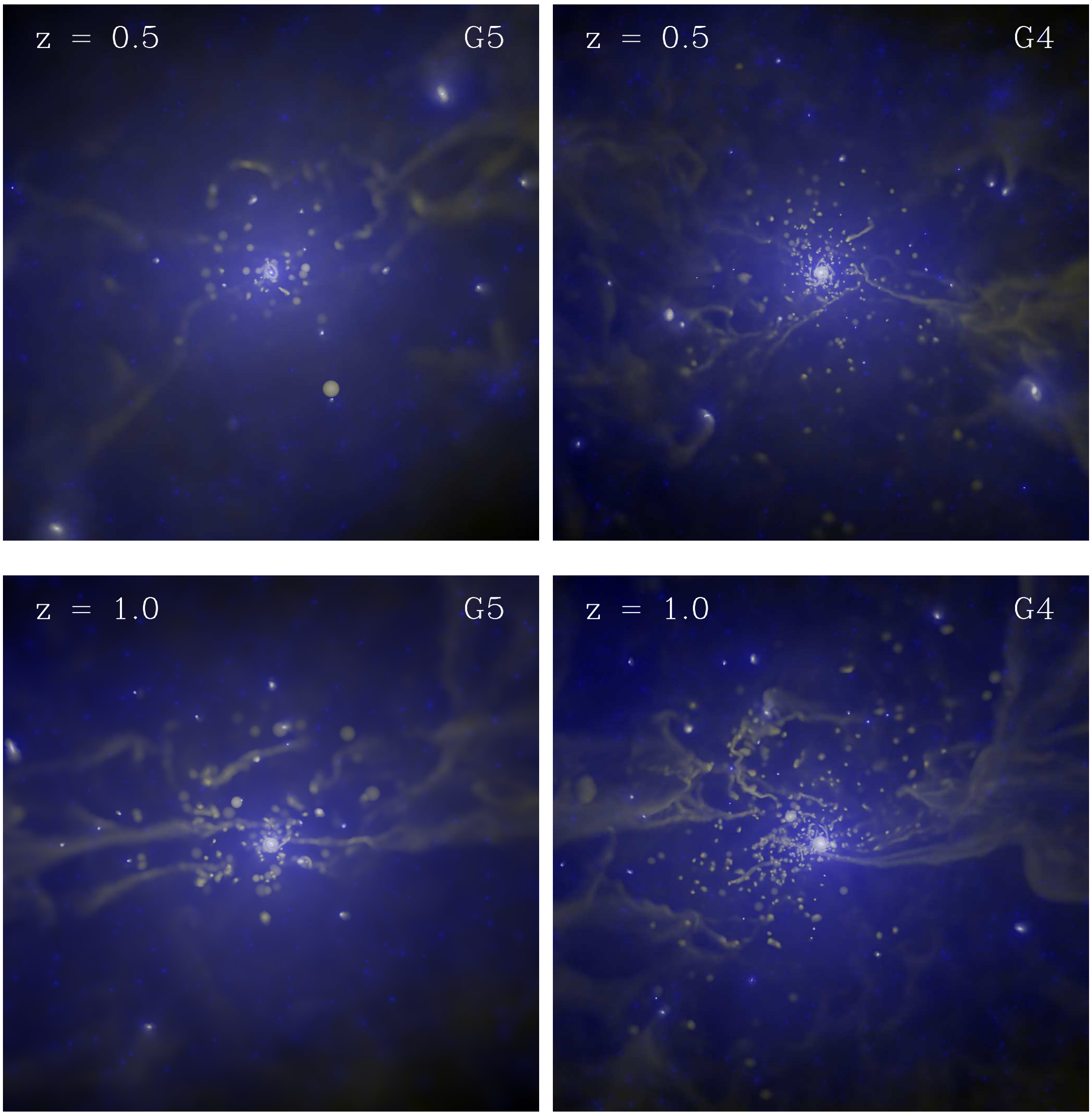

Figure 5.17: Cold gas clumps in the halo of our simulated galaxy in the G4 and G5 simulations. Here we plot the projected distribution of gas, weighted with ρ^2 in yellow, overlaid with the dark matter density in blue. Dense clumps of gas hence appear as yellow spots while the dark matter component of satellite galaxies appear as white spots. The sidelength of the projected cube is 1 Mpc. It is immediately obvious that the SPH runs shown here at $z = 1$ and $z = 0.5$ (as labeled) tend to form many dense gas clouds and filaments around the central object. With increasing resolution, the number of these object increases due to the higher mass resolution.

At the present epoch, displayed in the bottom row, the bulge-dominance of the galaxies has become even stronger, except for the A5-preheating run, which suffers earlier from the later-time perturbation and has had hence more time to regrow a nice disk towards the present time. This is also evident when the young stars (bluish colors)in the bottom row are considered. These are generally arranged in a clear disk component, but with an additional central nucleus of young stars, which invariable are produced out of the "gas spike" at the center seen in Fig. 5.7. Forming a pure exponential disk of young stars may

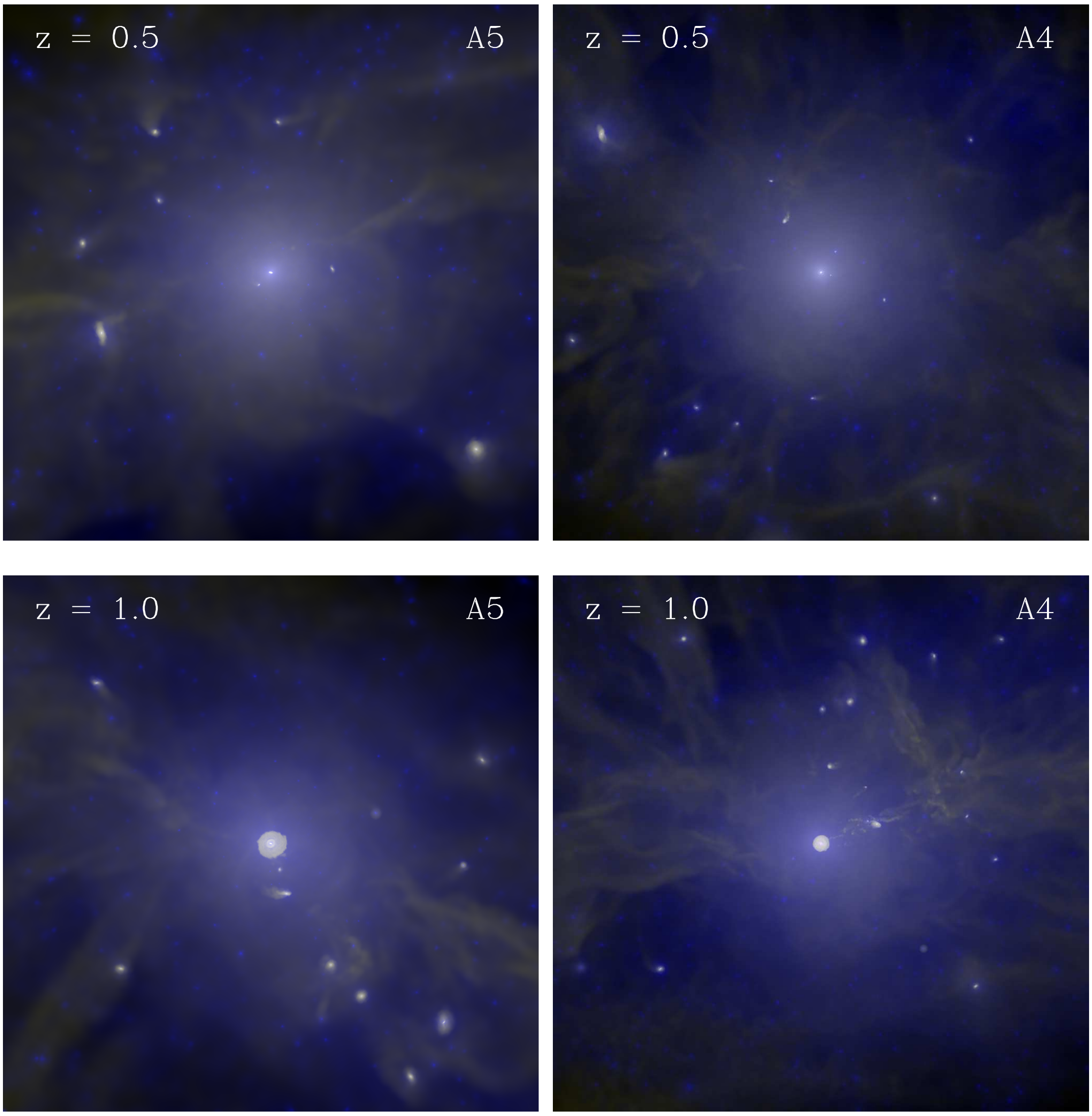

Figure 5.18: Same as figure 5.17, but for the A4 and A5 simulations based on AREPO. In contrast to the SPH results, the moving-mesh code produces a much smoother gaseous halo with hardly any dense gas clouds. The only gas concentrations in the halo of the galaxy are associated with dark matter substructures, so these objects represent small satellite galaxies of the central object.

hence require feedback processes that efficiently remove the low-angular momentum gas that ends up in this central gas concentration. The young star distributions also show evidence for strong bars present in some of the stellar systems at late times, particularly in the A5-cooloff run, but also in A5, A5-slowsfr and even in G5. The SPH run has clearly the smallest disk of young stars, consistent with the relatively low cooling efficiency and star formation rate at late times in this simulation.

In Figure 5.11, we compare the corresponding stellar surface density profiles of these runs, both at redshifts $z = 0$ and $z = 1$. The profiles are strongly dominated by a spheroidal component, which tends to hide the disk component for the most part. Only in the A5-cooloff run, a disk component of scale-length 3.7 kpc can be clearly identified. One may in fact decompose the profiles into a Sersic profile that matches the spheroidal component, and an exponential profile for the outer parts. A decomposition of the profile in terms of these two components is not robust in all cases, however, and the involved degeneracies make it unreliable in our simulations to estimate the disk and bulge masses through a simple profile decomposition.

The surface mass density profiles of the young stars shown in Figure 5.12 emphasize the large difference between the mesh-based calculations and the G5 run. The central, newly formed 'bulge-star' component that dominates in the inner 4 kpc is nearly identical in all the mesh-based simulations, only in the outer disk larger differences are found. Here the A5-preheat makes the biggest disk, with a truncation radius at 11 kpc, whereas the disk components of the other models have a lower surface density. In comparison, the G5 simulation produces a disk with a smaller scale length and a much smaller surface density.

It is also interesting to consider the surface density profiles of the old stars in turn, which are shown in Figure 5.13. These stars are all older than 8 Gyr, hence they form the complement to the sample just discussed. We clearly see that the old stars are very similarly distributed in all the simulations, except for the A5-preheat and A5-cooloff runs, which are the models that have implemented ad-hoc approaches to prevent high-redshift star formation. In fact, in A5-cooloff, only very few stars have formed by this time, and in A5-preheat, a very significant reduction is present as well. What is remarkable however about Figure 5.13 is that the distribution of old stars is so similar in all the simulations today. This is because both the integrated high-redshift star formation is very similar between the runs (including the SPH run in this case), and the stars are scattered similarly in phase-space in the merging processes that accompany the assembly of the galaxy.

5.4.1 Kinematic disk and bulge components

A kinematic decomposition of the stars in the simulated galaxy is shown in Figure 5.14, at redshifts $z = 2$, 1, and 0, as well as separately just for the young stars that were shown in Fig. 5.12. We analyze the distribution of ϵ defined as the ratio

$$\epsilon = \frac{j_z}{j_{\rm circ}}, \tag{5.1}$$

where j_z is the actual angular momentum of a star particle, and $j_{\rm circ}$ is the angular momentum of a circular orbit at the same radial distance. A razor-thin stellar disk should show up as a narrow distribution around $\epsilon = 1$ in this quantity, whereas a spherical, non-rotating bugle is expected to produce a symmetric and broad distribution around $\epsilon = 0$.

Clearly, most of our simulated galaxies shown in Fig. 5.14 have strongly dominating bulge components at the three redshifts analyzed. Only at $z = 2$, the A5-preheat and A5-cooloff simulations are clearly dominated by disk components. Interestingly this remains true for the A5-cooloff run even down to redshift $z = 0$, despite the fact that this model does not necessarily show the visually most convincing gas disk. The A5-preheating model's disk appears in part to be lost at $z = 1$, likely related to the perturbation that hits the system at about this time, and aided by a formed stellar bar. Because the A5-

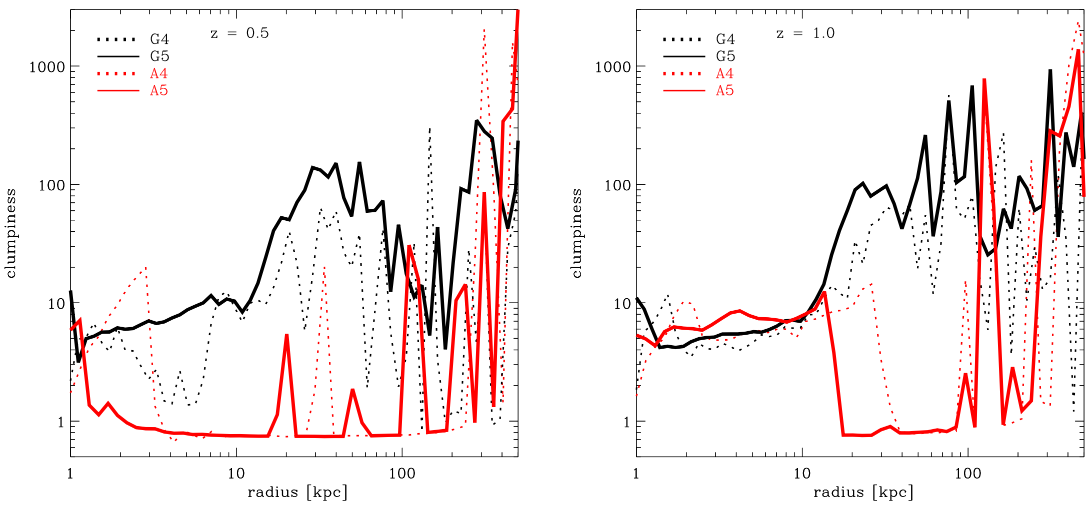

Figure 5.19: Radial profiles of the gas clumping factor in our default simulation models, simulated at resolution levels 4 and 5 with the GADGET and AREPO codes. We compare the results both at redshifts $z = 0.5$ (left panel) and $z = 1$ (right panel). Clearly evident is the much higher clumping of the gas in the SPH run between the virial radius and the edge for the star-forming phase.

cooloff run is affected by the satellite perturbation at an earlier time, it has managed to regrow a strong disk component already at $z = 1$. The other mesh-based simulations appear to be on route to achieve the same, with the A5-highthresh and A5-preheat runs lagging somewhat behind. The G5 run's disk component in the young stars at $z = 0$ is actually of similar relative strength, but the total stellar mass in it is considerably lower. Overall, we find that the two simulation runs that aggressively tried to prevent high-redshift star formation produce indeed the highest disk-to-bulge ratios at low redshifts, confirming the trend also identified in the *Aquila* project for other simulation codes and entirely different feedback recipes. The key for a successful galaxy morphology therefore appears to lie primarily in suppressing early star formation in favor of sufficiently strong late time star formation. The star formation threshold itself appears to just have a confounding influence on this basic connection.

In the bottom three panels of Figure 5.14, we show the corresponding ϵ distributions of the cold gas in the galaxies at redshifts $z = 2$, 1 and 0. As expected, the gas is in centrifugal equilibrium for the most part. At $z = 1$, there is a sizable amount of gas with little rotation in the A5-preheat run, presumably created by the same process responsible for the destruction of most of the disk at that redshift. Also, at $z = 0$, about half the cold gas in the SPH run shows insufficient rotation to be in the disk; this gas will hence produce further bulge stars. The A5-cooloff run also shows a disk-like component in the gas which lies at $\epsilon \sim 0.5$. This might be caused by problems to properly align the gas disk in the somewhat disturbed system; visually it looks as if there are two gaseous disks that are tilted relative to each other.

5.4.2 Comparison with observational constraints

All our simulations are based on a "minimum" feedback model that just regulates the conversion of cold gas to stars in accordance with the observed Kennicutt relation for today's late type galaxies. This model is not expected to produce a significant loss of baryons from the system through galactic winds, which is also confirmed by our measurements of the baryonic fraction as a function of time shown in Fig. 5.3. As is well known, we expect an overproduction of stars under such circumstances due to the intrinsically efficient radiative cooling of gas in dark matter halos.

In the left panel of Figure 5.15, we compare our simulated galaxies to data for the I-band Tully Fisher relation in order to investigate the size of the resulting discrepancy between our simulations and the data. We find that the model galaxies have an extremely large circular velocity that lies in fact essentially outside the range observed for ordinary late-type galaxies. This is primarily a consequence of the overly massive and highly concentrated stellar bulges that form in all our runs. Related to this, our galaxies are also too bright; they in fact also exceed the observed range of I-band luminosity in the plotted Tully Fisher data. The simulated galaxies are hence seriously discrepant compared to the observed galaxy population.

Another way to look at the stellar mass problem is to compare the stellar mass predicted by the simulations to the expected stellar mass based on the abundance matching analysis carried out by Guo et al. (2010), as shown in the right panel of Fig. 5.15. Under the assumption of a monotonic increase of stellar mass with halo mass, the abundance matching technique determines the expected stellar mass required for a given halo mass if the halo population of ΛCDM is supposed to match the observed stellar mass function of the SDSS. Our simulations overproduce the stellar mass expected in halos of Milky Way size by about a factor 3-4. This clearly shows that much stronger feedback processes than included in our models are crucial for having any chance to reproduce the observed luminosity density of the Universe, as well as the structural properties of individual galaxies. We note however that even in simulations that have tried to include such strong feedback it remains a serious challenge to reduce the stellar mass to the low values that appear required based on the abundance matching argument. This is true both on the scale of large galaxies (Guo et al., 2010) as well as for dwarf systems (Sawala et al., 2011). It seems however still possible that sufficiently strong feedback can reconcile the simulated galaxies with the Tully-Fisher relation, similar to the success in this regard achieved by Guedes et al. (2011).

5.5 Convergence and global differences

5.5.1 Resolution study

In Figure 5.16, we compare runs of our default physics model with the AREPO and GADGET codes at different numerical resolutions, corresponding to 'level-6', 'level-5' and 'level-4' Aquarius resolution. In the latter case, the models have a mass resolution of 0.05×10^6 $\mathrm{M}_\odot$ in the gas, corresponding to of nearly 5 million resolution elements in the halo. The A6 and G6 simulations on the other hand are lower in resolution by a factor 8 compared to our default level-5 runs. We note that the level-4 runs included here are of considerably higher resolution than the level-5 and level-6 resolutions employed in the studies of Scannapieco et al. (2009, 2011b) of the whole set of Aquarius systems, as well as in the *Aquila* project (Scannapieco et al., 2011a). Numerical resolution alone has sometimes been advocated as the critical component in producing well-defined disk galaxies, an aspect that we want to test here.

The panels in the top row of Figure 5.16 show gas density maps at redshift $z = 1$ of the simulations G6, G5, G4, A6, A5, and A4. The primary difference lies clearly between the SPH calculations on one hand and the moving-mesh calculations on the other hand, reflecting the difference in cooling and gas disk sizes between the hydrodynamical techniques that we have identified earlier. In particular, this systematic difference is much larger than any residual trend with numerical resolution. Interestingly, the moving-mesh runs appear to have a tendency to produce slightly more extended gas disks at poorer resolution, whereas this is just opposite in the case of SPH. However, these trends are not overly large, as can also be appreciated through a comparison of the gas surface density profiles, which is included in the panels at the bottom of Fig. 5.16. There can be some temporary fluctuations in these profiles, but on average they are closely reproduced by each of the two simulation codes despite drastic changes in numerical resolution. The problematic aspect, however, is that the two different simulation methods do not converge to the same result. This becomes especially clear when the stellar profiles are considered. Both the stellar surface density maps and the surface density profiles shown in Fig. 5.16 indicate a good convergence for each of the two simulation methods separately. This convergence in fact excellent in the case of SPH, but also quite good in the case of AREPO, apart from a small increase in the stellar mass at very large radius at the lowest mesh-based resolution.

We hence conclude that the problematic morphology of our simulated galaxies is not caused by inadequate resolution or gravitational softening length. Instead, the relative difference is robustly preserved over the resolution range that we could examine here. It thus appears that only much stronger feedback processes can fundamentally change this outcome.

5.5.2 Clumpy halos

Finally, we want to highlight another interesting difference between the different simulation methodologies, which may well have something to do with the large cooling difference that we identified. In Figure 5.17, we show the gaseous halos in the G4 and G5 simulations based on GADGET, at redshifts $z = 1$ and $z = 0.5$. In the images, the gas has been weighted by ρ^2 in order to more clearly highlight dense gas concentrations. It is seen that the inner halo of the SPH simulations is populated by a multitude of dense gas clumps. The higher resolution G4 run shows clearly more of the clumps, and they also appear to be somewhat smaller, which presumably simply reflect its better mass resolution. The gas distribution in the halos is reminiscent of the clumps found by Kaufmann et al. (2006) in their simulations of cooling flows in an isolated disk galaxy forming inside out. In particular, they suggested that these clumps are formed by a thermal instability in the hot halo gas, but it has remained an open issue whether numerical effects are also at play in creating this phenomenon (see for example Rice et al., 2011).

In Figure 5.18, we show the corresponding projections for the A4 and A5 simulations, for comparison. Interestingly, here the clumps are largely absent. The much smaller number of still visible gaseous substructures are associated with real dark matter subhalos, and are hence qualitatively different from the clumps found in the SPH simulation. A more quantitative assessment of this difference is given in Figure 5.19, where we compare measurements for the clumping factor of the gas as a function of radius for the two simulation types, both at $z = 1$ and $z = 0.5$. This clumping factor is here defined as

$$C \equiv \frac{\langle \rho^2 \rangle}{\langle \rho \rangle^2} = \frac{V_\mathrm{s}^{-1} \int_{V_\mathrm{s}} \rho^2 \,\mathrm{d}V}{[V_\mathrm{s}^{-1} \int_{V_\mathrm{s}} \rho \,\mathrm{d}V]^2}. \tag{5.2}$$

We measure it for the halo gas distribution in a set of narrow shells of volume V_s as a function of radius. The result in Fig. 5.19 clearly shows a substantial and significant difference between the two simulation methodologies, manifesting itself in a much higher clumping factor on average in the SPH runs compared with the moving-mesh simulations. This difference is highly significant for the diffuse gas within the virial radius, where it is also robustly reproduced in runs of different numerical resolution. For the star-forming gas at the center of the halo and outside the virial radius, no clear systematic difference is found. In the latter regime, the clumping factor is dominated by the halos and substructures in the halo infall region, which is expect to be quite similar in both simulation techniques.

The reasons for the large qualitative and quantitative difference in the diffuse gas distribution in the halo are only partially clear. On one hand, it has been shown by Sijacki et al. (2011) that gas stripping in SPH out of infalling satellites is delayed relative to mesh-codes, due to the suppression of fluid instabilities in SPH across large density discontinuities. Puchwein et al. (2010) has found that cold gas can be pushed out of satellites by ram-pressure stripping in SPH, thereafter surviving in the intracluster medium without being necessarily dispersed, sometimes even continuing to form stars – unlike in a mesh code. We suspect that this effect contributes to the clumping difference. However, in the simulations of Kaufmann et al. (2006), no substructure was present, and the SPH clumps simply formed out of the cooling halo phase. This could be caused by numerically triggering a thermal cooling instability whose growth is given an unphysical head start by the larger density noise in SPH. It will be interesting to examine this phenomenon in more detail in the future to see whether it is indeed influenced by numerical effects or rather represents the correct physical evolution.

5.6 Conclusions

In this work, we have studied high resolution hydrodynamical simulations of the formation of a Milky Way-sized galaxy. In particular, we focused on a more detailed analysis of two simulation techniques included in the recent *Aquila* comparison project of cosmological galaxy formation codes (Scannapieco et al., 2011a). The models we examine are based on the ‘minimum’ feedback model of Springel & Hernquist (2003), which encapsulates the regulation of star formation in the ISM through a simple effective equation-of-state. Due to this feature, the model is numerically well posed, and hence particularly well suited for a comparison of different numerical techniques, which is one of the primary goals of this paper. Specifically, we have compared the SPH code GADGET and the new moving-mesh code AREPO, using an identical treatment of cooling and star formation, and an identical set of initial conditions.

Using the much higher resolution possible in zoom-setups, we confirm the finding of Vogelsberger et al. (2011) and Keres et al. (2011), obtained in simulations of homogeneously sampled cosmological boxes, that there is a substantial difference in the amount of gas that cools out of virialized halos at late times. The moving-mesh simulations produce a stronger cooling flow at low redshift, yielding larger cold gas disks and in turn also larger and more massive stellar disks at the present epoch. In our SPH simulations instead, there appears to be a spurious numerical heating of some of the gas in the halo at late times, capable of not only greatly reducing the amount of gas that cools out, but even of slightly lowering the mean baryonic density enclosed in the virial radius, such that the universal baryon fraction is not quite reached anymore. Also, the inner halo of the SPH simulations is filled with dense cold clumps of gas that are not present in the moving-mesh runs. It has been suggested that these clumps might form from a thermal cooling instability, but as they are absent in the mesh-based calculations, it appears more likely that they represent a numerical artifact.

Despite the more accurate numerical treatment of the gas afforded by our moving-mesh simulations, the structure of the final galaxy formed by $z = 0$ in the selected target halo turns out to be still far from a realistic late-type spiral galaxy. The most significant defect is the much too large total stellar mass, something that is in fact aggravated by the higher cooling efficiency of the mesh-based simulation. The formed galaxy is overly luminous and rotates too fast to be compatible with observational constraints. A large fraction of the excessive stellar mass is formed at high redshift and ends up in the bulge, which in fact dominates over the disk component in most of our realizations. It is hence clear that much stronger feedback processes are required to curtail cooling and reduce star formation in halos of this size. It seems furthermore required that these feedback processes are especially effective at high redshift, such that the central bulge component is prevented from forming and galaxies with a dominating disk can be produced.

In order to test whether simple modifications of the star formation or cooling prescriptions can change the qualitative outcome of our simulations, we have carried out a number of variants of our moving-mesh run of the target halo. We considered two models where the star formation threshold or alternatively the star formation timescale was raised substantially, as both of these parameters have recently been suggested to have a major influence of the final galaxy morphology (Agertz et al., 2011; Guedes et al., 2011). However, we have here found only a weak influence of these parameters on the final galaxy morphology, and we also confirmed that our results are remarkably robust with respect to numerical resolution, which we varied by a factor of 64 in total.

In addition, we studied simulations where we modified the high-redshift cooling behavior in an ad-hoc fashion, either invoking a strong pre-heating event at $z = 12$, or disabling cooling altogether until $z = 2.5$. Interestingly, while these aggressive (and ad-hoc) measures to suppress high-redshift cooling initially led to the desired result, namely the formation of nicely disk-dominated galaxies at intermediate redshifts, this success did not last until the present epoch. This is largely due to a perturbing event at $z \sim 0.7$ in the evolution of the Aq-C halo that we have selected here, and which was also used in the *Aquila* project. Remarkably, this unfortunate satellite interaction occurs even though this particular system had originally been selected among all the *Aquarius* halos as one that looked particularly promising for making a large disk, due to its relatively quiet merger history at late times. Meanwhile it has however been pointed out that simple criteria such as a quiet merger history or a large halo spin are at best poor predictors of the ability of a halo to make a disk (e.g. Scannapieco et al., 2009), so our results can be viewed as a case in point of this conclusion. Furthermore, Aq-C itself appears as a relatively unusual outlier in semi-analytic models of galaxy formation, where this system is predicted to contain an unusually high stellar mass for the halo mass (Guo et al., 2011; Scannapieco et al., 2011a). This hence strongly cautions against drawing too strong conclusions about specific galaxy formation models from just a single realization of a forming Milky Way-sized halo.

In sum, our study has provided further evidence that the accuracy of the treatment of hydrodynamics is an important factor in determining the success of galaxy formation simulations. At the same time, this alone is not sufficient to make thin, disk-dominated galaxies in halos that cool an unusual amount of gas for their mass and in addition suffer from late-time dynamical perturbations, such as the Aq-C system. Also, our numerical experiments have shown that the successful formation of disk galaxies is unlikely to hinge on a single aspect of the parameterization of star formation, such as the density threshold or the star formation efficiency. Rather, the problem remains of challenging complexity, probably requiring further progress in the parameterization of feedback physics as well as in the accuracy and numerical resolution of the employed numerical codes. Recently, significant progress in attempts to directly simulate all relevant feedback physics on the scale of whole galaxies in isolation has been achieved (e.g. Hopkins et al., 2011), without alluding to an explicit subresolution model. It appears particularly promising to try this approach also in ultra-high resolution cosmological simulations of the formation of late-type galaxies.

6 Final conclusions and outlook

In this work, we have studied numerous simulations of the formation of a Milky Way sized galaxy starting from cosmological initial conditions. Thanks to the improvements in the available computational power and numerical algorithms, we are now able to simulate the formation of a Milky Way sized galaxy at quite high resolution at only moderate computational cost, enabling us to run several realizations of such systems with varying physical models and numerical parameters. This allows a systematic comparison of the influence of a diverse set of individual factors, giving insight into their individual importance and scope. At the same time, we are now finally able to push the resolution limit even further, unveiling also the structure and formation history of intermediate and high mass satellite galaxies orbiting around the central Milky Way-sized galaxy.

In the first part of our investigations, we have taken advantage of the high numerical resolution feasible today and carried out the first hydrodynamical simulation study of the formation and evolution of the population of satellite galaxies around a Milky Way like galaxy. Here we investigated the effects of AGN feedback, supernova driven galactic outflows and cosmic rays on the population of satellite galaxies, focusing on their luminosity function but also on their individual evolution. Not unexpected, the thermal feedback form a central supermassive black hole (AGN) seems to have no significant influence on the final population of satellite galaxies. This can largely be attributed to the fact that most of the satellite galaxies do not grow massive enough to host a sizable central supermassive black hole. Additionally, the effect of the SMBH of the central galaxy on the outer parts of the galactic halo, which is the region satellite galaxies are mostly orbiting in, is very weak. Quite in contrast to this finding, the inclusion of galactic outflows driven by SN explosions shows some quite strong effect on the satellite luminosity function as it can efficiently reduce the gas content of the most massive satellites. It thus helps to decrease the discrepancy at the high luminosity end of the observed and the simulated luminosity function, where the latter lies too high. However, at the low luminosity end, the inclusion of galactic winds turned out to have basically no effect. We caution however that we cannot exclude that this is caused in part by a too simplistic treatment of kinetic feedback in our models. An opposite effect was achieved by the inclusion of a cosmic ray model which accounted for the production of cosmic ray particles by SN explosions. The non-thermal population of high-energy protons acted as an additional pressure component with a dissipation timescale quite different from the local radiative cooling time. With this model, we were able do suppress star formation especially strongly in low mass satellites, rendering this model the most successful one in matching the faint-end of the observed satellite luminosity function. Taking these results together, we would hence expect that a combination of the kinetic feedback and the cosmic ray model provides the most promising scenario for explaining the observed satellite luminosity within the ΛCDM model.

Assuming the same surface brightness detection threshold as inferred for the SDSS survey, the number of in principle observable satellite galaxies we obtain ranges from 17 to 77 in our simulations. Compared to an extrapolated observed number of 57 when the SDSS sky covering factor is accounted for, these estimates are a great improvement compared to earlier predictions of at least several hundreds of expected satellites. The assumptions in these earlier works were based on simplified treatments of the filtering mass at the time of reionization or the time of infall, which we also compared to our findings. We detected no good evidence that any of these propositions work well. Rather, we were able to show that the detailed evolution of the individual satellite galaxy, including its gas component, its exact orbit, and its surrounding hot halo gas are key ingredients to predict the final luminosity of a satellite galaxy. Complex interactions like tidal and ram pressure stripping turned out to have very important effect on the final properties of each individual satellite.

We have then changed our focus from the satellite galaxies to the properties of the central galaxy. Here, we have first performed a large, international code comparison project (dubbed the *Aquila* project) that included 13 different codes, run by nine groups around the world. We have been responsible for the runs with the GADGET and AREPO codes, and coordinated the project in collaboration with C. Scannpieco and O. Parry. We have also been responsible for devising the common analysis programs. Our goal in this project was to present an unbiased and fair comparison of the outcome of each code. To this end, we tried to eliminate any possible variation in the assumed initial conditions as well as in the post processing by defining and distributing detailed definitions and post processing algorithms to all attendees. As a result, we are able to make sure that any identified discrepancies between the simulated galaxies exclusively reflected the individual codes and their different implementations of hydrodynamics or feedback descriptions. This led to a very comprehensive panoramic view of the most important cosmological codes applied at the present time to the problem of galaxy formation, making the study similar to the well-known Santa-Barbara cluster comparison project from a decade ago. However, the simulations considered here are much more challenging as they include physics beyond the non-radiative gas dynamics considered in the Santa Barbara cluster comparison.

Our findings in the Aquila project showed that basically all of our simulated models are suffering from an overly large stellar bulge component which is produced at very early times. They are hence in general not really satisfactory counterparts to observed galaxies as seen in SDSS and other surveys. Depending on the amount and form of feedback included in the individual simulation codes, the presence, extent and mass of the stellar disk varied enormously, ranging from basically a complete absence of a disk component to a clearly defined disk-dominated galaxy. However, even disk-dominated systems were not able to fit the observed scaling relations like the Tully-Fisher relation, and they did often not compare well with observations in terms of their current star formation rate, stellar and gaseous half mass radii or star formation efficiency.

Summarizing our extensive and systematic analysis of the simulated galaxies, we were able to conclude that all of our simulations suffer from excessive early star formation, leading to a large loss of angular momentum in the baryonic component. This causes the formation of a huge stellar bulge and halo component, hampering the later formation of an extended stellar disk. We also noted a systematic difference between particle (SPH) based and grid based (AMR, moving mesh) numerical implementations of hydrodynamical processes. We can thus conclude that a combination of strong feedback processes, especially at early times, together with a careful treatment of hydrodynamics is necessary to improve the current state of the art in forming disk galaxies. Interestingly, the differences caused by the different treatments of hydrodynamics, which were in part already noticed in the Santa-Barbara cluster comparison project, have only recently gained full attention. Our comparison study showed clear evidence that grid based methods tend to cool more gas than SPH, an important systematic difference that is ultimately caused by numerical inaccuracies. This numerically induced difference leads to higher star formation rated at later times and better conditions for forming late-type galaxies.

In order to extend these results, we started another, more focused comparison of the treatment of hydrodynamics on the one hand and different ways to suppress early star formation on the other hand. We were able to clearly confirm recent findings of another group that there are substantial differences in the amount of gas that cools out of virialized halos at late times depending on hydrodynamical technique. However, while their results were based on homogeneously sampled cosmological boxes at comparatively low resolution we could achieve much higher resolution in one particular halo through our zoom setup. This is important to make sure that the effect is not just an artifact caused by insufficient numerical resolution. The more efficient cooling leads to larger stellar and gaseous disks in the case of the mesh-based simulations. Additionally, we were able to show that the vast abundance of cold, dense gas clumps that populate the inner parts of the galactic halo in SPH-based simulations are absent in the very same halos when simulated with the mesh-based method. As the numerical treatment of cooling, star formation and feedback, as well as the gravity solver, are identical in both cases, we are led to conclude that these differences are caused by a numerical artifact of the SPH method.

Addressing the findings of earlier works and the *Aquila* project, in particular, we also investigated different methods to suppress early star formation. To this end we adopted a few simple changes in our star formation model, motivated by recent propositions in the literature. However, none of these modified simulations was able to significantly improve our results compared to our reference simulation which was based on our standard treatment of star formation. It thus appears unlikely that simple changes of the key parameters of the star formation modeling are sufficient to solve the present problems of galaxy formation simulations. In light of this finding, we also considered two artificial models especially designed to hamper or even prohibit early time star formation. These models in turn showed relatively promising stellar and gaseous disks at early times compared with the other simulations. But still, the final $z = 0$ galaxy was again suffering form a very dense and massive bulge component. As our analysis showed, a perturbing event at $z \approx 0.7$ occurring in all of our simulations destroyed the already accreted cold gas disk, inhibiting star formation for some time and thus preventing the formation of an extended stellar disk. Despite the fact that this particular halo had been selected as a promising halo for the formation of a large disk, we thus showed that relying only on information from the evolution of a dark matter only simulation, like a quiet merger history at late times, is not sufficient to predict the baryonic appearance of the galaxy forming in the corresponding halo.

In sum, our thesis research showed that the current methods applied to describe the numerous physical processes relevant for shaping the baryonic component of our Universe provide still only poor approximations to the real physical world, and that there are obviously several improvements needed to more successfully simulate galaxy formation in a fully self-consistent fashion. Regardless, the progress achieved thus far is encouraging, and the approach to compare results of different and independent simulation models has emerged as a powerful method to identify weaknesses and strengths of different physical models and numerical techniques. Intensifying such efforts will be crucial in the future for unlocking the full predictive power of scientific simulation codes, and to make further progress in understanding the complex processes in galaxy formation.

References

List of figures

1.1 Hubble Tuning-Fork of Galaxy Morphologies . . . 6
1.2 First map of the Milky Way . . . 11
1.3 The satellite problem . . . 12

2.1 2D Voronoi tessellation . . . 19
2.2 Flux geometry . . . 20

3.1 Differential luminosity function of satellite galaxies . . . 33
3.2 Cumulative luminosity function of satellites . . . 34
3.3 Cumulative number of luminous satellites . . . 35
3.4 Satellite V-band luminosity vs. velocity dispersion . . . 38
3.5 Mass evolution of three high mass satellites . . . 39
3.6 Mass evolution of three intermediate satellites . . . 40
3.7 Mass evolution of three low mass satellites . . . 40
3.8 Current stellar mass vs. maximum circular velocity at $z = 6$ . . . 41
3.9 Current stellar mass vs. current maximum circular velocity . . . 42
3.10 Stellar mass vs. maximum circular velocity at $z = 6$ . . . 44
3.11 Baryon fraction vs. circular velocity . . . 46
3.12 Evolution of the baryonfraction . . . 47
3.13 Average cumulative star formation histories of satellites . . . 48
3.14 Satellite scaling relations . . . 49
3.15 Relation between mass-to-light ratio and satellite luminosity . . . 50
3.16 Photometric V-band surface brightness of satellites . . . 51
3.17 Satellite dark matter mass vs. stellar mass . . . 52

4.1 Star formation efficiency / Kennicutt-Schmidt law . . . 57
4.2 Dark matter maps of the Aquarius initial conditions . . . 62
4.3 Projected stellar surface density maps of the main Aquila simulations . . . 65
4.4 Distribution of stellar circularities of the main Aquila simulations . . . 66
4.5 Projected stellar surface density maps and distribution of stellar circularities for the additional Aquila simulations . . . 67
4.6 Stellar mass vs. virial mass . . . 68
4.7 Half-mass radii vs. stellar mass . . . 69
4.8 Rotation curves . . . 71
4.9 Cumulative star formation history . . . 73
4.10 Star formation history . . . 74
4.11 Star formation rate vs. stellar mass . . . 75
4.12 Star formation time scale vs. stellar disk fraction / total stellar mass . . . 75
4.13 R-band magnitude vs. gas fraction . . . 77
4.14 Tully-Fisher relation . . . 78

5.1 Projected gas density maps . . . 90

5.2 Comparison of star formation rates 91
5.3 Evolution of virial radius 92
5.4 Evolution of the dark matter halo shape 93
5.5 Velocity field of the gas disk 94
5.6 Velocity profile of the gas disk 95
5.7 Gas surface density profiles 98
5.8 Evolution of the cold gas mass 99
5.9 Comparison of star formation rate histories 100
5.11 Stellar surface density profiles 103
5.12 Surface brightness profiles of young stars 104
5.13 Surface density profiles of old stars 105
5.14 Distribution functions of gas and stellar circularities 106
5.15 Tully-Fisher relation and stellar mass fraction 107
5.16 Gas density maps with varying resolution 108
5.17 Gas clumps in Gadget simulations 109
5.18 Gas clumps in AREPO simulations 110
5.19 Clumpiness profiles 112

List of tables

3.1 List of simulations presented in chapter 3 30
3.2 Compilation of all presently known Milky Way satellite galaxies 31

4.1 Summary of code characteristics and implemented physics. 61
4.2 Code parameters for simulations of level 5 resolution (level 6 parameters are given in parentheses where appropriate) 63
4.3 Properties of simulated galaxies at $z = 0$, for the level 5 (upper row) and level 6 (lower row) resolution simulations. 81

5.1 Simulation overview 87

Bibliography

A. Unsoeld, B. B. (2005), *Der neue Kosmos*, Springer-Verlag, Berlin

Agertz, O., Moore, B., Stadel, J., Potter, D., Miniati, F., Read, J., Mayer, L., Gawryszczak, A., Kravtsov, A., Nordlund, Å., Pearce, F., Quilis, V., Rudd, D., Springel, V., Stone, J., Tasker, E., Teyssier, R., Wadsley, J., Walder, R. (2007), *Fundamental differences between SPH and grid methods*, MNRAS, 380, 963

Agertz, O., Teyssier, R., Moore, B. (2011), *The formation of disc galaxies in a ΛCDM universe*, MNRAS, 410, 1391

Aharonian, F., Akhperjanian, A. G., Bazer-Bachi, A. R., Beilicke, M., Benbow, W., Berge, D., Bernlöhr, K., Boisson, C., Bolz, O., Borrel, V., Braun, I., Breitling, F., Brown, A. M., Chadwick, P. M., Chounet, L.-M., Cornils, R., Costamante, L., Degrange, B., Dickinson, H. J., Djannati-Ataï, A., Drury, L. O., Dubus, G., Emmanoulopoulos, D., Espigat, P., Feinstein, F., Fontaine, G., Fuchs, Y., Funk, S., Gallant, Y. A., Giebels, B., Gillessen, S., Glicenstein, J. F., Goret, P., Hadjichristidis, C., Hauser, D., Hauser, M., Heinzelmann, G., Henri, G., Hermann, G., Hinton, J. A., Hofmann, W., Holleran, M., Horns, D., Jacholkowska, A., de Jager, O. C., Khélifi, B., Klages, S., Komin, N., Konopelko, A., Latham, I. J., Le Gallou, R., Lemière, A., Lemoine-Goumard, M., Leroy, N., Lohse, T., Marcowith, A., Martin, J. M., Martineau-Huynh, O., Masterson, C., McComb, T. J. L., de Naurois, M., Nolan, S. J., Noutsos, A., Orford, K. J., Osborne, J. L., Ouchrif, M., Panter, M., Pelletier, G., Pita, S., Pühlhofer, G., Punch, M., Raubenheimer, B. C., Raue, M., Raux, J., Rayner, S. M., Reimer, A., Reimer, O., Ripken, J., Rob, L., Rolland, L., Rowell, G., Sahakian, V., Saugé, L., Schlenker, S., Schlickeiser, R., Schuster, C., Schwanke, U., Siewert, M., Sol, H., Spangler, D., Steenkamp, R., Stegmann, C., Tavernet, J.-P., Terrier, R., Théoret, C. G., Tluczykont, M., van Eldik, C., Vasileiadis, G., Venter, C., Vincent, P., Völk, H. J., Wagner, S. J. (2006), *Discovery of very-high-energy γ-rays from the Galactic Centre ridge*, Nature, 439, 695

Alpher, R. A., Herman, R., Gamow, G. A. (1948), *Thermonuclear Reactions in the Expanding Universe*, Physical Review, 74, 1198

Balsara, D. S. (1995), *von Neumann stability analysis of smooth particle hydrodynamics–suggestions for optimal algorithms*, Journal of Computational Physics, 121, 357

Banerjee, A., Jog, C. J. (2011), *Progressively More Prolate Dark Matter Halo in the Outer Galaxy as Traced by Flaring H I Gas*, ApJ, 732, L8

Bauer, A., Springel, V. (2011), *Shocking results without shocks: Subsonic turbulence in smoothed particle hydrodynamics and moving-mesh simulations*, ArXiv e-prints, arXiv:1109.4413

Bekki, K. (2008), *A Possible Common Halo of the Magellanic Clouds*, ApJ, 684, L87

Bell, E. F., de Jong, R. S. (2000), *The stellar populations of spiral galaxies*, MNRAS, 312, 497

Bell, E. F., McIntosh, D. H., Katz, N., Weinberg, M. D. (2003), *The Optical and Near-Infrared Properties of Galaxies. I. Luminosity and Stellar Mass Functions*, ApJS, 149, 289

Belokurov, V., Walker, M. G., Evans, N. W., Faria, D. C., Gilmore, G., Irwin, M. J., Koposov, S., Mateo, M., Olszewski, E., Zucker, D. B. (2008), *Leo V: A Companion of a Companion of the Milky Way Galaxy?*, ApJ, 686, L83

Belokurov, V., Walker, M. G., Evans, N. W., Gilmore, G., Irwin, M. J., Just, D., Koposov, S., Mateo, M., Olszewski, E., Watkins, L., Wyrzykowski, L. (2010), *Big Fish, Little Fish: Two New Ultra-faint Satellites of the Milky Way*, ApJ, 712, L103

Belokurov, V., Walker, M. G., Evans, N. W., Gilmore, G., Irwin, M. J., Mateo, M., Mayer, L., Olszewski, E., Bechtold, J., Pickering, T. (2009), *The discovery of Segue 2: a prototype of the population of satellites of satellites*, MNRAS, 397, 1748

Belokurov, V., Zucker, D. B., Evans, N. W., Kleyna, J. T., Koposov, S., Hodgkin, S. T., Irwin, M. J., Gilmore, G., Wilkinson, M. I., Fellhauer, M., Bramich, D. M., et.al (2007), *Cats and Dogs, Hair and a Hero: A Quintet of New Milky Way Companions*, ApJ, 654, 897

Belokurov, V., Zucker, D. B., Evans, N. W., Wilkinson, M. I., Irwin, M. J., Hodgkin, S., Bramich, D. M., Irwin, J. M., Gilmore, G., Willman, B., Vidrih, S., Newberg, H. J., et.al (2006), *A Faint New Milky Way Satellite in Bootes*, ApJ, 647, L111

Benson, A. J. (2010), *Galaxy formation theory*, Phys. Rep., 495, 33

Benson, A. J., Frenk, C. S., Baugh, C. M., Cole, S., Lacey, C. G. (2001), *The clustering evolution of the galaxy distribution*, MNRAS, 327, 1041

Benson, A. J., Frenk, C. S., Lacey, C. G., Baugh, C. M., Cole, S. (2002), *The effects of photoionization on galaxy formation - II. Satellite galaxies in the Local Group*, MNRAS, 333, 177

Berger, M. J., Colella, P. (1989), *Local adaptive mesh refinement for shock hydrodynamics*, Journal of Computational Physics, 82, 64

Blitz, L., Rosolowsky, E. (2006), *The Role of Pressure in GMC Formation II: The H_2-Pressure Relation*, ApJ, 650, 933

Book, L. G., Benson, A. J. (2010), *The Role of Ram Pressure Stripping in the Quenching of Cluster Star Formation*, ApJ, 716, 810

Booth, C. M., Schaye, J. (2010), *Dark matter haloes determine the masses of supermassive black holes*, MNRAS, 405, L1

Borgani, S., Finoguenov, A., Kay, S. T., Ponman, T. J., Springel, V., Tozzi, P., Voit, G. M. (2005), *Entropy amplification from energy feedback in simulated galaxy groups and clusters*, MNRAS, 361, 233

Boylan-Kolchin, M., Springel, V., White, S. D. M., Jenkins, A. (2010), *There's no place like home? Statistics of Milky Way-mass dark matter haloes*, MNRAS, 406, 896

Boylan-Kolchin, M., Springel, V., White, S. D. M., Jenkins, A., Lemson, G. (2009), *Resolving cosmic structure formation with the Millennium-II Simulation*, MNRAS, 398, 1150

Brooks, A. (2010), *Toward the Formation of Realistic Galaxy Disks*, in *New Horizons in Astronomy: Frank N. Bash Symposium 2009*, edited by L. M. Stanford, J. D. Green, L. Hao, & Y. Mao, volume 432 of *Astronomical Society of the Pacific Conference Series*, 17

Brooks, A. M., Solomon, A. R., Governato, F., McCleary, J., MacArthur, L. A., Brook, C. B. A., Jonsson, P., Quinn, T. R., Wadsley, J. (2011), *Interpreting the Evolution of the Size-Luminosity Relation for Disk Galaxies from Redshift 1 to the Present*, ApJ, 728, 51

Bruzual, G., Charlot, S. (2003), *Stellar population synthesis at the resolution of 2003*, MNRAS, 344, 1000

Bullock, J. S., Stewart, K. R., Kaplinghat, M., Tollerud, E. J., Wolf, J. (2010), *Stealth Galaxies in the Halo of the Milky Way*, ApJ, 717, 1043

Busha, M. T., Alvarez, M. A., Wechsler, R. H., Abel, T., Strigari, L. E. (2010), *The Impact of Inhomogeneous Reionization on the Satellite Galaxy Population of the Milky Way*, ApJ, 710, 408

Cervantes-Cota, J. L., Smoot, G. (2011), *Cosmology today–A brief review*, in *American Institute of Physics Conference Series*, edited by L. A. Ureña-López, H. Aurelio Morales-Técotl, R. Linares-Romero, E. Santos-Rodríguez, & S. Estrada-Jiménez , volume 1396 of *American Institute of Physics Conference Series*, 28–52

Charlier, C. V. L. (1922), Arkiv for Matematik, Astronomi och Fysik, 22, 16

Colín, P., Avila-Reese, V., Valenzuela, O. (2000), *Substructure and Halo Density Profiles in a Warm Dark Matter Cosmology*, ApJ, 542, 622

Cooper, A. P., Cole, S., Frenk, C. S., White, S. D. M., Helly, J., Benson, A. J., De Lucia, G., Helmi, A., Jenkins, A., Navarro, J. F., Springel, V., Wang, J. (2010), *Galactic stellar haloes in the CDM model*, MNRAS, 406, 744

Courteau, S., Dutton, A. A., van den Bosch, F. C., MacArthur, L. A., Dekel, A., McIntosh, D. H., Dale, D. A. (2007), *Scaling Relations of Spiral Galaxies*, ApJ, 671, 203

Crain, R. A., Theuns, T., Dalla Vecchia, C., Eke, V. R., Frenk, C. S., Jenkins, A., Kay, S. T., Peacock, J. A., Pearce, F. R., Schaye, J., Springel, V., Thomas, P. A., White, S. D. M., Wiersma, R. P. C. (2009), *Galaxies-intergalactic medium interaction calculation - I. Galaxy formation as a function of large-scale environment*, MNRAS, 399, 1773

Crampin, D. J., Hoyle, F. (1964), *On the Angular-Momentum Distribution in the Disks of Spiral Galaxies.*, ApJ, 140, 99

Croton, D. J., Springel, V., White, S. D. M., De Lucia, G., Frenk, C. S., Gao, L., Jenkins, A., Kauffmann, G., Navarro, J. F., Yoshida, N. (2006), *The many lives of active galactic nuclei: cooling flows, black holes and the luminosities and colours of galaxies*, MNRAS, 365, 11

Dalla Vecchia, C., Schaye, J. (2008), *Simulating galactic outflows with kinetic supernova feedback*, MNRAS, 387, 1431

Davis, M., Efstathiou, G., Frenk, C. S., White, S. D. M. (1985), *The evolution of large-scale structure in a universe dominated by cold dark matter*, ApJ, 292, 371

Dekel, A., Silk, J. (1986), *The origin of dwarf galaxies, cold dark matter, and biased galaxy formation*, ApJ, 303, 39

Di Matteo, T., Springel, V., Hernquist, L. (2005), *Energy input from quasars regulates the growth and activity of black holes and their host galaxies*, Nature, 433, 604

Diemand, J., Kuhlen, M., Madau, P. (2007), *Dark Matter Substructure and Gamma-Ray Annihilation in the Milky Way Halo*, ApJ, 657, 262

Diemand, J., Kuhlen, M., Madau, P., Zemp, M., Moore, B., Potter, D., Stadel, J. (2008), *Clumps and streams in the local dark matter distribution*, Nature, 454, 735

Dolag, K., Borgani, S., Murante, G., Springel, V. (2009), *Substructures in hydrodynamical cluster simulations*, MNRAS, 399, 497

Dubois, Y., Teyssier, R. (2008), *On the onset of galactic winds in quiescent star forming galaxies*, A&A, 477, 79

Einstein, A. (1905), *Zur Elektrodynamik bewegter Körper*, Annalen der Physik, 322, 891

Einstein, A. (1915), *Zur allgemeinen Relativitätstheorie*, Sitzungsberichte der Königlich Preußischen Akademie der Wissenschaften (Berlin), Seite 778-786., 778–786

Enßlin, T. A., Pfrommer, C., Springel, V., Jubelgas, M. (2007), *Cosmic ray physics in calculations of cosmological structure formation*, A&A, 473, 41

Fall, S. M., Efstathiou, G. (1980), *Formation and rotation of disc galaxies with haloes*, MNRAS, 193, 189

Ferland, G. J., Korista, K. T., Verner, D. A., Ferguson, J. W., Kingdon, J. B., Verner, E. M. (1998), *CLOUDY 90: Numerical Simulation of Plasmas and Their Spectra*, PASP, 110, 761

Frenk, C. S., White, S. D. M., Davis, M., Efstathiou, G. (1988), *The formation of dark halos in a universe dominated by cold dark matter*, ApJ, 327, 507

Gilmore, G., Wilkinson, M. I., Wyse, R. F. G., Kleyna, J. T., Koch, A., Evans, N. W., Grebel, E. K. (2007), *The Observed Properties of Dark Matter on Small Spatial Scales*, ApJ, 663, 948

Gingold, R. A., Monaghan, J. J. (1977), *Smoothed particle hydrodynamics - Theory and application to non-spherical stars*, MNRAS, 181, 375

Gnedin, N. Y. (2000), *Effect of Reionization on Structure Formation in the Universe*, ApJ, 542, 535

Governato, F., Brook, C., Mayer, L., Brooks, A., Rhee, G., Wadsley, J., Jonsson, P., Willman, B., Stinson, G., Quinn, T., Madau, P. (2010), *Bulgeless dwarf galaxies and dark matter cores from supernova-driven outflows*, Nature, 463, 203

Governato, F., Mayer, L., Wadsley, J., Gardner, J. P., Willman, B., Hayashi, E., Quinn, T., Stadel, J., Lake, G. (2004), *The Formation of a Realistic Disk Galaxy in Λ-dominated Cosmologies*, ApJ, 607, 688

Governato, F., Willman, B., Mayer, L., Brooks, A., Stinson, G., Valenzuela, O., Wadsley, J., Quinn, T. (2007), *Forming disc galaxies in ΛCDM simulations*, MNRAS, 374, 1479

Graham, A. W. (2011), *A review of elliptical and disc galaxy structure, and modern scaling laws*, ArXiv e-prints

Grebel, E. K. (2000), *The Star Formation History of the Local Group*, in *Star Formation from the Small to the Large Scale*, edited by F. Favata, A. Kaas, A. Wilson, volume 445 of *ESA Special Publication*, 87

Guedes, J., Callegari, S., Madau, P., Mayer, L. (2011), *Forming Realistic Late-type Spirals in a ΛCDM Universe: The Eris Simulation*, ApJ, 742, 76

Guo, Q., White, S., Boylan-Kolchin, M., De Lucia, G., Kauffmann, G., Lemson, G., Li, C., Springel, V., Weinmann, S. (2011), *From dwarf spheroidals to cD galaxies: simulating the galaxy population in a ΛCDM cosmology*, MNRAS, 413, 101

Guo, Q., White, S., Li, C., Boylan-Kolchin, M. (2010), *How do galaxies populate dark matter haloes?*, MNRAS, 404, 1111

Haardt, F., Madau, P. (1996), *Radiative Transfer in a Clumpy Universe. II. The Ultraviolet Extragalactic Background*, ApJ, 461, 20

Haardt, F., Madau, P. (2001), *Modelling the UV/X-ray cosmic background with CUBA*, in *Clusters of Galaxies and the High Redshift Universe Observed in X-rays*, edited by D. M. Neumann & J. T. V. Tran

Haynes, M. P., Giovanelli, R., Chamaraux, P., da Costa, L. N., Freudling, W., Salzer, J. J., Wegner, G. (1999), *The I-Band Tully-Fisher Relation for SC Galaxies: 21 Centimeter H I Line Data*, AJ, 117, 2039

Herschel, W. (1785), *O the Construction of the Heavens.*, Royal Society of London Philosophical Transactions Series I, 75, 213

Hoeft, M., Yepes, G., Gottlöber, S., Springel, V. (2006), *Dwarf galaxies in voids: suppressing star formation with photoheating*, MNRAS, 371, 401

Hohl, F. (1970), *Computer Models of Spiral Structure*, in *The Spiral Structure of our Galaxy*, edited by W. Becker & G. I. Kontopoulos, volume 38 of *IAU Symposium*, 368

Holmberg, E. (1941), *On the Clustering Tendencies among the Nebulae. II. a Study of Encounters Between Laboratory Models of Stellar Systems by a New Integration Procedure.*, ApJ, 94, 385

Hopkins, P. F., Hernquist, L., Cox, T. J., Di Matteo, T., Robertson, B., Springel, V. (2006), *A Unified, Merger-driven Model of the Origin of Starbursts, Quasars, the Cosmic X-Ray Background, Supermassive Black Holes, and Galaxy Spheroids*, ApJS, 163, 1

Hopkins, P. F., Quataert, E., Murray, N. (2011), *The Structure of the Interstellar Medium of Star Forming Galaxies*, ArXiv e-prints, arXiv:1110.4636

Hubble, E. P. (1925), *Cepheids in Spiral Nebulae*, Popular Astronomy, 33, 252

Hubble, E. P. (1936), *Realm of the Nebulae*

Ibata, R., Lewis, G. F., Irwin, M., Totten, E., Quinn, T. (2001), *Great Circle Tidal Streams: Evidence for a Nearly Spherical Massive Dark Halo around the Milky Way*, ApJ, 551, 294

Irwin, M. J., Belokurov, V., Evans, N. W., Ryan-Weber, E. V., de Jong, J. T. A., Koposov, S., Zucker, D. B., Hodgkin, S. T., Gilmore, G., Prema, P., Hebb, L., et.al (2007), *Discovery of an Unusual Dwarf Galaxy in the Outskirts of the Milky Way*, ApJ, 656, L13

Jubelgas, M., Springel, V., Ensslin, T., Pfrommer, C. (2008), *Cosmic ray feedback in hydrodynamical simulations of galaxy formation*, A&A, 481, 33

Kalberla, P. M. W., Dedes, L. (2008), *Global properties of the H I distribution in the outer Milky Way. Planar and extra-planar gas*, A&A, 487, 951

Kant, I. (1755), *Allgemeine Naturgeschichte und Theorie des Himmels*

Katz, N., Weinberg, D. H., Hernquist, L. (1996), *Cosmological Simulations with TreeSPH*, ApJS, 105, 19

Kaufmann, T., Mayer, L., Wadsley, J., Stadel, J., Moore, B. (2006), *Cooling flows within galactic haloes: the kinematics and properties of infalling multiphase gas*, MNRAS, 370, 1612

Kaufmann, T., Mayer, L., Wadsley, J., Stadel, J., Moore, B. (2007), *Angular momentum transport and disc morphology in smoothed particle hydrodynamics simulations of galaxy formation*, MNRAS, 375, 53

Kennicutt, Jr., R. C. (1989), *The star formation law in galactic disks*, ApJ, 344, 685

Kennicutt, Jr., R. C. (1998), *The Global Schmidt Law in Star-forming Galaxies*, ApJ, 498, 541

Keres, D., Vogelsberger, M., Sijacki, D., Springel, V., Hernquist, L. (2011), *Moving mesh cosmology: characteristics of galaxies and haloes*, ArXiv e-prints, arXiv:1109.4638

Klypin, A., Kravtsov, A. V., Valenzuela, O., Prada, F. (1999), *Where Are the Missing Galactic Satellites?*, ApJ, 522, 82

Kobayashi, C. (2004), *GRAPE-SPH chemodynamical simulation of elliptical galaxies - I. Evolution of metallicity gradients*, MNRAS, 347, 740

Kobayashi, C., Nakasato, N. (2011), *Chemodynamical Simulations of the Milky Way Galaxy*, ApJ, 729, 16

Kobayashi, C., Springel, V., White, S. D. M. (2007), *Simulations of Cosmic Chemical Enrichment*, MNRAS, 376, 1465

Komatsu, E., Smith, K. M., Dunkley, J., Bennett, C. L., Gold, B., Hinshaw, G., Jarosik, N., Larson, D., Nolta, M. R., Page, L., Spergel, D. N., Halpern, M., Hill, R. S., Kogut, A., Limon, M., Meyer, S. S., Odegard, N., Tucker, G. S., Weiland, J. L., Wollack, E., Wright, E. L. (2011), *Seven-year Wilkinson Microwave Anisotropy Probe (WMAP) Observations: Cosmological Interpretation*, ApJS, 192, 18

Koposov, S., Belokurov, V., Evans, N. W., Hewett, P. C., Irwin, M. J., Gilmore, G., Zucker, D. B., Rix, H., Fellhauer, M., Bell, E. F., Glushkova, E. V. (2008), *The Luminosity Function of the Milky Way Satellites*, ApJ, 686, 279

Kravtsov, A. V., Gnedin, O. Y., Klypin, A. A. (2004), *The Tumultuous Lives of Galactic Dwarfs and the Missing Satellites Problem*, ApJ, 609, 482

Kroupa, P., Tout, C. A., Gilmore, G. (1993), *The distribution of low-mass stars in the Galactic disc*, MNRAS, 262, 545

Kuhlen, M., Diemand, J., Madau, P. (2008), *The Dark Matter Annihilation Signal from Galactic Substructure: Predictions for GLAST*, APJ, 686, 262

Law, D. R., Majewski, S. R. (2010), *The Sagittarius Dwarf Galaxy: A Model for Evolution in a Triaxial Milky Way Halo*, ApJ, 714, 229

Leitner, S. N., Kravtsov, A. V. (2011), *Fuel Efficient Galaxies: Sustaining Star Formation with Stellar Mass Loss*, ApJ, 734, 48

Li, Y., De Lucia, G., Helmi, A. (2010), *On the nature of the Milky Way satellites*, MNRAS, 401, 2036

Liu, C., Hu, J., Newberg, H., Zhao, Y. (2008), *Candidate Milky Way satellites in the Galactic halo*, A&A, 477, 139

Longair, M. S. (1999), *Galaxy Formation*, Springer, Berlin

Lucy, L. B. (1977), *A numerical approach to the testing of the fission hypothesis*, AJ, 82, 1013

Macciò, A. V., Fontanot, F. (2010), *How cold is dark matter? Constraints from Milky Way satellites*, MNRAS, L28

Macciò, A. V., Kang, X., Fontanot, F., Somerville, R. S., Koposov, S., Monaco, P. (2010), *Luminosity function and radial distribution of Milky Way satellites in a ΛCDM Universe*, MNRAS, 402, 1995

Madau, P., Diemand, J., Kuhlen, M. (2008), *Dark Matter Subhalos and the Dwarf Satellites of the Milky Way*, ApJ, 679, 1260

Marigo, P. (2001), *Chemical yields from low- and intermediate-mass stars: Model predictions and basic observational constraints*, A&A, 370, 194

Martin, N. F., de Jong, J. T. A., Rix, H.-W. (2008), *A Comprehensive Maximum Likelihood Analysis of the Structural Properties of Faint Milky Way Satellites*, ApJ, 684, 1075

Martin, N. F., Ibata, R. A., Chapman, S. C., Irwin, M., Lewis, G. F. (2007), *A Keck/DEIMOS spectroscopic survey of faint Galactic satellites: searching for the least massive dwarf galaxies*, MNRAS, 380, 281

Mateo, M. L. (1998), *Dwarf Galaxies of the Local Group*, ARA&A, 36, 435

Miller, R. H., Prendergast, K. H. (1968), *Stellar Dynamics in a Discrete Phase Space*, ApJ, 151, 699

Miller, R. H., Prendergast, K. H., Quirk, W. (1969), *Computer Simulation of Galactic Evolution*, in *Bulletin of the American Astronomical Society*, volume 1 of *Bulletin of the American Astronomical Society*, 355

Monaghan, J. J. (1992), *Smoothed particle hydrodynamics*, ARA&A, 30, 543

Monaghan, J. J., Gingold, R. A. (1983), *Shock Simulation by the Particle Method SPH*, Journal of Computational Physics, 52, 374

Moore, B., Ghigna, S., Governato, F., Lake, G., Quinn, T., Stadel, J., Tozzi, P. (1999), *Dark Matter Substructure within Galactic Halos*, APJ, 524, L19

Muanwong, O., Thomas, P. A., Kay, S. T., Pearce, F. R. (2002), *The effect of cooling and preheating on the X-ray properties of clusters of galaxies*, MNRAS, 336, 527

Murante, G., Monaco, P., Giovalli, M., Borgani, S., Diaferio, A. (2010), *A subresolution multiphase interstellar medium model of star formation and supernova energy feedback*, MNRAS, 405, 1491

Navarro, J. F., Steinmetz, M. (2000), *Dark Halo and Disk Galaxy Scaling Laws in Hierarchical Universes*, ApJ, 538, 477

Okamoto, T., Eke, V. R., Frenk, C. S., Jenkins, A. (2005), *Effects of feedback on the morphology of galaxy discs*, MNRAS, 363, 1299

Okamoto, T., Frenk, C. S. (2009), *The origin of failed subhaloes and the common mass scale of the Milky Way satellite galaxies*, MNRAS, 399, L174

Okamoto, T., Frenk, C. S., Jenkins, A., Theuns, T. (2010), *The properties of satellite galaxies in simulations of galaxy formation*, MNRAS, 406, 208

Okamoto, T., Gao, L., Theuns, T. (2008a), *Mass loss of galaxies due to an ultraviolet background*, MNRAS, 390, 920

Okamoto, T., Nemmen, R. S., Bower, R. G. (2008b), *The impact of radio feedback from active galactic nuclei in cosmological simulations: formation of disc galaxies*, MNRAS, 385, 161

Olive, K. A. (2010), *The violent Universe: the Big Bang*, ArXiv e-prints

Oliver, S., Frost, M., Farrah, D., Gonzalez-Solares, E., Shupe, D. L., Henriques, B., Roseboom, I., Alfonso-Luis, A., Babbedge, T. S. R., Frayer, D., Lencz, C., Lonsdale, C. J., Masci, F., Padgett, D., Polletta, M., Rowan-Robinson, M., Siana, B., Smith, H. E., Surace, J. A., Vaccari, M. (2010), *Specific star formation and the relation to stellar mass from* $0 < z < 2$ *as seen in the far-infrared at 70 and 160* μm, MNRAS, 405, 2279

Oort, J. H. (1970), *The formation of galaxies and the origin of the high-velocity hydrogen.*, A&A, 7, 381

Oppenheimer, B. D., Davé, R. (2006), *Cosmological simulations of intergalactic medium enrichment from galactic outflows*, MNRAS, 373, 1265

Orban, C., Gnedin, O. Y., Weisz, D. R., Skillman, E. D., Dolphin, A. E., Holtzman, J. A. (2008), *Delving Deeper into the Tumultuous Lives of Galactic Dwarfs: Modeling Star Formation Histories*, ApJ, 686, 1030

Peebles, P. J. E. (1993), *Principles of Physical Cosmology*

Penzias, A. A., Wilson, R. W. (1965), *A Measurement of Excess Antenna Temperature at 4080 Mc/s.*, ApJ, 142, 419

Pfrommer, C. (2008), *Simulating cosmic rays in clusters of galaxies - III. Non-thermal scaling relations and comparison to observations*, MNRAS, 385, 1242

Pfrommer, C., Enßlin, T. A., Springel, V. (2008), *Simulating cosmic rays in clusters of galaxies - II. A unified scheme for radio haloes and relics with predictions of the γ-ray emission*, MNRAS, 385, 1211

Pfrommer, C., Enßlin, T. A., Springel, V., Jubelgas, M., Dolag, K. (2007), *Simulating cosmic rays in clusters of galaxies - I. Effects on the Sunyaev-Zel'dovich effect and the X-ray emission*, MNRAS, 378, 385

Piontek, F., Steinmetz, M. (2011), *The modelling of feedback processes in cosmological simulations of disc galaxy formation*, MNRAS, 410, 2625

Pizagno, J., Prada, F., Weinberg, D. H., Rix, H.-W., Pogge, R. W., Grebel, E. K., Harbeck, D., Blanton, M., Brinkmann, J., Gunn, J. E. (2007), *The Tully-Fisher Relation and its Residuals for a Broadly Selected Sample of Galaxies*, AJ, 134, 945

Pizagno, II, J. L. (2006), *The Tully-Fisher relation, its residuals, and a comparison to theoretical predictions for a broadly selected sample of galaxies*, Ph.D. thesis, The Ohio State University

Portinari, L., Chiosi, C., Bressan, A. (1998), *Galactic chemical enrichment with new metallicity dependent stellar yields*, A&A, 334, 505

Primack, J. R. (2009), *Cosmology: small-scale issues*, New Journal of Physics, 11(10), 105029

Puchwein, E., Springel, V., Sijacki, D., Dolag, K. (2010), *Intracluster stars in simulations with active galactic nucleus feedback*, MNRAS, 406, 936

Rasera, Y., Teyssier, R. (2006), *The history of the baryon budget. Cosmic logistics in a hierarchical universe*, A&A, 445, 1

Rees, M. J., Ostriker, J. P. (1977), *Cooling, dynamics and fragmentation of massive gas clouds - Clues to the masses and radii of galaxies and clusters*, MNRAS, 179, 541

Rice, W. K. M., Forgan, D. H., Armitage, P. J. (2011), *Convergence of smoothed particle hydrodynamics simulations of self-gravitating accretion discs: sensitivity to the implementation of radiative cooling*, MNRAS, 2111

Robertson, B., Yoshida, N., Springel, V., Hernquist, L. (2004), *Disk Galaxy Formation in a Λ Cold Dark Matter Universe*, ApJ, 606, 32

Saitoh, T. R., Daisaka, H., Kokubo, E., Makino, J., Okamoto, T., Tomisaka, K., Wada, K., Yoshida, N. (2008), *Toward First-Principle Simulations of Galaxy Formation: I. How Should We Choose Star-Formation Criteria in High-Resolution Simulations of Disk Galaxies?*, PASJ, 60, 667

Sales, L. V., Navarro, J. F., Schaye, J., Dalla Vecchia, C., Springel, V., Booth, C. M. (2010), *Feedback and the structure of simulated galaxies at redshift z= 2*, MNRAS, 409, 1541

Sales, L. V., Navarro, J. F., Schaye, J., Dalla Vecchia, C., Springel, V., Haas, M. R., Helmi, A. (2009), *The origin of extended disc galaxies at* $z = 2$, MNRAS, 399, L64

Sawala, T., Guo, Q., Scannapieco, C., Jenkins, A., White, S. (2011), *What is the (dark) matter with dwarf galaxies?*, MNRAS, 413, 659

Scannapieco, C., Tissera, P. B., White, S. D. M., Springel, V. (2005), *Feedback and metal enrichment in cosmological smoothed particle hydrodynamics simulations - I. A model for chemical enrichment*, MNRAS, 364, 552

Scannapieco, C., Tissera, P. B., White, S. D. M., Springel, V. (2006), *Feedback and metal enrichment in cosmological SPH simulations - II. A multiphase model with supernova energy feedback*, MNRAS, 371, 1125

Scannapieco, C., Tissera, P. B., White, S. D. M., Springel, V. (2008), *Effects of supernova feedback on the formation of galaxy discs*, MNRAS, 389, 1137

Scannapieco, C., Wadepuhl, M., Parry, O. H., Navarro, J. F., Jenkins, A., Springel, V., Teyssier, R., Carlson, E., Couchman, H. M. P., Crain, R. A., Dalla Vecchia, C., Frenk, C. S., Kobayashi, C., Monaco, P., Murante, G., Okamoto, T., Quinn, T., Schaye, J., Stinson, G. S., Theuns, T., Wadsley, J., White, S. D. M., Woods, R. (2011a), *The Aquila comparison Project: The Effects of Feedback and Numerical Methods on Simulations of Galaxy Formation*, ArXiv e-prints

Scannapieco, C., White, S. D. M., Springel, V., Tissera, P. B. (2009), *The formation and survival of discs in a* Λ*CDM universe*, MNRAS, 396, 696

Scannapieco, C., White, S. D. M., Springel, V., Tissera, P. B. (2011b), *Formation history, structure and dynamics of discs and spheroids in simulated Milky Way mass galaxies*, MNRAS, 417, 154

Scannapieco, E., Thacker, R. J., Davis, M. (2001), *High-Redshift Galaxy Outflows and the Formation of Dwarf Galaxies*, ApJ, 557, 605

Schaye, J., Dalla Vecchia, C. (2008), *On the relation between the Schmidt and Kennicutt-Schmidt star formation laws and its implications for numerical simulations*, MNRAS, 383, 1210

Schaye, J., Theuns, T., Rauch, M., Efstathiou, G., Sargent, W. L. W. (2000), *The thermal history of the intergalactic medium**, MNRAS, 318, 817

Schombert, J. M., McGaugh, S. S., Eder, J. A. (2001), *Gas Mass Fractions and the Evolution of Low Surface Brightness Dwarf Galaxies*, AJ, 121, 2420

Shen, S., Wadsley, J., Stinson, G. (2010), *The enrichment of the intergalactic medium with adiabatic feedback - I. Metal cooling and metal diffusion*, MNRAS, 407, 1581

Sijacki, D., Vogelsberger, M., Keres, D., Springel, V., Hernquist, L. (2011), *Moving mesh cosmology: the hydrodynamics of galaxy formation*, ArXiv e-prints, arXiv:1109.3468

Simon, J. D., Geha, M. (2007), *The Kinematics of the Ultra-faint Milky Way Satellites: Solving the Missing Satellite Problem*, ApJ, 670, 313

Sofue, Y., Honma, M., Omodaka, T. (2009), *Unified Rotation Curve of the Galaxy – Decomposition into de Vaucouleurs Bulge, Disk, Dark Halo, and the 9-kpc Rotation Dip –*, PASJ, 61, 227

Somerville, R. S. (2002), *Can Photoionization Squelching Resolve the Substructure Crisis?*, ApJ, 572, L23

Sommer-Larsen, J., Götz, M., Portinari, L. (2003), *Galaxy Formation: Cold Dark Matter, Feedback, and the Hubble Sequence*, ApJ, 596, 47

Spergel, D. N., Bean, R., Doré, O., Nolta, M. R., Bennett, C. L., Dunkley, J., Hinshaw, G., Jarosik, N., Komatsu, E., Page, L., Peiris, H. V., Verde, L., Halpern, M., Hill, R. S., Kogut, A., Limon, M., Meyer, S. S., Odegard, N., Tucker, G. S., Weiland, J. L., Wollack, E., Wright, E. L. (2007), *Three-Year Wilkinson Microwave Anisotropy Probe (WMAP) Observations: Implications for Cosmology*, ApJS, 170, 377

Springel, V. (2005), *The cosmological simulation code GADGET-2*, MNRAS, 364, 1105

Springel, V. (2010a), *E pur si muove: Galilean-invariant cosmological hydrodynamical simulations on a moving mesh*, MNRAS, 401, 791

Springel, V. (2010b), *Smoothed Particle Hydrodynamics in Astrophysics*, ARA&A, 48, 391

Springel, V., Di Matteo, T., Hernquist, L. (2005a), *Modelling feedback from stars and black holes in galaxy mergers*, MNRAS, 361, 776

Springel, V., Frenk, C. S., White, S. D. M. (2006), *The large-scale structure of the Universe*, Nature, 440, 1137

Springel, V., Hernquist, L. (2002), *Cosmological smoothed particle hydrodynamics simulations: the entropy equation*, MNRAS, 333, 649

Springel, V., Hernquist, L. (2003), *Cosmological smoothed particle hydrodynamics simulations: a hybrid multiphase model for star formation*, MNRAS, 339, 289

Springel, V., Wang, J., Vogelsberger, M., Ludlow, A., Jenkins, A., Helmi, A., Navarro, J. F., Frenk, C. S., White, S. D. M. (2008), *The Aquarius Project: the subhaloes of galactic haloes*, MNRAS, 391, 1685

Springel, V., White, S. D. M., Jenkins, A., Frenk, C. S., Yoshida, N., Gao, L., Navarro, J., Thacker, R., Croton, D., Helly, J., Peacock, J. A., Cole, S., Thomas, P., Couchman, H., Evrard, A., Colberg, J., Pearce, F. (2005b), *Simulations of the formation, evolution and clustering of galaxies and quasars*, Nature, 435, 629

Springel, V., White, S. D. M., Tormen, G., Kauffmann, G. (2001), *Populating a cluster of galaxies - I. Results at z=0*, MNRAS, 328, 726

Stadel, J., Potter, D., Moore, B., Diemand, J., Madau, P., Zemp, M., Kuhlen, M., Quilis, V. (2009), *Quantifying the heart of darkness with GHALO - a multibillion particle simulation of a galactic halo*, MNRAS, 398, L21

Steinmetz, M., White, S. D. M. (1997), *Two-body heating in numerical galaxy formation experiments*, MNRAS, 288, 545

Stinson, G., Seth, A., Katz, N., Wadsley, J., Governato, F., Quinn, T. (2006), *Star formation and feedback in smoothed particle hydrodynamic simulations - I. Isolated galaxies*, MNRAS, 373, 1074

Stinson, G. S., Bailin, J., Couchman, H., Wadsley, J., Shen, S., Nickerson, S., Brook, C., Quinn, T. (2010), *Cosmological galaxy formation simulations using smoothed particle hydrodynamics*, MNRAS, 408, 812

Stoehr, F., White, S. D. M., Tormen, G., Springel, V. (2002), *The satellite population of the Milky Way in a* Λ*CDM universe*, MNRAS, 335, L84

Strigari, L. E., Bullock, J. S., Kaplinghat, M., Diemand, J., Kuhlen, M., Madau, P. (2007), *Redefining the Missing Satellites Problem*, ApJ, 669, 676

Strigari, L. E., Bullock, J. S., Kaplinghat, M., Simon, J. D., Geha, M., Willman, B., Walker, M. G. (2008), *A common mass scale for satellite galaxies of the Milky Way*, Nature, 454, 1096

Strigari, L. E., Frenk, C. S., White, S. D. M. (2010), *Kinematics of Milky Way satellites in a Lambda cold dark matter universe*, MNRAS, 1311

Sutherland, R. S., Dopita, M. A. (1993), *Cooling functions for low-density astrophysical plasmas*, ApJS, 88, 253

Swaters, R. A., Schoenmakers, R. H. M., Sancisi, R., van Albada, T. S. (1999), *Kinematically lopsided spiral galaxies*, MNRAS, 304, 330

Teyssier, R. (2002), *Cosmological hydrodynamics with adaptive mesh refinement. A new high resolution code called RAMSES*, A&A, 385, 337

Thacker, R. J., Couchman, H. M. P. (2001), *Star Formation, Supernova Feedback, and the Angular Momentum Problem in Numerical Cold Dark Matter Cosmogony: Halfway There?*, ApJ, 555, L17

Thacker, R. J., Scannapieco, E., Davis, M. (2002), *Violence in the Dark Ages*, ApJ, 581, 836

Theuns, T., Bernardi, M., Frieman, J., Hewett, P., Schaye, J., Sheth, R. K., Subbarao, M. (2002), *Detection of He II Reionization in the Sloan Digital Sky Survey Quasar Sample*, ApJ, 574, L111

Tollerud, E. J., Bullock, J. S., Strigari, L. E., Willman, B. (2008), *Hundreds of Milky Way Satellites? Luminosity Bias in the Satellite Luminosity Function*, APJ, 688, 277

Torrey, P., Vogelsberger, M., Sijacki, D., Springel, V., Hernquist, L. (2011), *Moving Mesh Cosmology: Properties of Gas Disks*, ArXiv e-prints, arXiv:1110.5635

van den Bergh, S. (1994), *The outer fringes of the local group*, AJ, 107, 1328

van den Bergh, S. (2000), *The galaxies of the local group*, Cambridge Univ. Press, Cambridge

Verheijen, M. A. W. (2001), *The Ursa Major Cluster of Galaxies. V. H I Rotation Curve Shapes and the Tully-Fisher Relations*, ApJ, 563, 694

Vogelsberger, M., Sijacki, D., Keres, D., Springel, V., Hernquist, L. (2011), *Moving mesh cosmology: numerical techniques and global statistics*, ArXiv e-prints, arXiv:1109.1281

Wadepuhl, M., Springel, V. (2011a), *Effects of feedback physics and hydrodynamical technique in simulations of disc galaxy formation*, MNRAS, in preparation

Wadepuhl, M., Springel, V. (2011b), *Satellite galaxies in hydrodynamical simulations of Milky Way sized galaxies*, MNRAS, 410, 1975

Wadsley, J. W., Stadel, J., Quinn, T. (2004), *Gasoline: a flexible, parallel implementation of TreeSPH*, New A, 9, 137

Walker, M. G., Mateo, M., Olszewski, E. W., Peñarrubia, J., Wyn Evans, N., Gilmore, G. (2009), *A Universal Mass Profile for Dwarf Spheroidal Galaxies?*, ApJ, 704, 1274

Walsh, S. M., Jerjen, H., Willman, B. (2007), *A Pair of Boötes: A New Milky Way Satellite*, ApJ, 662, L83

Walsh, S. M., Willman, B., Sand, D., Harris, J., Seth, A., Zaritsky, D., Jerjen, H. (2008), *Boötes II ReBoöted: An MMT/MegaCam Study of an Ultrafaint Milky Way Satellite*, APJ, 688, 245

Wang, J., Navarro, J. F., Frenk, C. S., White, S. D. M., Springel, V., Jenkins, A., Helmi, A., Ludlow, A., Vogelsberger, M. (2011), *Assembly history and structure of galactic cold dark matter haloes*, MNRAS, 413, 1373

Watkins, L. L., Evans, N. W., Belokurov, V., Smith, M. C., Hewett, P. C., Bramich, D. M., Gilmore, G. F., Irwin, M. J., Vidrih, S., Wyrzykowski, Ł., Zucker, D. B. (2009), *Substructure revealed by RRLyraes in SDSS Stripe 82*, MNRAS, 398, 1757

White, S. D. M., Rees, M. J. (1978), *Core condensation in heavy halos - A two-stage theory for galaxy formation and clustering*, MNRAS, 183, 341

Wiersma, R. P. C., Schaye, J., Smith, B. D. (2009a), *The effect of photoionization on the cooling rates of enriched, astrophysical plasmas*, MNRAS, 393, 99

Wiersma, R. P. C., Schaye, J., Theuns, T., Dalla Vecchia, C., Tornatore, L. (2009b), *Chemical enrichment in cosmological, smoothed particle hydrodynamics simulations*, MNRAS, 399, 574

Willman, B., Blanton, M. R., West, A. A., Dalcanton, J. J., Hogg, D. W., Schneider, D. P., Wherry, N., Yanny, B., Brinkmann, J. (2005a), *A New Milky Way Companion: Unusual Globular Cluster or Extreme Dwarf Satellite?*, AJ, 129, 2692

Willman, B., Dalcanton, J., Ivezić, Ž., Jackson, T., Lupton, R., Brinkmann, J., Hennessy, G., Hindsley, R. (2002), *An SDSS Survey For Resolved Milky Way Satellite Galaxies. I. Detection Limits*, AJ, 123, 848

Willman, B., Dalcanton, J. J., Martinez-Delgado, D., West, A. A., Blanton, M. R., Hogg, D. W., Barentine, J. C., Brewington, H. J., Harvanek, M., Kleinman, S. J., Krzesinski, J., Long, D., Neilsen, Jr., E. H., Nitta, A., Snedden, S. A. (2005b), *A New Milky Way Dwarf Galaxy in Ursa Major*, ApJ, 626, L85

Wolf, J., Martinez, G. D., Bullock, J. S., Kaplinghat, M., Geha, M., Muñoz, R. R., Simon, J. D., Avedo, F. F. (2010), *Accurate masses for dispersion-supported galaxies*, MNRAS, 778

Woo, J., Courteau, S., Dekel, A. (2008), *Scaling relations and the fundamental line of the local group dwarf galaxies*, MNRAS, 390, 1453

Wright, T. (1750), *An original theory or new hypothesis of the Universe, founded upon the laws of nature, and solving by mathematical principles the general phenomena of the visible creation: and particularly the via Lactea*, London

York, D. G., Adelman, J., Anderson, Jr., J. E., Anderson, S. F., Annis, J., Bahcall, N. A., Bakken, J. A., Barkhouser, R., Bastian, S., Berman, E., Boroski, W. N., et.al (2000), *The Sloan Digital Sky Survey: Technical Summary*, AJ, 120, 1579

Zucker, D. B., Belokurov, V., Evans, N. W., Kleyna, J. T., Irwin, M. J., Wilkinson, M. I., Fellhauer, M., Bramich, D. M., Gilmore, G., Newberg, H. J. (2006a), *A Curious Milky Way Satellite in Ursa Major*, ApJ, 650, L41

Zucker, D. B., Belokurov, V., Evans, N. W., Wilkinson, M. I., Irwin, M. J., Sivarani, T., Hodgkin, S., Bramich, D. M., Irwin, J. M., Gilmore, G., Willman, B., Vidrih, S., et.al (2006b), *A New Milky Way Dwarf Satellite in Canes Venatici*, ApJ, 643, L103